LEGIBILITY NOTICE

A major purpose of the Technical Information Center is to provide the broadest dissemination possible of information contained in DOE's Research and Development Reports to business, industry, the academic community, and federal, state and local governments.

Although a small portion of this report is not reproducible, it is being made available to expedite the availability of information on the research discussed herein.

ORNL/TM--11158

DE89 015656

Metals and Ceramics Division

SIMULATION OF THE WELDING OF IRRADIATED MATERIALS

Hua Tay Lin

Date Published - July 1989

Prepared for the
DOE Office of Fusion Energy
AT 15 02 03 A

Prepared by the
OAK RIDGE NATIONAL LABORATORY
Oak Ridge, Tennessee 37831-6285
MARTIN MARIETTA ENERGY SYSTEMS, INC.
for the
U.S. DEPARTMENT OF ENERGY
under contract DE-AC05-84OR21400

TABLE OF CONTENTS

LIST OF TABLES

LIST OF FIGURES

SIMULATION OF THE WELDING OF IRRADIATED MATERIALS

Hua Tay Lin

ABSTRACT

Helium was uniformly implanted using the "tritium trick" technique to levels of 0.18, 2.5, 27, 105 and 256 atomic part per million (appm) for type 316 stainless steel, and 0.3 and 1 appm for Sandvik HT-9 (12 Cr-1MoVW). Both full penetration as well as partial penetration welds were then produced on control and helium-containing materials using the autogenous gas tungsten arc (GTA) welding process under full constraint conditions. For full penetration welds, both materials were successfully welded when they contained less than 0.3 appm helium. However, welds of both materials, when containing greater than 1 appm helium, were found to develop cracks during cooling of the weld. In type 316 stainless steel, catastrophic intergranular failure occurred during cooling in the heat-affected zone (HAZ), leading to a crack extending nearly the length of the plate at the completion of the weld. When the helium content of type 316 stainless steel exceeded 100 appm both HAZ cracking and brittle failure along the center line of the fusion zone occurred during cooling. In HT-9 the observed cracking was limited to only the beginning region of the weld. The cracking was found to be intergranular in nature and occurred along prior-austenite grain boundaries of the HAZ. For partial penetration welds, underbead intergranular cracking occurred in the HAZ of type 316 stainless steel containing helium greater than 2.5 appm.

Transmission and scanning electron microscopy indicated that the HAZ cracking was caused by the growth and coalescence of grain boundary (GB) helium bubbles. This cracking occurred as a result of the combination of high temperatures and high shrinkage tensile stresses. The cracking in the fusion zone was found to result from the precipitation of helium along dendrite interfaces. A model based on the kinetics of diffusive cavity growth is presented to explain the observed results. The model proposes a helium bubble growth mechanism which leads to final intergranular rupture in the heat-affected zone. Results of the present study demonstrate that the use of conventional fusion welding techniques to repair materials degraded by exposure to irradiation environments may be difficult if the irradiation results in the generation of helium equal to or greater than 1 appm. However, preliminary welding studies of helium-doped 20% cold-worked type 316 stainless steel, rapidly solidified type 304 stainless steel and PCA (Ti-modified type 316 stainless steel) indicate that the HAZ cracking tendency can be significantly reduced through modification of alloy composition and fabrication.

I. INTRODUCTION

The bombardment of materials with energetic neutrons produces significant physical damage by the displacement of atoms from their normal atomic sites and consequent generation of lattice defects [1,2]. The displacement damage occurs when the recoil energy transferred from impinging particles exceeds the threshold energy for displacement of atoms (in the range of 20-40 eV for metals). In a typical fission reactor, neutrons have energies of a few hundred KeV and thus easily exceed the lattice displacement threshold energy. The consequent displacement cascades result in the generation of point defects, vacancies and interstitials, which further cluster into voids, stacking-faults, or dislocation loops. In addition, thermal neutrons as well as high energy neutrons of a few MeV also produce transmutation reactions which produce considerable concentrations of foreign elements such as the insoluble inert gas, helium. The physical damage induced by energetic radiation alters the physical properties of irradiated materials noticeably. In particular, changes in dimensions (induced by swelling and irradiation creep), chemical composition and mechanical properties may be extreme. Consequently, the gradual deterioration of mechanical properties and corrosion resistance plays a decisive role in the life time of components of nuclear reactors. It is reasonable, therefore, to anticipate that the repair and replacement of degraded

reactor components, such as the reactor vessel and interiors of fission reactors and the first wall and blanket structures in fusion reactors, will be required as a result of this aging process. Such repair processes will require the use of conventional welding techniques.

Attempts to weld irradiated materials have been conducted by several investigators [3-5]. Only mixed results have been achieved. Their results will be discussed in detail in the literature review section of this thesis. The critical issue in determining the post-irradiation weldability of a material is the fact that neutron irradiated material will contain entrapped helium (He) which is not initially present. This helium is generated as the result of (n,α) reactions with alloy constituents, such as B, Ni and Fe [6,7]. The nature of helium in metals, such as its solubility, nucleation to form bubbles, migration and growth of these bubbles, are known to drastically affect the materials' properties. These effects will be discussed in the section entitled behavior of helium in metals. The very low solubility of helium in metals [8,9] results in its tendency to precipitate out as bubbles. Preferred nucleation sites for the helium bubbles are inhomogeneities, such as precipitate interfaces, dislocations, and, most importantly, grain boundaries. At elevated temperatures, these bubbles will grow rapidly under the influence of either internal or external (creep) stresses which weaken the grain boundaries (GBs). As these bubbles coalesce along the grain boundaries, premature intergranular fracture or helium embrittlement

will occur. Since welding processes produce internal stresses (differential thermal expansion) and elevated temperatures, the entrapped helium may severely affect the weldability and post weld properties of the irradiated material. Furthermore, welding produces severe gradients in both stress and temperature which enhance the growth rate of helium bubbles further degrading the material properties.

A detailed study of welding of irradiated materials would be extremely difficult because of the hostile radioactive environment and airborne contamination generated by the welding process. Such studies would therefore be limited to in-situ reactor locations or engineered radioactive isolation chambers known as "hot cells". Developing a fully quantitative understanding by performing well-controlled, instrumented tests in such facilities is very difficult and time consuming. The radiological hazards associated with the handling and analysis of radioactive materials alone limits the scope of such studies and insures that they will be extremely costly.

The present study was carried out to provide a scientific background for understanding the effects of neutron irradiation on the subsequent weldability of materials. To avoid remote hot cell investigations, which are both lengthy and expensive, welding was performed on helium-doped material to simulate the principal effects which occur during the joining of irradiated materials. Helium was uniformly implanted into the test material via the "tritium trick" [10]. Type 316 stainless steel (austenitic stainless steel) and

Sandvik HT-9 (ferritic stainless steel) were chosen for the study because of the extensive data base detailing their properties and microstructure in both unirradiated and irradiated conditions. However, the present study is primarily focused on type 316 stainless steel. A theoretical model to describe the helium bubble growth which leads to intergranular fracture of the heat-affected zone (HAZ) is proposed.

II. REVIEW OF LITERATURE

Only a few studies involving the welding of irradiated materials have been reported. Unfortunately, none of these have provided a systematic characterization of the observed weld defects. The first section in this chapter will describe previously reported experiments which have involved the welding of irradiated materials. Both the conditions (material and machine conditions) under which the welding was conducted and the success of the welding will be described to the extent allowed by interpretation of the original publication. This section will be followed by a review of important theoretical and experimental studies conducted to investigate the behavior of helium in metals. Solubility, bubble formation, helium and helium bubble migration, bubble growth, and helium embrittlement will be discussed. This information will provide the basis for development of the proposed model of grain boundary bubble growth which leads to final intergranular rupture in the HAZ during cooling of irradiated material welds.

History of Welding Irradiated Materials

The first publicly known attempt to weld irradiated materials was reported in 1969 by J. P. Maloney, et al. [3]. The program was initiated to repair cracks in the wall of the C-Reactor tank located at

the Savannah River Plant site in South Carolina. The tank is constructed of type 304 stainless steel. These cracks, located in regions known as knuckles, were judged to be intergranular and caused by a combination of corrosion and residual stresses. Repairing cracks in a radiation field > 10^5 R/hr presented a challenging problem and specialized remote welding equipment and techniques were developed. Patches were welded remotely over the cracks using Gas Tungsten Arc (GTA) welding. After repair, no leak was detected, and the results were deemed satisfactory. In 1984, leaks in the HAZ of these welds were again detected [11]. A similar repair was undertaken in 1986, but was not successful. Toe cracks developed in the repair weld HAZ. The cracks found at the perimeters of the patches were hypothesized to be caused by the presence of helium bubbles that formed an interconnected web of porosity at grain boundaries in the HAZ of the welds. In the knuckle region, the helium concentration was theoretically estimated to be 3 atomic part per million (appm). The C production reactor was retired from service in 1986 because of the lack of an effective method to repair weld cracks.

Results of GTA welding of fast breeder reactor irradiated AISI 304L stainless steel tubing was reported by M. M. Hall, Jr., et al. in 1978 [4]. The materials were irradiated in EBR-II at temperatures between 454 and 487°C to integrated fast fluences ranging from 1.38 x 10^{26} n/m^2 to 7.51 x 10^{26} n/m^2 (E > 0.1 MeV). The helium concentration in the 304L stainless steel tubing was not measured, but is estimated

to be approximately 3 to 15 appm. This estimate of helium concentration is based upon a helium generation rate of 2 appm/10^{26} n/m^2 for EBR-II [12]. Welding was performed remotely in a hot cell without external constraint of the weld parts. In two of the eleven developmental welds examined, intergranular fracture in the HAZ was observed. Pressure proof tests of 29 of these welded creep test capsules resulted in only two catastrophic failures. These failures occurred in the fusion-HAZ boundary. The occurrence of intergranular fracture in the HAZ was suggested to be caused by the precipitation of helium bubbles at the grain boundaries, coupled with thermal shrinkage of the tube following weld pool solidification. However, based upon the high success rate, it was concluded by Hall, et al. that irradiated materials may be successfully welded using conventional GTA welding techniques.

Weld bend tests on irradiated 20% cold-worked (CW) 316 stainless steel were conducted by Atkin [5] in 1981. This work was conducted to investigate the feasibility of repair welding stainless steel materials in a fusion reactor. The material studied was sectioned from a 20% CW 316 stainless steel EBR-II duct which was irradiated at approximately 400°C to a peak fluence of 12.6 x 10^{26} n/m^2 (63 dpa) (E > 0.1 Mev). The helium level in the 20% CW 316 stainless steel was not measured, but is estimated to be between 4 and 25 appm. The helium generation rate indicated above was used to make this estimate [12]. The irradiated material which, was 1 mm thick, was butt-welded using pulsed GTA welding without externally constraining the plates. Post-weld bend

tests were performed at deflection rates between 10^{-4} and 10^{-2} mm/sec at temperatures between 400 and 620°C. Results of weld bend tests indicated that all welded specimens were sound and free from cracks. This study concluded that 20% CW 316 stainless steel irradiated to fluence levels of 12.6×10^{26} n/m^2 (E > 0.1 Mev) can be successfully welded using conventional GTA welding techniques.

Behavior of Helium in Metals

An understanding of the behavior of helium in metals will provide the basis for the development of a model of grain boundary bubble growth which leads to intergranular cracking and final rupture in the HAZ during cooling of irradiated material welds. In this section and subsequent subsections, descriptions of the solubility, bubble formation, helium and helium bubble migration, bubble growth, and helium embrittlement, developed by previous investigators, will be presented.

Solubility

The subject of inert gases in metals has been extensively reviewed by Blackburn [13]. The closed shell electronic configuration leads the inert gases to exhibit a complete lack of chemical reactivity with metals. The behavior of helium atoms in metals is governed by the energies in different lattice sites which determine the solubility, the migration paths, the trapping to defects and the nucleation and growth of helium bubbles. Rimmer and Cottrell [14] have applied empirical potentials, an average of the He-He and Cu-Cu potentials, to calculate

the energy of interstitial and substitutional solutions of helium atoms in Cu. The energies of solution for interstitial and substitutional solutions are 2.5 eV and 5.5 eV, respectively. The high solution energy indicates that helium has an extremely low solubility in metals either interstitially or substitutionally. Theoretical helium concentrations can be obtained by [15]

$$C_{He} = [h/(2\pi mkT)^{1/2}]^3(P/kT)\exp[(\Delta S/k)-(\Delta H/kT)] \quad (1)$$

where m is the mass of gas atom, P is the pressure, T is the temperature, h is Planck's constant, k is Boltzmann's constant, ΔS is the nonconfigurational contribution to the entropy by the solution atom and ΔH is the change of solution enthalpy when a gas atom at rest is brought into the lattice. The theoretical values of ΔH for substitutional and interstitial solutions of helium in nickel [16] are approximately 2.94 eV and 4.52 eV, respectively. As a consequence, the concentration of helium in thermal equilibrium in interstitial sites, C_{Hei}, will be much smaller than in substitutional sites, C_{Hes}, since

$$C_{Hei}/C_{Hes} = \exp[(\Delta H_i-\Delta H_s)/kT] \ll 1 \quad (2)$$

Using equation (1) the theoretical helium concentration in nickel at 1700K at 10 MPa was calculated to be approximately 10^{-14} appm [16]. Experimentally, the helium concentration was measured to be less than 10^{-10} appm [8].

Helium Bubble Formation

Because of the extremely low solubility of helium in metals, high supersaturation levels of helium are easily obtained during doping. This inevitably leads to the formation of helium clusters or bubbles.

Three helium bubble formation mechanisms have been proposed by previous investigators. These mechanisms are: self-interstitial emission [17-20], loop punching [21,22] and thermal vacancy absorption [23]. If the vacancy concentration is much smaller than the helium concentration, bubbles can form by athermal processes, such as self-interstitial emission and loop punching. These mechanisms are favored at low temperatures ($T < T_m/3$, where T_m is the melting point of metals) and in the absence of displacement damage which creates vacancies. The formation of helium-vacancy clusters in metals by self-interstitial emission has been studied through computer simulation by Wilson, et al. [17-20]. This theory, also referred to as the self-trapping model, calculates and analyzes the binding energies for various helium cluster-metal atom configurations. These investigations indicate that the helium interstitial produces considerable distortion to the surrounding lattice and, hence, might well create an elastic strain field which could trap other helium atoms. It has also shown that the metal atom could be ejected by the force of a surrounding cluster of helium atoms. Calculations show a cluster of five helium atoms (as shown in Figure 1a) would be sufficient to eject a metal atom. The ejected metal atom then spontaneously becomes a self-interstitial, leaving a vacancy for the helium interstitials to fall into (Figure 1b). Once the helium cluster is in the vacancy it is deeply trapped by a considerable energy. It was also pointed out by Wilson that the self-interstitials have a strong propensity to agglomerate to form dislocation loops at the embryonic helium bubble due to the resultant

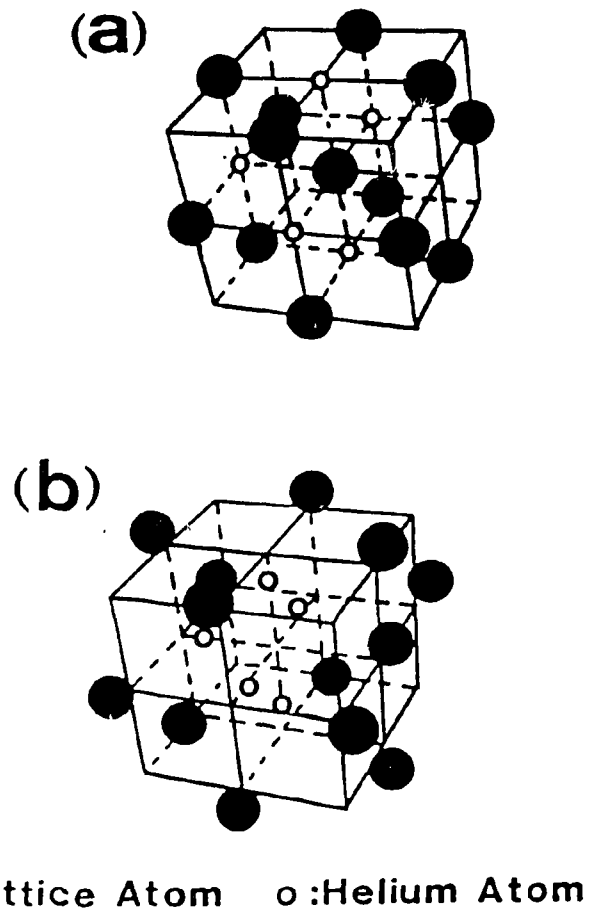

Fig. 1. Self-interstitial emission mechanism for helium bubble formation. (a) Elastic strain field traps five helium interstitial atoms, and (b) the ejection of a metal lattice atom resulting in the formation of a metal-helium near-Frenkel pair (after Wilson [18]).

reduction in elastic strain. By continuous repetition of this self-trapping process helium bubbles will form in the absence of thermal vacancies or radiation damage. The homogeneous nucleation of helium bubbles can be enhanced by the introduction of traps such as impurities or inclusions in stainless steels. Experimentally, the formation of helium bubbles and interstitial dislocation loops at an energy level below the displacement threshold energy have been reported by several investigators [24,25]. These results support the proposed self-interstitial emission model.

A helium bubble can also be formed by the mechanism of loop punching proposed by Greenwood, et al. [21]. Figure 2 shows the schematic for the loop punching process. The loop punching mechanism can occur if helium pressure in the cluster exceeds a threshold value given by

$$P > 2\gamma_s/r + \mu b \log(r/b)/2\pi r \qquad (3)$$

where P, r and γ_s are the pressure, radius and surface energy of the helium bubble, μ is the shear modulus of the material and b is the length of the Burger's vector of the resulting dislocation loop. In this mechanism, an over-pressurized bubble can produce its own vacancies, and relieve its pressure by punching out a platelet of interstitial atoms along a glide plane thus producing an interstitial dislocation loop. Direct evidence of this mechanism has been argued by Evans, et al. [22], who observed dislocation loops adjacent to helium bubbles lying parallel to a common (111) glide plane in molybdenum.

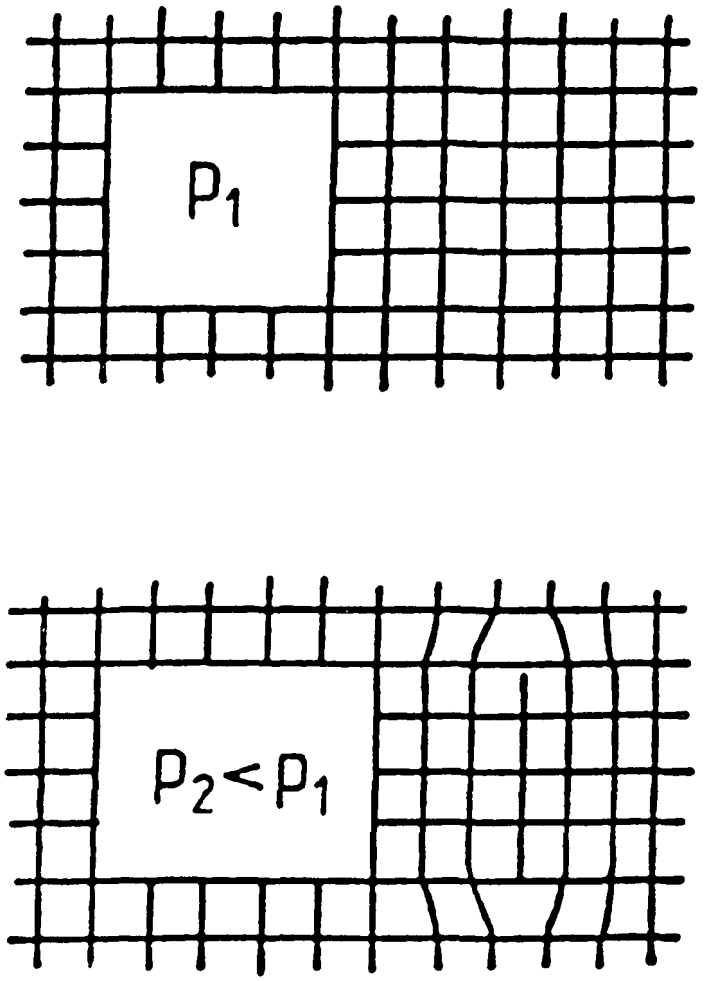

Fig. 2. Dislocation loop punching mechanism. Athermal relaxation of very high pressures in small bubbles occurs through the creation of interstitial loops. P_1 is initial bubble pressure and P_2 is the lower final pressure after creation of an interstitial loop (after Ullmaier [26]).

At elevated temperatures, where sufficient thermal vacancies are available ($T > 0.5\ T_m$), thermal vacancy absorption becomes important. The bubbles under this mechanism form by thermal nucleation involving helium atoms and vacancies [23]. Helium desires to precipitate at vacancy sites due to the strong binding energy of a helium atom and vacancy. Only a nucleation barrier stands in the way of precipitation in such cases. Since the nucleation barrier can be strongly reduced by the presence of lattice heterogeneities (defects, dislocations, grain boundaries and precipitates), these often serve as preferred nucleation sites.

Helium and Helium Bubble Diffusion

The diffusion of helium atoms in metals is achieved by three mechanisms: interstitial migration, vacancy migration and impeded interstitial migration [26]. Figure 3 shows a schematic of these three migration mechanisms. At low temperatures ($T < 0.5\ T_m$) and under conditions where there are no thermal vacancies nor traps for helium, helium atoms can migrate via jumps between interstitial locations (Figure 3a) with very small activation energy (< 0.5 eV). At temperatures above $0.5\ T_m$, helium atoms can migrate by the vacancy mechanism in which helium-vacancy pairs interact with a further vacancy (Figure 3b), giving an effective helium migration energy similar to that of self-diffusion. The energy of the vacancy mechanism is predicted to be 2.9 eV [23]. At elevated temperatures the substitutional helium atoms may dissociate from their vacancies, and then migrate interstitially until they are again trapped (Figure 3c).

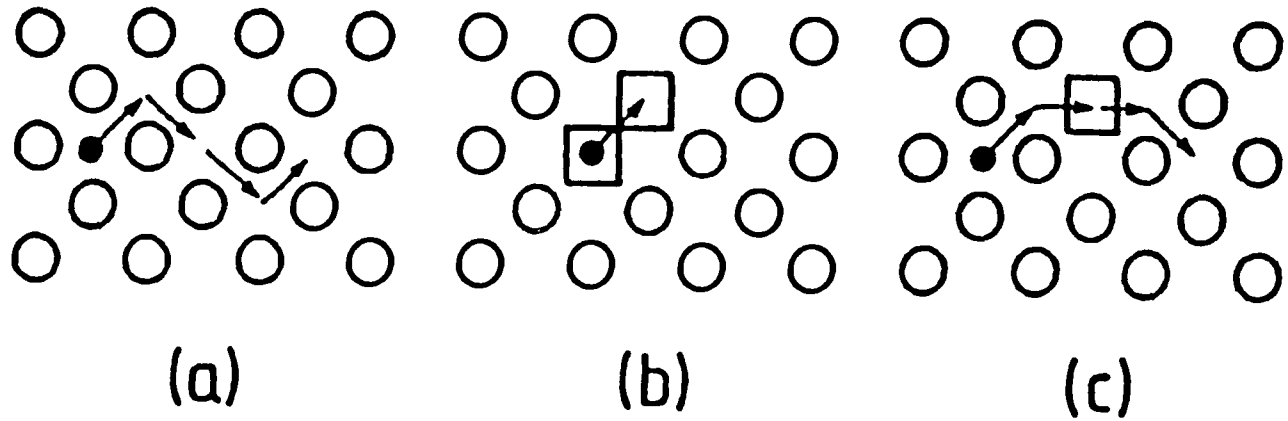

Fig. 3. Three possible mechanisms of helium atom diffusion through the lattice by (a) interstitial migration, (b) vacancy mechanism, and (c) impeded interstitial migration (after Ullmaier [26]).

In the absence of external influences, such as irradiation, dissociation can occur by thermal activation. The energy for impeded interstitial migration is predicted to be 0.8 eV [27]. The above mentioned mechanisms are only valid for materials without extended defects. In reality, the diffusion of helium may be enhanced by easy migration paths, such as dislocations or grain boundaries. It may be impeded by trapping on impurity atoms, precipitates and voids.

The first observation that helium bubbles can migrate bodily through the metal was reported by Barnes [25] in Cu which was bombarded by high-energy α-particles. The migration may occur in a random manner when no driving forces are imposed on the materials or it may be biased due to an imposed gradient. The possible mechanisms for bubble movement (D_b) are surface diffusion (D_s), volume diffusion through the matrix (D_{sd}) or volume diffusion through the vapor phase (vapor transport) (D_g). Figure 4 shows a schematic of mechanisms of helium bubble migration. It is generally believed, also concluded by Shewmon [29], that surface diffusion is the dominant transport mechanism for bubble migration. Greenwood [30] and Gruber [31] have shown that bubble diffusivity, D_b, is related to the surface diffusivity, D_s, by the equation

$$D_b = 0.301(a_o/r)^4 D_s \qquad (4)$$

where a_o is the lattice parameter and r is the bubble radius.

The bubble may also migrate in the presence of driving forces, such as thermal gradients, stress gradients, moving dislocations and grain boundaries. The bubble velocity (v_b), as developed by Nichols

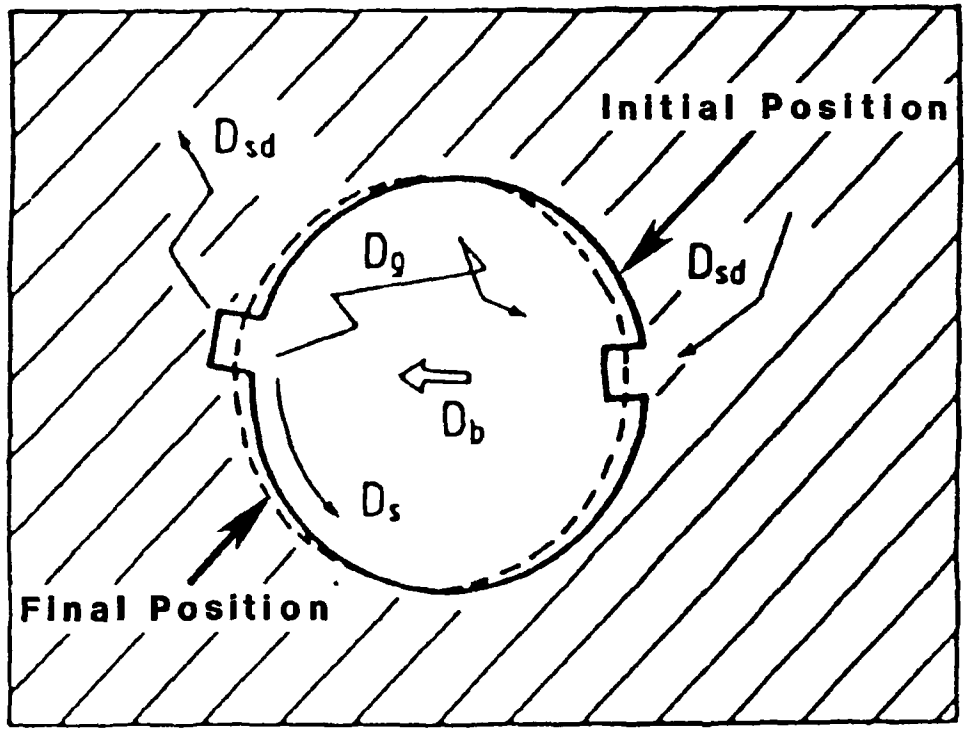

Fig. 4. Helium bubble migration (D_b) can occur by surface diffusion (D_s), volume diffusion (D_{sd}) or vapor transport (D_g) of lattice atoms (after Ullmaier [26]).

[32], can be related to its mobility (M_b) by the equation

$$v_b = M_b F_b \tag{5}$$

Where M_b is the bubble mobility and F_b is the force on the bubble. The relationship between bubble mobility and bubble diffusivity can be expressed by the Nernst-Einstein equation:

$$M_b = D_b/kT \tag{6}$$

If the force on the bubble is known, combination of equations (5) and (6) provides the following equation between v_b and D_b:

$$v_b = D_b F_b/kT \tag{7}$$

The directed bubble migration in a temperature gradient has been analyzed by Shewmon [29] and Speight [33]. The migration velocity of bubbles under the action of a temperature gradient is expressed by

$$v_b = (3D_s Q_s a_o/kT^2 r)(dT/dx) \tag{8}$$

where Q_s is the heat of transport for surface thermal self-diffusion. For the case of a stress gradient, the force on the bubble is given by [34-36]

$$F_b = -[4\pi r^4 \sigma/(3\sigma r + 4\gamma_s)](d\sigma/dx) \tag{9}$$

where σ is the applied stress and γ_s is the surface energy. The bubble velocity can then be obtained by the combination of equations (7) and (9)

$$v_b = -D_b[4\pi r^4 \sigma/(3\sigma r + 4\gamma_s)](d\sigma/dx)/kT. \tag{10}$$

It is known that nucleation of helium bubbles can readily occur on dislocation lines and grain boundaries. Their motion, therefore, will be constrained to the movement of dislocations and grain boundaries.

An applied stress will cause a dislocation to bow, and a force $F = 2\Gamma\cos\theta$, will be exerted upon the bubble, where Γ is the line tension of the dislocation (about μb^2, where μ is the shear modulus and b is the Burgers vector of the dislocation line) and 2θ is the angle between the two dislocation segments at their point of intersection with the bubble surface. For a restraining force less than $2\Gamma\cos\theta$, the bubble will be dragged along by the moving dislocation. The velocity of the moving bubble is given by [37]

$$v_b = (1/8\pi)(D_s/kT)(a_o/r)^4 F \qquad (11)$$

where F is the applied force. If a force in excess of 2Γ is applied to the dislocation it will leave the bubble. Similarly, any migration of a grain boundary will cause a bubble to move along under a restraining force of $\pi r\gamma_{gb}\sin 2\phi$ where γ_{gb} is the interfacial energy of the grain boundary, and ϕ is the angle the curved boundary makes at the bubble surface with the position of a plane boundary. However, if the applied force is greater than $\pi r\gamma_{gb}$, the bubble will pull away from the grain boundary. In the case of welding, the driving forces on dislocations and grain boundaries originate from the thermal and stress gradients.

Helium Bubble Growth

After nucleation is complete, helium bubbles can grow under the presence or absence of an externally applied stress. The bubbles in the grain interior and in stress-free grain boundaries may grow by two possible mechanisms: bubble migration and coalescence [30,31,37,38] and/or Ostwald ripening [39,40]. These mechanisms have been studied extensively to determine their role in fission gas swelling. The first

theory of swelling by bubble migration and coalescence was reported by Greenwood, et al. [30]. Subsequently, the work was extended by Gruber [31] and Baroody [38] using analytical computational methods. The bubble migration and coalescence mechanism is based on the following assumptions: 1) the gas in the bubble obeys the ideal gas law, 2) the bubbles are in mechanical equilibrium with an unstressed solid ($p = 2\gamma_s/r$), 3) the bubbles migrate randomly by a surface diffusion mechanism, 4) there is no bubble interaction except immediate coalescence on contact, and 5) the bubbles are spherical in shape and initially have the same size. With these assumptions, the mean radius (r) of the bubble after several generations of coalescence, as given by the bubble migration and coalescence theory, is

$$r^5 = 1.48(a_o^4 D_s NkT/\gamma)t \qquad (12)$$

where N is the total number of gas atoms and t is the time spent for bubble coalescence [31].

In addition to the migration and coalescence mechanism, Ostwald ripening [39,40] is also an important process for bubble growth. Ostwald ripening occurs due to a reduction in surface energy achieved by dissolution of small bubbles and growth of larger ones. This process may be thought of as driven by the different pressures in bubbles of different size which cause concentration gradients and thus permeation of gas atoms from small to large bubbles (Figure 5). As reported by Greenwood, et al. [39], the growth rate of a bubble of radius r by Ostward ripening is,

$$dr/dt = D_{He}(1/r_m - 1/r)\exp(-G/kT) \qquad (13)$$

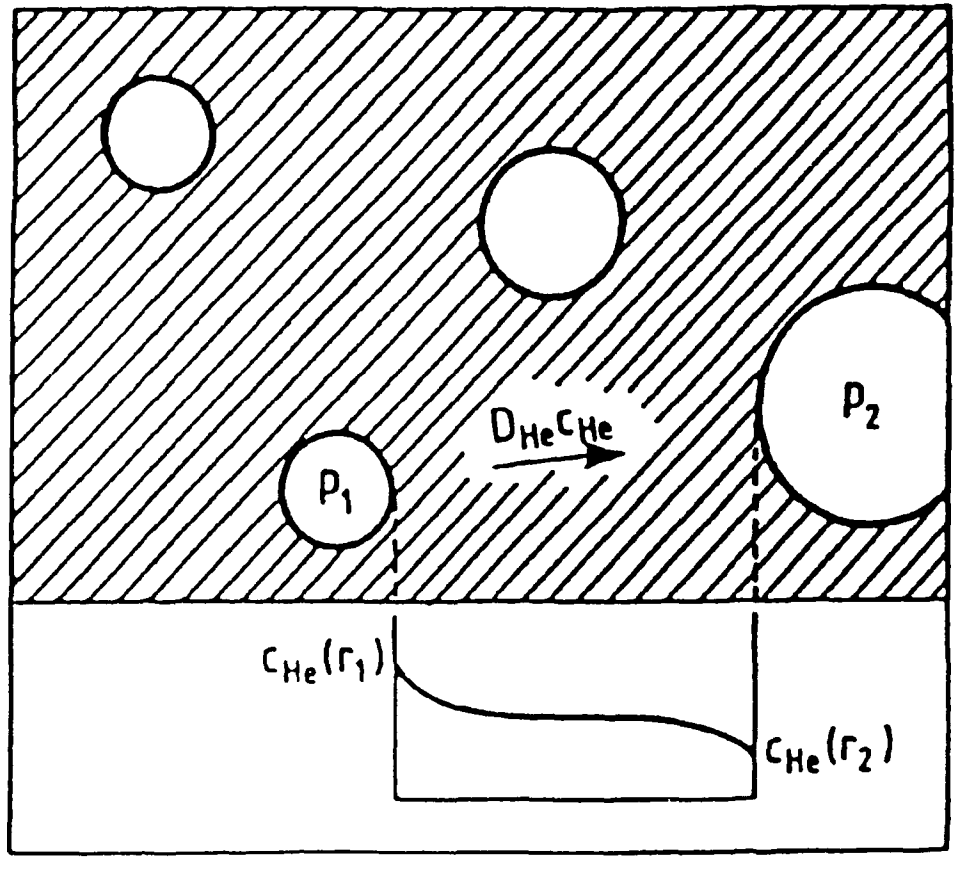

Fig. 5. Ostwald ripening mechanism. Different pressures in bubbles of different size cause concentration gradients and thus permeation of gas atoms from small to large bubbles. In diagram $P_1 > P_2$ (after Ullmaier [26]).

where D_{He} is helium atom diffusivity, G is the free energy of solution of the helium, and r_m is the arithmetic mean of the bubble radii at any instant.

When a material is subjected to an external stress, the bubbles (voids) in grain interiors and grain boundaries may grow by the sweeping of the small bubbles by moving dislocations and grain boundaries at high temperature [41] or vacancy condensation. It is generally accepted that the growth of helium bubbles on the grain boundaries is the primary cause of high-temperature embrittlement of irradiated materials. Therefore, only GB bubble growth will be considered in the following discussion. There are two limiting kinds of cavity growth: unconstrained and constrained cavity growth (Figure 6). In the case of unconstrained cavity growth, cavities are present on all of the grain boundaries in the solid and are free to grow to the point of complete failure. In the case of constrained cavity growth, cavities are present only on isolated boundaries. Here cavity growth on the boundary can proceed only if the surrounding matrix creeps. In the cases of helium-doped and/or neutron-irradiated materials, where helium bubbles are often found to be uniformly distributed on the grain boundaries, cavity growth will occur in an unconstrained manner. The following discussion is therefore limited to unconstrained cavity growth.

It is generally believed that the basic growth mechanism of cavities on grain boundaries is stress-induced diffusion of vacancies along the grain boundary. The void will grow when the applied stress σ

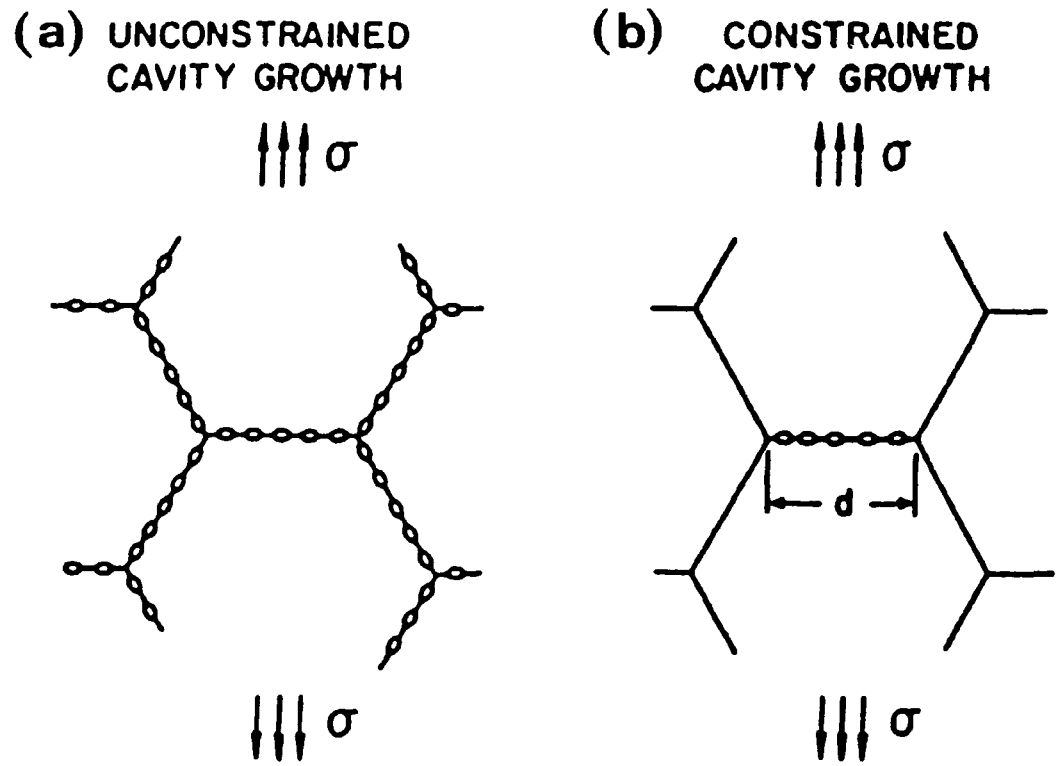

Fig. 6. Illustration of (a) unconstrained cavity growth, and (b) constrained cavity growth.

is greater than 0.76 γ_s/r [42], where γ_s is the surface tension of the void and r is the void radius. For the case of the over-pressurized helium bubble the internal pressure will provide an additional driving force to enhance bubble growth as has been discussed in detail by Gruber [43,44]. During cavity growth, atoms are transported from the cavity surface to the adjoining grain boundary. This diffusion occurs first along the cavity surface and then along the grain boundary where the atoms are eventually deposited. The process is anticipated to be controlled by the slowest of these diffusional mechanisms. Thus, two types of diffusive growth mechanisms can be distinguished: cavity growth controlled by grain boundary diffusion (equilibrium growth) and cavity growth controlled by surface diffusion (non-equilibrium growth) (Figure 7). The subject of diffusive cavity growth has been reviewed by Reidel in detail [45].

If diffusion in the grain boundary is slower than diffusion along the cavity surface, the growth process is controlled by grain boundary diffusion (Figure 7a). Surface diffusion occurs so rapidly that the cavities are able to maintain an equilibrium shape as they grow. This type of growth mechanism was first proposed by Hull and Rimmer [46] and has been studied extensively [47-51]. The most complete and exact treatment of this growth mechanism has been given by Speight and Beere [50]. Their results can be expressed as [46]

$$dr/dt = 2\pi\delta_{gb}\Omega D_{gb}\sigma/arkT \qquad (14)$$

where a is the spacing between centers of cavities, D_{gb} is the self-diffusion coefficient on grain boundaries, δ_{gb} is the thickness of

ORNL-DWG 89-2222

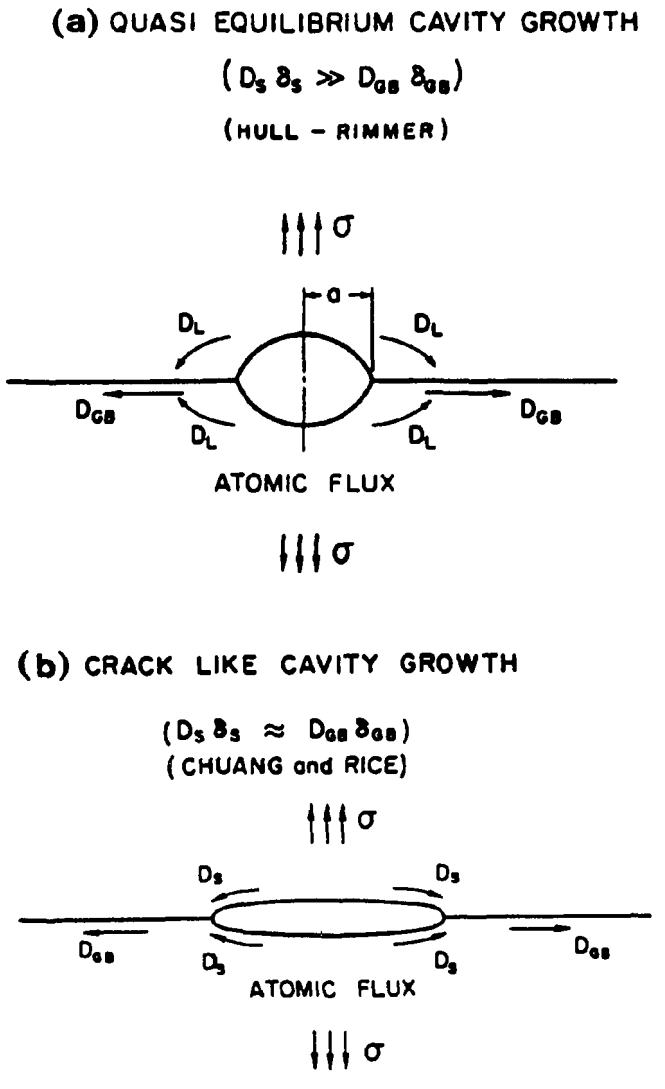

Fig. 7. Illustration of (a) quasi-equilibrium (Hull-Rimmer) cavity growth, and (b) crack-like (Chuang-Rice) cavity growth.

grain boundary available for diffusion, Ω is the atomic volume, σ is the applied stress and kT has its usual meaning.

If diffusion along cavity surfaces is slower than diffusion along the grain boundaries, then the cavity growth will be controlled by surface diffusion (Figure 7b). The cavity develops a crack-like shape as it grows because atoms are removed from the tip of the cavity faster than they are replaced by surface diffusion from other parts of the cavity surface. This is called non-equilibrium cavity growth because the cavities have a non-equilibrium shape during growth. The first study of crack-like cavity growth was performed by Chuang and Rice [52] and Chuang, et al [53]. At high stresses or when the surface diffusivity is much greater than the grain boundary diffusivity, the cavity growth can be approximately expressed by [53]

$$dr/dt = \Omega(D_{gb}\delta_{gb})^{3/2}\sigma^{3/2}/2kT(D_s\delta_s)^{1/2}a^{3/2}\gamma_s^{1/2} \qquad (15)$$

where D_s is the surface diffusivity, δ_s is the thickness available for surface diffusion and γ_s is the surface energy. In addition, Chen [54] has proposed that the crack-like cavity growth may be caused by grain boundary sliding, which distorts and sharpens the shape of the cavity to prompt crack-like surface diffusion. This sharpening causes the tip velocity during cavity growth to be limited by surface diffusion regardless of the magnitude of D_s/D_{gb}. Nevertheless, cavity growth by grain boundary sliding is not likely to occur under very high surface diffusivity. Under such cases, surface diffusion restores the cavity shape to its original configuration resulting in no change in the volume of the cavity.

Another possible mechanism for bubble growth in grain boundaries is the coalescence of GB helium bubbles [55]. This mechanism was proposed to describe the growth of sub-critical bubbles on grain boundaries. It was assumed that bubbles attached to grain boundary dislocations can move through a combination of glide and climb along the grain boundary during high temperature creep. The dislocation interactions within the boundary will lead to continuous bubble impingement and coalescence. As the bubbles reach a critical size, they may then grow by a stress-induced diffusion of vacancies along grain boundaries.

Helium Embrittlement

The first observation of the degradation of high-temperature mechanical properties of neutron irradiated materials due to helium bubbles was reported by Barnes [6]. After two decades of research, stress-enhanced growth of helium bubbles as suggested by Barnes is still accepted as the mechanism of helium embrittlement. Under this mechanism, helium bubbles precipitate on grain boundaries and grow under the influence of high temperature and stress. The growing bubbles first weaken the grain boundaries and finally perforate them leading to premature intergranular fracture. Trinkaus and Ullmaier [56-59] have published the most complete helium embrittlement theory to date. In addition, a detailed review of the influence of helium on the properties of structural materials, including tensile, creep, fatigue and swelling has been reported by Ullmaier [23].

In general, austenitic stainless steels are known to embrittle severely at high temperatures, above 600°C (> 0.45 T_m). However, the temperature at which helium embrittlement occurs depends on the materials' helium content. Tensile properties of solution annealed (SA) type 316 stainless steel as a function of helium concentration and test temperature (equivalent to irradiation temperature) have been reported in detail by Bloom [60]. The ductility of specimens irradiated in HFIR to high He:dpa ratios, high helium concentrations (about 4000 appm), is in the range of 0.6 - 2.6% for temperatures up to 575°C. At higher temperatures the total elongation drops to zero. Specimens with low helium contents (about 25 appm) have reasonable values of ductility (10 to 20%) for temperatures below 700°C. Ductility then drops to below 2% at higher temperatures. The yield strength of irradiated specimens is greater than control specimens for temperatures below 650°C. The increase in yield strength results from the strengthening effect caused by displacement damage. Above 650°C the specimens which contain high amounts of helium fail in the elastic region.

The creep-rupture properties of SA type 316 stainless steel, which was irradiated in EBR-II to a maximum fluence of 2.7 x $10^{22}/cm^2$, were reported by Bloom and Stiegler [61]. Results of the post-irradiation tests indicated that both rupture life and strain after creep testing at high temperatures were dramatically reduced by the presence of helium (about 5 appm). The rupture life was reduced by a factor of 3 or less in the temperature range 550 to 700°C. At 750°C the rupture

life was reduced by 1 to 2 orders of magnitude. In addition, the creep rates and stress dependency of the creep rate were not significantly affected by helium concentration in the temperature range 550 to 700°C. The creep rate was, however, markedly increased at 750°C. Analysis of creep strain data showed that high temperature embrittlement caused by helium started at around 550°C.

The effect of helium on fatigue behavior of SA type 316 stainless steel was reported by Sonnenberg, et al. [62,63]. The helium was implanted using α-implantation techniques. Results showed that the fatigue life is only slightly reduced as a result of helium implantation up to 1000 appm for temperatures below 500°C. At higher temperatures an intergranular fracture mode associated with strong reductions in fatigue life was observed. Results also indicated that the number of cycles to failure, N_f, decreases with decreasing cyclic frequency. This was due to the dilatational part of the fatigue cycle which must be long enough so that grain boundary helium bubbles are able to overcome the barrier to unstable growth by stress-induced diffusional growth.

Fatigue behavior of the irradiated 20% cold-worked type 316 stainless steel has been studied extensively by Grossbeck, et al. [64-66]. Specimens were irradiated in the HFIR at 430, 550°C to damage levels as high as 15 dpa. Helium produced in the materials varies from 200 to 900 appm depending on neutron exposure level. Fatigue tests were conducted at the same temperatures as for irradiation. Further tests were conducted at 650°C on materials irradiated at 550°C.

Results indicated that fatigue life was reduced by about a factor of 3-10 upon irradiation at 430°C. Also, irradiation reduced the strain range level for the endurance limit from 0.35 to 0.3%. At 550°C, no effect on the fatigue curves was observed. However, the endurance limit was again reduced from 0.35 to 0.3% upon irradiation. Fatigue testing at 650°C revealed that cyclic life was not significantly affected by the irradiation at 550°C. Nevertheless, unlike the results of tests of the same materials at 550°C, no endurance limit was observed. This was attributed to thermal creep during the tension portion of the fatigue cycle.

A study of the effect of helium on the tensile properties of HT-9 (12Cr-1MoVW) has been conducted and reported in detail by Klueh [67, 68]. The 12 Cr steels were doped with 2% Ni prior to irradiation to achieve helium levels characteristic of fusion reactors. Standard HT-9 contains less than 0.5% Ni. Specimens were then irradiated in HFIR at 50, 300, 400 and 500°C to 10 dpa to produce up to 103 appm helium. The specimens were then tested at 300, 400, 500 and 700°C in a vacuum at a strain rate of 4×10^{-4} s^{-1}. Results show that there is no apparent decrease in total elongation of the HT-9 up to 103 appm helium at these test temperatures. In the worst case, the total elongation is still greater than 3%. The yield strength of irradiated HT-9 is generally higher than that of control material for temperatures below 500°C. The increase in yield strength is attributed to irradiation strengthening. The increase in number of helium-vacancy clusters, cavities, and dislocations are believed to provide the microstructural basis for

strengthening. Fatigue behavior of the same Ni-doped alloy was reported by Grossbeck, et al. [69]. The material was irradiated in the HFIR at 55°C to damage levels of 25 dpa to produce helium levels of 210 and 410 appm. Tests were conducted at room temperature. Results indicated that the irradiated Ni-doped materials exhibited shorter fatigue life than their control materials, but the difference was small. Helium concentrations up to 410 appm produced cyclic strengthening about 30% over unirradiated materials. This cyclic hardening, attributable largely to helium, resulted in degradation of the fatigue life. However, the fatigue life remained comparable to or better than unirradiated 20% cold-worked type 316 sstainless steel.

Only limited creep-rupture data on helium containing HT-9 are available. The German martensitic steel DIN 1.4914, which is similar to HT-9, was irradiated in the BR2 reactor at 600°C to produce about 90 appm helium [70]. The specimens were then creep tested at 600°C. The creep-rupture strain of the irradiated DIN 1.4914 was somewhat less than that of the unirradiated material. However, the rupture strain shows only a small decrease with decreasing strain rate in contrast to the irradiated austenitic steel. For the lowest strain rate, the ductility is still greater than 5%. Based on experimental results, HT-9 exhibits much more resistance to helium embrittlement than type 316 stainless steel at elevated test temperatures.

III. EXPERIMENTAL PROCEDURES

The objective of the experiments was to systematically characterize the effects of helium on the weldability of type 316 stainless steel. Studies of helium concentration effects, variable welding power input, and externally applied constraint conditions were conducted. The weldability of a second helium-containing material, the martensitic alloy (Sandvik HT-9), was also investigated to determine the applicability of the type 316 stainless steel results to other classes of steel. Helium contents ranging from 0.18 to 256 appm were introduced into type 316 stainless steel and 0.3 and 1 appm into HT-9 via the "tritium trick" technique. Two welding speeds, 3.6 mm/sec and 0.36 mm/sec, and two current input conditions, 24 A and 13 A, were investigated. The two current valus were used to produce full penetration and partial penetration welds to investigate the effects of variable heat input on HAZ cracking susceptibility. Furthermore, welds were completed with and without external constraint to compare the effects of external constraint on the cracking phenomena. The resulting weld defects and helium bubble morphology in the fusion zone and HAZ were characterized using scanning and transmission electron microscopy. Mechanical properties of welds were characterized by microhardness and tensile tests. A flow chart describing the overall

experimental program is shown in Figure 8. Detailed descriptions of the experimental procedures and techniques follows.

Material Preparation

Alloys from the austenitic and ferritic classes of stainless steel have been chosen as candidates for application as Fusion First Wall Materials [71]. The austenitic stainless steels are the most attractive alloys for near term fusion reactor applications. Their attractiveness stems from the developed technology for producing, fabricating, and welding complex structures with a high degree of reliability, combined with physical and chemical properties that are adequate for initial fusion test reactor requirements. In addition, the irradiation effects data base for the austenitic stainless steels far exceeds that of any of the other candidate alloy. Ferritic stainless steels have been extensively used in high temperature applications such as superheater and reheater tubing in fossil fired plants and in nuclear power plants. Also, they have been actively investigated in the U. S. Liquid Metal Fast Breeder Reactor (LMFBR) Materials and Structures Program since 1974 [72]. The irradiation data indicate that ferritic steels exhibit little swelling under fast neutron and thermal neutron bombardment [73-75]. Also, these steels swell much less than austenitic stainless steels exposed to similar conditions. However, the irradiation results in HFIR reveal that void swelling increased with increasing helium generation [75]. This indicates that helium enhances the swelling of ferritic steels under

ORNL-DWG 89-2221

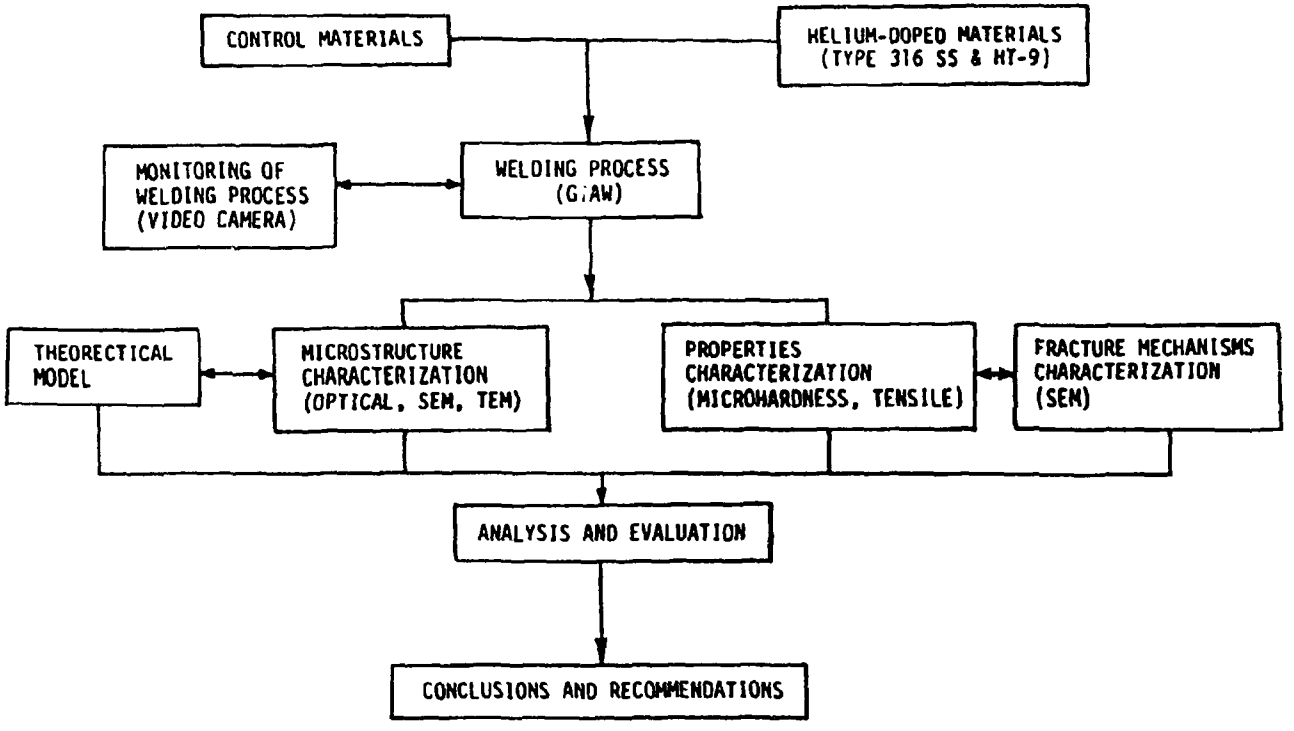

Fig. 8. Flow chart of experimental procedures.

irradiation. Nevertheless, these irradiation data, combined with the large commercial data base available and the favorable physical and mechanical properties of ferritic steels lead them to be considered as candidates for fusion reactor applications. For these reasons, Type 316 stainless steel (LMFBR Program reference heat 8092297) and HT-9 (Combustion Engineering Co. heat 9607-R2) were investigated in this program. The chemical compositions for both alloys are listed in Table 1.

The type 316 stainless steel was received in the form of 1.52 mm cold rolled plates. These plates were annealed at 1050°C for one hour in an inert atmosphere followed by cold-rolling to 0.76 mm (50% cold work). The 0.76 mm plates were then mechanically polished and ultrasonically cleaned in acetone. Following the cleaning process, the test specimens were again solution annealed at 1050°C for 1 hour in an inert gas atmosphere which resulted in an average grain size of 70 μm. Optical photomicrographs of type 316 stainless steel etched electrolytically with 40% HNO_3-H_2O solution are shown in Figure 9a. The average grain size was determined by measuring six different regions using an intercept method [76].

The HT-9 was received in the form of 0.76 mm cold rolled plates. These plates were solution annealed at 1050°C for one half hour in an inert gas atmosphere, and air-cooled. They were then given a tempering treatment at 700°C for 1 hour in an inert gas atmosphere followed by air-cooling. The resulting optical microstructure of HT-9 is tempered

Table 1. Chemical composition of type 316 stainless steel (Reference Heat 8092297) and HT-9 (Heat 9607R2)

Element (wt%)	316 SS	HT-9
C	0.057	0.2
Mn	1.86	0.57
Si	0.58	0.17
Ni	13.48	0.51
Cr	17.25	12.10
Mo	2.34	1.04
V	-	0.28
P	0.024	0.016
S	0.019	0.003
Ti	0.02	0.001
N	0.03	0.027
W	-	0.45
Al	-	0.006
Co	0.02	-
Cu	0.10	-
Pb	0.003	-
Sn	0.004	-
B	0.0005	-
Fe	Balance	Balance

YE-13831

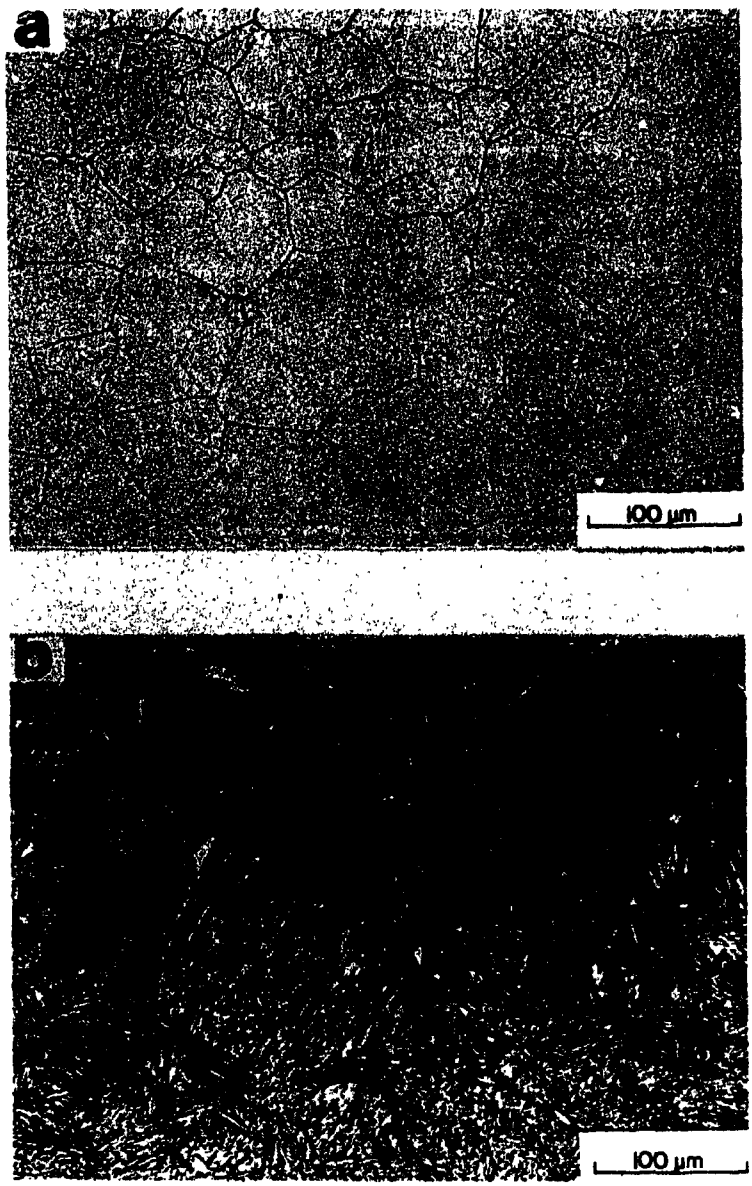

Fig. 9. Optical microstructure of plate surfaces prior to welding. (a) Type 316 stainless steel, and (b) HT-9.

martensite as shown in Figure 9b. A solution of 90% HO_2, 9% ml HNO3 and 1% HF was used to etch the sample.

Following the heat treatment, tensile specimens for control and helium-doping purposes were prepared using a punch and die in an orientation transverse to the rolling direction. Figure 10 shows the dimensions of tensile specimens tested in this program.

Helium-Doping Process

Helium was implanted in the test specimen using the "tritium trick" [10]. In this process, radioactive tritium is diffused at high temperatures into the material and then allowed to decay to form insoluble helium. Tritium which has a half life of 12.3 years undergoes the decay reaction $^3H \rightarrow \beta^- + {}^3He$. The "tritium trick" technique has the advantage of being able to charge large numbers of samples with a sizable concentration of helium in a relatively short time. Also, tritium decay involves only low-energy beta particles (18.6 KeV maximum, 5.7 KeV average), so specimen handling does not require shielding. Additionally, the recoil energy associated with the beta-decay of tritium is much too low to create any atomic displacement damage. Therefore, the effects caused by displacement damage, which are considered to be second order effects, can be isolated from the hypothesized principal effects of helium.

Figure 11 shows the high pressure charging vessel (autoclave) used for the tritium charging process. This doping process was conducted at Sandia National Laboratories (Livermore, California) through a collaborative research program between Auburn University, Oak Ridge

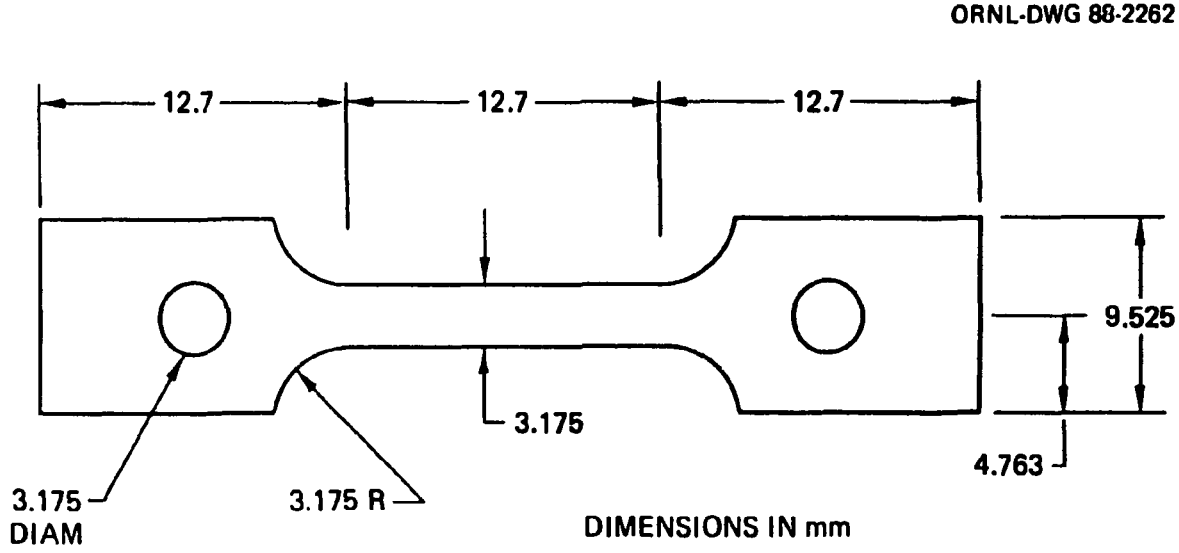

Fig. 10. Dimensions of tensile specimen.

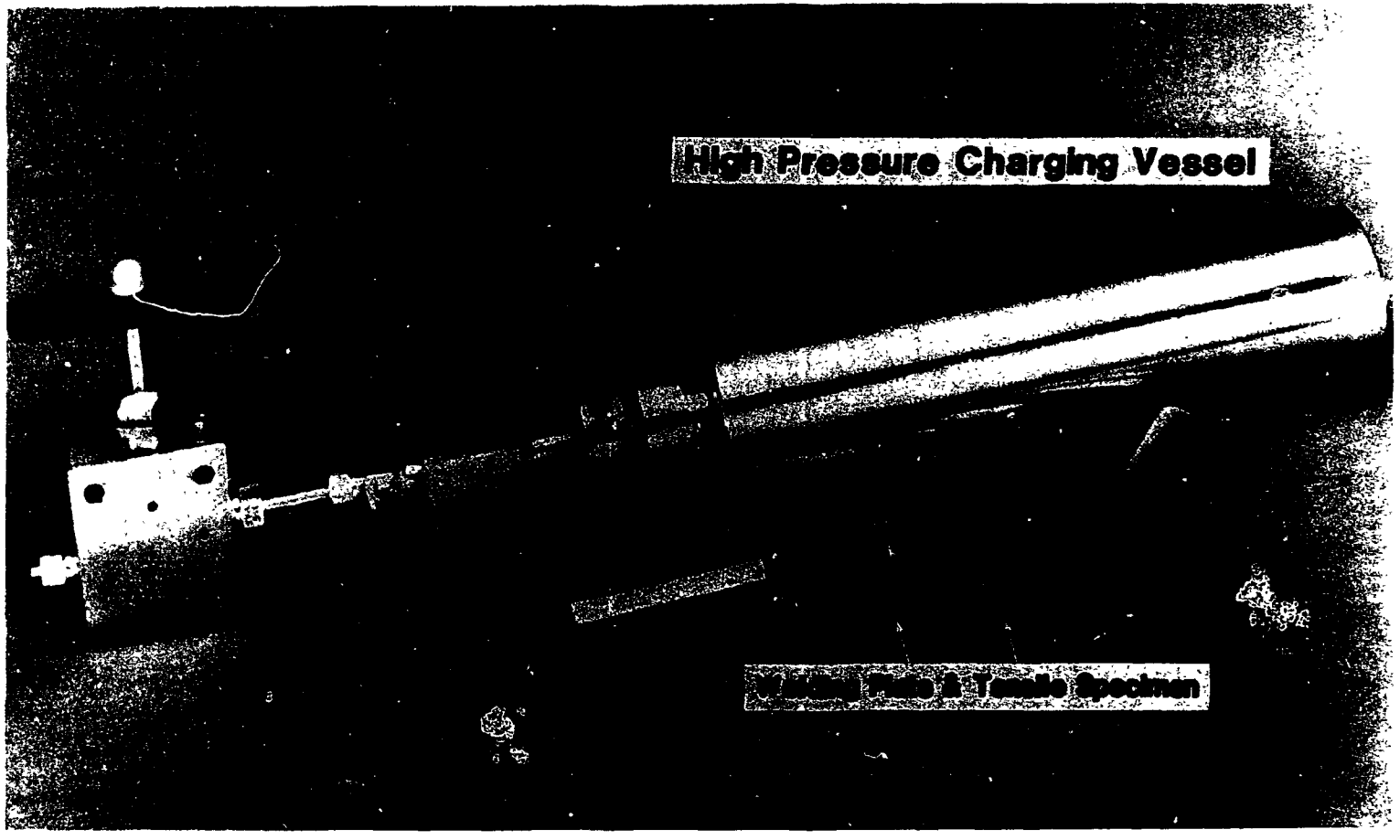

Fig. 11. Charging vessel used to diffuse tritium uniformly into the material.

National Laboratory and Sandia National Laboratories. All test materials, tensile specimens and thin plates (dimensions of 38 mm x 28 mm x 0.76 mm) were mechanically polished, and then ultrasonically cleaned sequentially in an acetone and ethanol prior to helium-doping. A schematic diagram describing the tritium charging process is shown in Figure 12. In order to generate specimens with helium levels on the order of 10 appm, the sheet stock of type 316 stainless steel was exposed to tritium gas at a pressure of 38 MPa for 30 days according to ASTM standard. Since the diffusivity of tritium in stainless steel is high at 300°C, approximately 10^{-7} cm^2/sec [77-82], this charging (also aging) period ensured that a uniform concentration of tritium (and therefore a uniform distribution of helium) was established through the thickness of the starting material. At the end of this "aging" period, the exposed material was removed from the high pressure charging vessel and held at 400°C at 10^{-3} Pa in order to remove residual tritium and to stop the further generation of helium. The off-gassing rate was measured to be 4 $mCi/m^3/hr$, and the residual activity of tritium was measured to be 74 $\mu Ci/gm$ [83]. From the residual activity of tritium (74 $\mu Ci/gm$), the remaining tritium concentration in the charged material was calculated to be approximately 0.1 appm. To prepare the lower and higher helium containing specimens (0.1, 1 and 100 appm), the same procedure was followed except the tritium charging pressure was 0.07 MPa, 1.7 MPa and 125 MPa, respectively. To obtain a 256 appm helium concentration, specimens charged at 125 MPa and 300°C were removed from the charging vessel after 30 days and stored at -40°C for

ORNL-DWG 88-13037

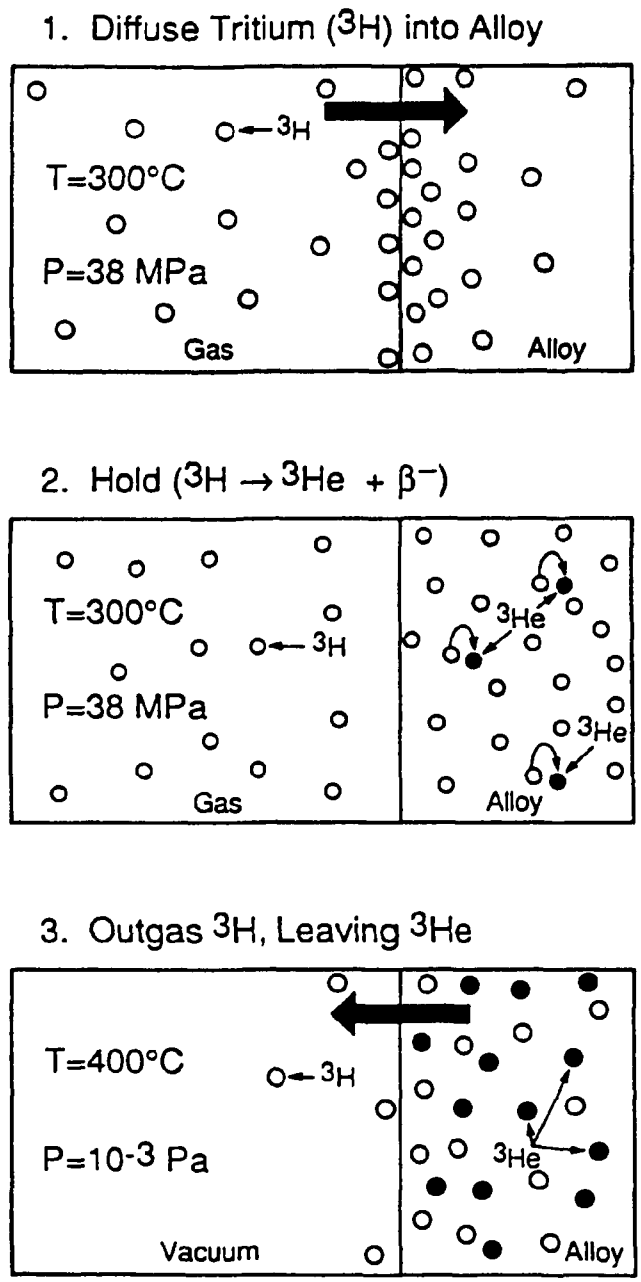

Fig. 12. Schematic diagram showing helium-doping processes.

six months to allow additional helium to be generated. The detailed charging conditions for each helium level are given in Table 2.

The concentrations of helium after doping were then measured quantitatively using a vacuum/fusion mass spectrographic technique [84] and were found to be 0.18, 2.5, 27, 105 and 256 appm, respectively, for type 316 stainless steel and 0.3 and 1 appm for HT-9. HT-9 materials were charged at the same conditions as the 2.5 and 27 appm helium levels of type 316 stainless steel. However, the resulting helium concentration in HT-9 (0.3 and 1 appm) is an order of magnitude smaller than those achieved in type 316 stainless steel. This is due to the fact that body-centered cubic material (such as α-ferrite) has a higher enthalpy of solution for hydrogen than type 316 stainless steel (face-centered cubic) [85]. This causes a lower solubility of tritium and hence leads to the generation of lower helium concentrations in HT-9.

To ensure that the weld defects which occurred during welding resulted from the presence of helium rather than residual tritium, type 316 stainless steel was also charged in hydrogen under the same conditions used to produce the higher helium content specimens (300°C, 125 MPa and 21 days). Because of the high diffusivity of hydrogen, the hydrogen-charged specimens were stored in a freezer before welding and testing to prevent hydrogen from escape. The specimens were then welded in the hydrogen-doped condition.

To reduce the tritium hazards during handling, all materials were decontaminated following the helium-doping process by mechanical polishing and wiping with a Butyl cleaner solution (produced by Joe's

Table 2. Helium-doping conditions of type 316 stainless steel and HT-9

Material	He Level (appm)	Pressure (MPa)	Temp. (°C)	Time (hrs)
316 SS[a]	0.18	0.07	300	720
	2.50	1.70	300	720
	27.00	38.00	300	720
	105.00	125.00	300	720
	256.00[b]	125.00	300	720
	Hydrogen	125.00	300	500
HT-9[a]	0.30	1.70	300	720
	1.00	38.00	300	720

[a]Materials Were Degassed at 10^{-3} Pa and 400°C for 118 Hours.
[b]Materials Were Stored at -40°C for 6 Months after "Tritium Trick".

Garage Co., Knoxville, TN). Specimens were then ultrasonically cleaned in acetone prior to welding. The decontamination process was very effective for stainless steels reducing the surface level of tritium from greater than 10^8 dpm (disintegration per minute) to between 500 and 700 dpm. This is well within the permissible level, referred to as green tag level (1000 dpm), for unshielded transfer and bare handling.

Welding Process

Autogenous bead-on-plate welds were made on control (parent material), helium-doped and hydrogen-charged materials using the gas tungsten arc (GTA) welding process. Welding of tritiated materials was conducted at Oak Ridge National Laboratory (ORNL) in Tennessee through the ORAU SHaRE program. Figure 13 shows the welding station that was located in a high velocity airhood with air flow rate of 1.5 m/s. The semiautomatic motion of the welding torch was controlled by a Unislide 8201M stepping motor translator (manufactured by Velmex, Inc., Bloomfield, NY). The motor controller is equipped with an internal clock for independent control of speed and acceleration. The motor speed was variable from 8 to 4000 steps/s. The acceleration time is front-panel-adjustable from 0 to 2.5 seconds. The welding power supply used was a Miller 330 P constant current AC/DC arc welding power source capable of ac and dc Shielded Metal Arc and GTA welding (manufactured by Miller Electric MFG. Co., Appleton, WI). The air-cooled GTA torch was a Weldcraft WP-9P, with thoriated tungsten electrode (EWTH-2) which was 1.6 mm in diameter.

YE-13833

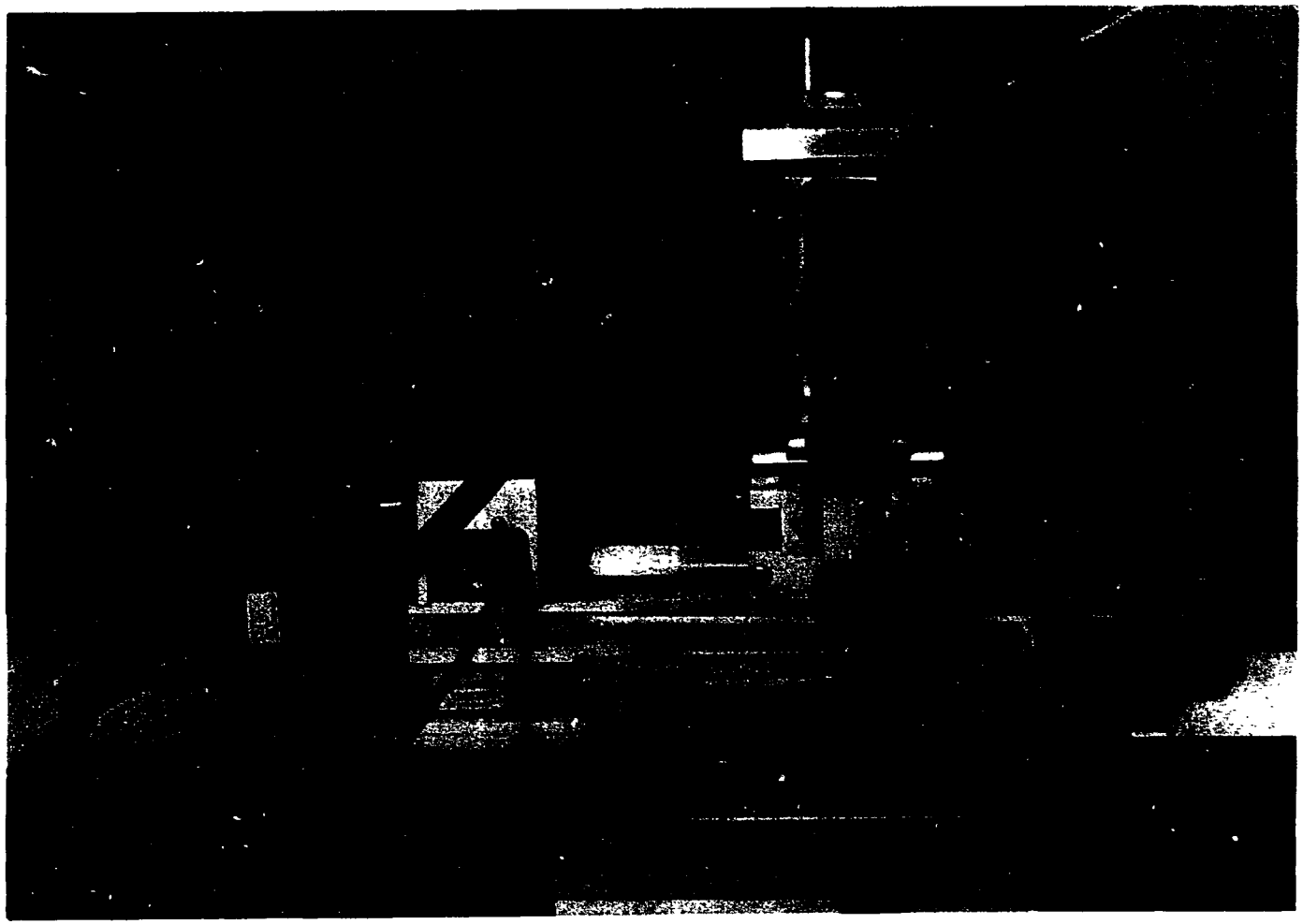

Fig. 13. Experimental welding station located in a high velocity airhood.

For type 316 stainless steel, welding was performed at 10 V-dc, 24 A at a travel speed of 3.6 mm/s under a protective argon atmosphere, enclosed by a plastic chamber. These conditions produced full penetration welds in the 29 mm wide × 38 mm long × 0.76 mm thick plate. To produce a uniform weld bead over the entire length of the weld plate, two pieces of 316 stainless steel (runoff tabs) were placed in front and in back of the plate to initiate and to terminate the arc. The plates were laterally constrained with two pieces of 12.7 mm square stainless steel bar during the welding procedure to simulate the structural restraint experienced by actual irradiated components during weld repair and to insure uniform heat flow away from the weld region. To prevent the back side of the weld from oxidation, a backing argon gas was kept flowing during welding. A gas flow of 1.57×10^{-4} m^3/sec (20 ft^3/hr) argon was used. For HT-9, full penetration welds were made at 10 V-dc, 28 A at a travel speed of 3.6 mm/s under the same constraint conditions as type 316 stainless steel. The as-tempered HT-9 plates were not preheated prior to welding. The welding process of type 316 stainless steel was video taped to provide a permanent record of time and macroscopic response (cracking) of specimens. Following welding, specimens of type 316 stainless steel containing 27 and 105 appm helium were sectioned. Samples from the fusion zone and HAZ were taken for residual helium measurement. Results showed that the fusion zone lost 80% of the original amount of helium, while the HAZ lost 74% during the welding experiment.

Additionally, the effect of high heat input on the helium bubble morphology in the weld pool of type 316 stainless steel was investigated by changing the welding parameters. Experiments were conducted at 8 V-dc and 18 A at 0.36 mm/s (1/10 of the initial speed). The resulting heat flux, defined by voltage multiplied by current divided by speed, is 400 J/mm which is six times higher than the normal heat input welds (66.7 J/mm) used in this investigation. Partial penetration welds, ranging from 30 to 50%, were also made at 10 V-dc, 11-13 A at a travel speed of 3.6 mm/s to investigate the effect of variable heat input on the cracking susceptibility of welds. Both partial penetration and high heat input welds were conducted under fully constrained conditions. Furthermore, butt-joint welds without external constraint were conducted to study the effect of an externally applied constraint on the cracking phenomena in the HAZ. Butt-joint welds with full penetration were made at 10 V-dc, 24 A at a travel speed of 3.6 mm/s. The detailed welding conditions for both type 316 stainless steel and HT-9 are given in Table 3.

The temperature profiles in the HAZ of welds, as a function of transverse position from the fusion line and time, were measured to study the thermal history during the welding. Four K-type thermocouples (Chromel-Alumel), 0.127 mm in diameter, were spot welded at four different locations transverse to the welding direction. Thermocouples were placed 0.5 mm apart beginning from the anticipated fusion line. The temperature data were captured by a Nicolet 4049 digital oscilloscope (manufactured by Nicolet Instrument Corp.,

Table 3. Welding conditions of type 316 stainless steel and HT-9

Welding Condition	He Level (appm)	No. of Welds
	316 Stainless Steel	
Full Penetration		
Normal Heat Input	0.18	5
	2.5	5
	27.0	7
	105.0	7
	256.0	7
High Heat Input	27.0	3
	105.0	3
Butt-Joint	27.0	2
	105.0	2
Partial Penetration		
	2.5	2
	27.0	2
	105.0	2
	256.0	2
	HT-9	
Full Penetration		
Normal Heat Input	0.3	4
	1.0	4

Madison, WI) capable of four channel data acquisition at a rate of 10^6 points/s. The data acquisition speed used in the temperature measurement experiment was 500 points/s per channel. The temperature data, expressed in voltage units, were converted into celsius using standard Type K reference tables.

Microstructure Characterization

The helium bubble morphology, prior to and after welding and under variable welding conditions, was characterized to determine the helium bubble growth mechanism. This was a key task which would provide insight into the mechanisms leading to intergranular fracture in the HAZ. Examinations were conducted using a Philips CM-12 transmission electron microscope (TEM) operated at 120 KeV (manufactured by Philips Export B.V., Eindhoven, Netherlands). The CM-12 was equipped with an energy-dispersive analysis of X-ray (EDAX) detector. Thin TEM foils were prepared from 4 mm square discs cut from 0.76 mm sheet using an Isomet low speed saw (manufactured by Buehler Ltd., Lake Bluff, Il). The precision cutting reduced the amount of plastic deformation which would have been induced if the TEM specimens had been manufactured using the standard punching process. The discs were then ground to 3 mm in diameter and polished on 600 grit paper to about 0.2 mm thickness in a glove box. Samples of both type 316 stainless steel and HT-9 were subsequently electropolished to perforation in a Struers Tenupol (manufactured by Struers A/S, Copenhagen, Denmark) using a 12.5% sulfuric acid (H_2SO_4) in methanol solution at -15°C using 120 mA and 20

V-dc. To minimize tritium contamination, the polishing tasks for tritium-treated discs were performed in a hood.

To characterize the helium bubble morphology, the helium bubble microstructures were taken in an under-focused condition. At this focusing condition, a helium bubble appears as a white dot surrounded by a dark, Fresnel-like ring. The bubble diameter was then measured by determining the diameter of the white portion of the image. The diameter measurements were made using a Zeiss particle size analyzer (Model TGZ-3) (manufactured by Zeiss, Carl, Inc., Thornwood, NY). Ten micrographs were taken from each TEM specimen to obtain an average measurement of bubble size in both grain boundary and matrix. In addition, foil thickness measurement was made to determine the bubble density. In this study foil thickness was determined using stereo pairs. The stereo pairs were taken using the same diffraction vector at a tilt angle of 15° between microphotographs. Stereo measurements were made with a Hilger and Watts Folding Mirror Stereoscope (model SB180) (manufactured by Hilger and Walls Ltd., London, England). To obtain adequate statistics, the parallax, P, was measured from four areas of each stereo pair with four readings per area. An average foil thickness was calculated for each micrograph. The thickness, h, was calculated from the equation $h = P/[2M\sin(\theta/2)]$ where M is the magnification of the micrographs and θ is the tilt angle of the stereo pair.

The weld microstructures were examined by preparing metallographic sections transverse to the welding direction. The metallographic

sections of type 316 stainless steel were mechanically polished, and then electrolytically etched in a solution of 40% nitric acid (HNO_3) and 60% distilled H_2O. The metallographic sections of HT-9 were etched chemically in a solution of 1% HF, 9% HNO_3 and 90% H_2O. Both as-polished and etched conditions were examined.

Properties Characterization

Scoping mechanical properties tests were conducted on control and helium-doped materials in unwelded and welded conditions. The results of control specimens served as a base line for comparison. Results were used to determine the effect of helium concentration and bubble morphology on the mechanical properties and to develop relationships between properties and corresponding microstructures. Mechanical testing consisted of microhardness and tensile tests. Following metallographic examinations, Vickers microhardness traverses were performed across the weld using a Schimadzu microhardness tester (manufactured by Schimadzu Corp., Kyoto, Japan) with 500 grams load.

Tensile tests were performed on an Instron mechanical testing machine (manufactured by Instron Corp., Canton, MA) with 4500 N capacity at a fixed cross head speed of 8.5×10^{-3} mm/s. Tests were conducted at temperatures between 20 and 700°C in a vacuum of 4×10^{-5} Pa. For testing at elevated temperatures, specimens were held at temperature for 15 minutes prior to test initiation. Temperature profiles along the gage section (12.7 mm) of the tensile specimens were monitored using three K-type thermocouples spread 4 mm apart. The variation in test temperature was ± 5°C. Tensile specimens of welded

materials were prepared using a punch and die in an orientation transverse to the welding direction. The dimensions of the tensile specimens were the same as unwelded ones (Figure 6). The center of the gage section contained both fusion zone and HAZ which comprised approximately 50% of the gage length (12.7 mm). Prior to tensile testing, all of the tensile specimens of welded materials were mechanically polished until even surfaces in the gage sections were obtained. Specimens of type 316 stainless steel and HT-9 were then etched, using previously described solutions, to ensure no visible surface defects existed.

Scanning Electron Microscopy Fractography

Fractographic analyses of weld defects and failed tensile specimens were conducted using a JEOL JSM-35CF scanning electron microscope (SEM) (manufactured by JEOL Ltd., Tokyo, Japan) equipped with an EDAX detector. All specimens were ultrasonically cleaned in acetone prior to examination. In addition, SEM examination was also used as a nondestructive method to investigate weld defects arising from different helium contents, material and welding conditions. Studies of helium bubble size distribution in the fusion zone of the welds were carried out by examination of metallographic specimens using SEM following cross-sectional metallographic sample preparation. Six photos were examined from each specimen across the weld zones to obtain a statistically significant result. The bubble diameter was measured using a Zeiss particle size analyzer (Model TGZ-3).

Heat Treatment to Investigate the Effect of Aging on the Properties of Helium-Doped Type 316 Stainless Steel

To isolate the effect of temperature on the mechanical properties and helium bubble morphology of type 316 stainless steel, tensile specimens and TEM disks containing 256 appm helium were heat treated at 1300, 1050, 900 and 800°C for one hour. The tensile specimens were mechanically polished, and then electrolytically etched in a solution of 40% nitric acid and 60% distilled H_2O prior to heat treatment. The TEM disks (3 mm diameter) were cut from the as-received helium-doped plates using a punch, and were then mechanically polished to 0.25 mm and ultrasonically cleaned in acetone. Subsequently, both tensile specimens and TEM disks were wrapped in tantalum foil, and encapsulated in a quartz tube to obtain a vacuum environment. The specimens were then heat treated at the above temperatures for one hour. Tensile tests were performed at room temperature at a strain rate of 5×10^{-4} s^{-1}.

IV. RESULTS

This chapter reports the results obtained by the experimental program described in the previous chapter. The weldability of two alloys, type 316 stainless steel and HT-9, with varying helium contents was investigated using the GTA welding process. In this study, type 316 stainless steel was primary alloy and HT-9 was secondary alloy. For type 316 stainless steel, effects of variable heat input and external constraint conditions on the weld responses were studied. Following welding, both type 316 stainless steel and HT-9 were characterized by optical microscopy and electron microscopy. Particular attention was paid to the HAZ cracking features and helium bubble morphology since the HAZ was the location which experienced the highest temperature and thermal stress in the solid state.

The first section of this chapter describes measurements of peak temperature and thermal cycle experienced by a fixed point in the HAZ. Characterizations of weld defects and microstructures of type 316 stainless steel are reported in two categories according to the depth of penetration: full penetration and partial penetration. This separation provides information on the effects of variable heat input on the HAZ cracking. The section of full penetration welds of type 316 stainless steel is further divided into three subsections: normal heat

input welds, high heat input welds and butt joint welds. The objective of high heat input welds was to study the effects of high power input on the density and size of pores (helium bubbles) in the resolidified weld pool. Attention was also given to the effect of external constraint on the HAZ cracking. Properties of welds characterized by microhardness and tensile tests are also reported.

Following tensile tests, it was important to determine the difference in failure mode, if any. Both helium-free and helium-containing specimens were examined using scanning electron microscopy. Since, the primary objective of this study was the characterization of the HAZ cracking, results of tensile specimen failure analysis are reported in APPENDIX I.

Measured Peak Temperatures and Thermal Cycles in the Heat-Affected Zone

This experiment was conducted to determine the peak temperature (and/or position) at which the HAZ cracking occurred. It was also performed to determine the temperature and/or time at which the HAZ cracking initiated after the passing of the torch. Figures 14 and 15 show the temperature-position and temperature-time profiles in the HAZ for type 316 stainless steel. Figure 14 shows the experimentally measured peak temperature as a function of position in the HAZ. For comparison purposes, theoretical peak temperatures as predicted by the Adams equation [86] (case of a thin specimen) are also shown. The appropriate Adams equation was obtained by substituting the following

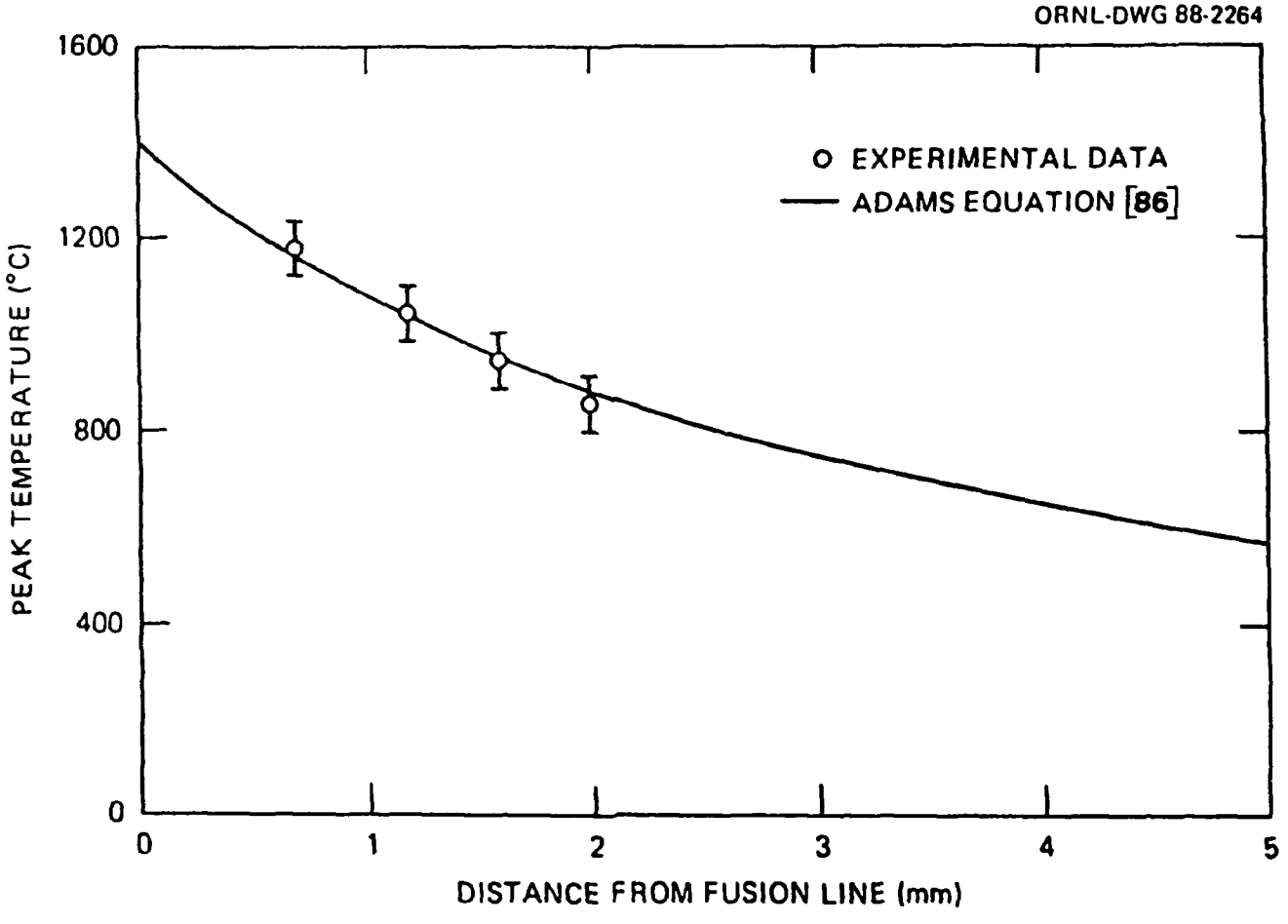

Fig. 14. Temperature-position profile in the heat-affected zone of type 316 stainless steel.

experimental parameters: V = 10 V-dc, I = 24 A, ρC_p = 4.7 × 10^6 J/m2^3K (volume thermal capacity), v = 3.6 mm/s (welding speed), T_m = 1400°C (melting point) and h = 0.76 mm (plate thickness). The resulting equation is

$$T(x) = 20 + 1380/(0.30636x + 1) \quad (16)$$

where x is the transverse position from the fusion line. The results in Figure 14 reveal that the experimental curve tends to have a greater slope than that predicted by the Adams equation leading to a higher extraplolated melting point and lower peak temperatures in the edge of the HAZ. This deviation is probably due to the assumed boundary conditions (no heat loss on the top and bottom surfaces) used in the development of the Adams equation. This results in the prediction that temperature will drop more slowly with distance than actually observed. Nevertheless, the good agreement between measured and predicted temperatures (Figure 14) indicates that peak temperature as a function of position in the HAZ is well described by the Adams equation. The measured temperature-time profiles of a fixed point in the HAZ which experiences peak temperatures of 1172 and 1036°C are shown in Figure 15. The time dependence of the temperature distribution is compared with that predicted using the Rosenthal equation [87] for a thin plate. The same parameters used in the Adams equation were applied to obtain the specific Rosenthal equation for our experimental case. The comparison between the experimental data and theoretical predictions indicates that measured results tend to have a faster cooling rate than that predicted by Rosenthal equation. This is may also be attributed

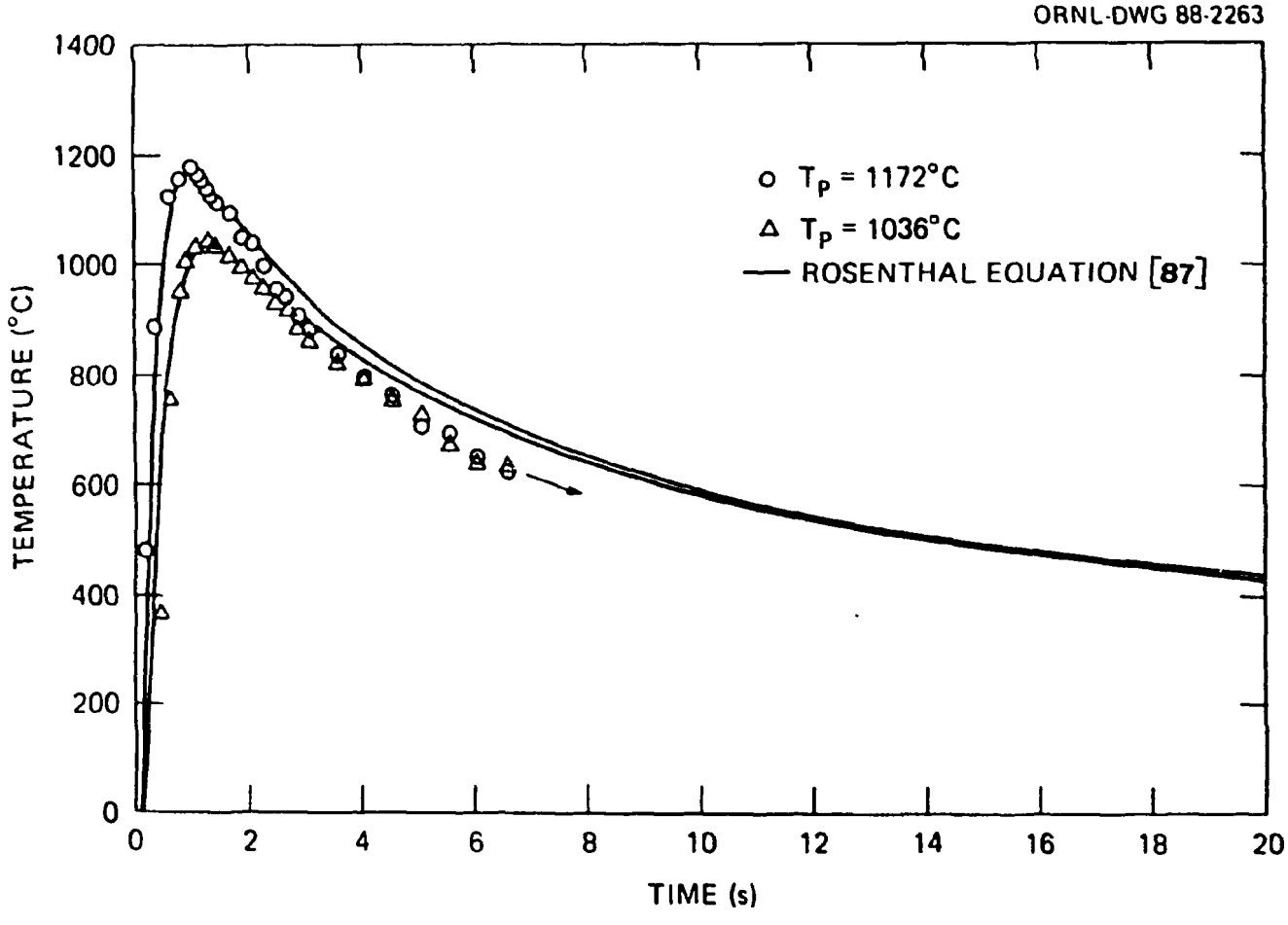

Fig. 15. Thermal cycle experienced by a fixed point in the heat-affected zone as the weld torch passes type 316 stainless steel for peak temperatures of 1172 and 1036°C.

to the assumption that no heat is lost through the sheet surfaces. However, good agreement between the experimental data and theoretical predictions are observed (Figure 15). Therefore, the thermal cycle in the HAZ for a fixed point which experiences a given peak temperature can be reasonably expressed by the Rosenthal equation, as

$$T(t) = 20 + 1906\exp\{-668388/[t(Tmax-293)^2]\}/t^{\frac{1}{2}} \quad (17)$$

where Tmax is the peak temperature that a point experiences in the HAZ.

Austenitic Stainless Steel

Full Penetration Welds

Normal heat input welds

Figure 16 shows the typical macroscopic features of the as-welded control and helium-doped specimens (0.18, 2.5 and 105 appm). APPENDIX A (Figure 56) shows the as-welded features for the specimens containing 15,000 appm hydrogen, 27 and 256 appm helium. In the control and hydrogen-charged materials (Figures 16a and 56a) all of the welded plates were sound and free of any visible weld defects. The welded plates with the lowest helium levels of 0.18 appm (Figure 16b) also were sound and free of any weld cracking. However, in materials containing 2.5 and 27 appm helium, continuous, through-the-thickness cracking in the HAZ was consistently observed in all of the as-welded plates (Figures 16c and 56b). In the higher helium content materials (105 and 256 appm), all of the welded plates showed HAZ cracking; in addition, more than 60% of the welded plates exhibited centerline cracking in the fusion zone (Figures 16d and 56c). All of the welded plates were examined in detail using SEM following visual examination.

YE-13834

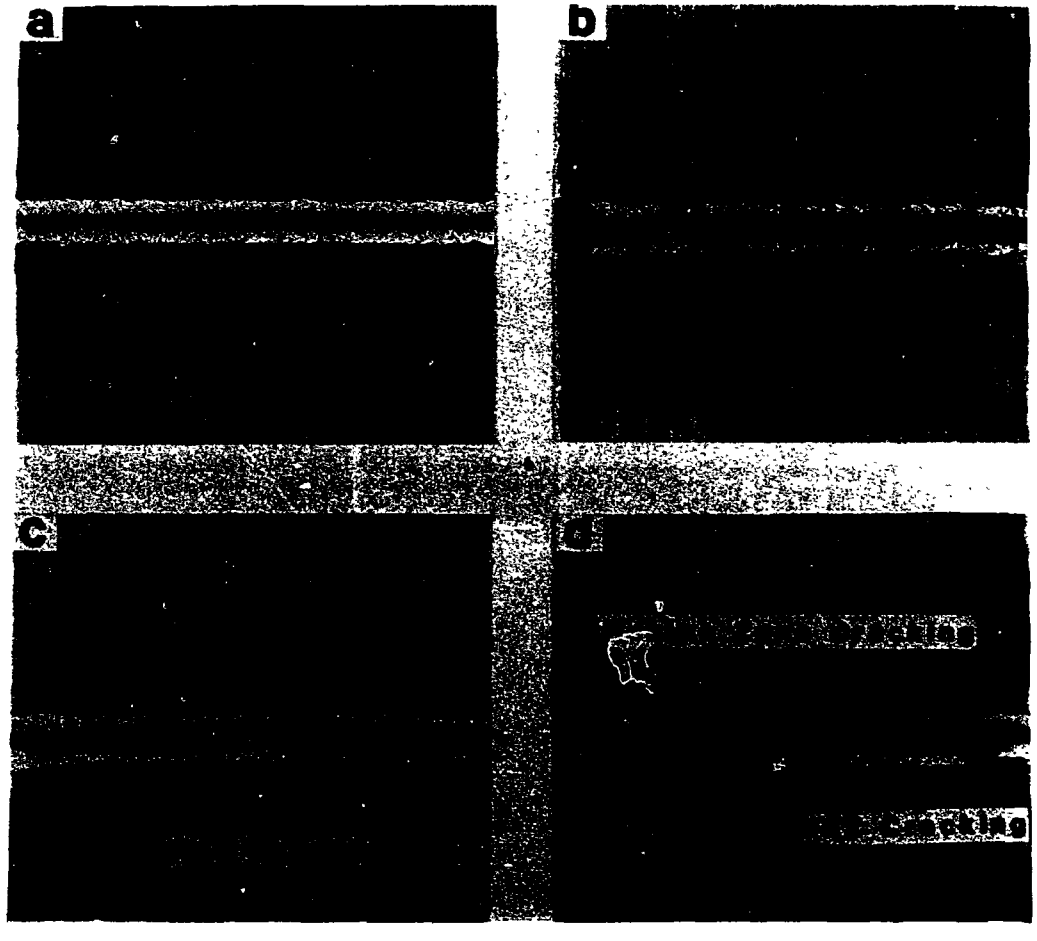

Fig. 16. Macroscopic features of as-welded type 316 stainless steel. (a) Control materials, (b) 0.18 appm (no cracking observed), (c) 2.5 appm (continuous HAZ cracking), and (d) 105 appm (continuous HAZ and centerline fusion zone cracking).

Figures 17 and 18 show the typical microscopic features of the weld defects in the materials containing 2.5 and 105 appm helium respectively. The microscopic features for the welded plates containing 27 and 256 appm helium are shown in APPENDIX B (Figures 57 and 58). Typically, the HAZ cracking was fully intergranular in nature (Figures 17b and 18b) and occurred within one to three grain diameters of the fusion boundary. Since no external loads were applied, in all cases, the cracking resulted from the generation of shrinkage stresses as the laterally constrained plates cooled after welding. This hypothesis was further investigated by using a Panasonic TV camera with a microscopic lens to record the welding process. Recorded video tape showed that the cracking in the HAZ occurred approximately one second after the passing of the torch.

Fractography of weld cracks in the HAZ and fusion zone were studied in detail using scanning electron microscopy. Figures 17 and 18 show the typical surface features for the helium levels of 2.5 and 105 appm. As stated above, the weld cracking in the HAZ was fully intergranular in nature, and at higher magnification the grain boundary facets were observed to be decorated with a uniform distribution of dimples (Figures 17c and 18c). These observed dimples were attributed to helium bubbles. The average dimple size was approximately 1 μm and was independent of helium concentration. However, the dimple morphology (symmetry and spacing) observed on grain facets varied from grain to grain. The variation is attributed to grain boundary characteristics, such as local dislocation structure, thermal history,

YE-13835

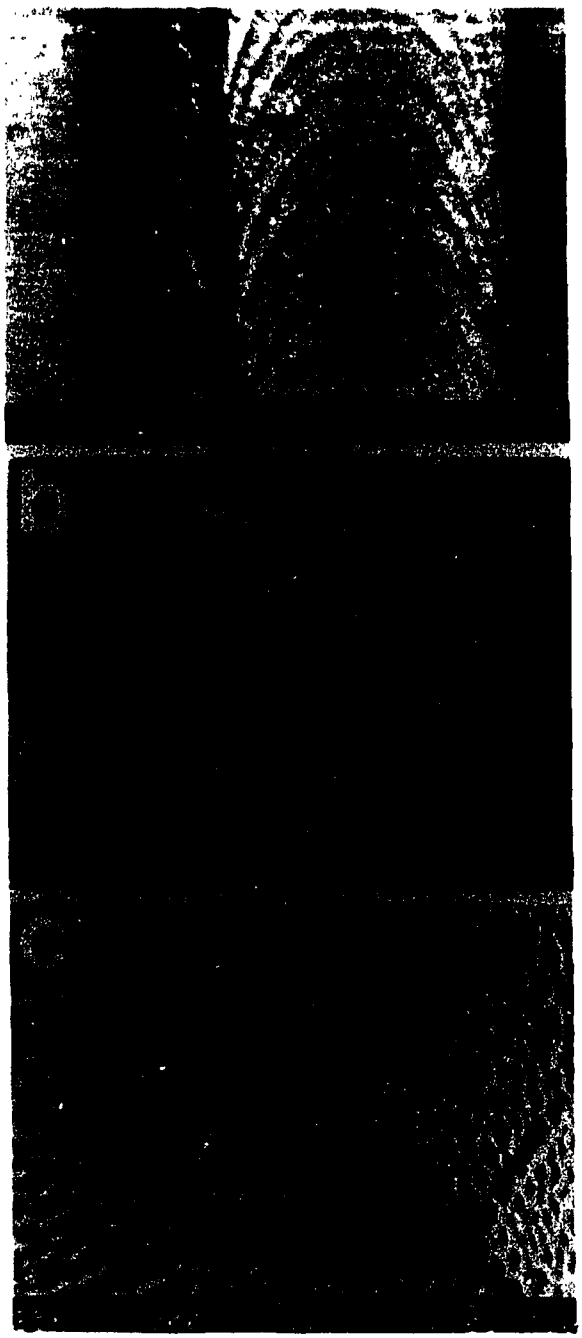

Fig. 17. Structure of as-welded type 316 stainless steel with 2.5 appm helium. (a) Photomacrograph of heat-affected zone showing intergranular fracture, (b) SEM micrograph showing details of intergranular fracture, and (c) SEM micrograph of grain boundary facets decorated with a uniform distribution of dimples.

YE-13836

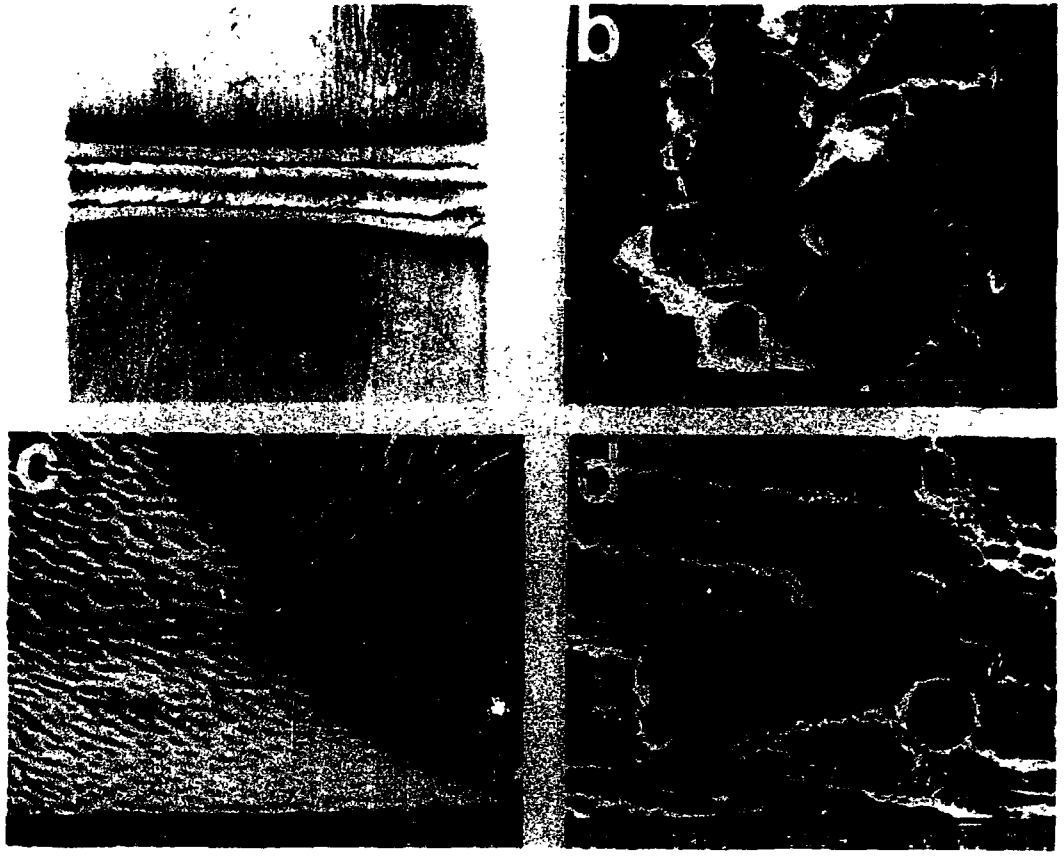

Fig. 18. Structure of as-welded type 316 stainless steel with 105 appm helium. (a) Photomacrograph of brittle fracture in fusion and heat-affected zones, (b) SEM micrograph showing details of intergranular fracture, (c) SEM micrograph of grain boundary facets decorated with a uniform distribution of dimples, and (d) SEM micrograph showing brittle failure proceeds along an interdendritic path.

and residual stress experienced by each individual grain boundary in the HAZ. The dimples on the exposed facets exhibited symmetrical features which indicated that they were formed from cavities that grew under the action of stresses normal to the boundary. Incipient cracking, arising from coalescence of cavities, was also observed along the grain boundary intersections (Figures 17c and 18c). The shear ligaments separating the dimples have been rounded by surface diffusion, indicating that the cracking occurred at high temperatures early in the weld cooling cycle. This is consistent with video tape observations that cracking occurred approximately one second after the passing of the torch. According to the measured thermal history in the HAZ, the temperature at which fracture occurred was about 1150°C (Figures 14 and 15). This predicted temperature was obtained by using the following calculation procedures. First, the average peak temperature at one to three grain diameters from the fusion boundary was calculated to be 1330°C using equation (16). Then, the temperature one second after the passing of the torch (1150°C) was calculated using equation (17). Examination of the fusion zone centerline cracking indicated that the brittle failure proceeded along an interdendritic path during weld metal resolidification (Figure 18d). Isolated spherical pores resulting from the migration and coalescence of the entrapped helium were also observed on the fracture surface.

Figure 19 shows the optical metallography of the welds from a section taken transverse to the welding direction for the control and specimens containing 0.18, 27 and 105 appm helium. APPENDIX C

YE-13837

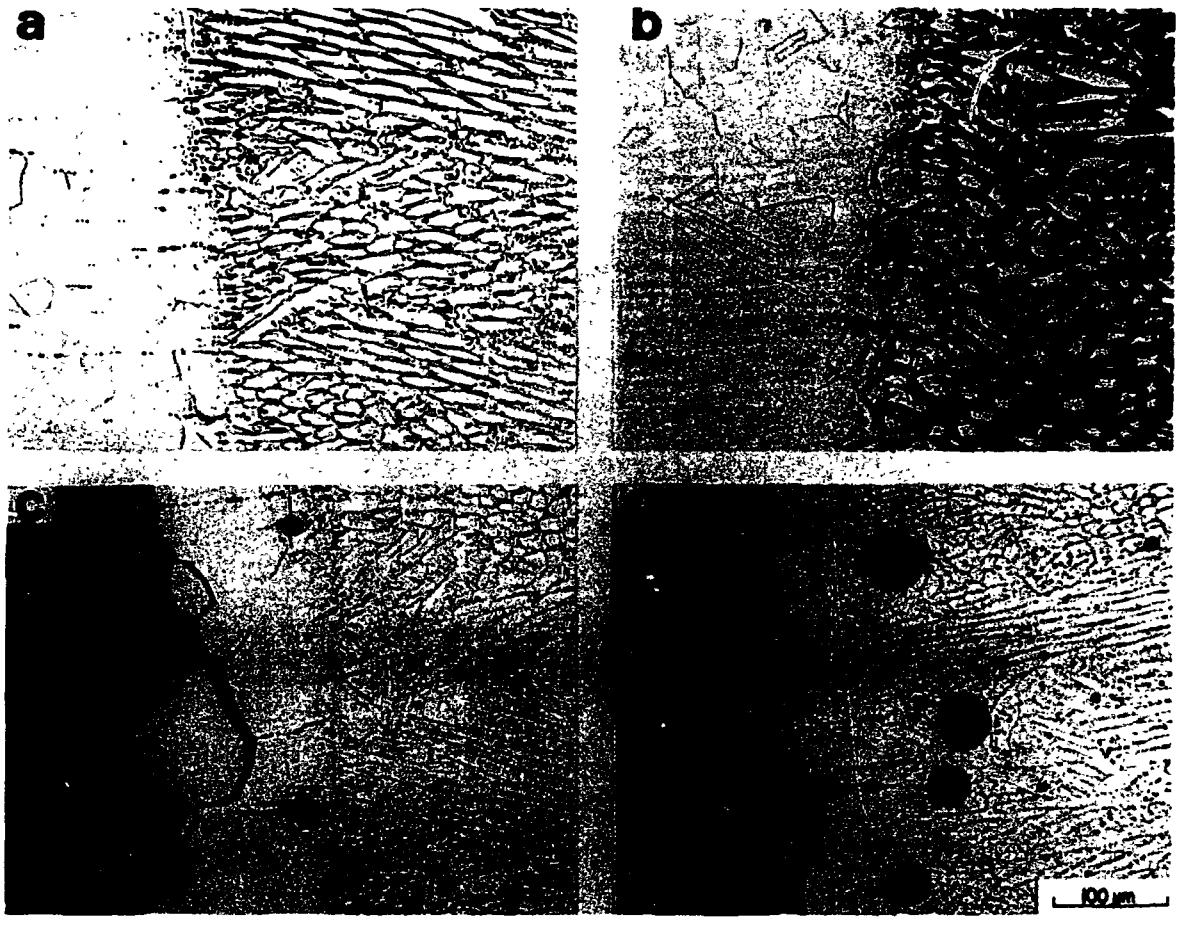

Fig. 19. Optical metallography of normal heat input welds of type 316 stainless steel taken transverse to the welding direction. (a) Control, (b) 0.18 appm, (c) 27 appm, and (d) 105 appm. Failure occurred in the heat-affected zone. Larger pore size and greater density of helium bubbles occurred in the fusion zone near the fusion boundary.

(Figure 59) shows the optical metallography of the hydrogen-charged and helium-containing materials (2.5 and 256 appm). Generally, the microstructure of the fusion zone was primary austenite with ferrite precipitations in the interdendrite boundaries. Small amounts of ferrite precipitation were also observed surrounding grain boundaries at the fusion boundary. The presence of ferrite was confirmed by chemically etching the metallographic specimens in a boiling solution of 77 wt% H_2O, 11.5 wt% potassium hydroxide (KOH) and 11.5 wt% potassium ferricyanide ($K_3Fe(CN)_6$) for 30 seconds which preferentially colored the ferrite with respect to the matrix. The presence of ferrite reduces the tendency of the material for hot cracking in both fusion and HAZ zones. In the helium-doped materials, visible spherical pores decorating the solidification dendrite boundaries were observed. The degree to which the pores decorate the interdendrite boundaries is clearly shown in the SEM photomicrographs, as shown in APPENDIX C (Figure 60). Based on a comparison of the observed features in the helium-free and helium-containing materials, it was concluded that visible isolated pores in the fusion zone are helium bubbles. In addition, it is clear by comparing Figures 19b-19d that the degree and size of the porosity in helium-doped welds were found to increase with increasing helium concentrations. Data for the density and size of pores as a function of helium contents is given in APPENDIX D. These results are tabulated in Table 4. The observations also indicate that the larger pores were preferentially located in the fusion zone close to the fusion boundary. The tendency to form bigger helium bubbles in

Table 4. Density and size of pore in the fusion zone as a function of helium level and heat input

Heat Input (J/mm)	He Level (appm)	Density ($10^{13}/m^3$)	Mean Size (μm)
66.7	2.5	3.6	0.8
	27.0	5.6	1.0
	105.0	10.3	1.3
	256.0	13.1	1.5
400.0	27.0	1.3	1.3
	105.0	2.2	1.4

the fusion zone adjacent to the weld interface suggests that convective flow patterns in the weld pool act to sweep the helium toward that region. The stagnant flow of molten metal next to the weld interface then enhances bubble coalescence.

Results of metallography (Figures 19 and 59a) indicated that both the control and hydrogen-charged specimens were again found to be uncracked and free of any damage. Thus, it is clear that the loss of alloy weldability, the tendency for material to suffer fusion zone and HAZ cracking, is entirely related to the entrapped helium rather than to residual hydrogen or tritium. Also, the metallographic analysis revealed that the intergranular cracking in the HAZ occurred not at the fusion-HAZ boundary but into the HAZ. This suggests that peak temperature alone is not responsible for cracking. In addition, secondary cracking away from the main fracture was also observed along with porosity on the grain boundaries. Fracture appears therefore to occur due to the growth and coalescence of helium bubbles along grain boundaries. This occurs in the region of solid material which experiences the combination of the highest temperatures and the highest shrinkage stresses. The observed features again suggest that the peak temperature alone is not necessarily the main driving force for helium bubble growth and coalescence. Rather, a combination of stress and temperature controls the bubble growth and fracture process.

High heat input welds

In order to study the effect of high heat input on the helium bubble morphology in the solidified weld pool and surrounding regions,

specimens containing 27 and 105 appm helium were welded at 8 V-dc and 18 A at 0.36 mm/s with external constraint. Under these welding conditions, the heat input is 400 J/mm which is six times higher than normal full penetration welds made in this study. Results again revealed HAZ cracking in both as-welded plates. Figure 20 shows the typical photomicrographs for specimens containing 27 and 105 appm helium. The optical photomicrographs showed that intergranular cracking occurred in the HAZ close to the fusion boundary. These are the same features as observed in Figure 19 for the normal heat input welds. The photos also show that spherical pores (helium bubbles) decorated the dendrite boundaries. Based on a comparison of Figure 19 with Figure 20, it is clear that the size of porosity in the fusion zone increases with decreasing welding speed (increasing heat input). This is due to the longer period of ti that the weld pool stays in the molten state. This leads to more time for coalescence and growth of helium bubbles. Because of the larger time spent in the molten state it was anticipated that more helium would diffuse out through the surface of the weld pool. Quantitative measurements of residual helium in the fusion zone subsequent to welding were made to investigate this hypothesis. The data of helium bubble density and size in the fusion zone are tabulated in APPENDIX D. Results are given in Table 4. As can be seen from the data, the 27 appm helium material shows an increase in the gas volume (density times mean bubble volume), while the 105 appm material shows a decrease in the gas volume as the heat input is increased. This suggests that a critical mean bubble size may

YE-13838

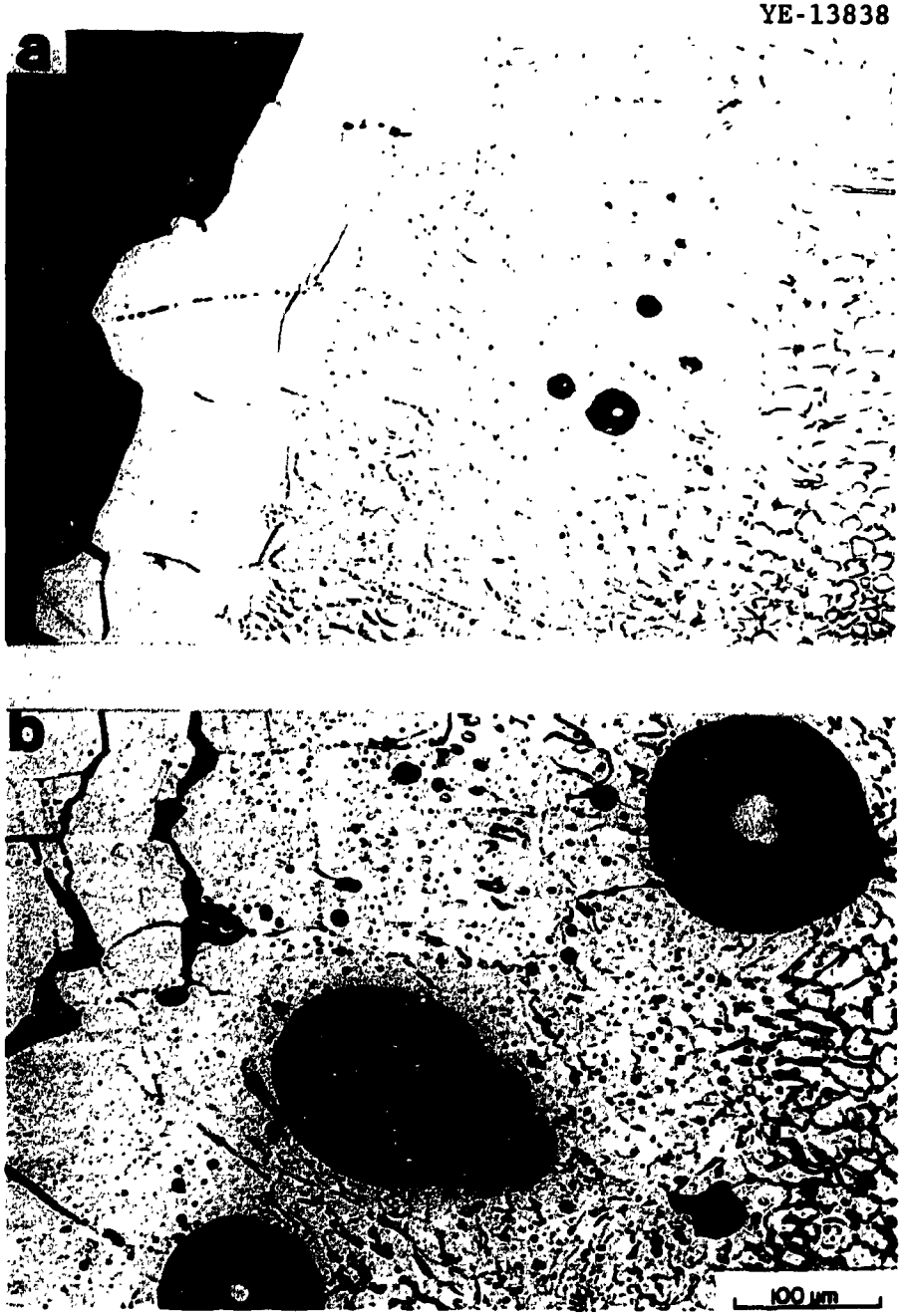

Fig. 20. Optical metallography of high heat input welds of type 316 stainless steel taken transverse to the welding direction. (a) 27 appm, and (b) 105 appm. Failure occurred in the heat-affected zone. Degree and size of porosity increase with decreasing welding speed.

be required for buoyancy forces to allow the bubbles to escape through the molten pool surface.

Butt-joint welds

Butt-joint welds under no constraint were made to investigate the role of the externally applied constraint on the HAZ weld cracking. Due to the limited material available, the study was only conducted on specimens containing 27 and 105 appm helium. Following welding, visual examination revealed no weld defects existed in the HAZ. To enlarge any un-observable cracks in the fusion and HAZ zones (if they did exist), open V-block bending tests were performed. The specimens were 6.40 mm wide × 3.80 mm long × 0.76 mm thick. Since the width-to-thickness ratio (8.42) is greater than 8, bending occurs under plane strain conditions, and bending ductility is therefore independent of the exact width-to-thickness ratio [88]. To obtain 180° bend angles, bent specimens were further pressed using a vice. Force was applied slowly and steadily. Visual examination following post-weld bend tests revealed that the 27 appm weld appeared sound while 105 appm welds exhibited cracking along the HAZ. Following visual examination, specimens were then examined in detail using a scanning electron microscope. The SEM observations (Figure 21) indicated that HAZ cracking observed in both welds was fully intergranular in nature, and at higher magnification the grain facets were observed to be decorated with a uniform distribution of dimples. In the 27 appm weld the shear ligaments separating dimples exhibited sharp edges indicating that these defects did not exist prior to the bending test. Some shear

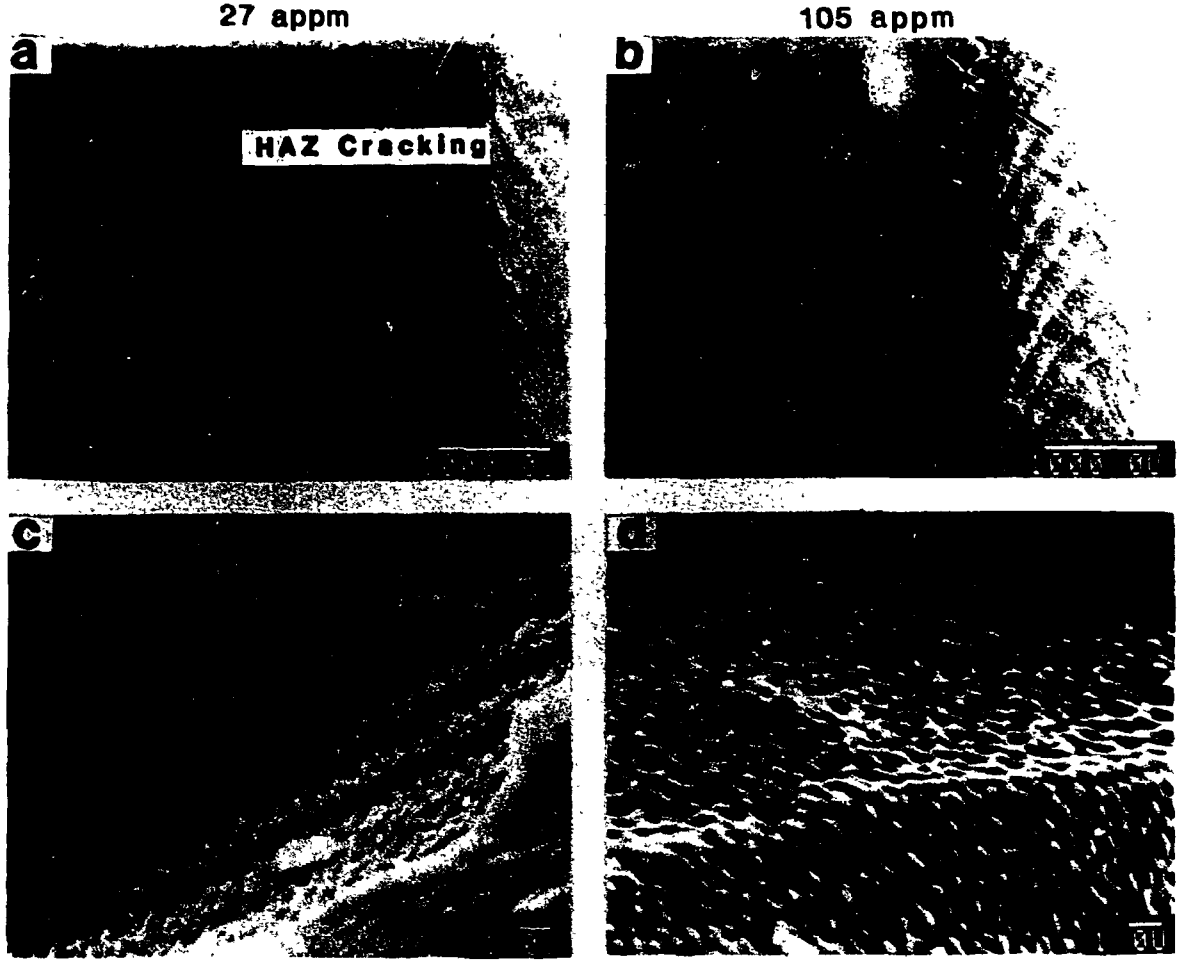

Fig. 21. Butt-joint welds of type 316 stainless steel following bending test. (a) and (c) SEM micrographs of 27 appm weld, and (b) and (d) SEM micrographs of 105 appm weld. Intergranular fracture occurred in the heat-affected zone. Fracture surface shows a uniform distribution of dimples.

ligaments observed in the 105 appm welds (Figure 21d) showed rounded features indicating that these cracks occurred during welding. These tests demonstrate that helium still degrades the weld integrity. In these cases where there was no external constraint, helium bubble growth and coalescence could still occur due to internal thermal stresses generated during heating and cooling of the weld. External applied constraint intensifies internal thermal stresses which in turn enhance helium bubble growth in the HAZ leading to catastrophic intergranular fracture.

Partial Penetration Welds

Partial penetration welds were made with constraint to study the effects of low heat input on the cracking sensitivity of welds containing 2.5 appm helium and above. Visual and SEM examination of as-welded plate surfaces showed no visible weld defects at all helium levels. Figure 22 shows representative SEM photomicrographs of transverse cross section of the welds for a control and 105 appm helium specimen. The SEM photomicrographs for specimens containing 2.5, 27 and 256 appm helium are given in APPENDIX C (Figure 61). Penetration of the welds ranged from 30 to 50% of the plate thickness (0.76 mm) as a result of variation in input power. The SEM micrographs of cross section of the welds show that the bigger helium bubbles tend to locate in the fusion zone-HAZ interface, similar to the observations that were made for full penetration welds (Figure 19). This is again due to the stagnant flow at the weld interface which enhances the coalescence and growth of helium bubbles. The helium bubbles were also observed to

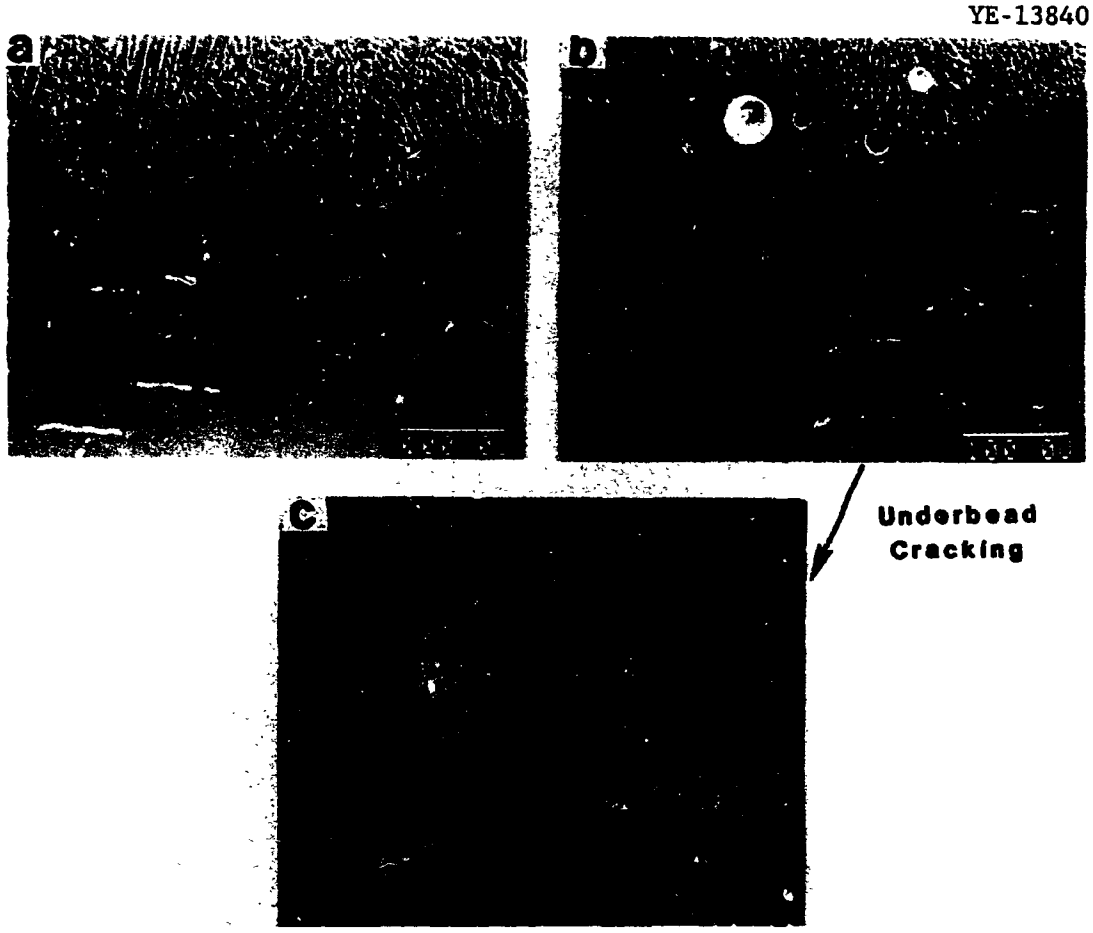

Fig. 22. SEM micrographs of partial penetration welds of type 316 stainless steel. (a) Control materials, and (b) 105 appm. Intergranular fracture occurred in the heat-affected zone directly below the center line of the weld. This is the region which experienced the critical combination of high temperature and high shrinkage tensile stress required to induce cracking.

decorate dendrite boundaries. Furthermore, the degree and size of porosity in the fusion zone increases with increasing helium content. All partial penetration welds containing helium levels equal to or greater than [illegible] appm showed intergranular cracking in the HAZ. This cracking occurred principally underneath the center region of the fusion zone (underbead cracking). Figure 22c shows this intergranular fracture at a higher magnification. This is the region of the partial penetration weld which is subjected to the highest shrinkage tensile stress during cooling. Thus, again it is clear that high temperature alone is not sufficient to induce catastrophic cracking. Rather, cracking is most pronounced in regions subjected to a critical combination of stress and temperature. These results suggest that low heat input welding techniques still induce intergranular HAZ cracking which arise from a combination of high temperature and residual tensile stress.

Transmission Electron Microscopy Characterization

Full penetration welds

Normal heat input welds. Transmission electron microscopy of the control and hydrogen-charged materials revealed a microstructure low in dislocation density and free of any grain boundary defects, as shown in APPENDIX E (Figure 63). The microstructures of the specimens containing helium concentrations of 256 appm prior to welding are shown in Figure 23. The detailed TEM morphology of the helium-doped materials (0.18, 2.5, 27 and 105 appm) after completion of charging is also shown in APPENDIX E (Figures 64-67). The microstructures of the

YE-13841

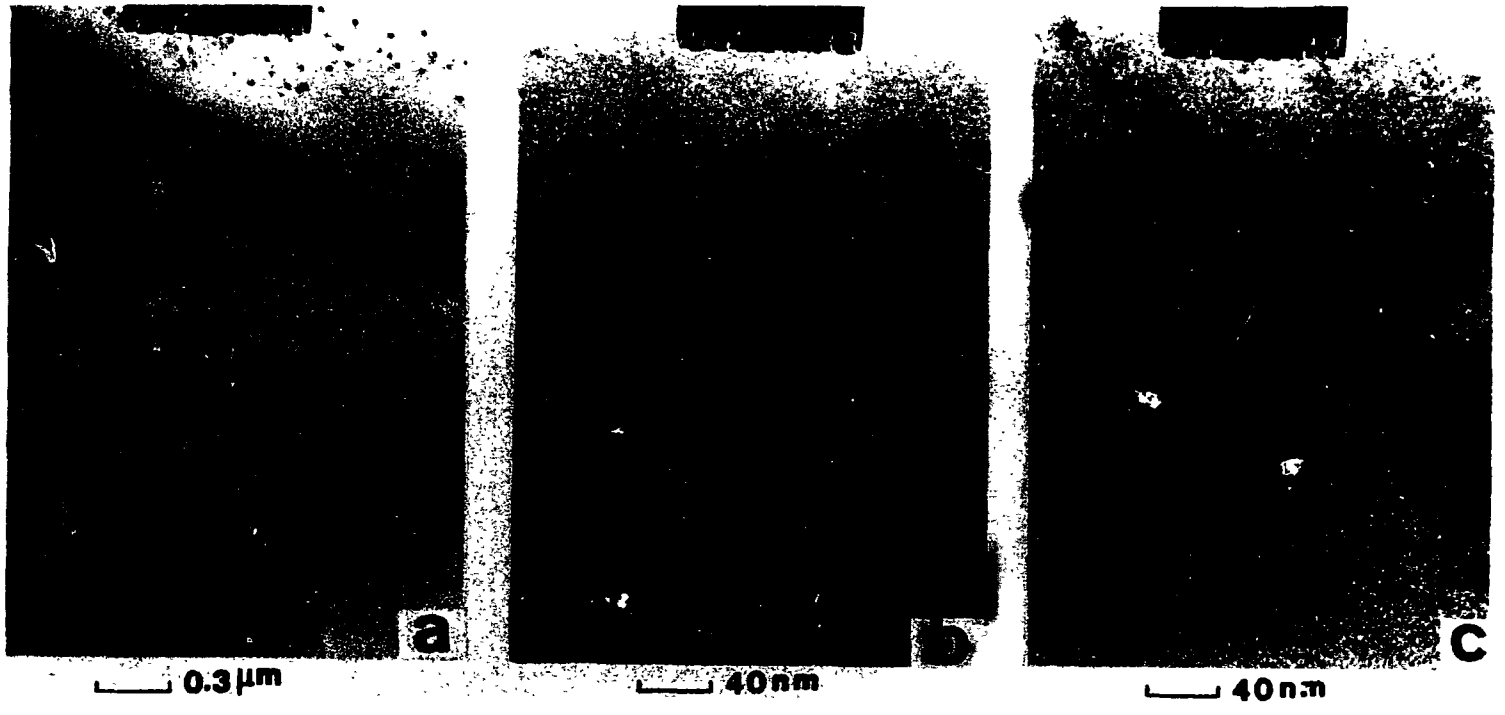

Fig. 23. TEM micrographs of type 316 stainless steel containing 256 appm helium. (a) Typical microstructure of dislocation loops, (b) helium bubble clusters in the matrix dislocation loops, and (c) grain boundary helium bubbles located in grain boundary dislocations.

helium containing specimens (Figure 23a) showed a dislocation structure (low dislocation density) similar to that of the parent metal (Figure 63a). However, they contained a uniform distribution of dislocation loops in the matrix. Values of dislocation loop densities as a function of helium level are given in Table 5. Results revealed that the dislocation loop density and size increase with increasing helium concentration. The formation of these dislocation loops is believed to be related to the mechanisms of helium bubble formation in the grains. It was interesting to note that the 0.18 appm specimens showed no dislocation loops in the grains.

A higher magnification of the microstructure in both the matrix and grain boundary (GB) regions of the helium-doped specimens (256 appm) is shown in Figures 23b and c. These photomicrographs (Figure 23b and c) show a helium bubble microstructure. Figure 23b shows matrix helium bubbles and Figure 23c shows GB helium. In the matrix, single helium bubbles and/or clusters were observed in the dislocation loops. These visible matrix helium bubbles were uniform in size and had a diameter of 1.6 nm. The GB helium bubbles were approximately 1.9 nm in diameter. They were often found to be attached to grain boundary dislocations (GBDs). The helium bubble density in the grain boundaries was approximately $7 \times 10^{14}/m^2$ which varied slightly with helium concentration. The observed number of bubbles in the grain boundaries varied from boundary to boundary and, therefore, might depend upon the specific orientation of adjacent grains. In the specimens containing 0.18 appm helium, helium bubbles were rarely

Table 5. Density and size of dislocation loop and helium bubble of type 316 stainless steel

He level (appm)	ρ_l ($10^{20}/m^3$)	D_l (nm)	ρ_m ($10^{20}/m^3$)	D_m (nm)	ρ_{gb} ($10^{14}/m^3$)	D_{gb} (nm)
0.18[a]	-	-	-	-	-	-
2.5	0.5	5.7	1.3	1.5	5.7	1.8
27.0	3.0	7.3	2.7	1.6	7.3	1.9
105.0	6.5	11.7	3.6	1.6	8.2	1.9
256.0	11.5	14.6	4.5	1.7	8.8	2.0

[a]Dislocation Loops and Helium Bubbles Were Rarely Observed.

ρ_l : Density of Dislocation Loop.
D_l : Diameter of Dislocation Loop.
ρ_m : Density of Matrix Helium Bubble.
D_m : Diameter of Matrix Helium Bubble.
ρ_{gb} : Density of Grain Boundary Helium Bubble.
D_{gb} : Diameter of Grain Boundary Helium Bubble.

observed. Relatively high GB helium bubble densities suggest that helium atoms are preferentially trapped at grain boundaries as a consequence of high binding energy.

The helium bubble morphology in the HAZ of welded helium-doped plates (256 appm) is shown in the Figure 24. The detailed TEM photomicrographs in the HAZ of the materials containing 0.18, 2.5, 27 and 105 appm helium are shown in APPENDIX F (Figures 68-71). In the HAZ of the 0.18 appm material, the GB helium bubbles were rarely observed (Figure 68). Those that were found were approximately 60 nm in size, much larger than those that had existed prior to welding. They remained, however, discrete and well separated. In general, most of the grain boundaries for materials containing 2.5 appm helium and above were preferentially perforated (Figure 24a) during the thinning process, making foil preparation extremely difficult. This was caused by the presence of very large helium bubbles which were located along the grain boundaries. The perforations were similar in size to the observed dimples on the HAZ fracture surface (Figures 17 and 18) indicating that the grain boundaries in the foils were very near the final stage of cracking.

Both the matrix and grain boundary bubbles subsequent to welding were much larger than those observed in the as-received condition. The increase in bubble size resulted from their growth which was enhanced by the actions of temperature and thermally induced stress. The number and size of helium bubbles in the HAZ also varied significantly from boundary to boundary. The differences were apparently due to the

YE-13842

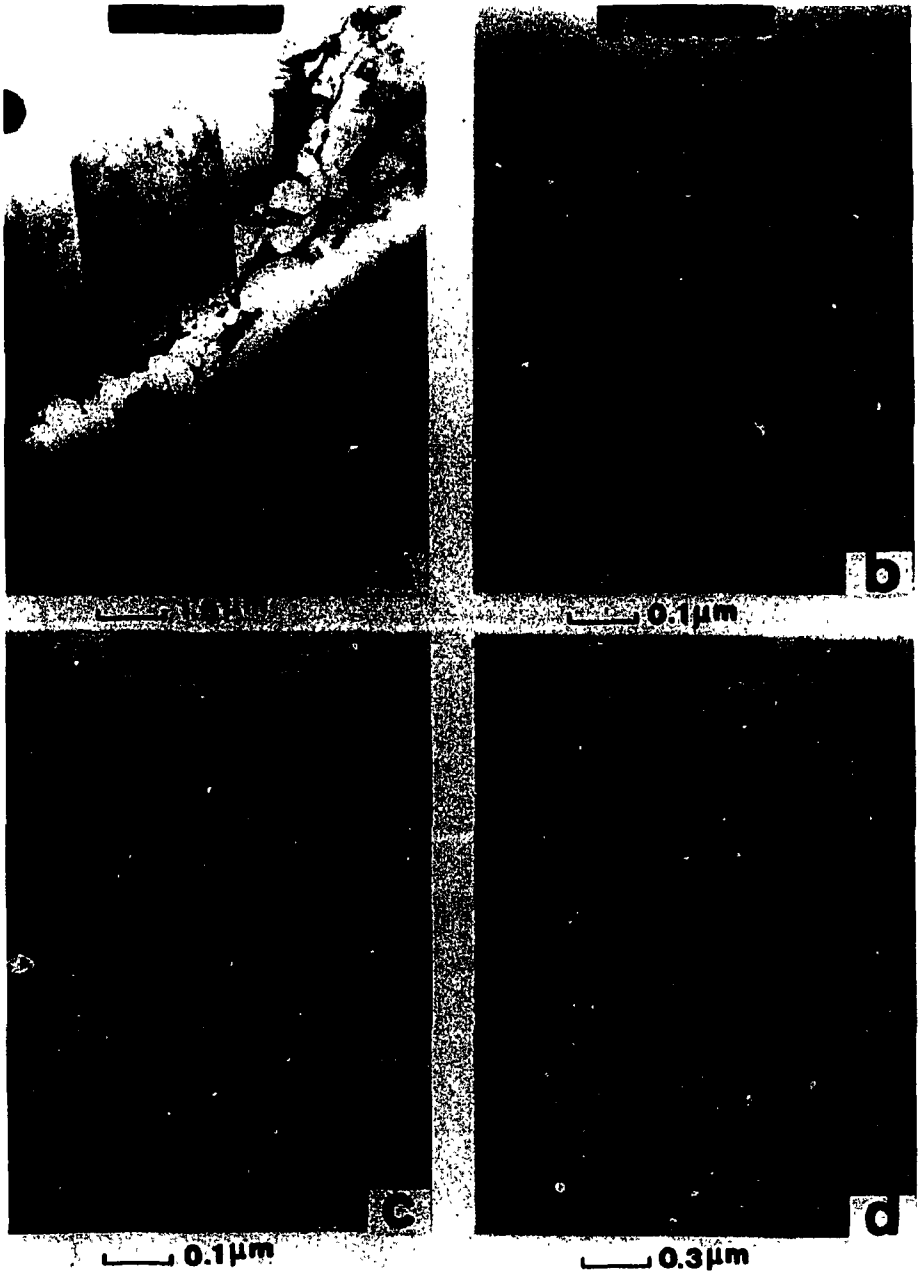

Fig. 24. TEM micrographs of the heat-affected zone of 256 appm weld with normal heat input. (a) Perforated grain boundary, (b) matrix helium bubbles attached to dislocations, (c) grain boundary helium bubbles, and (d) subgrain structure with helium bubbles.

variation in the orientation of grain boundaries relative to the thermal stress and to the thermal history experienced by each individual grain boundary. The boundaries which were normal to the thermal stress and experienced the highest temperature would be expected to have the largest helium bubbles. In addition, the extent of structural misfit in the grain boundary also affects the growth of helium bubbles. The higher the degree of incoherence, the more the growth will be enhanced. Most of the observed GB helium bubbles were equiaxed and crystallographic in shape (Figure 70c).

Observations revealed that the helium bubble density in the matrices increases with increasing helium concentrations. For the 0.18 appm material, the helium bubbles in the matrices were not observed in the TEM disks examined. In higher helium content welds, the visible helium bubbles in the matrices were equiaxied and crystallographic in shape. They were frequently located at lattice dislocations. These dislocations, which were not frequently seen in the as-charged specimens, were hypothesized to have been generated during the welding process by the thermal cooling stresses. Isolated helium bubbles were also observed in the matrices. They were generally smaller than those located at lattice dislocations. This is due to the fact that dislocations act as a high diffusivity path, referred to as pipe diffusion, for helium bubbles enhancing helium bubble growth. Additionally, the helium bubbles at the same dislocation were different in size indicating impingement and coalescence of small bubbles has occurred along the dislocations. Subgrain microstructures typical of

creep specimens were observed (Figure 24d). These subgrain boundaries were generated by high temperature dislocation climb. Helium bubbles were generally found to be associated with subgrain dislocations. Additionally, the density of helium bubbles in the subgrain regions was higher than in the matrix as a result of the higher dislocation density.

High heat input welds. Figure 25 shows the TEM morphology in the HAZ of 105 appm materials which were welded with a heat input of 400 J/s. The TEM features for the 27 appm material is shown in APPENDIX F (Figure 72). A thick TEM disc was again obtained as a result of the presence of very large GB helium bubbles (Figure 25a). The helium bubbles in the matrices were also frequently observed at the lattice dislocations (Figure 25b). Furthermore, the GB helium bubbles in the high heat input welds exhibited similar faceted shapes as the normal heat input welds (Figure 25c). In general, the helium bubble density and size in the matrices of high heat input welds was larger than that of normal heat input welds. This was due to the longer period at elevated temperatures for growth of helium bubbles to occur. Subgrain structure along with an associated higher density of helium bubbles was also observed in the HAZ of high heat input welds.

Butt-joint welds. The TEM morphology of butt-joint welds with 27 appm helium under no external constraint is shown in Figure 26. The microstructure of 105 appm butt-joint welds is also shown in APPENDIX F (Figure 73). The observed microstructure (Figure 26a) shows large GB

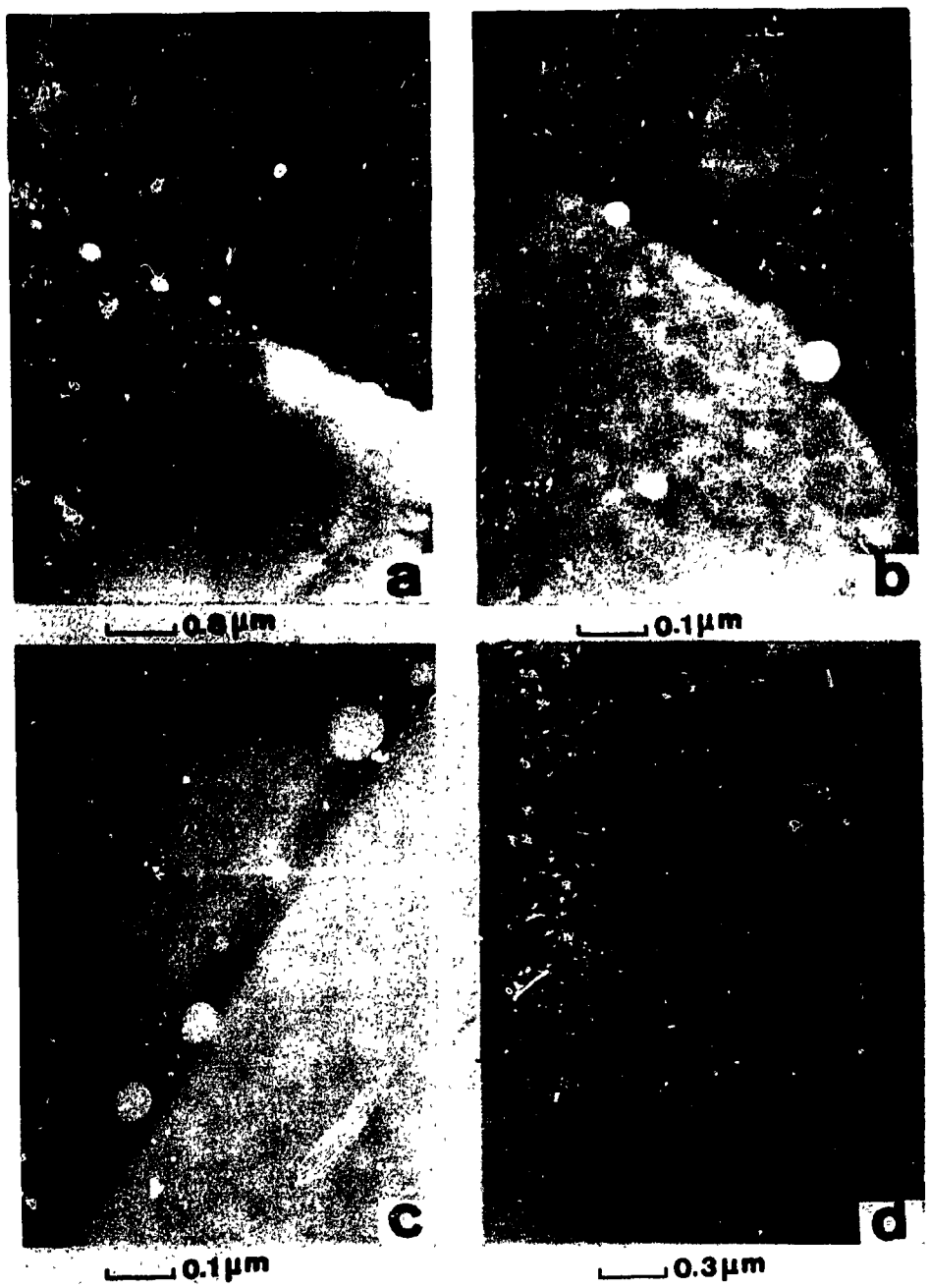

Fig. 25. TEM micrographs of the heat-affected zone of 256 appm weld with high heat input. (a) Nearly perforated grain boundary, (b) matrix helium bubbles attached to dislocations, (c) grain boundary helium bubbles, and (d) subgrain structure with helium bubbles.

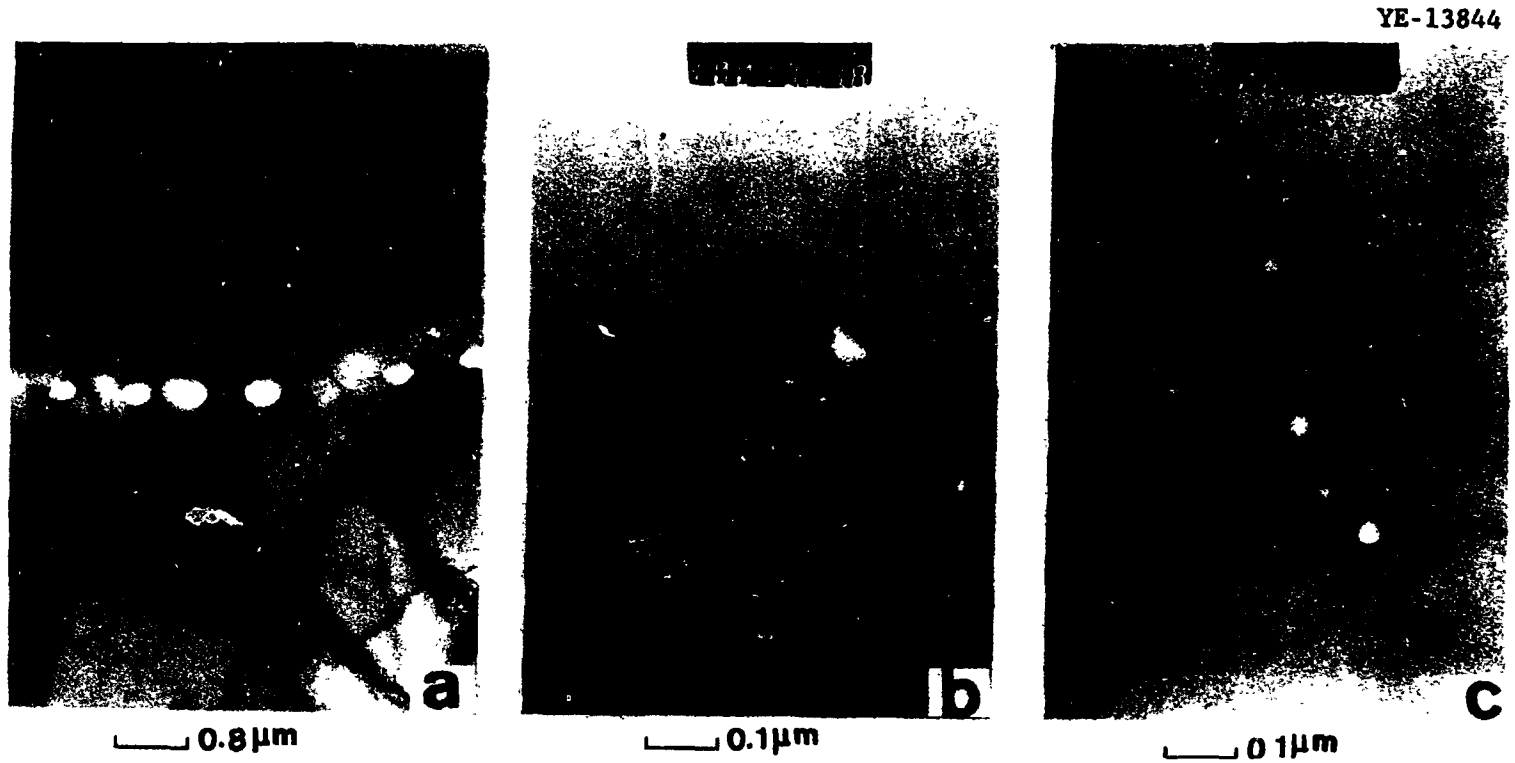

Fig. 26. TEM micrographs of the heat-affected zone of 27 appm butt-joint weld. (a) Nearly perforated grain boundary, (b) matrix helium bubbles attached to dislocations, and (c) grain boundary helium bubbles.

helium bubbles were perforated during the thinning process limiting further thinning and hence resulting in a thick TEM disk. Photomicrographs demonstrate that GB bubbles still obtain a size and density which degrades the weld integrity. This degradation occurs without the enhancement of an externally applied constraint. This result is further confirmed by SEM observations (Figure 21). Uniform dimple distributions were observed on post weld-bend specimens. In the matrix, helium bubbles were also observed at lattice dislocations and were different in size. Generally, subgrain structures were not observed in the TEM disks of butt-joint welds. However, a higher dislocation density than that of the as-received material was observed.

Partial penetration welds

The TEM micrographs of the HAZ of the partial penetration welds containing 256 appm helium are shown in Figure 27. The TEM microstructures of 2.5, 27 and 105 appm partial penetration welds are also shown in APPENDIX F (Figures 74-76). Perforation of grain boundaries were again observed in the 256 appm welds. Generally, the GB helium bubbles were frequently observed at grain boundary dislocations and were different in size. In partial penetration welds, a higher density of subgrain structure than that of full penetration welds was observed. This is probably due to the difference in temperatures and thermal stresses experienced by the region of the TEM foils examined. In the matrix, helium bubbles were frequently located at lattice dislocations and were larger in size than isolated helium

YE-13845

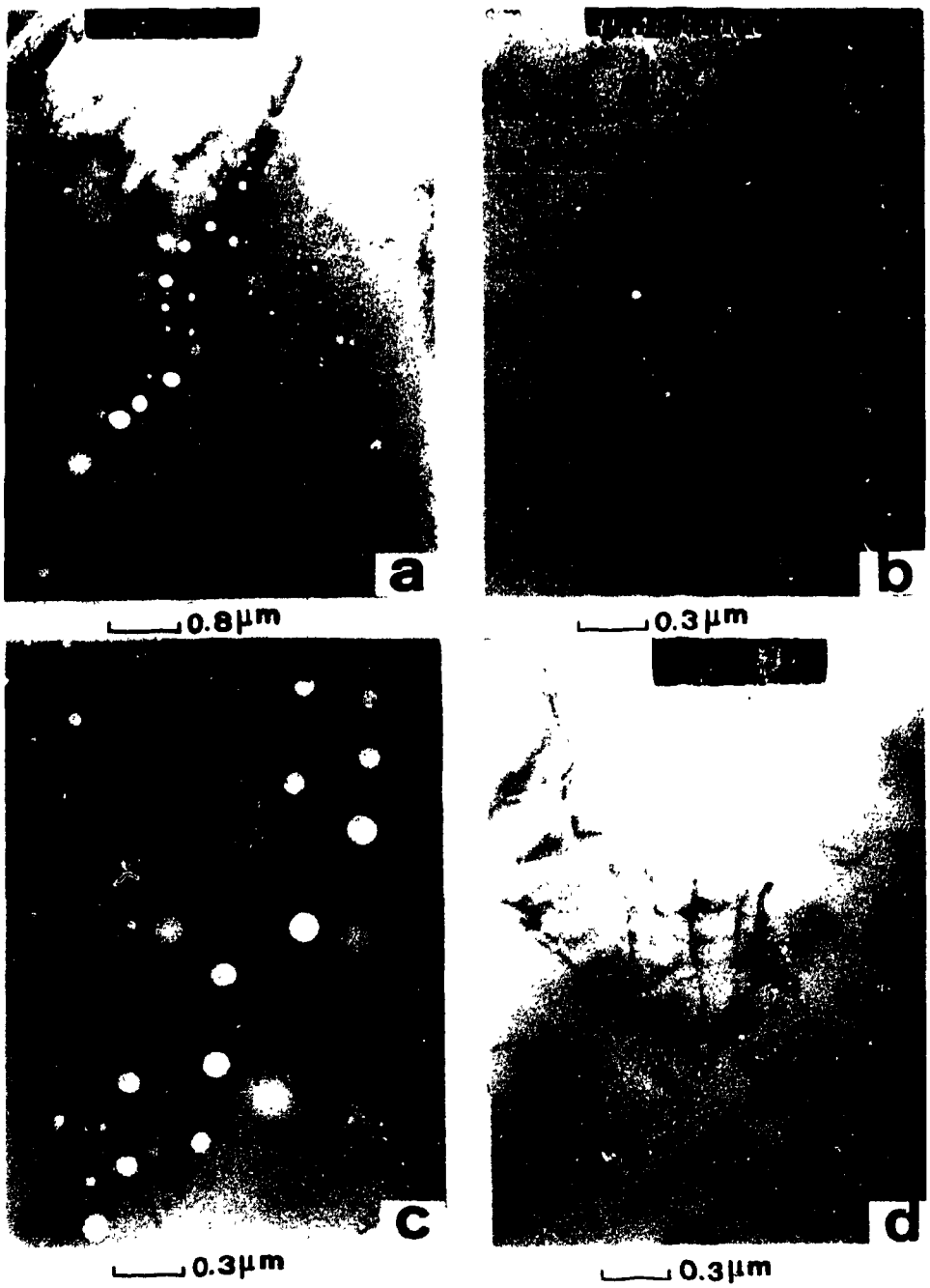

Fig. 27. TEM micrographs of heat-affected zone of 256 appm partial penetration weld. (a) Nearly perforated grain boundary, (b) matrix helium bubbles attached to dislocations, (c) grain boundary helium bubbles, and (d) subgrain structure with helium bubbles.

bubbles. In addition, helium bubble densities in the matrix increased with increasing helium concentrations.

Mechanical Properties

Microhardness and tensile tests were conducted on all the materials studied. Following optical metallographic examinations, Vickers microhardness tests were performed at room temperature. Figure 28 shows the microhardness traverses across the weld regions for the control and helium-doped specimens. Results indicated that the strength across the weld regions of all the specimens measured is insensitive to helium concentration. This observation implies that no strengthening occurs due to the presence of helium bubbles at the helium levels studied. The microhardness in the HAZ was higher than both fusion zone and base metal. The increase in strength in the HAZ was attributed to the strengthening effects which occurred during the temperature cycle induced by the welding. This strengthening is due to an increase in the dislocation density from deformation induced by internal tensile stresses, as shown in TEM micrographs of the HAZ (Figure 24). The fusion zone showed the lowest strength among the three weld regions. This was due to the precipitation of ferrite in the fusion zone.

Results of tensile tests on welded control and helium-doped specimens as a function of test temperature are shown in Figures 29 through 31. For comparison purposes, tensile results of unwelded control (parent metal) and helium-doped specimens are also shown. However, due to the limited number of available specimens, the welded

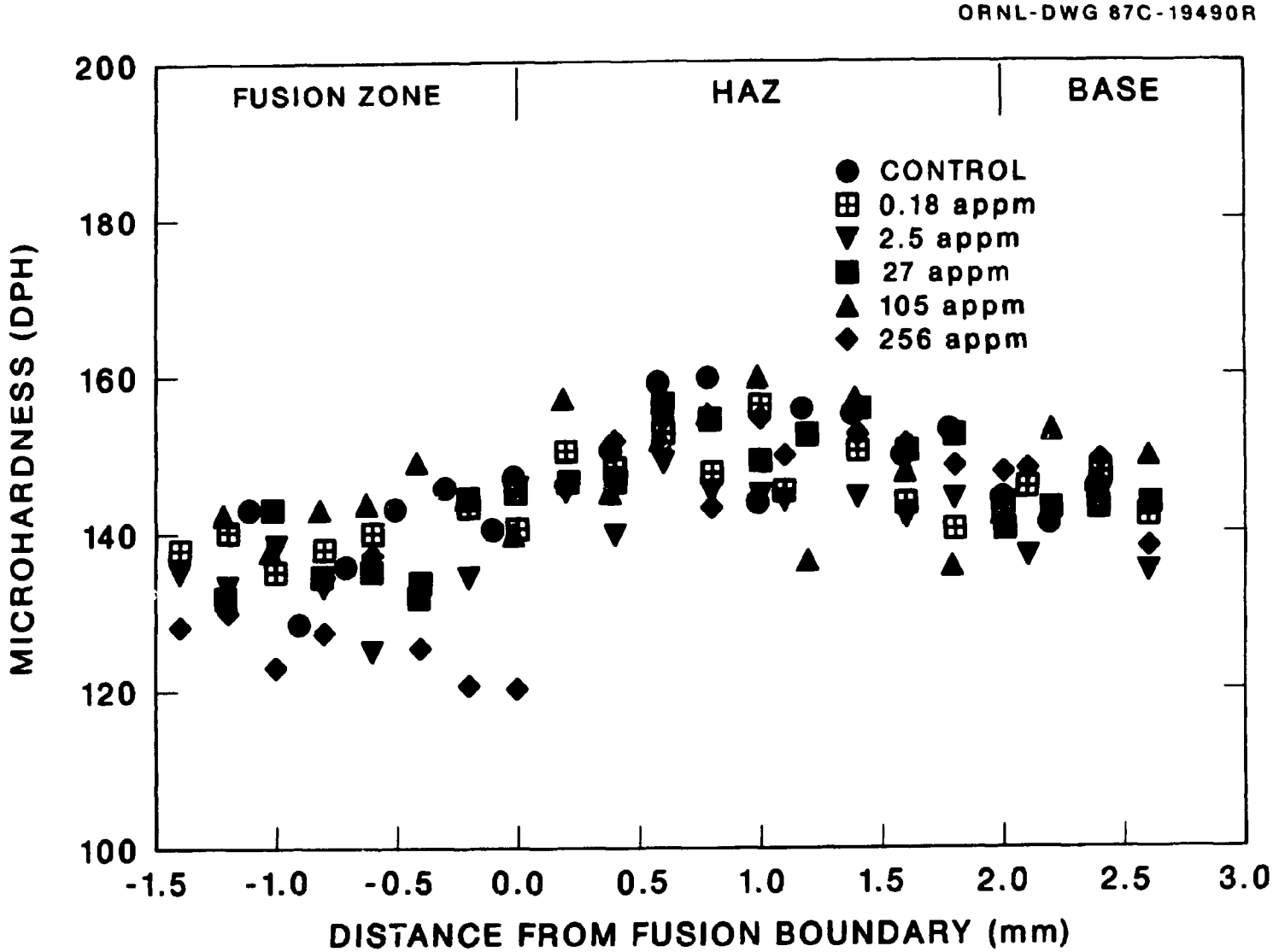

Fig. 28. Microhardness traverses across the weld regions of type 316 stainless steel. No strengthening effect of helium concentration was found.

specimens containing 2.5 appm helium were only tested at room temperature. Detailed dimensions and tensile data for all the specimens tested is given in APPENDIX G (Tables 8 and 9) and APPENDIX H (Tables 11 and 12) respectively.

The tensile results showed that yield strength (YS) decreased linearly with increasing temperature for all cases (Figure 29). The unwelded helium-doped materials at concentrations studied have the same yield strength as the control materials indicating no strengthening effect was incurred by the presence of helium. This observation is consistent with microhardness measurements. There was a significant increase in the yield strength of the welded materials, except for the 256 appm welds, relative to unwelded materials. The welds with 256 appm helium exhibited the lowest yield strength among all of the welded materials.

In all cases, the ultimate tensile strength (UTS) decreased with increasing test temperatures (Figure 30). The decrease in the strength is due to the annealing and recovery of the dislocation structure at elevated temperatures. For unwelded materials, the results reveal that the UTS was insensitive to the presence of helium at these concentrations. The strength of the welded control was the same as that of the unwelded control at room temperature. However, it was somewhat less at the elevated test temperatures. The welded specimens containing 0.18 appm helium showed strength similar to the welded control specimen. The UTS of specimens bearing helium concentrations equal to and greater than 2.5 appm, subsequent to welding, was severely

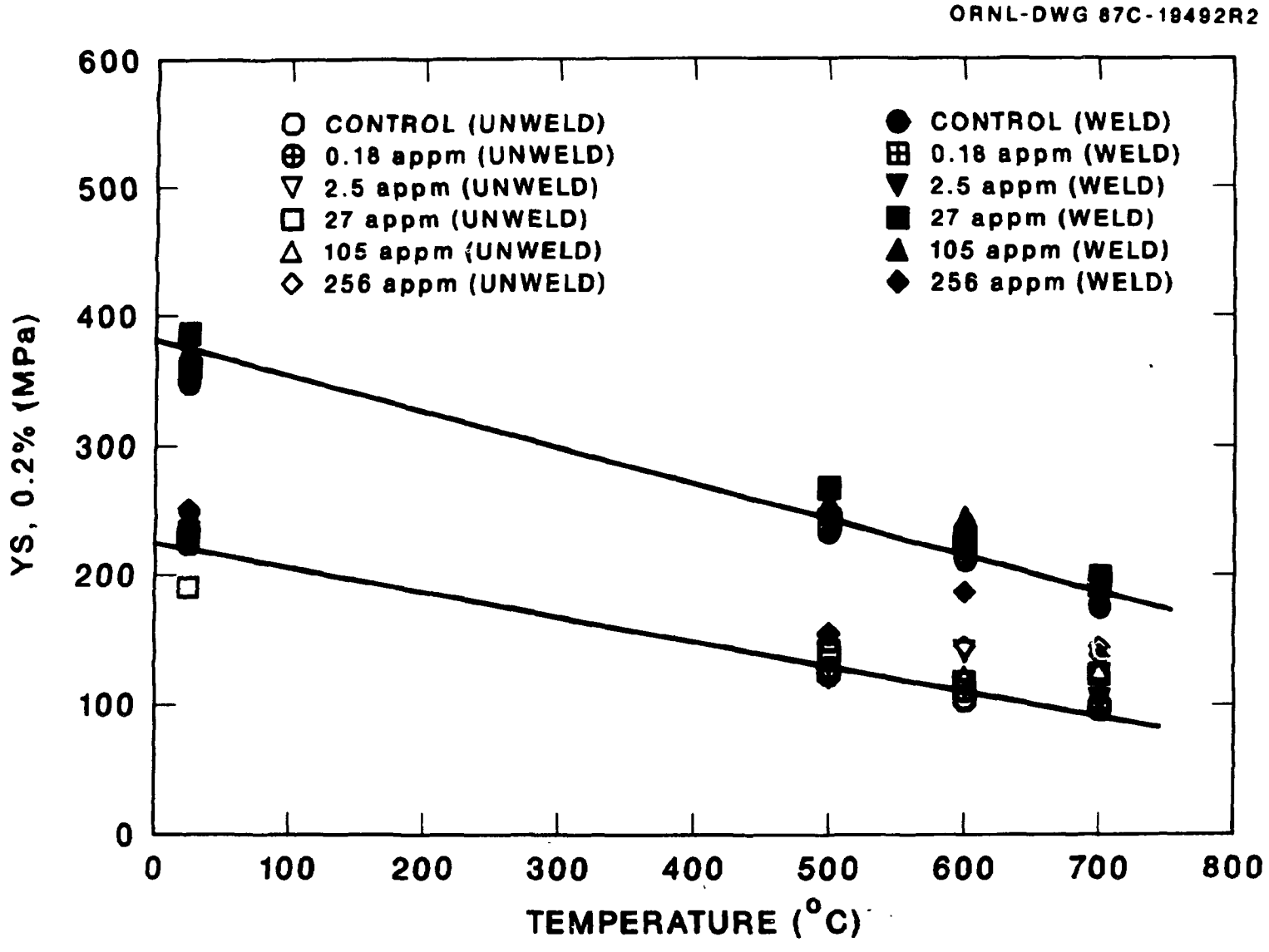

Fig. 29. Temperature and helium concentration dependence of yield strength of type 316 stainless steel. Welded materials generally show higher yield strength than unwelded materials.

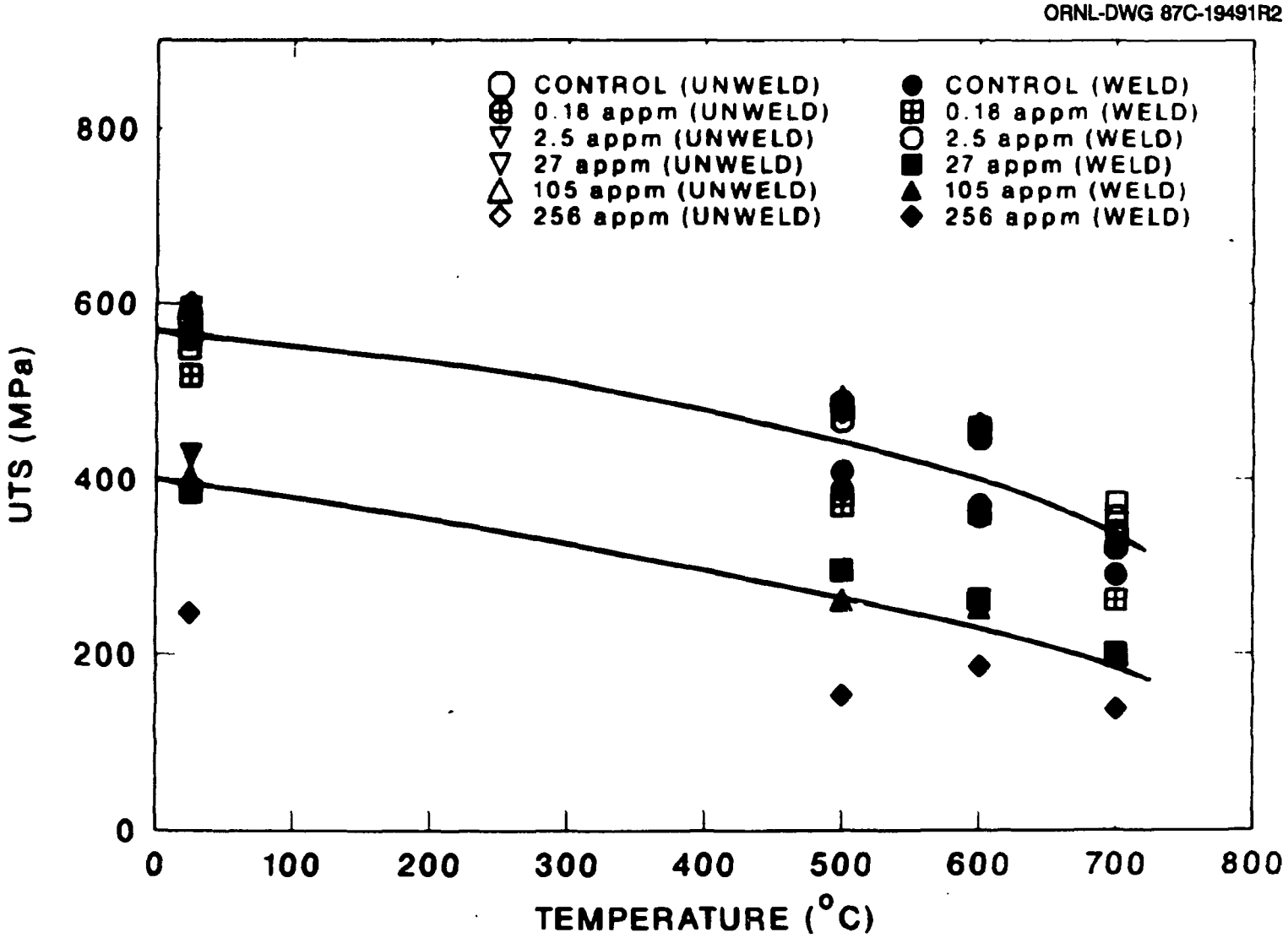

Fig. 30. Temperature and helium concentration dependence of ultimate tensile strength of type 316 stainless steel. Ultimate tensile strength and yield strength are nearly identical for welded helium-doped materials.

degraded. For welds with 256 appm helium, the degradation is very apparent. In fact, the UTS of the welded specimens with 2.5 appm helium and above was virtually identical to their yield strength as shown in APPENDIX H (Table 12), indicating that the specimens failed immediately upon yielding.

Prior to welding, helium-containing specimens had the same ductility as the control specimens up to 600°C (Figure 31). At 700°C the total elongation of helium-doped specimens decreased with increasing helium content but never fell below 10%. The ductility of welded control specimens was found to be lower than that of unwelded control specimens. This is due to the fact that the deformation and fracture is restricted to the fusion zone. The welded specimens with 0.18 appm helium had the same ductility as that of welded control material. The welded specimens containing 2.5 appm helium and above showed the lowest ductilities, generally less than 2% and as low as 0.2%. The results of total elongation indicated that material containing 0.18 appm helium had promising weld performance relative to welds with helium concentration equal to and greater than 2.5 appm. All welded specimens with 2.5, 27 and 105 appm helium failed at the fusion boundary at all test temperatures. The welds containing 256 appm helium failed at the fusion boundary at room temperature. Failure occurred in the fusion zone adjacent to fusion boundary at 500°C and above. Figure 32 shows a typical fracture surface of a welded specimen containing 2.5 appm helium tested at room temperature. The fracture surface was nearly 100 percent intergranular, and at high magnification

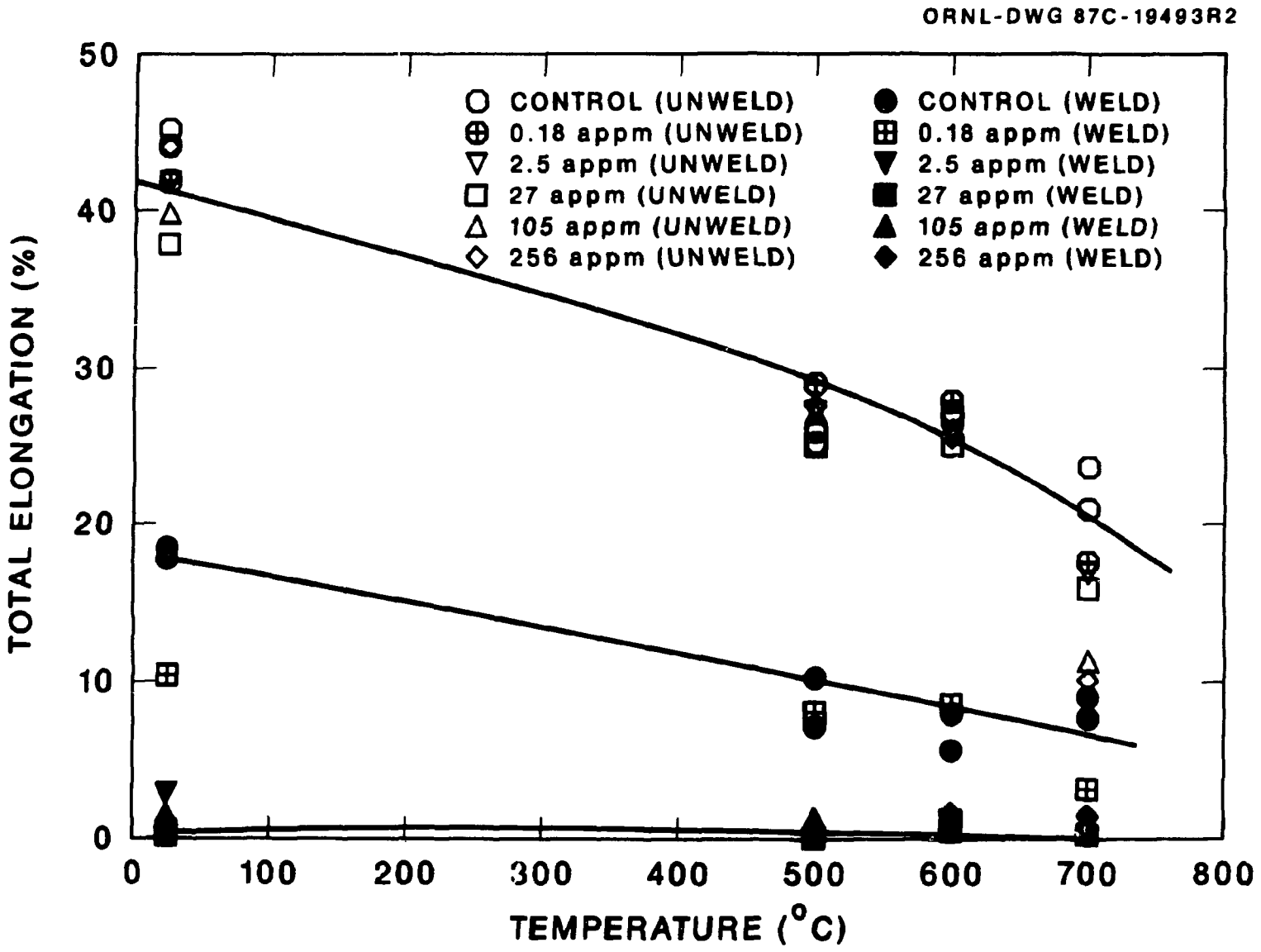

Fig. 31. Temperature and helium concentration dependence of total elongation of type 316 stainless steel. Welded helium-doped materials show the lowest ductility.

YE-13846

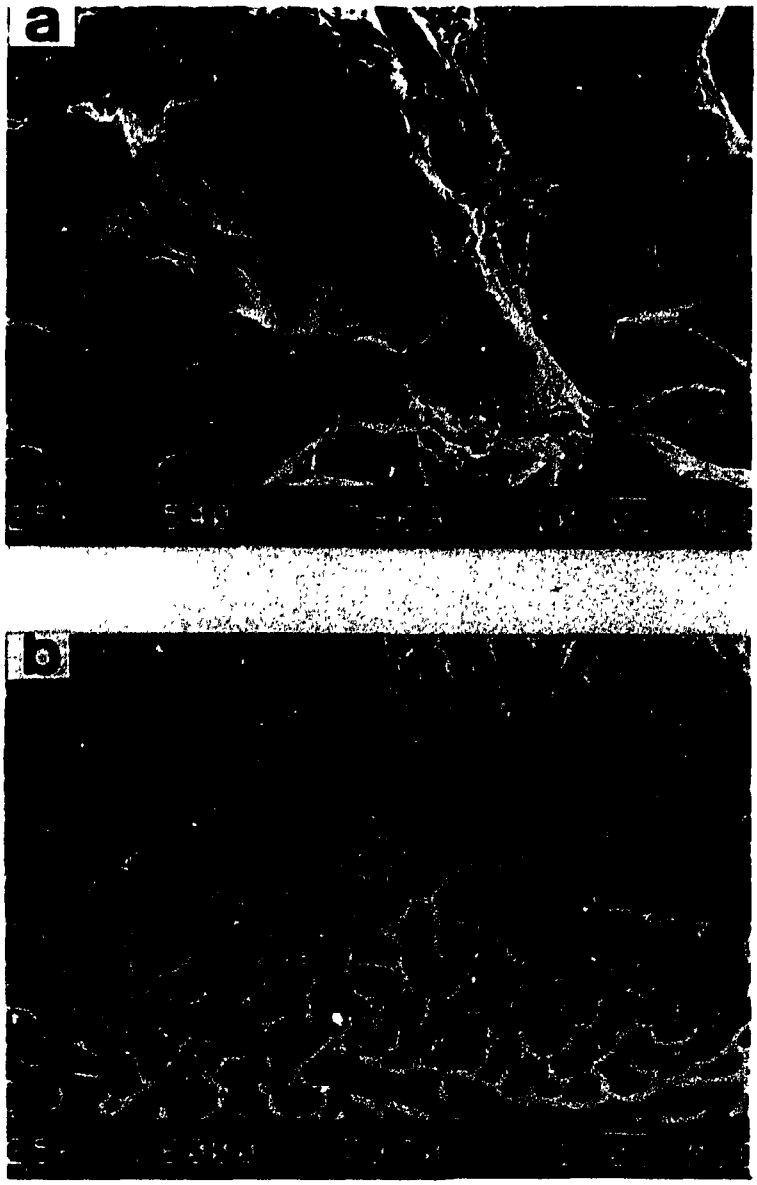

Fig. 32. SEM micrographs of welded type 316 stainless steel with 2.5 appm helium tested at 20°C. (a) Intergranular fracture, and (b) uniform distribution of dimples. Note sharp deformation of dimples since fracture occurs at room temperature.

the grain boundary facets exhibited a dimple structure that was quite similar to the weld crack surface in the HAZ (Figures 17,18). The main difference was that the dimple shear walls were much more sharply defined since fracture occurred at room temperature. Detailed fractography as a function of test temperature and helium concentration for both unwelded and welded specimens is described in APPENDIX I.

Aging Effect on the Properties of Helium-Doped Type 316 Stainless Steel

Figure 33 shows the room temperature mechanical properties as a function of aging temperature for specimens containing 256 appm helium. In general, both UTS and YS decrease with increasing aging temperatures. The decrease in strength is apparently due to the softening effect caused by the aging treatment. The total elongation is insensitive to aging temperatures between 800 and 1300°C. At 1300°C the total elongation decreases approximately 20%.

The fracture surfaces were examined in detail using SEM following tensile testing. Fractography of 256 appm specimens aged at 800, 900, 1050 and 1300°C for one hour is shown in Figure 34. The fracture surfaces of specimens aged below 1300°C revealed ductile transgranular fracture. Specimens aged at 1300°C failed predominantly by intergranular fracture. The grain facets of specimens aged at 1300°C were decorated with a uniform distribution of dimples about 1 μm in size. These dimples result from the growth of GB helium bubbles during aging. In spite of the observed intergranular fracture, the 1300°C aged specimen still shows good ductility (35%). These results support

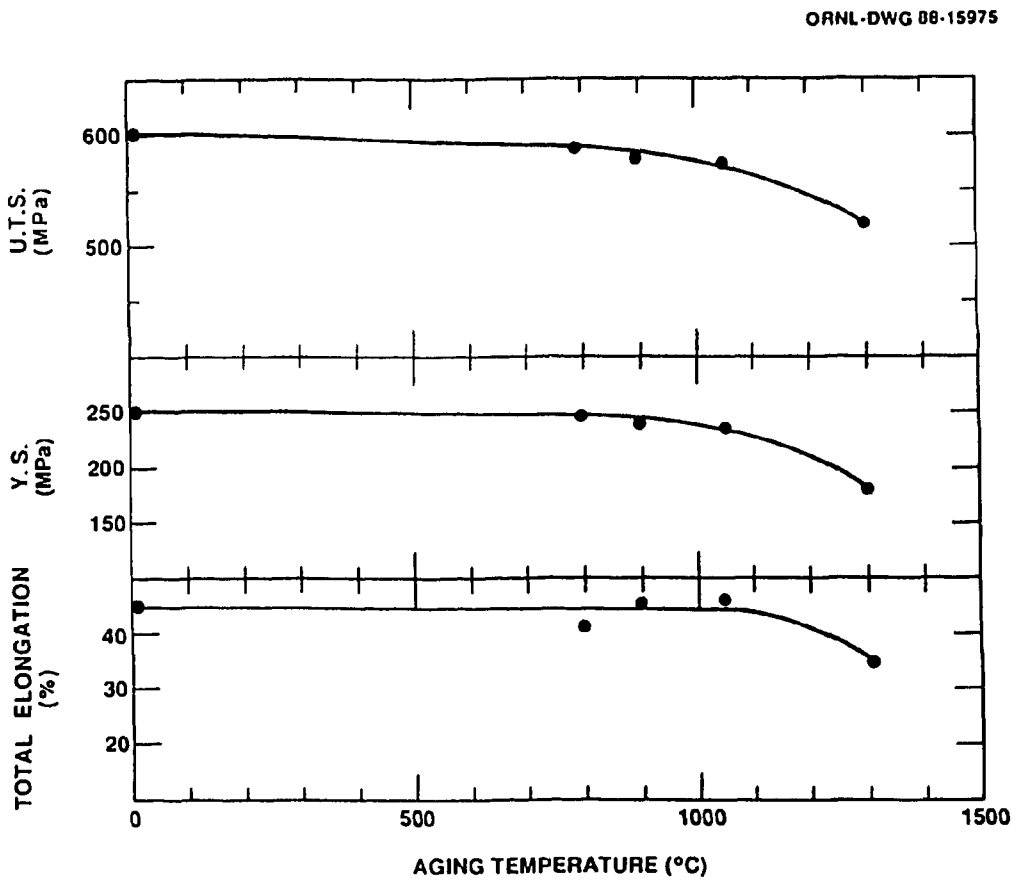

Fig. 33. Aging temperature dependence of tensile properties of type 316 stainless steel containing 256 appm helium.

YE-13847

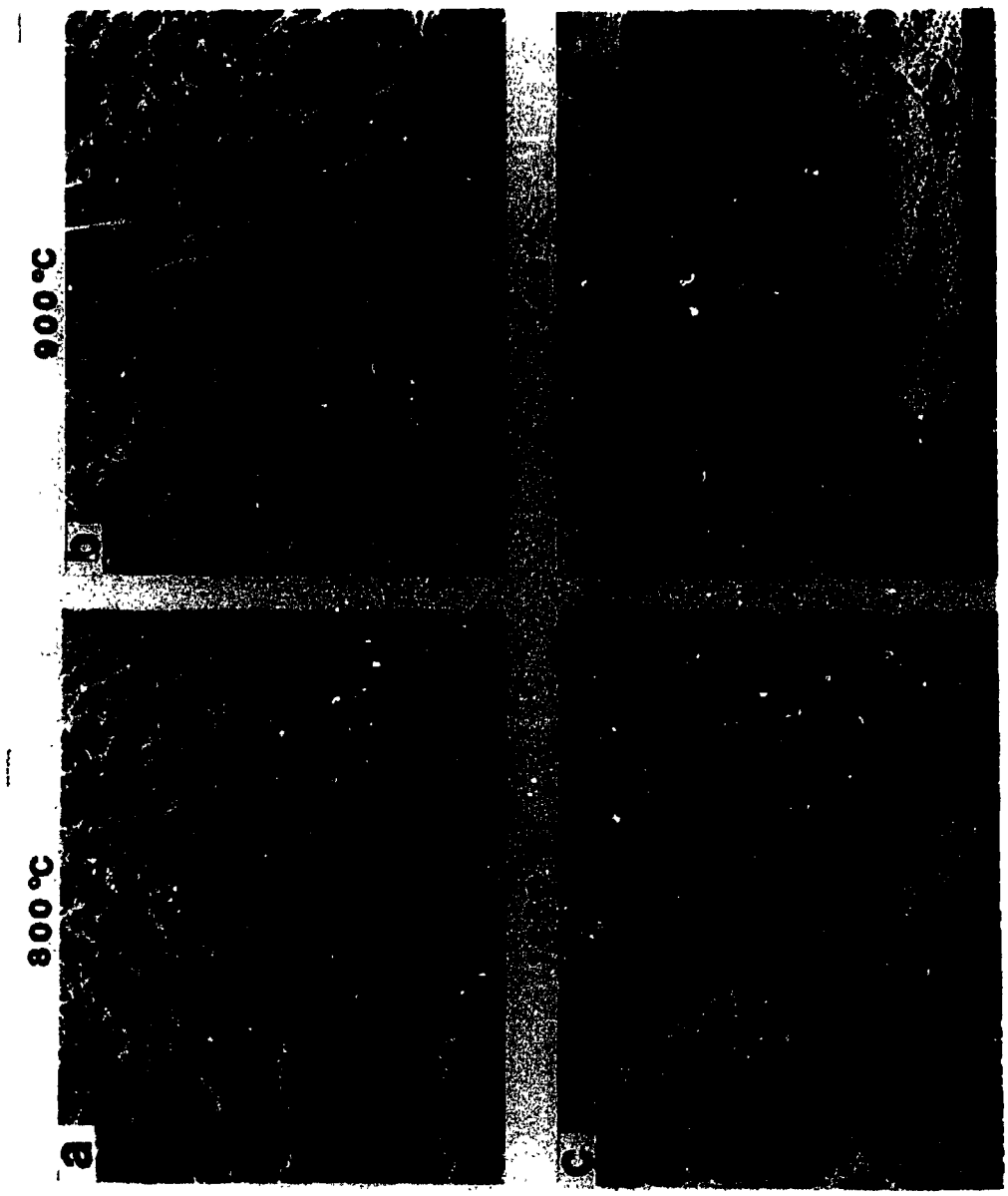

Fig. 34. Aging temperature dependence of fracture mechanism of type 316 stainless steel containing 256 appm helium. Note aged 1300°C specimens show intergranular fracture with a uniform distribution of dimples.

the hypothesis that high peak temperature alone is not sufficient to cause cracking of the weld.

The general helium bubble morphology after heat treatment at 1300 and 900°C is shown in Figure 35. The TEM photomicrographs for specimens aged at 1050, and 800°C are shown in APPENDIX F (Figure 77). The density and size of helium bubbles in both matrix and grain boundary as a function of aging temperature is listed in Table 6. The observed microstructures showed that the density of helium bubbles decreased with increasing aging temperature, while bubble size increased with aging temperature. This is due to the fact that the higher the aging temperature the greater the equilibrium concentration of vacancies which are available to aid in helium bubble growth. Additionally, the diffusivity of vacancies in both matrix and grain boundary increases with increasing temperature again enhancing bubble growth. Helium bubbles in the grain boundaries were equiaxied and faceted. In general, GB helium bubbles were larger than those in the matrix due to the higher diffusivity of vacancies along grain boundaries. However, some matrix helium bubbles located at dislocations were similar in size to those in grain boundaries indicating the important role of dislocation pipe diffusion in helium bubble growth. Specimens aged at 800 and 900°C showed segregation of precipitates along grain boundaries and in the matrices. These precipitates were often observed to be associated with helium bubbles.

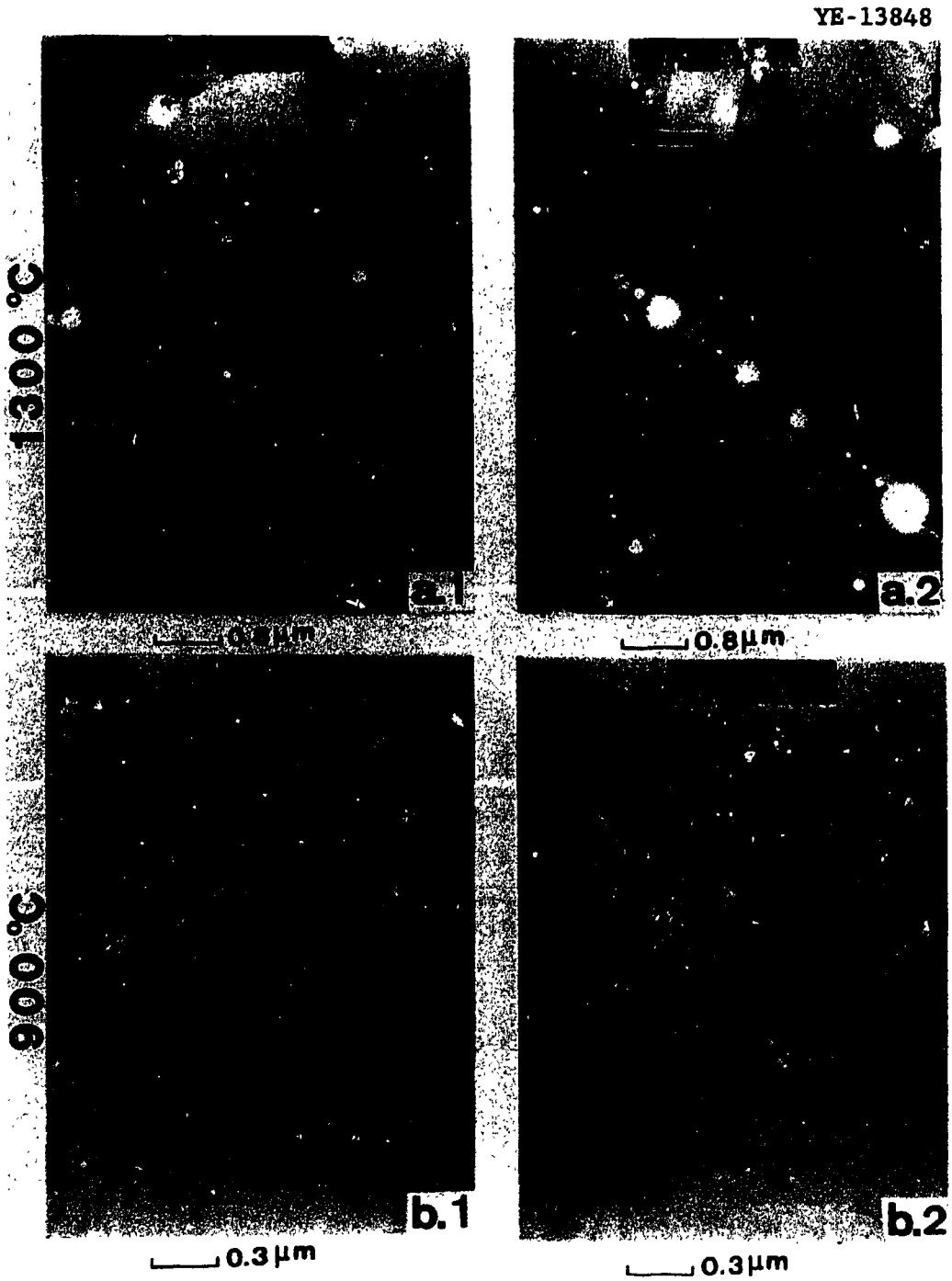

Fig. 35. TEM micrographs of aged specimens with 256 appm helium. (a) 1300°C, and (b) 900°C.

Table 6. Density and size of helium bubble as a function of aging temperature for 256 appm specimens

Temperature (°C)	ρ_m ($10^{20}/m^3$)	D_m (nm)	ρ_{gb} ($10^{14}/m^3$)	D_{gb} (nm)
1300	0.11	86.5	0.31	124.9
1050	2.01	39.5	0.56	39.0
900	2.30	13.0	0.57	18.3
800	4.20	7.8	4.10	5.3

ρ_m : Density of Matrix Helium Bubble.
D_m : Diameter of Matrix Helium Bubble.
ρ_{gb} : Density of Grain Boundary Helium Bubble.
D_{gb} : Diameter of Grain Boundary Helium Bubble.

Ferritic Stainless Steel

Full Penetration Welds

The macroscopic features of as-welded control and He-containing plates (0.3 and 1 appm) of HT-9 are shown in Figure 36. Macroscopically, all of the welded control and helium-doped materials were sound and free of visible weld cracking. All of the as-welded plates were examined in detail using scanning electron microscopy following the visual examinations. Results again indicated that control and 0.3 appm welds revealed no signs of any weld defects, while 1 appm welds showed discontinuous micro cracking in the HAZ one to three grains from the fusion boundary (Figure 37). The observed cracking was only limited to the beginning region of the weld. Observations showed that weld cracking occurred along prior-austenite grain boundaries and was fully intergranular in nature, as shown in Figure 37a. At high magnification, the grain facets were observed to be decorated with uniform dimples attributed to helium bubbles (Figure 37b). The shear ligaments separating the dimples have been rounded by surface diffusion, indicating that the cracking occurred at high temperatures. As stated in the case of type 316 stainless steel, the cracking resulted from shrinkage stresses as the laterally constrained plates cooled after welding. Again, the HAZ cracking had its origin in the growth and coalescence of GB helium bubbles.

The optical metallography of welded HT-9 containing 1 appm helium is shown in Figure 38. The microstructures of a control and a specimen containing 0.3 appm helium are shown in APPENDIX C (Figure 61). Generally, the microstructures consist of three distinct zones: fusion

YE-13849

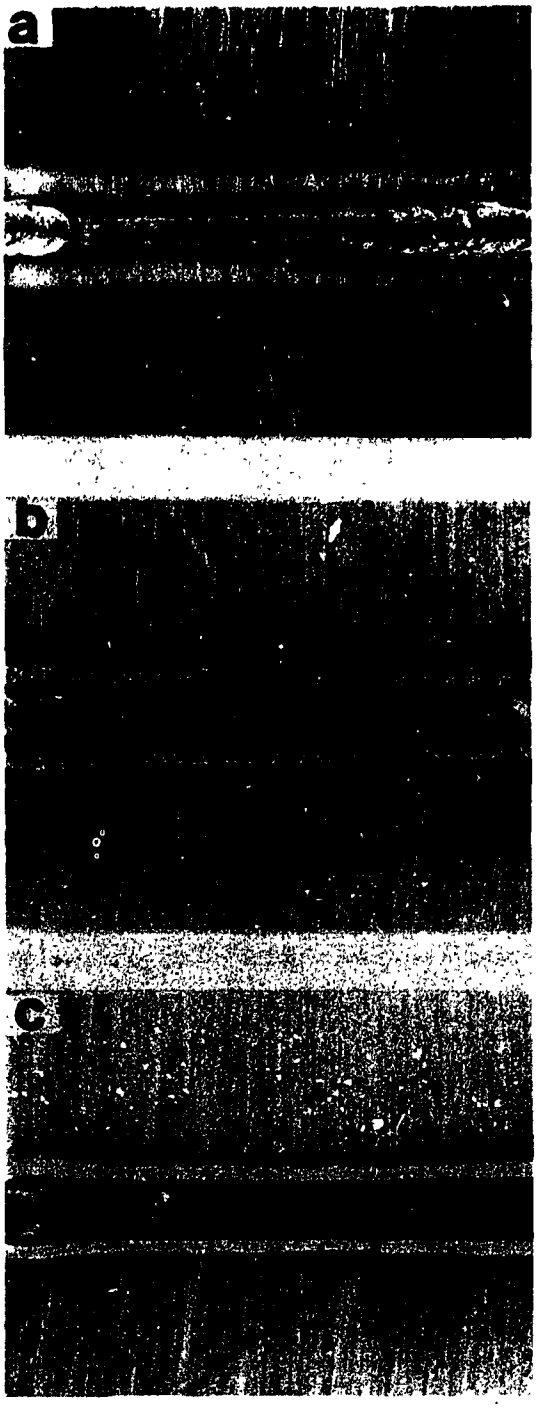

Fig. 36. Macroscopic features of as-welded HT-9. (a) Control material, (b) 0.3 appm, and (c) 1 appm. No macroscopic visible sign of cracking.

YE-13850

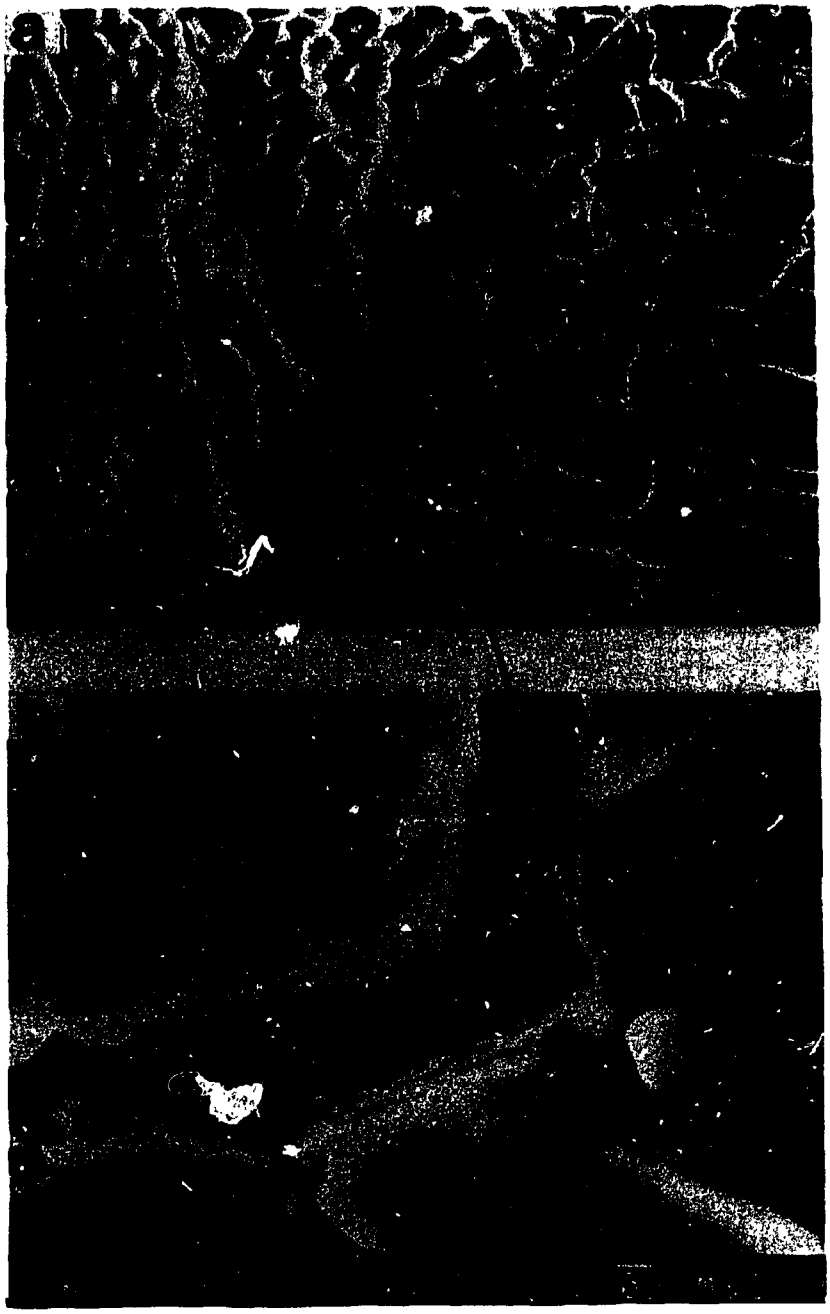

Fig. 37. Structure of as-welded HT-9 with 1 appm helium. (a) Intergranular fracture along prior-austenite grain boundaries, and (b) grain boundary facets decorated with a uniform distribution of dimples.

YE-13851

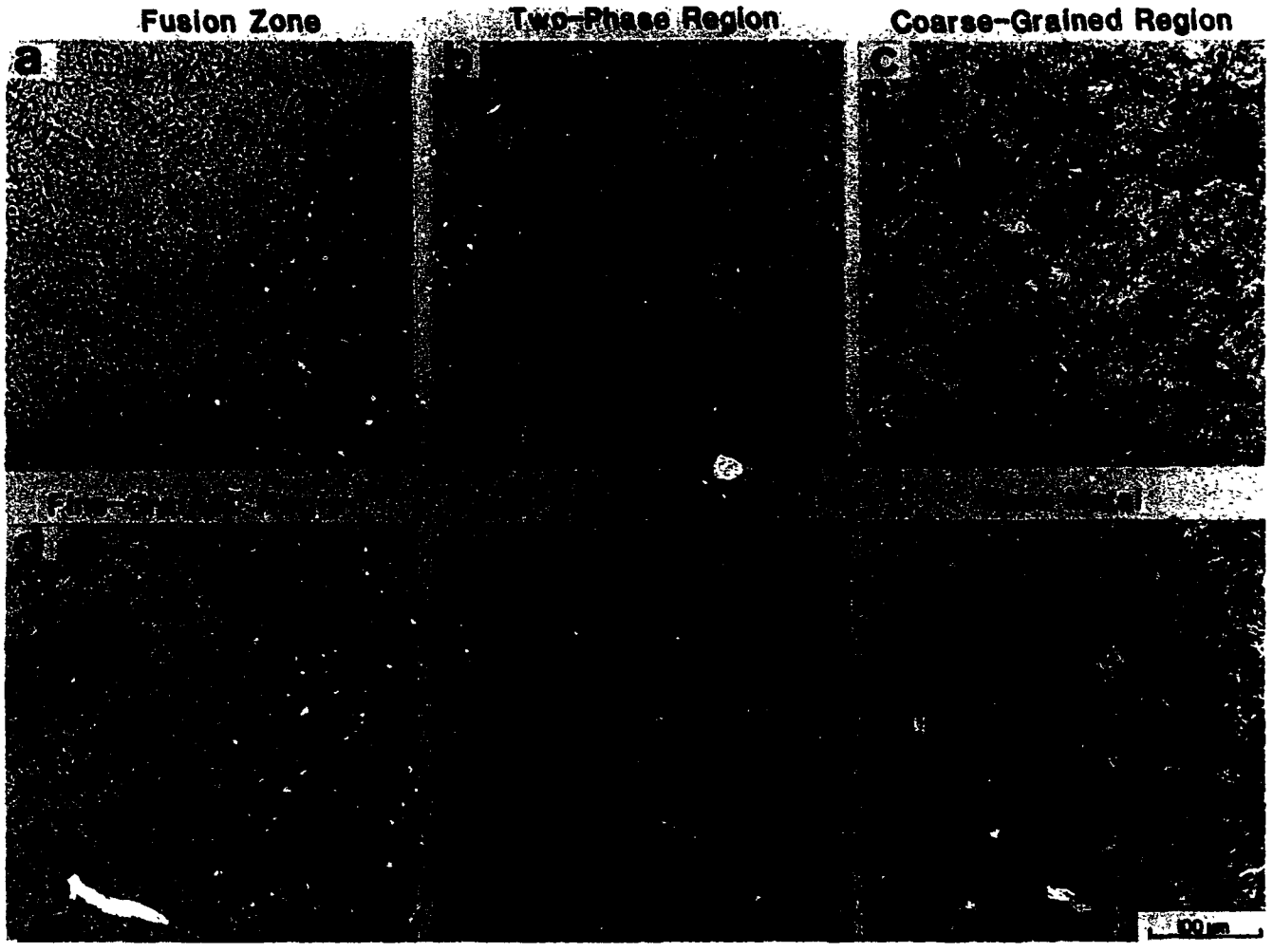

Fig. 38. Optical metallography of HT-9 weld with 1 appm helium. (a) Fusion zone, (b) - (e) subzones of heat-affected zone, and (f) base metal. Cracking occurred in the two-phase region of the heat-affected zone.

zone, HAZ and base metal. In the Fusion zone, the structure exhibited a mixture of untempered martensite and delta ferrite (Figure 38a). The microstructures in the HAZ have been identified to have four distinct regions: two-phase, coarse-grained, fine-grained and over-tempered regions. The two-phase region adjacent to fusion boundary consists of untempered martensite and delta ferrite (Figure 38b). The coarse-grained region is fully martensitic with a coarse prior-austenite grain size and a high hardness (Figure 38c). The fine-grained region is martensitic with a fine prior-austenite grain size interspersed with undissolved carbides (Figure 38d). The over-tempered region is a narrow softened band which was heat above the A_{c1}, and was typified by coarse martensite laths and carbides (Figure 38e). The base metal microstructure consisted of a mixture of lath-type martensite and carbides (Figure 38f). The metallographic results again indicated that control and 0.3 appm welds were free of any weld defects. One appm welds revealed intergranular fracture along prior-austenite grain boundaries. Metallographic specimens were further examined by SEM. Micro cracks were found to occur only in the HAZ.

Transmission Electron Microscopy Observations

The typical TEM microstructures of control and as-received helium-doped materials (0.3 and 1 appm) are shown in Figure 39. Figure 39a shows a typical microstructure of tempered martensite consisting of a tempered lath martensite network with carbide precipitates along prior-austenite grain boundaries and to a lesser degree along lath boundaries. In addition, no significant amount of ferrite was

YE-13852

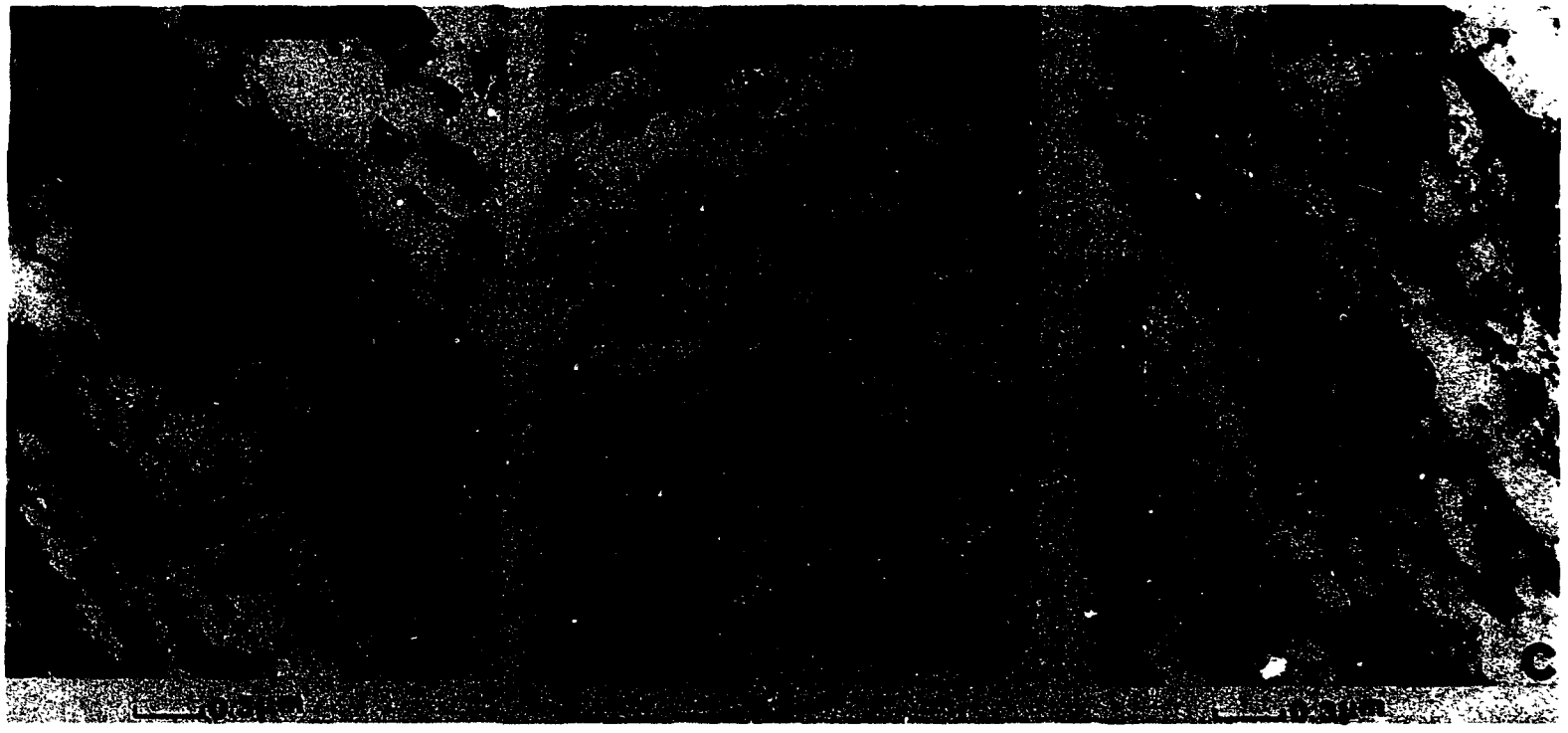

Fig. 39. TEM micrographs of HT-9 prior to welding. (a) Control, (b) 0.3 appm, and (c) 1 appm. Helium bubbles were not routinely visible until helium concentration levels exceeded 1 appm.

observed. For specimens containing 0.3 appm helium, no helium bubbles were visible in either lath or lath boundaries (Figure 39b). A few helium bubbles approximately 5 nm in size were observed at lath boundaries and located at dislocations in 1 appm specimens (Figure 39c). The microstructure of the HAZ of HT-9 welds containing 1 appm helium is shown in Figure 40. Large helium bubbles 80 nm in size were found at prior-austenite grain boundaries (Figure 40c). The HAZ microstructure revealed lath features with a higher dislocation density than the unwelded specimen. Subgrain structures were also observed in the HAZ specimens. In the welded 0.3 appm materials, helium bubbles were rarely observed in lath boundaries and prior-austenite grain boundaries.

Mechanical Properties

Following metallographic examination, 1000 gram load Vickers microhardness measurements were performed at room temperature. Figure 41 shows the microhardness traverses across the weld regions of welded control and helium containing materials. The results showed only minor variation in hardness in both the fusion zone and coarse-grained region of the HAZ. In addition, the hardness was insensitive to helium content indicating no detectable strengthening effect of the helium at these levels. Despite the presence of the softer ferrite phase, the fusion zone exhibited nearly full martensitic hardness. The fine-grained region exhibited a reduction in hardness relative to the hardness in the coarse-grained region. In addition, the over-tempered region showed a lower hardness than the base metal. The hardness

YE-13853

Fig. 40. TEM micrographs of the heat-affected zone of HT-9 with 1 appm helium. (a) High density dislocation structure observed in the heat-affected zone, (b) matrix helium bubble, and (c) large helium bubble along prior austenite grain boundary.

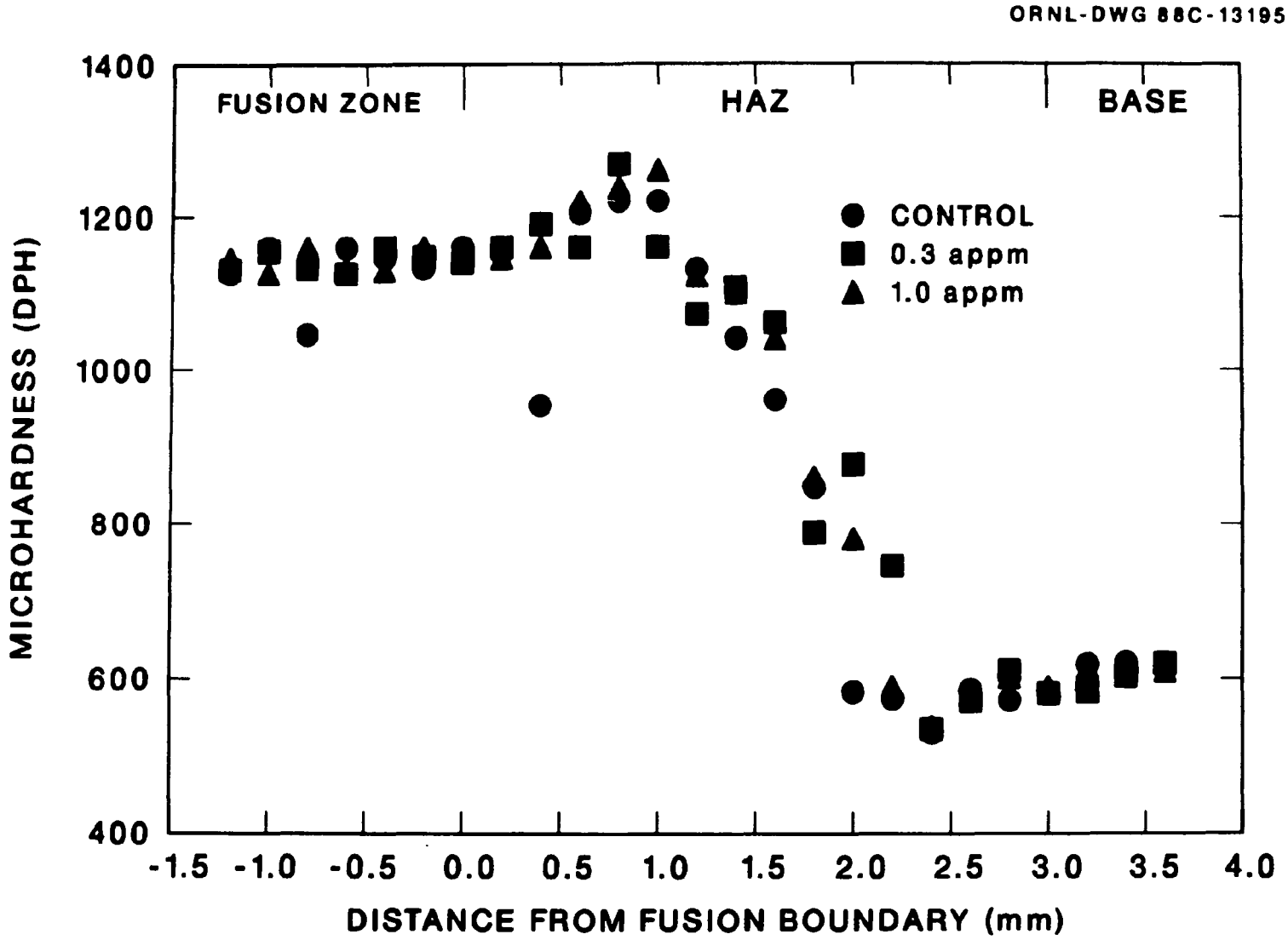

Fig. 41. Microhardness traverses across the weld regions of HT-9. No strengthening effect of helium concentration was observed.

traverses showed a rapid drop in hardness between fine grained and over-tempered regions. This results from the coexistence of untempered and tempered martensite in this region.

Tensile test results of control and helium-doped specimens in unwelded and welded conditions of HT-9 as a function of test temperature are shown in Figures 42 to 44. Tensile specimens of welded HT-9 materials were prepared using the same procedure as described for type 316 stainless steel. Detailed dimensions and tensile data are given in APPENDIX G (Table 10) and H (Table 13) respectively.

The tensile test results indicated that yield strength decreased with increasing temperature for all cases (Figure 42). The yield strength of unwelded helium-doped materials was the same as that of control materials at these test temperatures. Additionally, results indicated that the yield strength of welded HT-9 was similar to unwelded materials. This is due to the fact that all welded materials failed in the base metal.

For all cases, the ultimate tensile strength of HT-9 decreased with increasing test temperatures (Figure 43). Results revealed that the strength of helium-doped materials was the same as that of control materials at temperatures tested. The welded materials also exhibited the same strength as the unwelded materials.

Results of total elongation as function of test temperatures is given in Figure 44. In general, the total elongation increased with increasing test temperatures. Results also showed that the total elongation was insensitive to the presence of helium at these

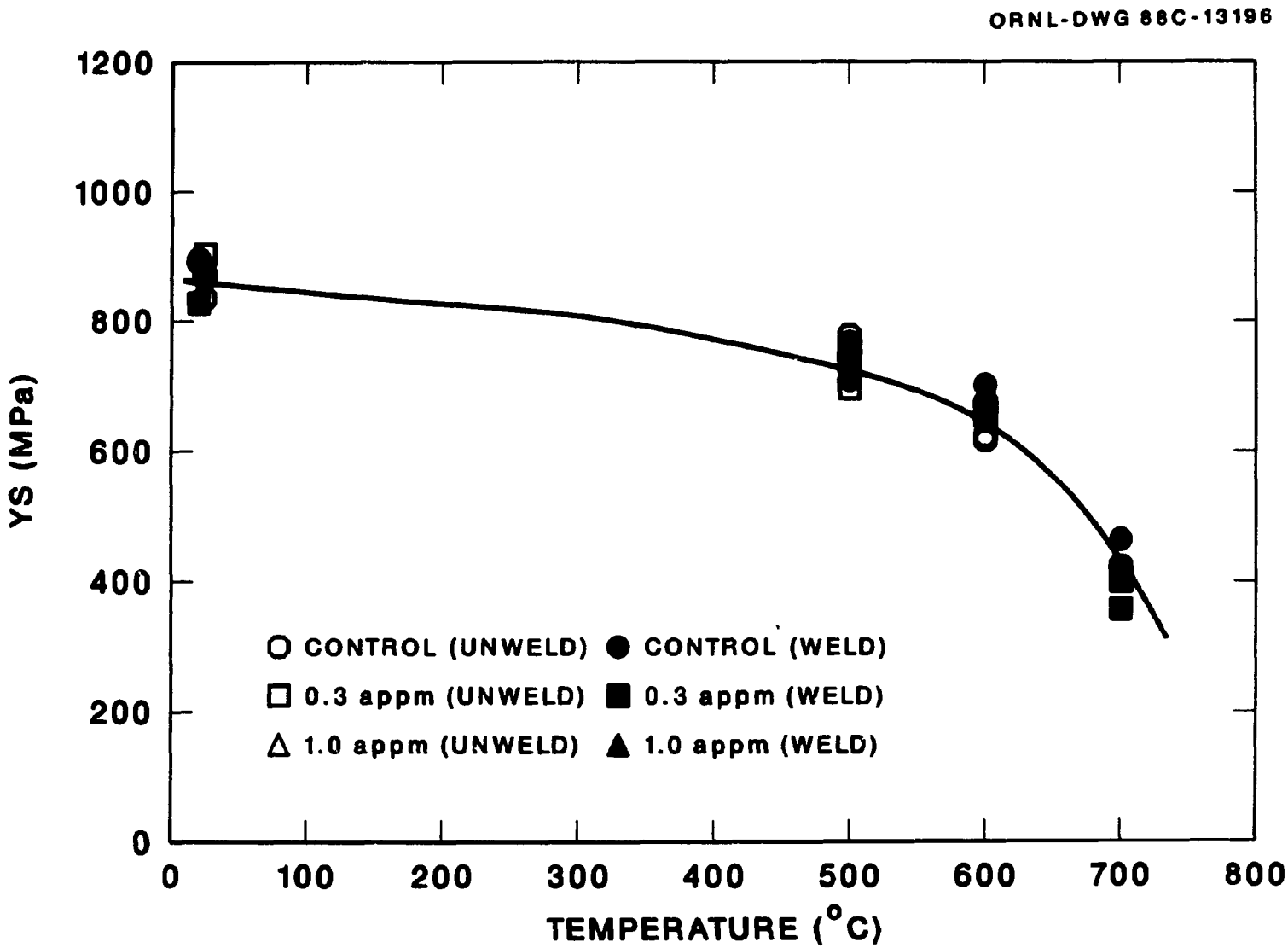

Fig. 42. Temperature and helium concentration dependence of yield strength of HT-9.

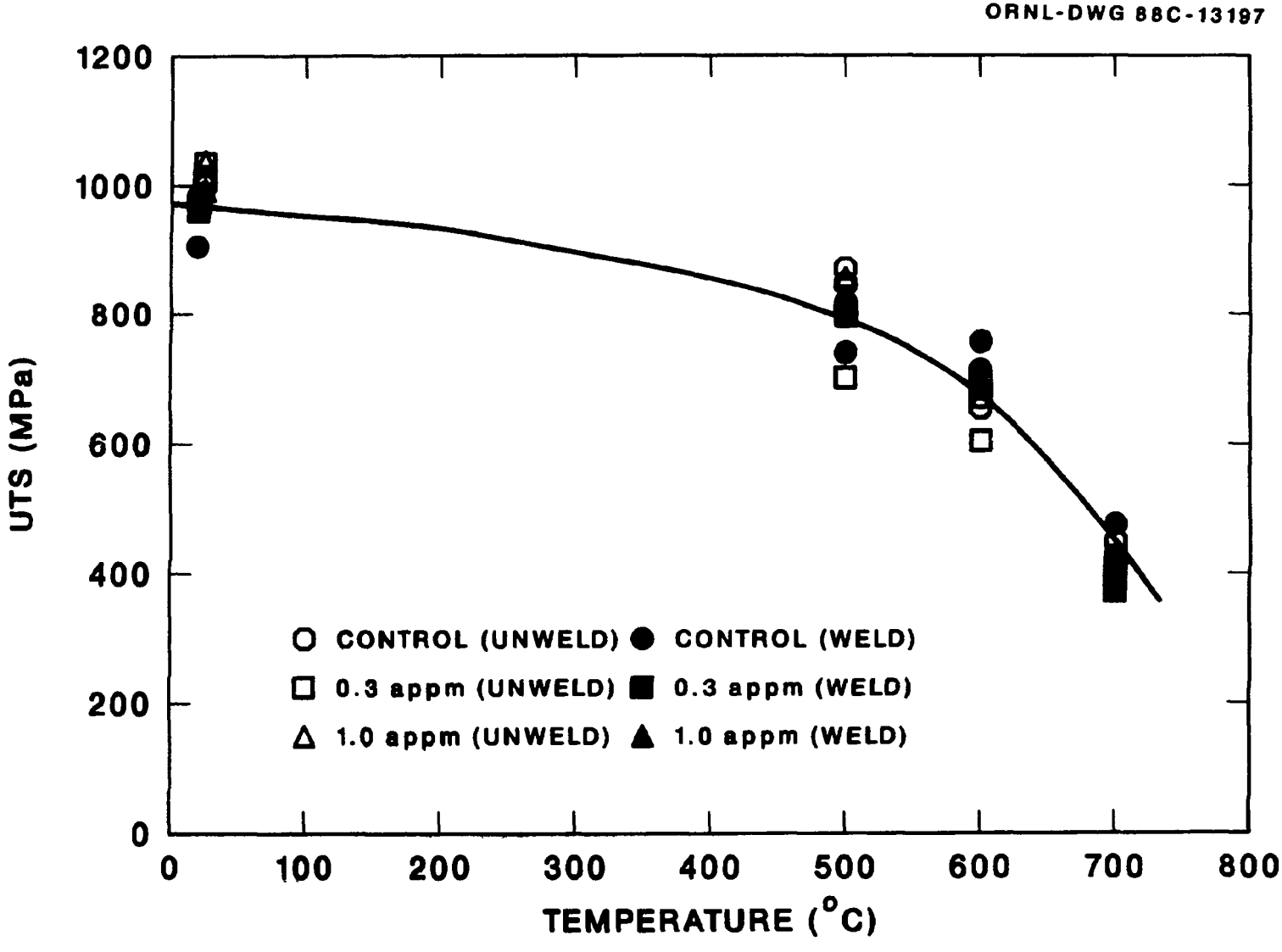

Fig. 43. Temperature and helium concentration dependence of ultimate tensile strength of HT-9.

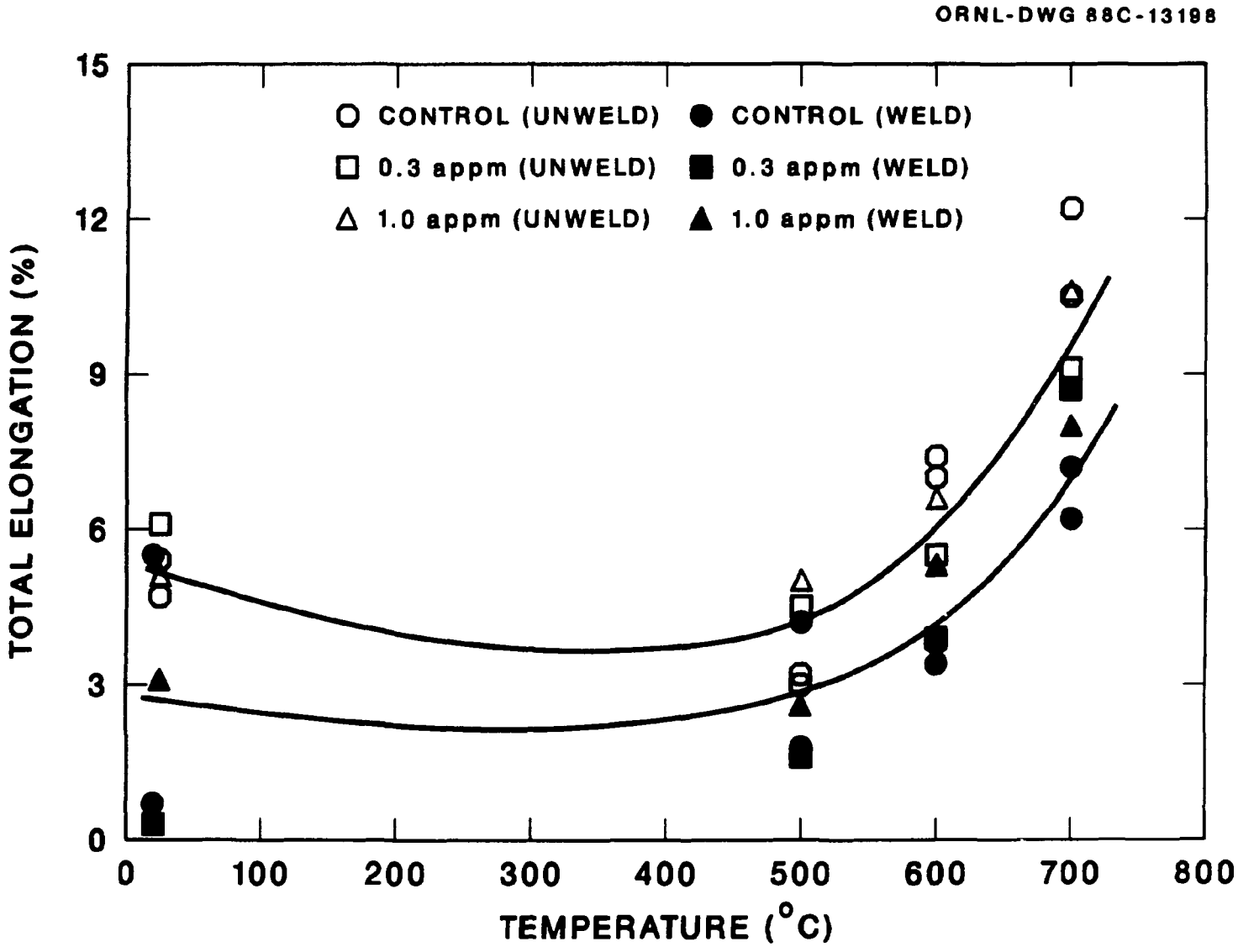

Fig. 44. Temperature and helium concentration dependence of total elongation of HT-9. Welded specimens show a reduction in ductility.

concentrations. Furthermore, results indicated that the unwelded HT-9 specimens exhibited greater total elongation than welded HT-9 specimens. It is due to the fact that the gage length of welded specimens available for plastic deformation is much less than that of control specimens. Detailed fractographic analysis of both control and helium-doped materials is shown in APPENDIX I.

V. PROPOSED MODEL OF GRAIN BOUNDARY BUBBLE GROWTH

One of the main objects of this study was to develop a mechanism which describes the HAZ cracking. This chapter details a proposed model for GB helium bubble growth in the HAZ which leads to final brittle fracture. It is known that the growth of GB helium bubbles is favored by conditions that promote high temperature and stress. For the case of welding, high temperatures are provided by the welding arc, and internal tensile stress is generated as the material contracts upon cooling of the constrained plates.

As a result of strong binding energy between helium atoms and grain boundaries, a well established GB helium bubble structure will be achieved after the relatively low 400°C offgassing treatment. Therefore, the nucleation and formation of GB helium bubbles will not be discussed here. The following section will be primarily focused on the development of growth kinetics of GB helium bubbles under welding conditions. The growth kinetics of GB helium bubbles in the HAZ can be divided into three sequential time regimes as shown in Figure 45. This division is made to recognize the different stress state and temperature that a fixed point in the HAZ experiences as the welding arc passes. Regime I is the heatup period before the temperature reaches the melting point (T_m). During this time regime, compressive

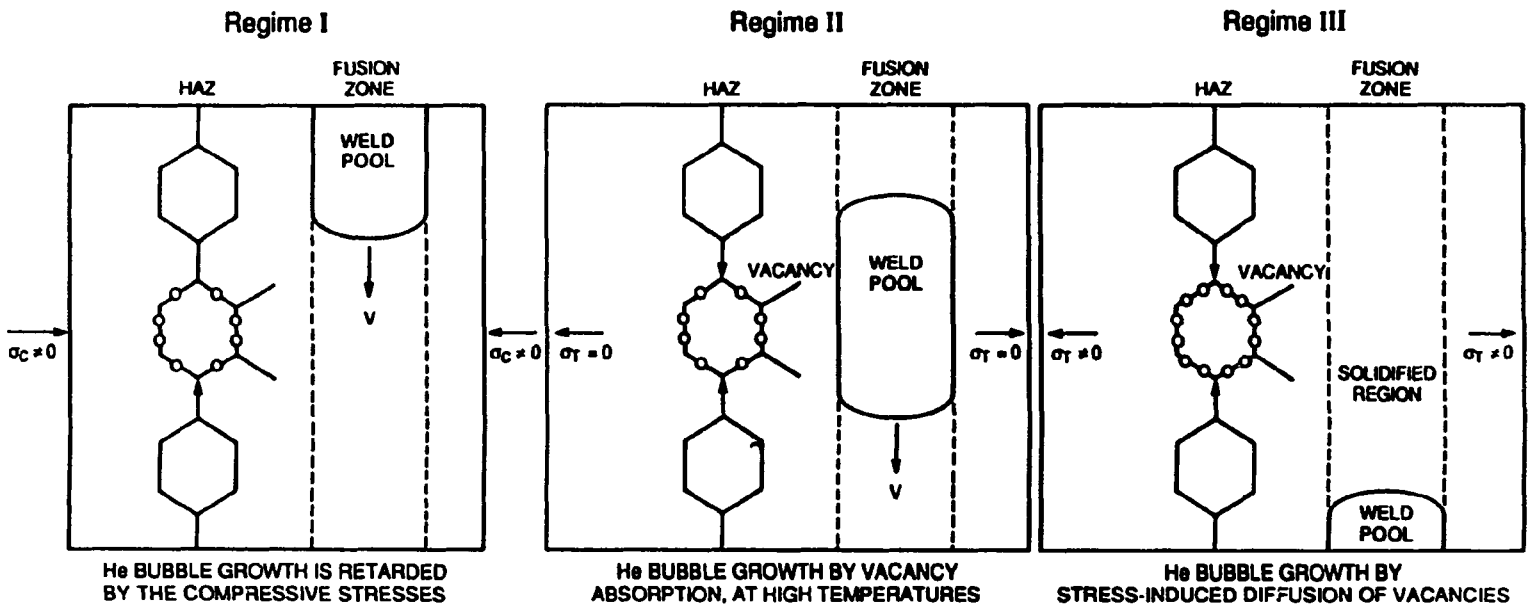

Fig. 45. Schematic showing the growth kinetics of grain boundary helium bubbles in the heat-affected zone during welding. (a) Time Regime I--Heatup period, compressive stresses, and weld centerline path temperature less than T_m; (b) Time Regime II--Molten pool present, stress-free state, and weld centerline path temperature greater than T_m; and (c) Time Regime III--Cooling period of resolidified metal, shrinkage tensile stresses, and weld centerline path temperature less than T_m.

stress is present. Regime II is chosen as the time interval during which the molten pool is present resulting in a stress-free state at the pool surface at the transverse direction. Regime III occurs after the molten pool has begun to re-solidify and internal tensile shrinkage stresses are generated in the constrained plate.

During the first regime, the nucleated helium bubbles in grain boundaries can grow by absorption of thermal vacancies during the heatup period. However, compressive stresses generated by the thermal expansion of the material will tend to retard bubble growth at grain boundaries normal to the compressive stresses. While bubble growth may not occur in materials that do not have a well stabilized GB bubble microstructure, combination of helium atoms and vacancies will occur resulting in GB bubble nucleation. Bubble growth therefore takes place p marily during time regimes II and III.

During regime II, Ostwald ripening [39,40] is one of the possible mechanisms by which GB helium bubbles may grow. However it is unlikely that this mechanism dominates since it depends on a reasonable level of solubility of gas atoms in the metal (exponential term of equation (13)) to effect efficient transfer of gas atoms from small to large bubbles. Since the solubility of helium in metals is negligible, coarsening via Ostwald ripening processes is not likely to be of importance in this regime.

The growth of GB bubbles may also occur by migration of matrix helium bubbles. These bubbles may be swept by moving dislocations

into grain boundaries [41]. Since the starting material is fully annealed and the time at elevated temperature short, the sweeping of bubbles into the grain boundaries by available dislocations is probably not important.

Growth of GB bubbles is also known to occur by grain boundary migration [55] and/or recrystallization. However, the prior annealing treatment at 1050°C for one hour insures that little driving force is available for such processes. Grain growth does occur in the HAZ during welding, but grain size changes by less than six percent. Hence grain boundary migration and recrystallization are not anticipated to cause significant helium bubble growth during welding of annealed material.

Accordingly, during regime II the growth of GB helium bubbles will occur primarily by the absorption of vacancies into bubbles. This process is particularly favored at temperatures close to the melting point where there is a high vacancy concentration. Since during regime II the HAZ is in a stress-free state, the driving force responsible for bubble growth will be the helium-gas overpressure in the bubbles. During the heatup period the GB helium bubbles, initially at equilibrium, will become overpressured. This overpressure is the difference of interior helium gas pressure and the surface-tension restraint, $2\gamma_s/r$, where γ_s is the surface free energy and r is the bubble radius. This overpressure prevents thermal emission of vacancies from the bubbles and results in a net vacancy flux to the bubbles. The derivation of the growth rate of helium

bubbles in the matrix by vacancy absorption has been given by Greenwood et al. [30]. This model is adopted and modified for a GB helium bubble. Let's consider a bubble of radius r_0 and assume the concentration of vacancies on a bubble surface ($r = r_0$) can be related to the equilibrium vacancy concentration (C_v^e) by

$$C_v(r_0) = C_v^e \exp[-(p-2\gamma_s/r_0)\Omega/kT] \tag{18}$$

where Ω is the atomic volume, p is the gas pressure, k is Boltzmann's constant, and C_v^e is the equilibrium concentration of vacancies at temperature T. The term C_v^e is given by

$$C_v^e = [\exp(\Delta S_v/k)\exp(-\Delta H_v/kT)]/\Omega \tag{19}$$

where ΔS_v is the vacancy formation entropy and ΔH_v is the vacancy formation energy. Let us assume that the equilibrium vacancy concentration is the same in the matrix as in the grain boundary. Although structural misfit provides an additional source of vacancies, it will not be considered here. For the case of GB helium bubbles, the concentration of vacancies along a grain boundary of thickness of δ_{gb} available for diffusion to a bubble can be approximated by

$$d^2C_v/dr^2 + (1/r)dC_v/dr = 0 \tag{20}$$

This equation gives the concentration C_v of vacancies at a distance r from the center of the bubble. The general solution to equation (20) is

$$C_v = A + B\ln r \tag{21}$$

where A and B are constants to be determined from the boundary conditions

$$C_v = C_v^e \exp[-(p-2\gamma_s/r_0)\Omega/kT] \quad \text{at} \quad r = r_0$$

$$C_v = C_v^e \qquad \text{at} \quad r = r_1 \tag{22}$$

where r_1 is the distance from the center of a bubble at which a thermal equilibrium concentration of vacancies is achieved. This is gives

$$B = C_v^e[1-\exp(-x)]/\ln(r_1/r_0) \tag{23}$$

where $x = (p-2\gamma_s/r_0)\Omega/kT$. The flux of vacancies into the bubble is given by

$$J_v = D_{gb}(dC_v/dr) = D_{gb}B/r \qquad \text{at } r = r_0 \tag{24}$$

where D_{gb} is the vacancy diffusion coefficient in the grain boundary. In general r_1 is of the order of several times r_0, hence the following approximation for J_v can be obtained

$$J_v \sim D_{gb}C_v^e\{1-\exp[-(p-2\gamma_s/r_0)\Omega/kT]\}/r \tag{25}$$

The growth of GB bubbles in turn can be expressed by

$$dV/dt = 2\pi r\delta_{gb}\Omega J_v. \tag{26}$$

Consequently, the change in bubble radius with respect to time is given by

$$dr/dt = \delta_{gb}\Omega D_{gb}C_v^e\{1-\exp[-(p-2\gamma_s/r_0)\Omega/kT]\}/(2r^2) \tag{27}$$

To numerically integrate equation (27), p must be expressed in terms of the bubble radius. This is difficult for a non-equilibrium gas bubble. However, for the case where $(p-2\gamma_s/r_0)\Omega$ is larger than kT the term $\exp[-(p-2\gamma_s/r_0)\Omega/kT] \ll 1$. Equation (27) therefore reduces to

$$dr/dt \sim \delta_{gb}\Omega D_{gb}C_v^e/2r^2 \tag{28}$$

The validity of this approximation for the helium-doped materials investigated in these experiments can be demonstrated by the following argument. Assume that the helium bubbles formed during the outgassing

of tritium are in equilibrium at the outgassing temperature (400°C). Then for the case where r = 1 nm (initial bubble radius as measured from TEM, Figure 23c), γ_s = 2 J/m^2 [89], and T = 673K, the number of helium gas atoms in the bubble can be calculated using the equation $n_g = 8\pi\gamma_s r^2/3kT$. This calculation yields a value of 1800 atoms. From Figure 15 the peak temperature that is seen one to three grain diameters from the fusion boundary (approximate position where cracking occurs) is 1600K. Assuming ideal gas behavior, the pressure in the helium bubble at 1600K is 9.5×10^9 N/m^2. Accordingly the driving force for bubble growth (given by $(p-2\gamma_s/r_0)\Omega$) at 1600K is 7.5×10^{-20} joules. This is three times larger than kT (2.2×10^{-20} joules). Therefore the term $\exp[-(p-2\gamma_s/r_0)\Omega/kT]$ is equal to 0.033, which is much smaller than 1. Hence the approximation is valid for the case under consideration.

The solution for equation (28) (with boundary condition $r=r_i$ at t=0) is

$$r^3 - r_i^3 = 3\delta_{gb}\Omega D_{gb} C_v^e \Delta t/2 \qquad (29)$$

where Δt is the time spent in the second regime. Equation (29) can therefore be used to calculate the size of bubbles in the HAZ at the end of regime II. Figure 46 shows the bubble size at the end of regime II as a function of transverse peak temperature in the HAZ (distance from fusion boundary). Curves for three different values of ΔH_v are shown. For instance for a peak temperature of 1600K and ΔH_v = 1.8 eV, at a grain boundary, two to three grain diameters from the fusion boundary, the bubble size is approximately 50 nm after regime

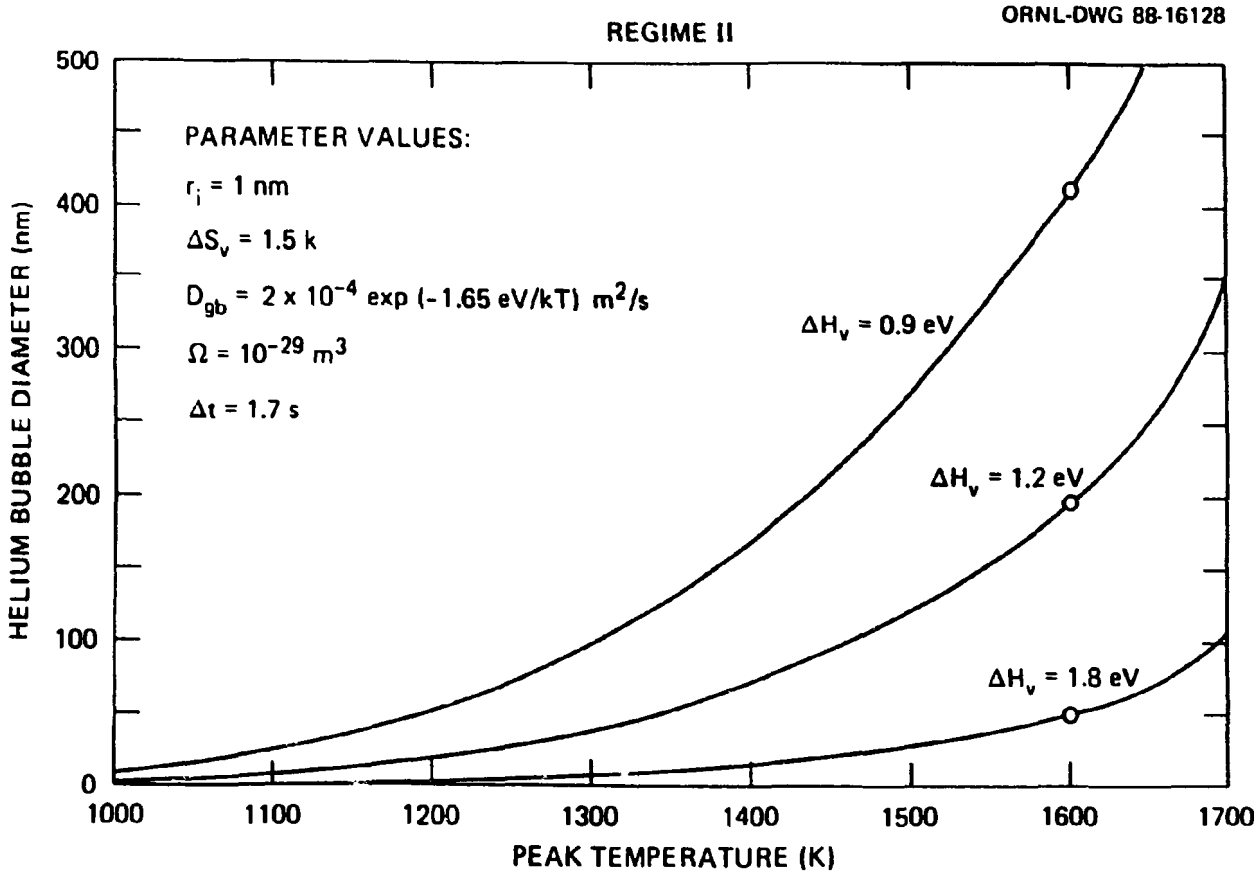

Fig. 46. Grain boundary helium bubble size as a function of peak temperature in the heat-affected zone after Regime II. Curves for three ΔH_v are presented.

II. These results indicate that bubble growth rate in the second regime is significantly affected by vacancy concentration. Also, for the cases of ΔH_V = 1.8 and 1.2 eV, · ·ificant bubble growth is predicted for temperatures below 10(300K).

Once the material in the weld carts to solidify (regime III), the kinetics of GB helium bubble growth in the HAZ is controlled by the internal tensile stresses developed during cooling. The laterally imposed external constraints will further enhance the magnitude of internal tensile stresses generated. In regime III, the possible mechanisms by which GB helium bubble growth may occur are grain boundary sliding (as proposed by Chen [54]) and stress enhanced diffusive cavity growth (as proposed by Hull-Rimmer [46]). Grain boundary sliding will occur due to the high shear stress and strain rate imposed on inclined grain boundaries. Even for transversely oriented grain boundaries, sliding may occur due to compatibility restrictions. For the bubble to grow by this mechanism, the rate of distortion due to sliding must exceed the shape recovery rate which is controlled by surface diffusion. A comparison of the GB sliding rate and the shape recovery rate shows that fast surface diffusion during this regime will remove any distortion achieved by sliding resulting in no growth in bubble size. This can be shown by the following argument. Assume that the rate of bubble distortion can be approximated by the grain boundary sliding rate, u, which is given by [90]

$$u = 0.3\dot{\epsilon}d \tag{30}$$

where $\dot{\epsilon}$ is the imposed strain rate due to shrinkage during cooling and d is the grain diameter. The strain rate can be approximated from a knowledge of the fusion zone cooling rate and solid metal thermal expansion coefficient (α). The cooling rate of the fusion zone, $(dT/dx)v$ was calculated using the following equation of Adams [86]

$$(dT/dx)v = 2\pi K\rho C_p(vh/IV)(T_p-T_0)^2 \quad (31)$$

where K is the thermal conductivity, ρ is the density, C_p is the specific heat, and v is the velocity of heat source. The parameters substituted into the equation (31) were the same as those used to generate Figure 13. The resulting cooling rate was calculated to be 154°C/s. Using a thermal expansion coefficient of 1.52×10^{-5}/°C, the resulting strain rate due to cooling is 2.34×10^{-3}/s. For a grain size of 70 μm, the bubble distortion rate, u, is therefore 4.9×10^{-8} m/s. The shape recovery rate, w, as formulated by Chung et al [53] and Harris [91] based on crack-like cavity growth kinetics is

$$w = D_s\delta_s\Omega\gamma_s(2\pi)^4/kTd^3 \quad (32)$$

where d is the grain size, and δ_s, D_s, γ_s, Ω and kT have their usual meaning as defined previously. The following values were substituted in equation (32): $D_s = 7.7\text{x}10^{-8}$ m^2/s [92], $\delta_s = 4\text{x}10^{-10}$ m, $\gamma_s = 1$ N/m, $\Omega = 10^{-29}$ m^3 and T = 1600K. The value of γ_s is smaller than previously used (2 N/m at 673K) due to the increased temperature. The shape recovery rate is therefore calculated to be 6.3×10^{-5} m/s. The bubble distortion rate, u, is therefore seen to be three orders of magnitude smaller than the shape recovery rate, w. This indicates

that fast surface diffusion will remove any distortion due to sliding resulting in no growth in bubble size.

The remaining mechanism by which grain boundary helium bubbles may grow is stress enhanced diffusive cavity growth. Models describing this process have been previously discussed in the literature review section. Since the helium bubbles of helium-doped materials distribute uniformly on the grain boundaries, the growth of GB helium bubbles occurs in an unconstrained manner. During cavity growth, atoms are transported from the cavity surface to the adjoining grain boundary. It is anticipated that the process of unconstrained cavity growth will be controlled by the slowest of either grain boundary or surface diffusion. For the case of type 316 stainless steel, the surface diffusivity is much greater than the grain boundary diffusivity, as shown by the calculations plotted in Figure 47. The grain boundary diffusivity used in this calculation is given by [93]

$$D_{gb} = 2\exp(-1.65\ eV/kT(t))\ cm^2/s. \quad (33)$$

Thus, the growth rate of GB helium bubbles is controlled by grain boundary diffusion (equilibrium growth) rather than surface diffusion. The growth rate of GB cavities can be obtained from

$$dr/dt = 2\pi\Omega\delta_{gb}D_{gb}\sigma/arkT \quad (14)$$

where a is the center to center cavity spacing, δ_{gb} is the thickness of grain boundary available for diffusion, σ is the shrinkage stress (transverse to the welding direction) normal to the grain boundary, and kT has its usual meaning. The bubble size can be obtained by integration of equation (14) if D_{gb}, σ and T as a function of time are

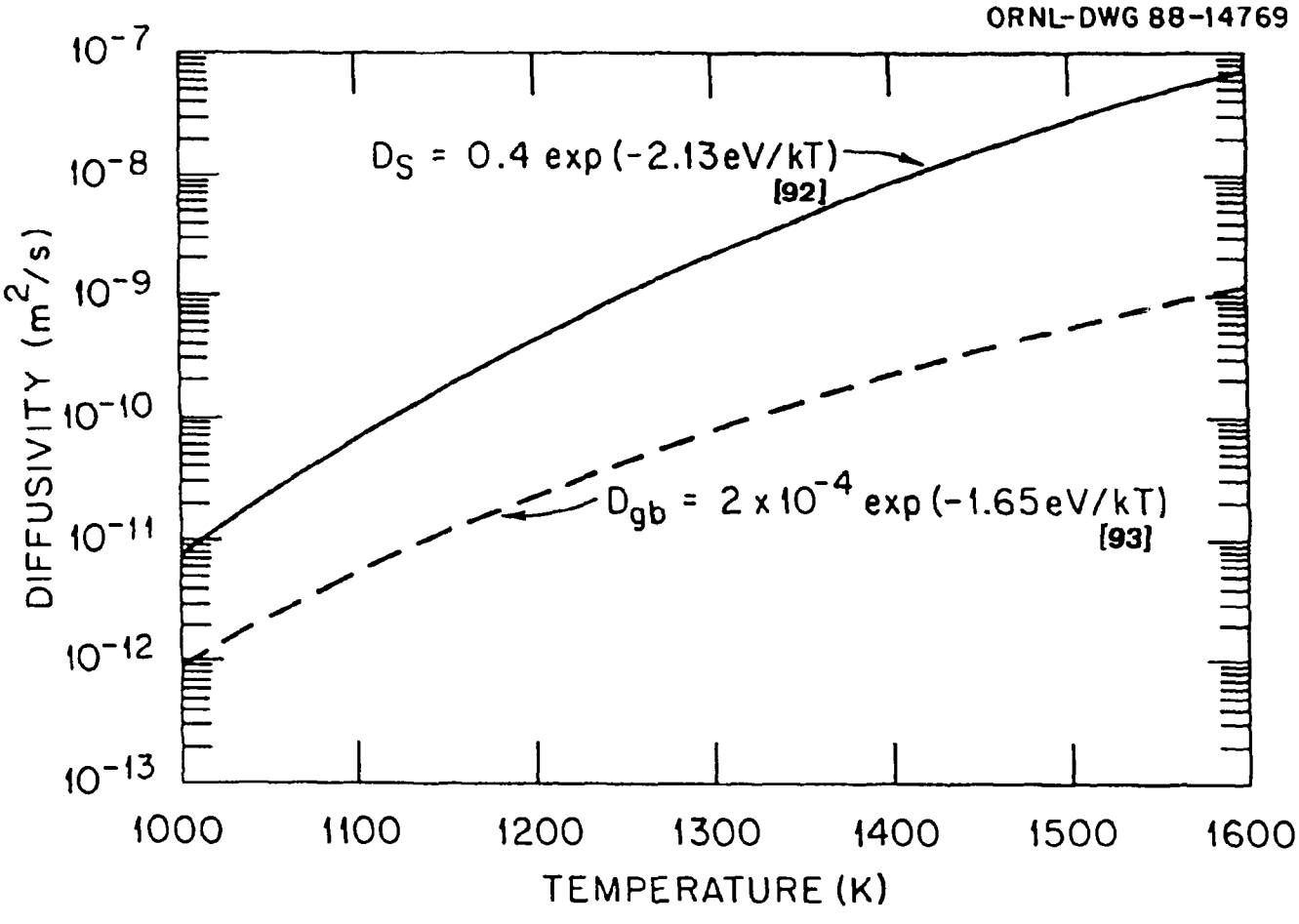

Fig. 47. Grain boundary diffusivity and surface diffusivity as a function of temperature. Surface diffusivity is 1 to 2 orders of magnitude greater than grain boundary diffusivity.

known. In general, these parameters can be obtained theoretically and/or experimentally as explicit functions of time.

For the present case the transverse shrinkage stresses (σ) resulting from cooling of the weld as a function of time are difficult to describe explicitly. The following method was used to approximate how these shrinkage stresses vary as a function of time. From elasticity theory, the thermal stress can be related to the Young's modulus (E) and the thermal expansion coefficient (α) which are functions of temperature and hence functions of time in this analysis. At any instant, the thermal stress present is given by

$$\sigma(t) = E(t)\alpha(t)\Delta T \tag{34}$$

Consequently, an approximate relationship between thermal shrinkage stress and time can be obtained. The instantaneous bubble size increment can then be expressed as

$$\Delta r = 2\pi\delta_{gb}\Omega D_{gb}(t)\sigma(t)\Delta t/ar(t)kT(t). \tag{35}$$

A numerical integration of equation (35) will be performed in order to obtain the GB bubble size after regime III. During integration, variables of r(t), $D_{gb}(t)$, T(t) and $\sigma(t)$ are assumed to be constant for a given time interval. During cooling, the temperature (in the HAZ) as a function of time, (experimentally verified in Figure 14), can be expressed by equation (17)

$$T(t) = 293 + 1906\exp\{-668388/[t(Tmax-293)^2]\}/t^{\frac{1}{2}} \tag{17}$$

Substituting equation (17) into equation (33), D_{gb} as a function of time can be obtained. In addition, Young's modulus and the thermal expansion coefficient of annealed type 316 stainless steel as a

function of temperature are known [94-99]. Accordingly, an approximate bubble size at the end of the third regime can be obtained by iterative numerical summation of equation (35). The computer program used to perform the numerical calculation is given in APPENDIX J. Figure 48 shows the bubble size as a function of time for three different ΔH_v and peak temperature of 1600K. Results indicate that the final bubble size in regime III is insensitive to the ΔH_v. Figure 49 shows the bubble size as a function of time for different peak temperatures (or locations) of the HAZ for the case of ΔH_v = 1.8 eV. Results show that the bubbles on grain boundaries located one to three grain diameters from the fusion zone (where temperature is estimated to be 1600K) should be about 0.85 μm in diameter approximately one second after resolidification of the weld pool.

During regime III the GB helium bubbles will grow until the contacting area of grain boundaries can no longer support the internal tensile stress, leading to final intergranular fracture. The stress, σ_f, required for fracture can be calculated by

$$\sigma_f = \sigma_{gb} \times (1-R^e) \tag{36}$$

where σ_{gb} is cohesive strength of a grain boundary at a specific temperature and R^e is the fraction of the grain boundary surface covered by helium bubbles. The effective area is defined as

$$R^e = \pi r_f^2/a^2 \tag{37}$$

where r_f is the bubble radius prior to fracture, and a is the center to center cavity spacing. Generally, the cohesive strength of grain boundaries is unknown. However, for a ductile material like type 316

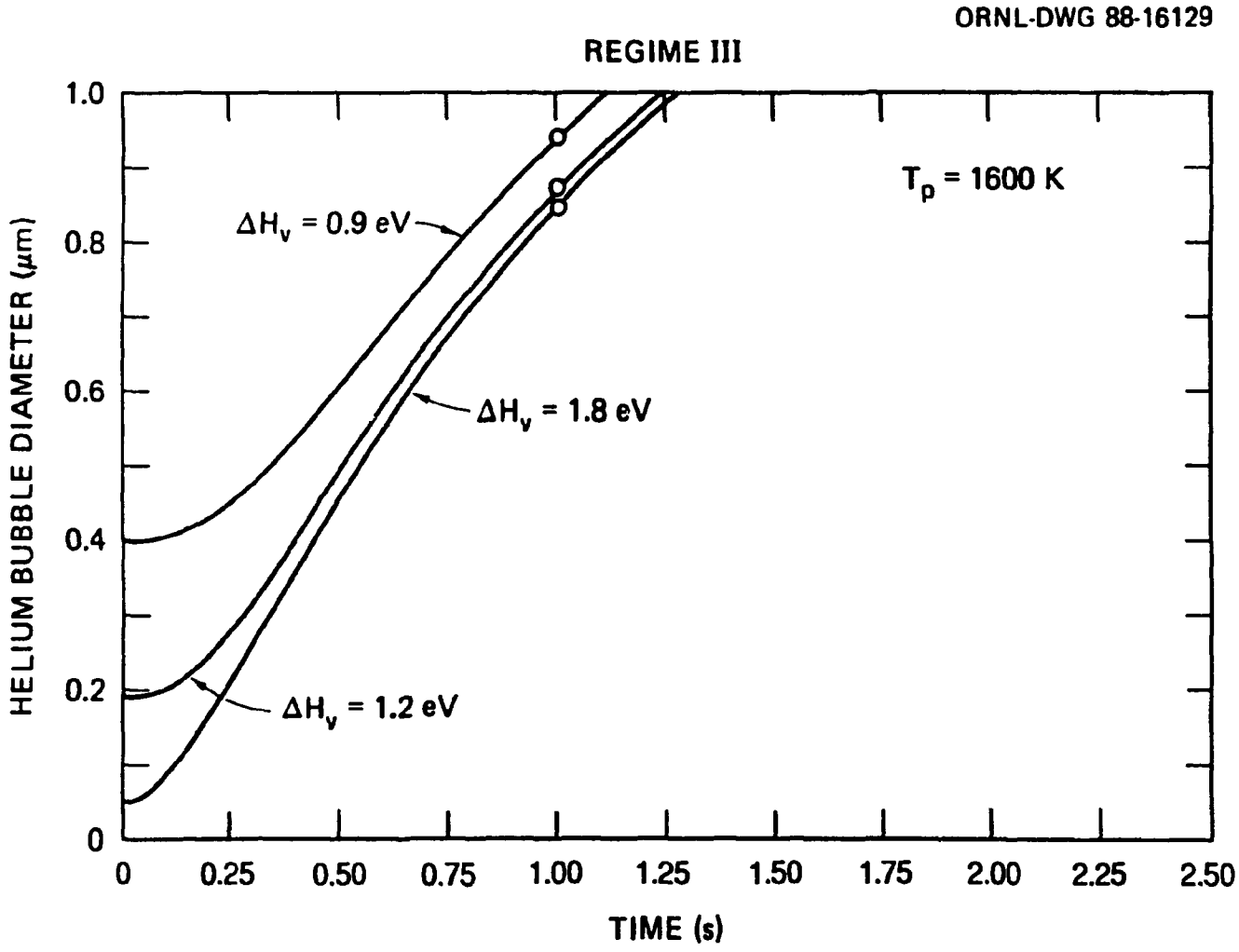

Fig. 48. Grain boundary helium bubble size during Regime III as a function of time for different ΔH_v and peak temperature of 1600K. Note final bubble size is insensitive to ΔH_v.

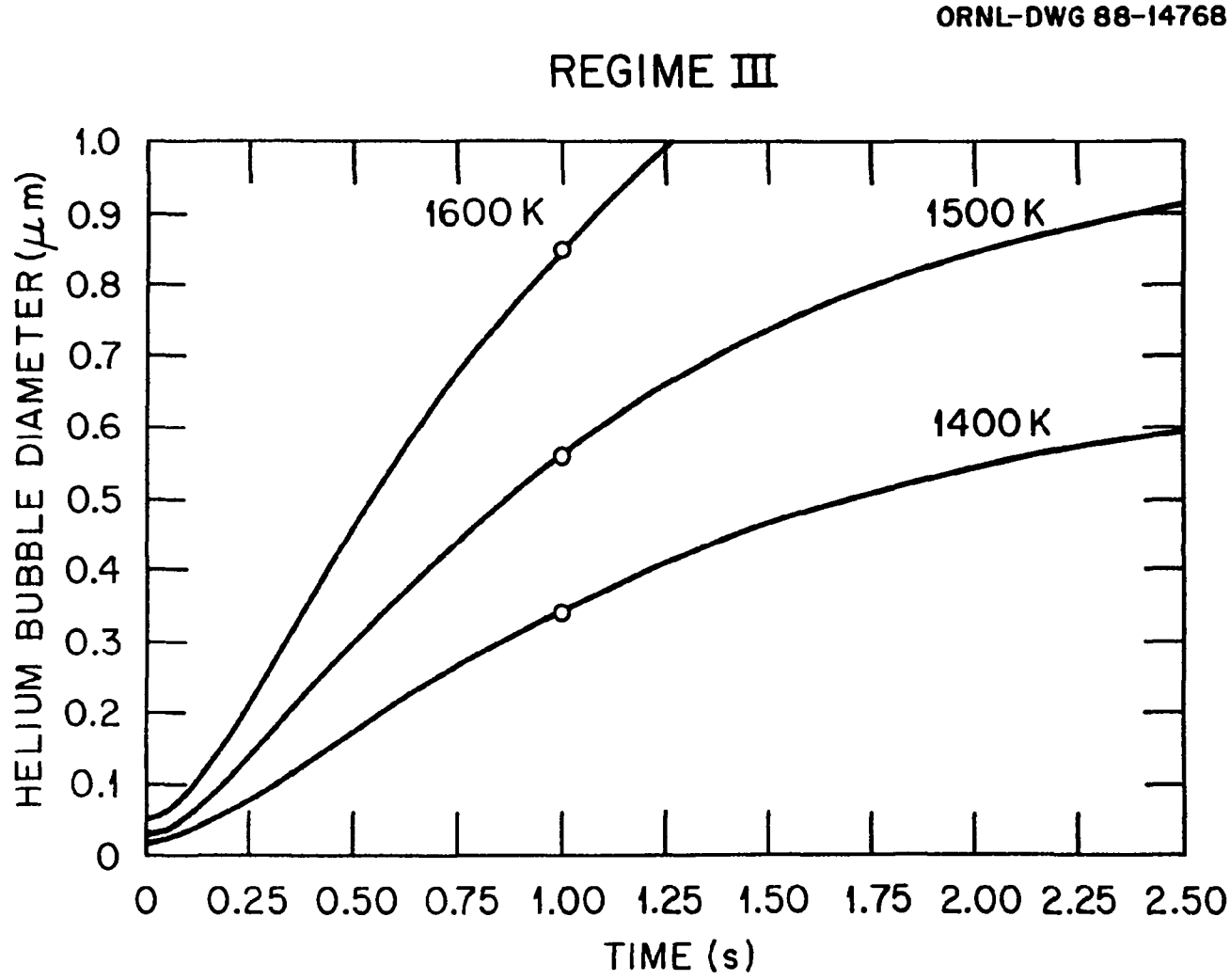

Fig. 49. Grain boundary helium bubble size during Regime III as a function of time for different locations in the heat-affected zone which experience different peak temperature.

stainless steel, it is reasonable to assume that grain boundary strength is similar to the matrix strength (such as the UTS) at elevated temperatures. Consequently, the stress at fracture can be approximated. For instance, the effective area ratio of helium bubbles (0.85 μm in size one second after the resolidificaiton of the weld metal) on grain boundaries one to three grain diameters from the fusion boundary is 0.57. The matrix strength at 1150°C is extrapolated from the results of tensile tests to be about 40 MPa [100,101]. Therefore, the fracture strength for this case is 17 MPa, well below the values of 100 MPa estimated for tensile shrinkage stresses.

VI. DISCUSSION

The objectives of this research were to investigate the effects of helium on the weldability of materials and to propose a theoretical model which could be used to explain the catastrophic cracking observed during weld cooling. The first section of this chapter (Heat-Affected Zone), discusses the characteristics of the HAZ cracking of both type 316 stainless steel and SandviK HT-9. The results are then compared with the proposed model presented in the previous chapter. Discrepancies between experimental results and theoretical predictions are also discussed. In the second section (fusion zone), the mechanism of the fusion zone cracking of the type 316 stainless steel containing 105 and 256 appm helium is discussed. Finally, ways to improve the weldability of helium containing materials are discussed which will hopefully provide guidelines for future research into this subject area.

Accuracy of Model in Predicting Heat-Affected Zone Behavior

Since both the control and hydrogen-charged specimens were welded successfully, it is evident that the loss of weldability in both type 316 stainless steel and HT-9 is due to entrapped helium rather than any remaining tritium. The SEM photomicrographs (Figures 15, 16 and 33) for both welded type 316 stainless steel and HT-9 revealed that

intergranular cracking occurred in the HAZ. Also, the grain boundary facets were observed to be decorated with a uniform distribution of dimples attributed to helium bubbles. The TEM microstructure (Figure 22) showed grain boundaries perforated by the presence of helium bubbles. These observations demonstrated that brittle fracture observed in the HAZ resulted from the precipitation and growth of GB helium bubbles under the actions of high temperature and shrinkage thermal stress. However, the fact that the lowest helium content materials, 0.18 appm type 316 stainless steel and 0.3 appm HT-9, were welded successfully suggests that a threshold level (between 0.18 and 1 appm) of helium exists below which materials my be welded successfully using conventional GTA welding techniques.

Since the explicit thermal history and stresses experienced by each grain boundary examined are unknown, it is, therefore, difficult to relate the observed TEM microstructure to the theoretical results. A theoretical model has been developed in the previous chapter which analyzes the growth of GB helium bubbles during the welding process. The model predicts that the bubbles on grain boundaries located one to three grain diameters from the fusion line should achieve a size of approximately 0.85 μm one second after the resolidification of the weld pool. The average dimple spacing was measured to be approximately 1 μm in diameter on exposed crack surfaces (Figure 17,18). From video tapes of the welding process the time elapsed between the passing of the torch and the observed HAZ cracking is

measured to be one second. The measured value of the dimples and the bubble size as predicted by the proposed theory is therefore in good agreement. Although it is likely that internal microcracks initiated earlier than the onset of the evident HAZ cracking as measured from the video tape, reasonable consistency between the predicted and measured bubble size is still achieved.

TEM micrographs of the HAZ (Figures 24-27 and 68-74) show that GB helium bubble density after welding is less than that prior to welding, and that GB bubbles vary in size. This indicates that bubble impingement and coalescence, due to geometrical inhomogeneities and/or bubble migration, have occurred during welding. The coalescence will further enhance the GB bubble growth rate shortening the time of initiation of the HAZ cracking. However, GB bubble coalescence was not taken into account in the development of the GB bubble growth model. This event may be argued to be an important factor in determining the bubble growth rate which may lead to the difference between the experimentally measured and theoretical time for onset of cracking. Nevertheless, the experimental results, onset of the HAZ cracking and bubble size, are reasonably consistent with those predicted by the proposed model detailed in Chapter V. This suggests that the contribution of bubble coalescence to bubble growth rate may not be significant.

As indicated in the section of helium bubble growth, the growth kinetics of equilibrium GB cavities have been studied extensively since Hull and Rimmer proposed the first theoretical model. These

models were derived on the basis of the same mechanism but with different boundary conditions. In the following section the differences and similarities of these models are discussed. Figure 50 shows the curves which describe GB helium bubble size as a function of time after regime III which were calculated using the Hull and Rimmer [46], Speight and Harris [47], Weertman [48] and Speight and Beere [50] equations for a peak temperature of 1600K. Results indicate that the Speight and Beere equation predicts the fastest growth rate of GB helium bubbles, while that predicted using the Weertman equation shows the slowest growth rate. Additionally, results predicted using the Hull and Rimmer equation are similar to those calculated using the Speight and Harris equation. In our case, it is apparent that these two equations (Hull-Rimmer and Speight-Harris) are appropriate ones for prediction of GB bubble growth in regime III.

The model of GB bubble growth in the HAZ developed for type 316 stainless steel can also be applied to the case of HT-9, although these materials have radically different microstructures. This is due to the fact that HT-9 undergoes a phase transformation at 850°C from the room temperature tempered martensite structure (BCT) to austenite (FCC). This is shown in the phase diagram of Figure 51 [102]. In the region, 850-1350°C, HT-9 is anticipated to behave very similarly to austenitic 316 stainless steel. The only difference in predictions would be due to differences in the specific diffusivities in this temperature range. Based upon similar diffusivities, it is

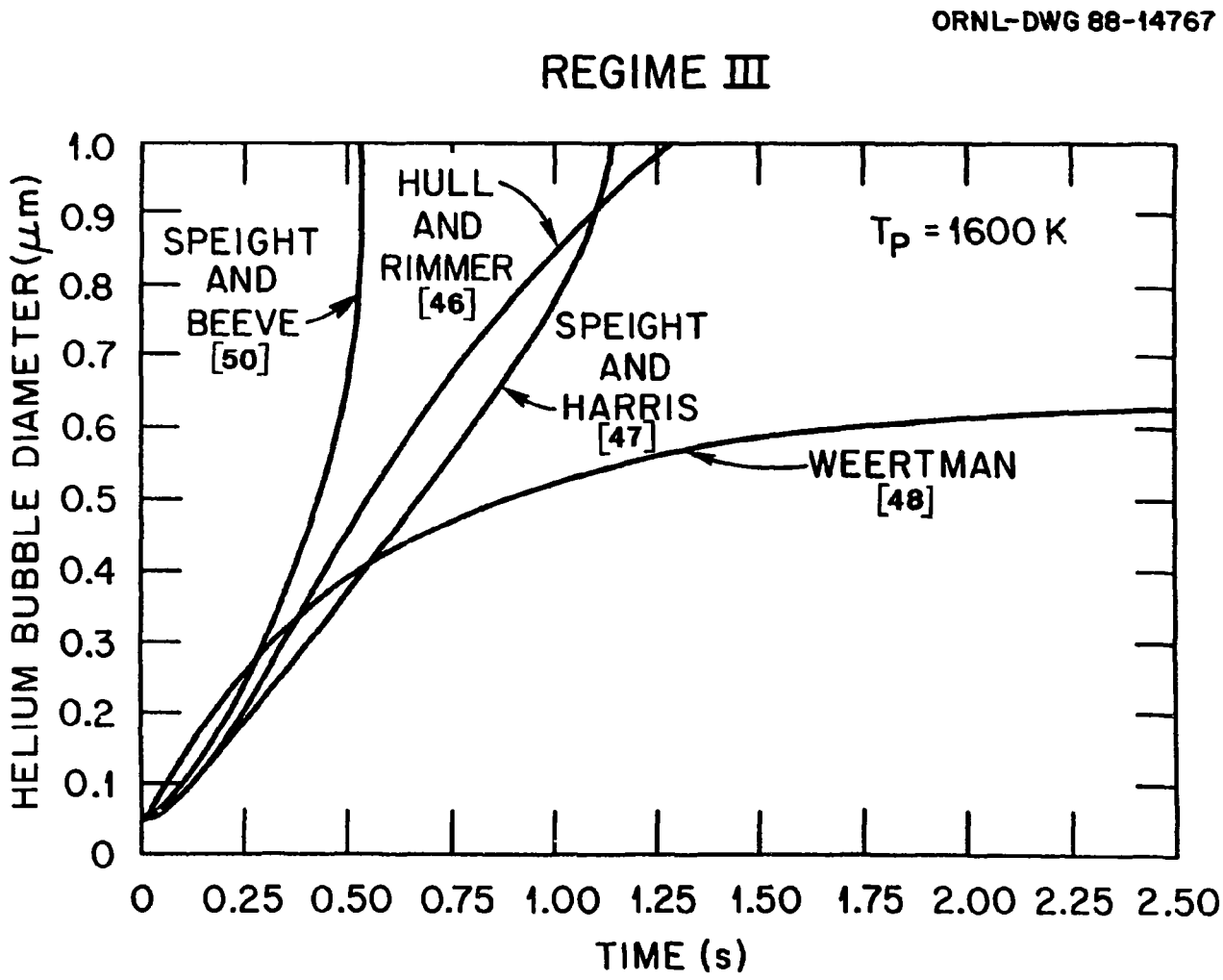

Fig. 50. Grain boundary helium bubble size during Regime III as a function of time for peak temperature of 1600K.

ORNL-DWG 88-13036

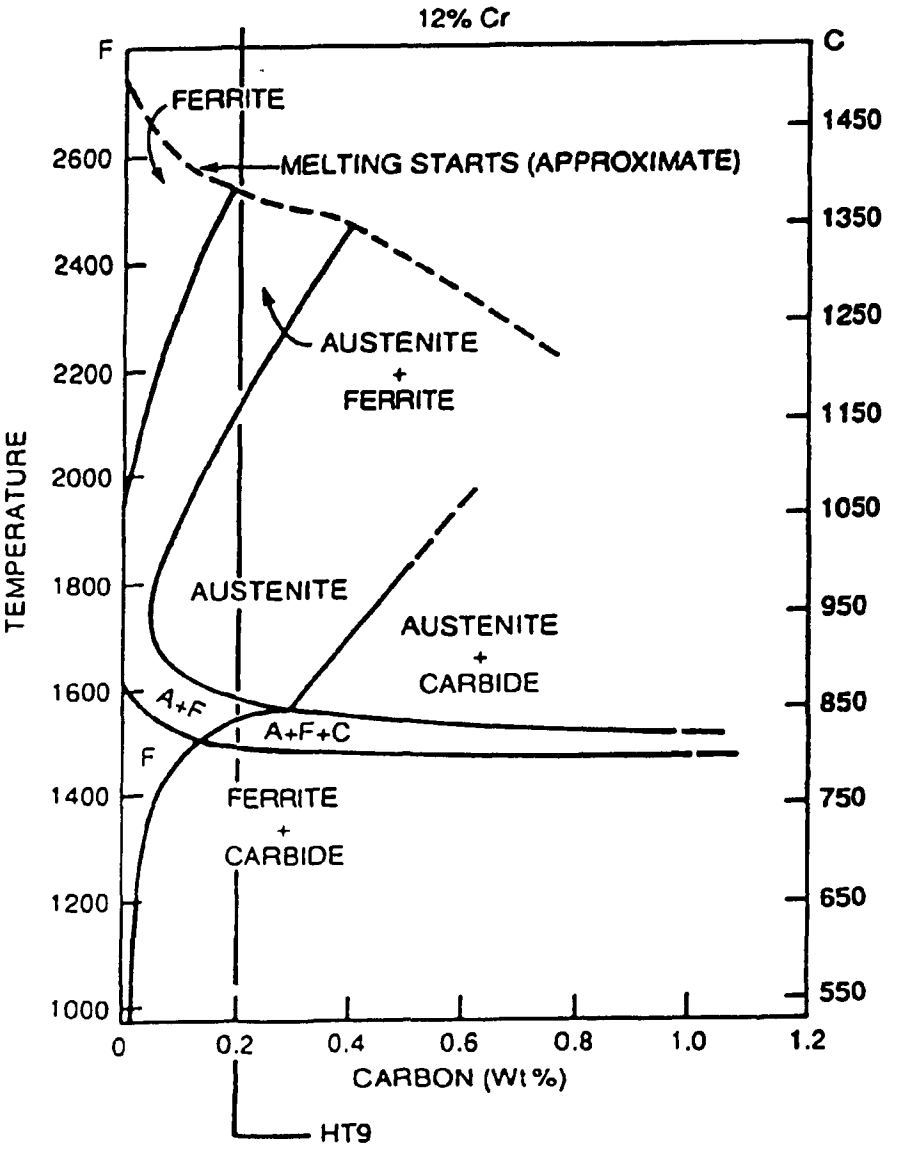

Fig. 51. 12% chromium section of the Fe-Cr-C diagram.

anticipated that the kinetics of GB bubble growth in the HAZ of HT-9 are same to those in type 316 stainless steel.

Fusion Zone

Fracture surface features of the fusion zone of welded type 316 stainless steel plates containing 105 and 256 appm helium (Figure 16d) revealed that brittle fracture occurred along interdendrite paths. SEM metallography of the fusion zone (Figure 52) suggests that brittle failure is caused by the precipitation of helium bubbles in the dendrite boundaries. As solidification proceeds, helium is rejected by the growing dendrites because of the low solubility of helium in the metal and is trapped between dendrites in regions which are the last to solidify. These bubbles coalesce into microcracks. Tensile shrinkage stresses, which are the highest at the fusion centerline [103], cause these cracks to propagate leading to brittle rupture along the center of the fusion zone.

Feasibility of Repairing Irradiated Materials Using Conventional Welding Techniques

The results of this study suggest that welding of irradiated structural components, which contain relatively small amounts of helium, may be very difficult. Fusion welding techniques input large amounts of heat into the material generating high temperatures and steep temperature gradients. Upon cooling, shrinkage tensile stresses enhanced by external constraints lead to rapid growth of GB helium bubbles and final catastrophic brittle fracture.

YE-13854

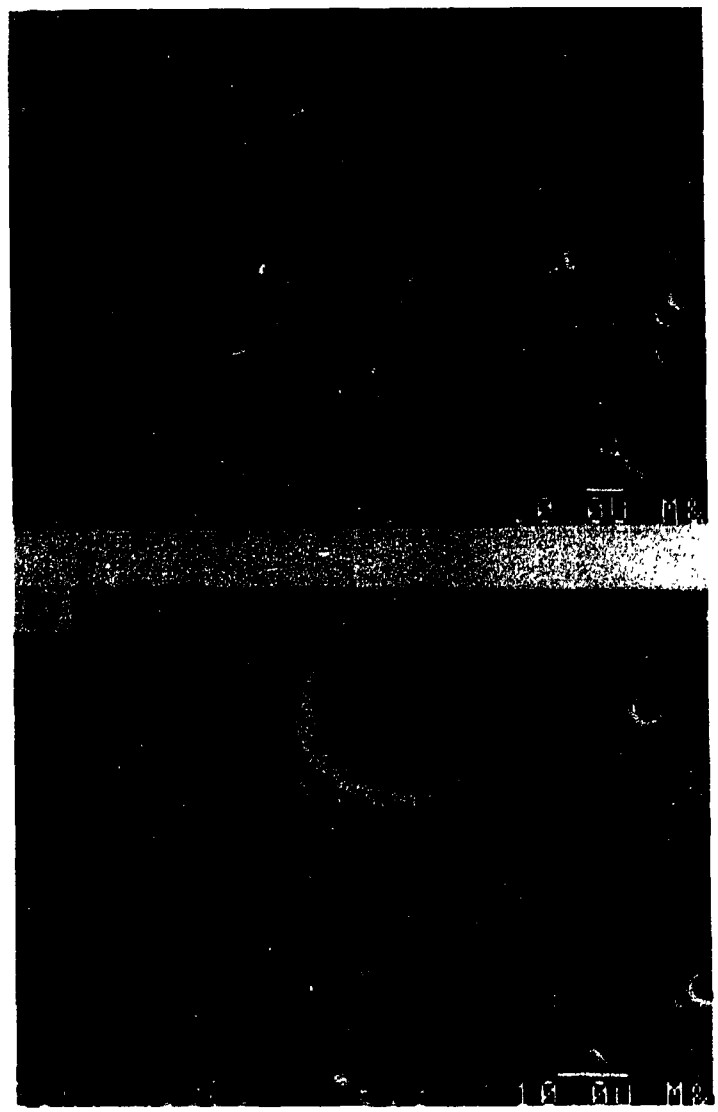

Fig. 52. SEM micrographs of the fusion zone of type 316 stainless steel with 105 appm helium. Brittle fracture resulted from bubble coalescence and growth at dendrite boundaries.

Both the models and experimental results demonstrate that high temperature alone is not sufficient to cause catastrophic brittle fracture. To successfully weld helium containing materials, the models and experiments suggest that either a large reduction in peak temperature or shrinkage stresses would lead to success. In fact through a reduction in both peak temperature and shrinkage stress successful welds may be obtained.

Two distinct paths of research which may lead to a solution of welding of irradiated materials are clearly identified by the results of this work. Path one involves the development of innovative welding techniques which avoid the conditions which lead to nucleation and growth of GB helium bubbles. The second path involves the alteration of chemical composition and microstructure through alloy modification and fabrication. The following section describes recommended research and preliminary results of experiments to obtain successful welds of irradiated materials.

Special techniques such as solid state welding, friction welding, and ultrasonic welding may allow the joining of helium containing materials without the application of large heat input and hence greatly reduced peak temperatures, temperature gradients and shrinkage stresses. It is likely that such techniques could be successfully employed to repair or replace degraded helium containing components.

Alternately, different materials which intrinsically exhibit resistance to helium embrittlement after being exposed to welding may be developed. Helium embrittlement resistant materials may be

achieved either through microalloying techniques and/or manufacturing processes. In austenitic stainless steels microalloying with titanium or niobium additions is being pursued [104-108]. This microalloying produces MC precipitation in the matrix and $M_{23}C_6$ at the grain boundaries which are expected to act as trapping sites for helium, therefore keeping helium from forming bubbles on the grain boundaries [104,109-111]. Experimentally, it has been found that formation of these carbides can substantially increase the embrittlement resistance following HFIR irradiation [108,112,113]. Creep-rupture results of German Ti-stabilized austentic stainless steel (DIN 1.4970) further support this hypothesis [114,115]. It was suggested that carbide formation such as MC within the grain boundaries directly traps helium and refines bubble distributions at particle interfaces and affects the grain boundary resistance to migration and its behavior as a sink for helium [110,114]. Accordingly, the helium accumulation at the grain boundary and the bubble growth rate can be retarded thus the occurrence of high temperature helium embrittlement prevented.

Research has been conducted on an alloy designated as Path A PCA (Ti-modified austenitic stainless steel) to demonstrate this hypothesis. The materials were solution-annealed at 1100°C for 30 minutes prior to being helium-doped with the "tritium trick". The 0.76 mm PCA plates containing 2 appm helium were prepared using the same helium-charging procedures as that for 2.5 appm type 316 stainless steel. The full penetration GTA welds were then produced under the same conditions as those for type 316 stainless steel. SEM

examinations indicated that only one of the three welded plates revealed HAZ cracking. The HAZ cracking was limited to the beginning region of weld. Results also showed that the degree of HAZ cracking (length of cracks) was significantly reduced from 80% down to 0.6% with respect to that observed in type 316 stainless steel, as shown in Figure 53. This suggests that the PCA exhibits much better resistance to high temperature helium embrittlement than type 316 stainless steel. Further study should be conducted to fully understand the microscopic mechanisms which control helium embrittlement resistance.

To investigate the effect of mechanical pretreatment on the HAZ cracking tendency of helium-containing materials, GTA welds of 20% CW type 316 stainless steel were made. Helium was implanted in the material under the same charging conditions as those used for PCA. Also, the materials were welded using the same conditions as those for PCA. Macroscopically, cracking occurred in the HAZ during cooling of the weld. The length of cracking was eight percent of the total length of the weld bead which is much less than that of SA type 316 stainless steel (80%), as shown in Figure 53. Results suggest that mechanical pretreatment may be used to reduce the HAZ cracking tendency of helium-containing materials. This tendency is probably attributed to two possible mechanisms: dislocation structures which act as a sink for helium atoms and vacancies, and recovery processes of cold-worked grains which consume most of the vacancies reducing available vacancies for bubble growth. Further study should be conducted to provide insight into the microscopic control mechanisms.

YE-13855

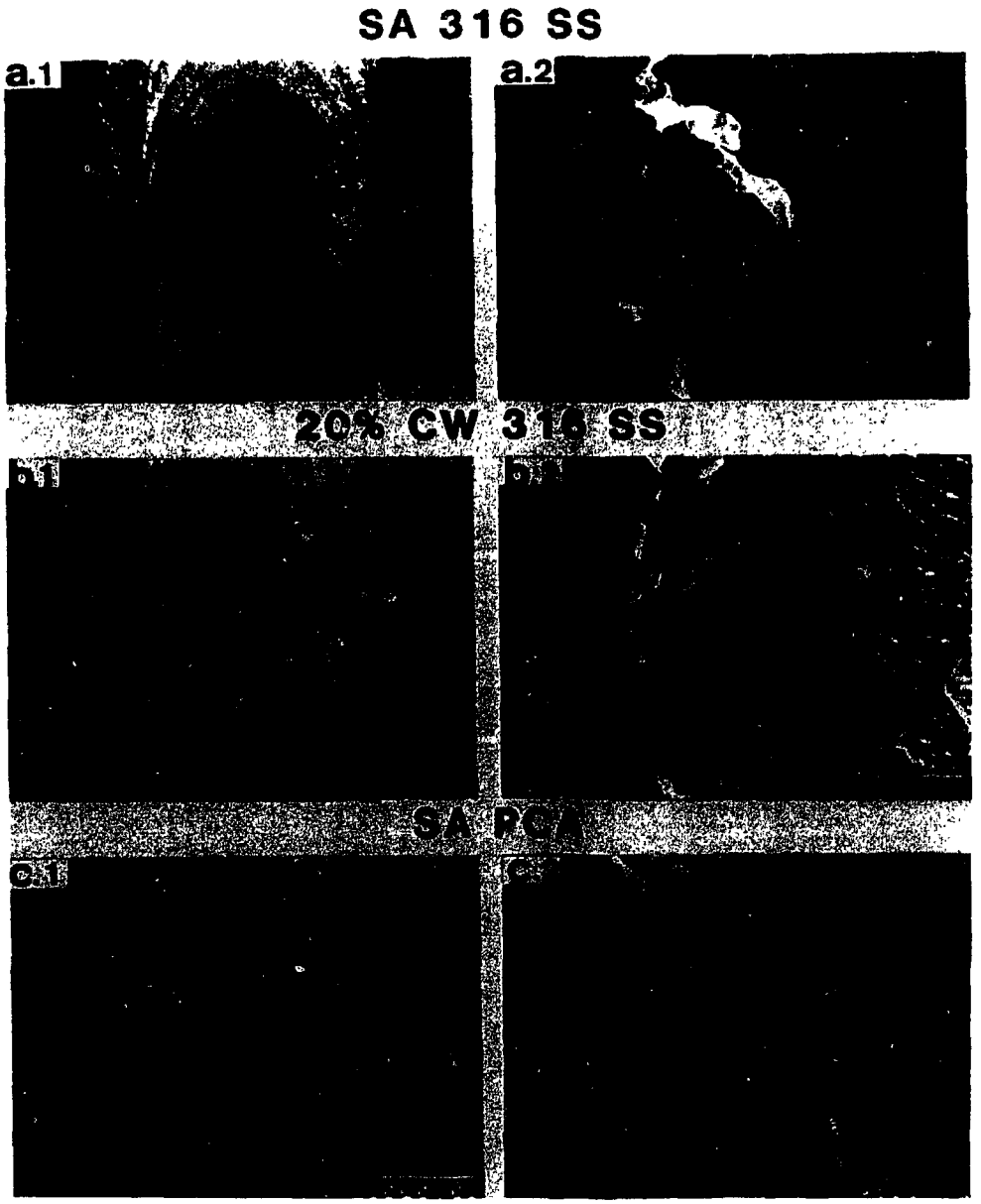

Fig. 53. Structure compares the cracking tendency of austenitic stainless steels containing 2 appm helium. (a) SA type 316 stainless steel, (b) 20% CW type 316 stainless steel, and (c) SA PCA. Note the degree of heat-affected zone cracking is significantly reduced in both 20% CW type 316 stainless steel and SA PCA.

Recently a set of experiments was conducted on a helium containing alloy which suggests that material processing may be used to produce a material resistant to embrittlement. GTA welds of rapidly-solidified-processing (RSP) type 304 stainless steel, containing 7 appm helium, were completed with no observable weld defects. No cracks were found in either the fusion (Figure 54a) or HAZ (Figure 54b). However large amounts of porosity were found in the fusion zone when the samples were polished, etched and examined using optical microscopy (Figure 55a).

The RSP 304 stainless steel powder had been produced by the centrifugal atomization (CA) process with an average particle diameter of 80 μm. The powder was produced by the Pratt & Whitney Government Products Division. In the CA process a stream of molten metal was poured onto a rapidly spinning cup which atomized the liquid. The droplets were then quenched in flight by radiative and convective cooling in a circulating helium atmosphere. Subsequently, these powders were consolidated by hot isostatic pressing (HIP) at 900°C and 207 MPa for 2.5 hours.

TEM examinations of the HAZ (Figure 55b) revealed no helium bubbles. It was also found that the dislocation structure of the as-fabricated condition was retained even after welding. The RSP 304 stainless steels produced by the CA process appeared to exhibit superior helium embrittlement resistance compared to conventional type 316 stainless steel. The mechanism related to this superiority, however, is not understood. It is hypothesized that GB oxide

YE-13856

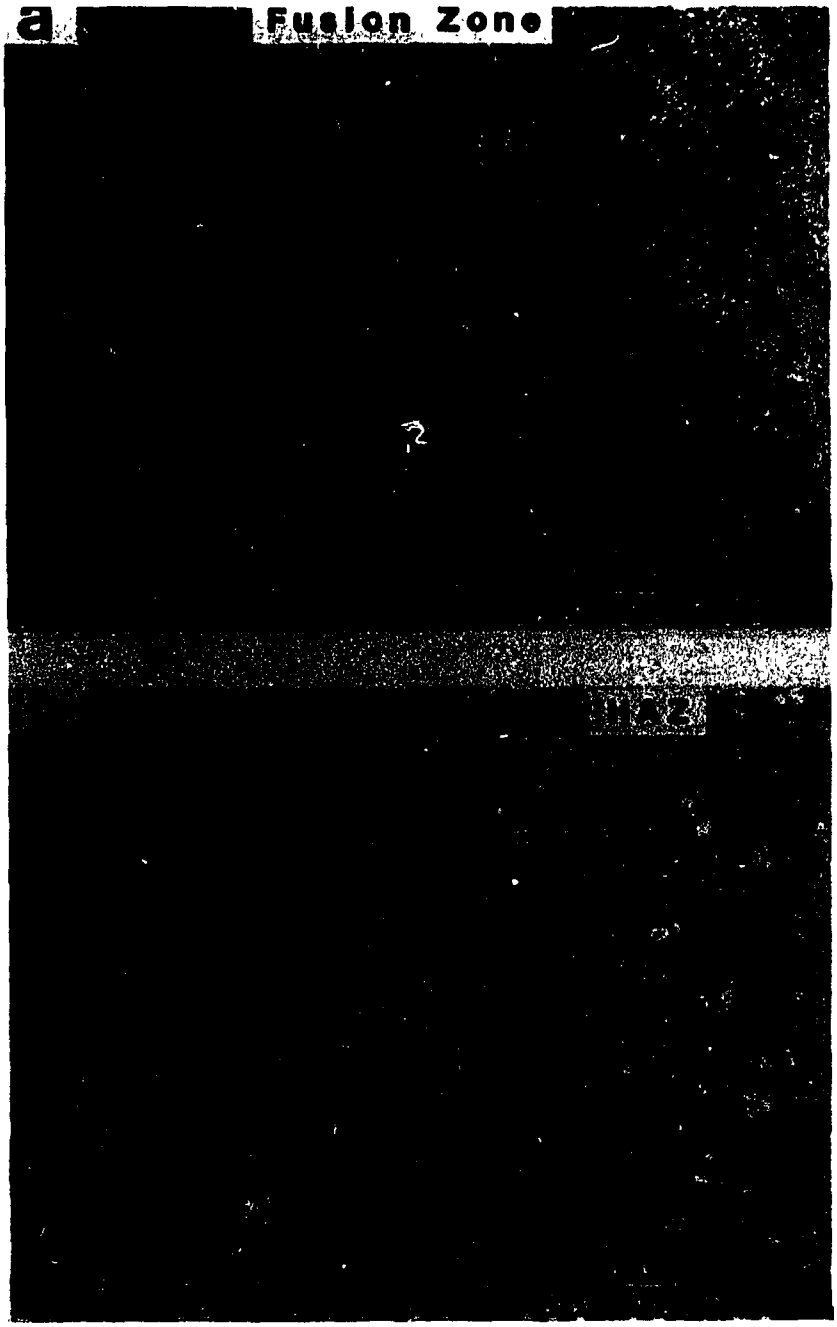

Fig. 54. Structure of as-welded rapid-solidified-processing 304 stainless steel. (a) Fusion zone and (b) heat-affected zone. No cracking in both fusion zone and heat-affected zone.

YE-13857

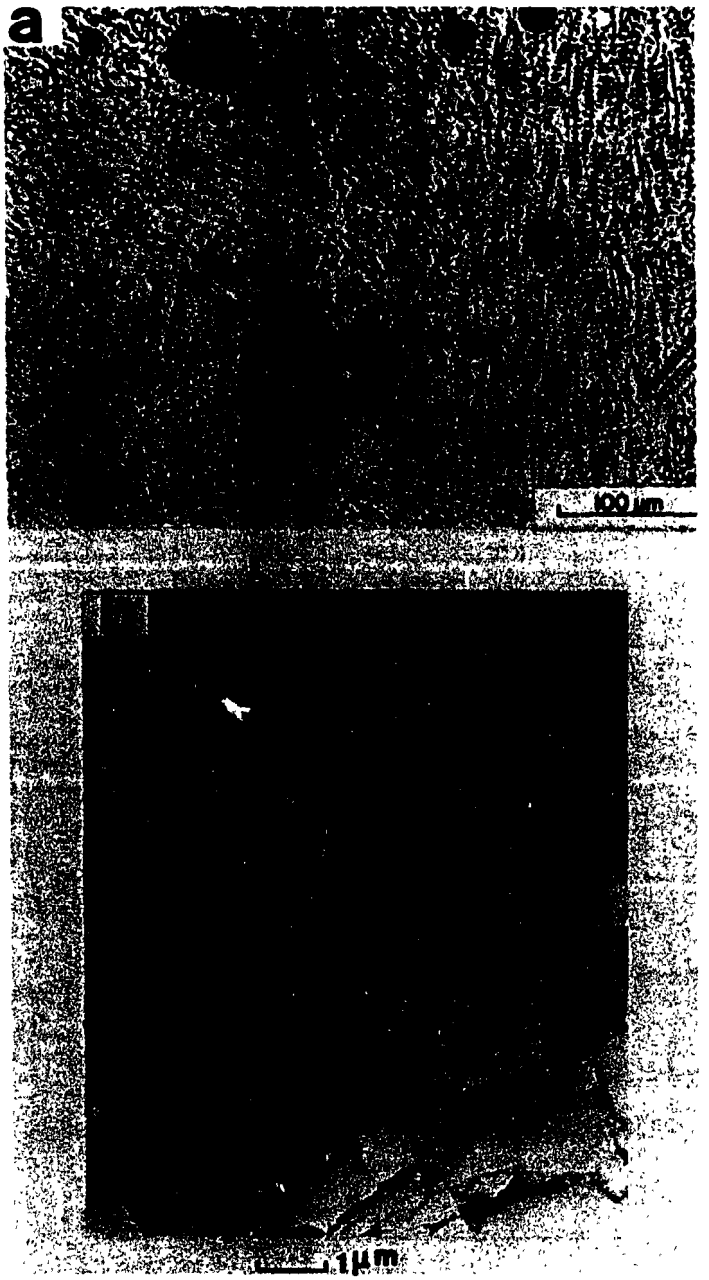

Fig. 55. Microstructure of rapid-solidified-processing 304 stainless steel. (a) Fusion zone and (b) heat-affected zone. Large pores were found in fusion zone. No helium bubbles were observed in the heat-affected zone.

particles from the original powder particle surface layers entrapped and stabilized the dissolved helium up to the melting point of material. Nucleation and subsequent growth of helium bubbles is thereby avoided, and hence brittle fracture was not observed after welding. An additional mechanism by which grain boundary helium bubbles might be avoided comes from the intrinsic pores which exist in powder metallurgy products. These intrinsic pores serve as sinks for entrapped helium thereby eliminating the need for nucleation of helium bubbles on grain boundaries. It is likely that both oxide particles and intrinsic pores play important roles in preventing RSP 304 stainless steel from helium embrittlement. Further study on this material is needed to determine the mechanism by which grain boundary helium embrittlement is avoided.

The present study has covered two different structural materials: austenitic and ferritic stainless steels. For the class of austenitic stainless steels, four alloys with different chemical composition and fabrication processes are involved. Results summarized in Table 6 show that materials contaning helium in the range from 1 to 7 appm reveal significantly different response to helium embrittlement as a result of different microstructure, chemical composition and fabrication processes. This table compares the cracking tendency in terms of the crack length per inch of the weld bead. Results show that helium-containing PCA, RSP 304 steel and HT-9 exhibit the lowest HAZ cracking tendency. This result suggests a research direction for developing alloys which are immune to helium embrittlement.

Table 7. Comparison of the HAZ cracking tendency

Material	He Level (appm)	# Welded	Crack Length (mm)/ mm of Weld Bead	Tendency to Crack
SA 316SS	2.5	5	0.79	High
20%CW 316SS	2.0	4	0.06	Low
SA PCA	2.0	4	0.0017	Very Low
RSP 304	7.0	3	0.0	None
HT-9	1.0	4	0.009	Very Low

VII. CONCLUSIONS

Conclusions of the Present Study

This study of helium effects on the subsequent weldability of austenitic and ferritic stainless steels leads to the following conclusions:

1. Catastrophic intergranular HAZ cracking occurred during cooling of GTA welded type 316 stainless steel and HT-9 plates containing helium levels equal to or greater than 1 appm.
2. High peak temperatures alone are not sufficient to induce heat-affected zone cracking. Weld constraint which induces high shrinkage tensile stresses during cooling is necessary.
3. Brittle fracture in the heat-affected zone of both alloys results from the growth and coalescence of helium bubbles on grain boundaries, while brittle fracture in the fusion zone of type 316 stainless steel arises from the precipitation of helium bubbles at dendrite interfaces.
4. The size and density of pores in the fusion zone of type 316 stainless steel increased with increasing helium concentration. The largest pores were found in the fusion zone near the fusion boundary.
5. Low-heat-input welding methods performed on type 316 stainless steel tend to induce under-bead intergranular cracking in the heat affected zone with helium levels as low as 2.5 appm.

6. Butt-joints of type 316 stainless steel with 27 and 105 appm helium welded without external constraints showed degradation due to the presence of grain boundary helium.
7. Welds of type 316 stainless steel containing helium concentrations equal to or greater than 2.5 appm exhibited poor tensile properties with ductilities close to zero. Fracture in these specimens was intergranular due to the presence of grain boundary helium bubbles.
8. A simple theory of bubble growth has been presented which divides the welding process into three consecutive time regimes. The model based on the kinetics of diffusive cavity growth is used to predict grain boundary bubble size as a function of time and position in the heat-affected zone. Predicted results were found to compare favorably with the time lag between the peak temperature and onset of cracking and the bubble size measured on the fracture surface.
9. PCA austenitic stainless steel exhibits much better resistance to helium embrittlement than type 316 stainless steel under welding conditions.
10. Cold working type 316 stainless steel reduces the HAZ cracking tendency.

11. Rapidly solidified type 304 stainless steel containing 7 appm helium can be successfully welded using conventional GTA welding techniques.

The results of the present study indicate that welding of irradiated structural components containing helium concentrations greater then 1 appm will be difficult in austenitic and ferritic stainless steels. Furthermore, even if such repairs can be made successfully, the very low ductility of the welds may still impose a severe risk for components which must serve at elevated temperatures under conditions of creep or fatigue loading.

Recommendations for Future Study

The present study provides quantitative data describing the joining of irradiated materials. The following studies are recommended to improve our understanding of welding irradiated materials. Two distinct paths of research which may lead to a solution to welding of irradiated materials are clearly identified by the results of this work. Recommendations are grouped into two subsections: innovative welding techniques and alloy modification and fabrication.

Innovative Welding Techniques

1. Tests should be conducted to quantitatively investigate the stress state at which catastrophic weld failure occurs in He-doped materials. One possible test is the SIGMAJIG which was developed by

Goodwin [116] to study hot-cracking in austenitic stainless steels. The SIGMAJIG test fixture holds a 50 mm x 50 mm square specimen between hardened steel grips and applies a transverse stress, sigma, prior to welding. The load is applied by a pair of strain-gaged bolts and maintained by stacks of Bellville washers in the load train. The loading system was calibrated with strain-gaged specimens. After preloading, an autogenous GTA weld is produced along the specimen centerline. As the stress is increased specimen by specimen, a level is reached where centerline cracking initiates. Accordingly, the SIGMAJIG test can be performed to quantify the effects of pre-applied transverse stresses on weld failure of helium-doped materials, and to define the threshold stress for the onset of the HAZ cracking.

2. Research needs to be performed to investigate the effects of stress and temperature gradient on GB helium bubble growth. To study the temperature gradient effect, specimens may be heated non-uniformly in a furnace or heated by passing an electrical current through a specimen with a non-uniform shape. Following differential heating treatment, the helium bubble morphology as a function of position along the thermal gradient could be determined using TEM. These results will provide quantitative information on whether the driving force from the temperature gradient affects growth kinetics of GB helium bubbles. To examine the stress gradient dependence of GB bubble growth, the helium containing specimens can be bent in a three-point bending configuration at variable elevated temperatures and held

for a short period of time. This constraint provides a constant stress gradient across the thickness. The GB helium bubble morphology as a function of position across the thickness of the strained specimens would then be examined using TEM. The results would quantitatively define the relationship between stress gradient and GB bubble growth. Based on this information criteria to successfully weld helium containing materials can be established.

3. Research on the properties and microstructures of helium containing materials subsequent to welding by special techniques, such as solid state welding (friction and ultrasonic), is recommended. Solid state welding processes are those that produce coalescence at temperatures below the melting point of base metals being joined. These processes involve either the use of deformation, or diffusion and limited deformation, to produce high quality joints between both similar and dissimilar materials. Friction welding is a process in which the heat for welding is produced by direct conversion of mechanical energy to thermal energy at the interface of the workpieces without the application of electric energy, or heat from other sources to the workpieces. Ultrasonic welding is used effectively for joining both similar and dissimilar metals with lap joint welds. High frequency vibrations, introduced into the areas to be joined, disrupt the metal atoms at the interface of the weld components and produce an interlocking of these atoms to achieve a mechanical joint. In this technique, no significant heating is involved and the moderate pressure applied during joining does not cause significant deformation

in the weld zone. Through this research, a better understanding of the effects of high temperatures and residual stresses generated during joining of helium containing materials will be obtained. Subsequently, a successful welding technique to join irradiated materials can be developed.

Alloy Modification and Fabrication

1. Research should be conducted on helium-doped Ti-modified type 316 stainless steel and PCA with different thermomechanical pretreatment to understand the mechanisms which control the superior resistance to helium embrittlement. Specimens can be prepared using a combination of solution-annealling, cold-working and aging processes to produce different TiC morphology and dislocation structures prior to helium doping using the "tritium trick". Full penetration GTA welds can be produced under full constraint conditions. Following welding, the helium bubble morphology in the HAZ can then be studied using TEM. The TEM microstructural results can provide the insight into the role of TiC morphology and dislocation structure on helium embrittlement resistance. An optimal thermomechanical pretreatment and chemical composition can then be achieved to prevent helium embrittlement.

2. A study of the effect of aging temperature on the microstructure of RSP 304 stainless steel is recommended. This may lead to an understanding of its intrinsic resistance to helium embrittlement. TEM specimens can be heat treated at different elevated temperatures under vacuum. Following the heat treatment,

microstructure as a function of aging temperature can be studied using TEM. Results of helium bubble morphology and recovery structure of RSP 304 stainless steel can then be obtained. This information will elucidate the role of oxide particles and/or intrinsic pores and the role they play in helium embrittlement resistance.

REFERENCES

1. H. S. Rosenbaum, "Microstructures of Irradiated Materials," *Treaties on Materials Science and Technology*, Vol. 7, Academic Press, Inc., New York, 1975.

2. J. O. Stiegler and L. K. Mansur, "Radiation Effects in Structural Materials," *Ann. Rev. Mater. Sci.*, 9 (1979), pp. 405-454.

3. J. P. Maloney, et al., "Repair of a Nuclear Reactor Vessel," *DP-1199*, E. I. du Pont de Nemours & Co., Savannah River Laboratory, Aiken, SC, June 1969.

4. M. M. Hall, Jr, A. G. Hins, J. R. Summers, and D. E. Walker, "Fusion Welding of Irradiated AISI 304L Stainless Steel Tubing," *Weldment: Physical Metallurgy and Failure Phenomena, Proceedings of the Fifth Bolton Landing Conference*, August 1978, pp. 365-378.

5. S. D. Atkin, "Weld Bend Tests on Irradiated, 20% Cold-Work 316 Stainless Steel," pp. 110-117 in *ADIP Semiannu. Prog. Rep., Sept. 30, 1981*. DOE/ER-0045/7, U.S. DOE, Office of Fusion Energy.

6. R. S. Barnes, "Embrittlement of Stainless Steels and Nickel-Based Alloys at High Temperature Induced by Neutron Radiation," *Nature*, 206 (1965), pp. 1307-1310.

7. D. R. Harries, "Neutron Irradiation-Induced Embrittlement in Type 316 and Other Austenitic Steels and Alloys," *J. Nucl. Mater.*, 82 (1979), pp. 2-21.

8. J.v.d. Driesch and P. Jung, "An Investigation on the Solubility of Helium in Nickel," *High Temperature - High Pressure*, 12 (1980), pp. 635-641.

9. J. Laakmann, P. Jung and W. Uelhoff, "Solubility of Helium in Gold," *Acta Metall.*, 35 (1987), pp. 2063-2069.

10. Annual Books and ASTM Standards, "Standard Guide for Simulation of Helium Effects in Irradiated Metals," Vol. 12.02, E492-83, pp. 808-811.

11. W. R. Kanne, C. L. Angerman and B. J. Eberhard, "Weldability of Tritium-Charged 304L Stainless Steel," *DP-1740*, E. I. du Pont de Nemours & Co., Savannah River Laboratory, Aiken, SC, (Feb. 1987).

12. W. N. Mcelroy and H. Farrar IV, "Helium Production in Stainless Steel and its Constituents as Related to LMFBR Development Programs," *Proceedings of the Radiation-Induced Voids in Metals*, Albany, New York, 1971, pp. 187-229.

13. R. Blackburn, "Inert Gases in Metals," *Metallurgical Reviews*, 11 (1966), pp. 159-176.

14. D. E. Rimmer and A. H. Cottrell, "The Solution of Inert Atoms in Metals," *Phil. Mag.*, 2 (1957), pp. 1345-1353.

15. R. B. Mclellan, "Solution Thermodynamics," *Treaties on Materials Science and Technology*, Vol. 5, H. Herman, Ed., Academic Press, New York, 1974.

16. W. D. Wilson and R. A. Johnson, "Interaction Potentials and Simulation of Lattice Defects," Plenum Press, New York, 1972, pp. 375-390.

17. W. D. Wilson, M. I. Baskes and C. L. Bisson, "Atomistic of Helium Bubble Formation in a Face-Centered-Cubic Metal," *Physical Review B*, 13 (1976), pp. 2470-2478.

18. C. L. Bisson and W. D. Wilson, "Atomistics of Tritium and Helium-3 in Metals," in *Proceedings of Tritium Technology in Fission, Fusion and Isotopic Applications*, Dayton, Ohio, 1980, pp. 78-84.

19. W. D. Wilson, C. L. Bisson and M. I. Baskes, "Self-Trapping of Helium in Metals," *Physical Review B*, 24 (1981), pp. 5616-5624.

20. W. D. Wilson, "Theory of Small Clusters of Helium in Metals," *Radiation Effects*, 78 (9183), pp. 11-24.

21. G. W. Greenwood, A. J. E. Foreman and D. E. Rimmer, "The Role of Vacancies and Dislocations in the Nucleation and Growth of Gas Bubbles in Irradiated Fissile Materials," *J. Nucl. Mater.*, 4 (1959), pp. 305-324.

22. J. H. Evans, A. V. Veen and L. M. Caspers, "Direct Evidence for Helium Bubble Growth in Molybdenum by the Mechanism of Loop Punching," *Scr. Metall.*, 15 (1981), pp. 323-326.

23. H. Ullmaier, "The Influence of Helium on the Bulk Properties of Fusion Reactor Structural Materials," *Nuclear Fusion*, 24 (1984), pp. 1039-1083.

24. G. J. Thomas and R. Bastasz, "Direct Evidence for Spontaneous Precipitation of Helium in Metals," *J. Appl. Phys.*, 52 (1981), pp. 6426-6428.

25. W. Jager, R. Lasser, T. Schober and G. J. Thomas, "Formation of Helium Bubbles and Dislocation Loops in Tritium-Charged Vanadium," *Radiation Effects*, 78 (1983), pp. 165-176.

26. H. Ullmaier, "Helium in Metals," *Radiation Effects*, 78 (1983), pp. 1-10.

27. V. Philipps, K. Sonnenberg and J. M. Williams, "Diffusion of Helium in Nickel", *J. Nucl. Mater.*, 107 (1982), pp. 271-279.

28. R. S. Barnes and D. J. Mazey, "The Migration and Coalescence of Inert Gas Bubbles in Metals," *Proceedings of Royal Society*, England, 275A (1963), p. 47.

29. P. G. Shewmon, "The Movement of Small Inclusions in Solids by Temperature Gradient," *Trans. Met. Soc. AIME*, 230 (1964), pp. 1134-1137.

30. G. W. Greenwood and M. V. Speight, "An Analysis of the Diffusion of Fission Gas Bubbles and its Effect on the Behavior of Reactor Fuels," *J. Nucl. Mater.*, 10 (1963), pp. 140-144.

31. E. E. Gruber, "Calculated Size Distribution for Gas Bubble Migration and Coalescence in Solids," *J. Apply. Phys.*, 38 (1967), pp. 243-250.

32. F. A. Nichols, "Kinetics of Diffusional Motion of Pores in Solids," *J. Nucl. Mater.*, 30 (1969), pp. 143-165.

33. M. V. Speight, "The Migration of Gas Bubbles in Material Subject to Temperature Gradient," *J. Nucl. Mater.*, 14 (1964), pp. 207-209.

34. B. L. Eyre and R. Bullough, "The Formation and Behavior of Gas Bubbles in a Non-uniform Temperature Environment," *J. Nucl. Mater.*, 26 (1968), pp. 249-266.

35. D. G. Martin, "The Migration of Equilibrium Gas Bubbles in a Solid Subject to a Stress Gradient," *J. Nucl. Mater.*, 33 (1969), pp. 23-29.

36. S. H. Leiden and F. A. Nichols, "Influence of Stress Interaction Effects upon Pore Motion in Solids," *J. Nucl. Mater.*, 38 (1971), pp. 309-318.

37. R. S. Barnes, "A Theory of Swelling and Gas Release for Reactor Materials," *J. Nucl. Mater.*, 11 (1964), pp. 135-148.

38. E. M. Baroody, "Calculation on the Collisional Coalescence of Gas Bubbles in Solids," *J. Apply. Phys.*, 38 (1967), pp. 4893-4903.

39. G. W. Greenwood and A. Boltax, "The Role of Fission Gas Re-Solution During Post-Irradiation Heat Treatment," *J. Nucl. Mater.*, 5 (1962), PP. 234-240.

40. A. J. Markworth, "On the Coarsening of Gas-Filled Pores in Solids," *Met. Trans.*, 4A (1973), pp. 2651-2656.

41. W. Beere, "An in Situ Observation of the Grain Boundary/Bubble Interaction," *Scripta Met.*, 9 (1975), pp. 999-1001.

42. E. D. Hyam and G. Sumner, "Irradiation Damage to Beryllium," *Proc. Conf. Radiation Damage in Solids*, Vol. 1 (IAEA, Vienna, 1962) pp. 323-331.

43. E. E. Gruber, "Diffusional Growth of Overpressured Fission-Gas Bubbles on Grain Boundaries," *J. Nucl. Mater.*, 110 (1982), pp. 223-229.

44. E. E. Gruber and J. M. Kramer, "Gas-Bubble Growth Mechanisms in the Analysis of Metal Fuel Swelling," *ASTM STP 955*, (1987), pp. 432-444.

45. H. Reidel, Fracture at High Temperatures, pp. 148-214. Springer-Verlag, New York, 1987.

46. D. Hull and D. Rimmer, "The Growth of Grain-Boundary Voids Under Stress," *Phil. Mag.*, 4 (1959), pp. 673-687.

47. M. V. Speight and J. E. Harris, "The Kinetics of Stress-Induced Growth of Grain-Boundary Voids," *Metal Sci. J.*, 1 (1967), pp. 83-85.

48. J. Weertman " Hull-Rimmer Grain Boundary Void Growth Theory A Correction, " *Scr Metall.* 7 (1973), pp. 1129-1130.

49. R. Raj and M. F. Ashby "Intergranular Fracture at Elevated Temperature," *Acta Metall.*, 23 (1975), pp. 653-666.

50. M. V. Speight and W. Beere, "Vacancy Potential and Void Growth on Grain Boundaries," *Metal Sci. J.*, 9 (1975), pp. 190-191.

51. H. Trinkaus, "Stress Induced Drift Diffusion in Grain Boundaries - Application to Creep and to the Growth of Grain Boundary Voids," *Ber. Bunsenges. Phys. Chem.*, 82 (1978), pp. 249-253.

52. T. J. Chung and J. R. Rice "The Shape of Intergranular Creep Cracks Growing by Surface Diffusion," *Acta Metall.*, 21 (1973), pp. 1625-1628.

53. T. J. Chung, K. I. Kagawa, J. R. Rice and L. B. Sills, "Non-Equilibrium Models for Diffusive Cavitation of Grain Interfaces," *Acta Metall.*, 27 (1979), pp. 265-284.

54. I. W. Chen, "Cavity Growth on a Sliding Grain Boundary," *Met. Trans.*, 14A (1983), pp. 2289-2293.

55. W. Beere, "The Growth of Sub-Critical Bubbles on Grain Boundaries," *J. Nucl. Mater.*, 120 (1984), pp. 88-93.

56. H. Trinkaus and H. Ullmaier, "A Model for the High-Temperature Embrittlement of Metals Containing Helium," *Phil. Mag.*, 39 (1979), pp. 563-580.

57. H. Trinkaus, "On the Modeling of the High-Temperature Embrittlement of Metals Containing Helium," *J. Nucl. Mater.*, 118 (1983), pp. 39-49.

58. H. Trinkaus, "Modeling of Helium Effects in Metals: High Temperature Embrittlement," *J. Nucl. Mater.*, 133&134 (1985), pp. 105-112.

59. H. Trinkaus, "Mechanisms Controlling High Temperature Embrittlement due to Helium," *Radiation Effects*, 101 (1986), pp. 91-107.

60. E. E. Bloom and F. W. Wiffen, "Mechanical Properties of Materials in Fusion Reactor First-Wall and Blanket Systems," *J. Nucl. Mater.*, 85 & 86 (1979), pp. 795-804.

61. E. E. Bloom and. J. O. Stiegler, "Effect of Irradiation on the Microstructure and Creep-Rupture Properties of Type 316 Stainless Steel," *ASTM STP-529* (1973), pp. 360-380.

62. K. Sonnenberg and H. Ullmaier, "Fatigue Properties of Type 316 Stainless Steel Under Helium and Hydrogen Bombardment," *J. Nucl. Mater.*, 103&104 (1981), pp. 859-864.

63. I. S. Batra, H. Ullmaier and K. Sonnenberg, "Frequency Dependence of the High Temperature Fatigue Properties of He-Implanted Stainless Steel," *J. Nucl. Mater.*, 116 (1983), pp. 136-140.

64. M. L. Grossbeck and K. C. Liu, "High-Temperature Fatigue Life of Type 316 Stainless Steel Containing Irradiation Induced Helium," *J. Nucl. Mater.*, 103&104 (1981), pp. 853-858.

65. M. L. Grossbeck and K. C. Liu, "Fatigue Behavior of Type 316 Stainless Steel Irradiated in a Mixed Spectrum Fission Reactor Forming Helium," *Nucl. Technol.*, 58 (1982), pp. 538-547.

66. M. L. Grossbeck ans K. C. Liu, "Fatigue Behavior at 650°C of 20% Cold-Worked Type 316 Stainless Steel Irradiated at 550°C in the High-Flux Isotope Reactor (HFIR)," *ASTM STP-870*, 1985 pp. 732-744.

67. R. L. Klueh and J. M. Vitek, "The Resistance of 9 Cr-1 MoVNb and 12 Cr-1 MoVW Steels to Helium Embrittlement," *J. Nucl. Mater.*, 117 (1983), pp. 295-302.

68. R. L. Klueh and J. M. Vitek, "Postirradiation Tensile Behavior of Nickel-Doped Ferritic Steels," *J. Nucl. Mater.*, 150 (1987), pp. 272-280.

69. M. L. Grossbeck, J.M. Vitek and K. C. Liu, "Fatigue Behavior of Irradiated Helium-Containing Ferritic Steels for Fusion Reactor Application," *J. Nucl. Mater.*, 141-143 (1986), pp. 966-972.

70. C. Wassilew, "Influence of Helium Embrittlement on Post-Irradiation Creep Rupture Behavior of Austenitic and martensitic Stainless Steel," *Proceedings of the International Conference on "Mechanical Behaviour and Nuclear Applications of Stainless Steel at Elevated Temperatures*, The Metals Society, London, 1982, pp. 172-181.

71. R. E. Gold et al., "Materials Technology for Fusion: Current Status and Future Requirements," *Nuclear Technology/Fusion*, 1 (1981), pp. 169-237.

72. B. A. Chin, R. J. Neuhold and J. L. Straalsund, "Materials Development for Fast Breeder Reactor Cores," *Nucl. Technol.*, 57 (1982), pp. 426-435.

73. E. A. Little and D. A. Stow, "Void-Swelling in Irons and Ferritic Steels," *J. Nucl. Mater.*, 87 (1979), pp. 25-39.

74. D. S. Gelles, "Microstructural Examination of Several Commercial Ferritic Alloys Irradiated to High Fluence," *J. Nucl. Mater.*, 103&104 (1981), pp. 975-980.

75. P. J. Maziasz, R. L. Klueh and J. M. Vitek, "Helium Effect on Void Formation in 9Cr-1MoVNb and 12Cr-1MoVW Irradiated in HFIR," *J. Nucl. Mater.*, 141-143 (1986), pp. 929-937.

76. Annual Books and ASTM Standards, "Standard Methods for Determining the Average Grain Size," Vol. 03.01, E-112-85, pp. 403-436.

77. J. H. Austin and T. S. Elleman, "Tritium Diffusion in 304-and 316-Stainless Steels in the Temperature Range 25 to 222°C," *J. Nucl. Mater.*, 43 (1972), pp. 119-125.

78. M. R. Louthan, Jr. and R. G. Derrick, "Hydrogen Transport in Austenitic Stainless Steel," *Corrosion Science*, 15 (1975), pp. 565-577.

79. T. Tanabe, Y. Yamanishi, K. Sawada and S. Imoto, "Hydrogen Transport in Stainless Steels," *J. Nucl. Mater.*, 122&123 (1984), pp. 1568-1572.

80. F. Reiter, J. Camposilvan, M. Caorlin, G. Saibene and R. Sartori, "Interaction of Hydrogen Isotopes with Stainless Steel 316 L," *Fusion Technology*, 8 (1985), pp. 2344-2351.

81. D. M. Grant, D. L. Cummings and D. A. Blackburn, "Hydrogen in 304 Steel: Diffusion, Permeation and Surface Reaction," *J. Nucl. Mater.*, 149 (1987), pp. 180-191.

82. D. M. Grant, D. L. Cummings and D. A. Blackburn, "Hydrogen in 316 Steel - Diffusion, Permeation and Surface Reaction," *J. Nucl. Mater.*, 152 (1988), pp. 139-145.

83. S. H. Goods, Sandia National Laboratories, Livermore, CA, Personal Communication (July, 1987).

84. B. M. Oliver, J. G. Bradley and H. Farrar IV, "Helium Concentration in the Earth's Lower Atmosphere," *Geochim et Cosmochim. ACTA*, 48 (1984), pp. 1759-1767.

85. H. G. Nelson, "Hydrogen Embrittlement," *Treaties on Materials Science and Technology*, Vol. 25, C. L. Briant and S. K. Banerji, Ed., Academic Press, New York, 1983.

86. C. M. Adams, Jr., "Cooling Rates and Peak Temperatures in Fusion Welding," *Welding Journal*, 37 (1958), pp. 210-s-215-s.

87. D. Rosenthal, "The Theory of Moving Sources of Heat and Its Application to Metal Treatments," *Trans. ASME*, 68 (1946), pp. 849-866.

88. Metals Handbook, "Bending Ductility Tests," *Mechanical Testing*, Vol. 8, American Society of Metals, Ohio, 1985.

89. L. E. Murr, R. J. Horylev and W. N. Lin, " Interfacial Energy and Structure in F.C.C. Metals and Alloys," *Phil. Mag.*, 22 (1970), pp. 515-542.

90. I. W. Chen and A. S. Argon, "Grain Boundary and Interphase Boundary Sliding in Power Law Creep," *Acta Metall.*, 27 (1979), pp. 749-754.

91. J. H. Harris, "Nucleation of Creep Cavities in Magnesium," *Trans. Metall. Soc. AIME*, 233 (9165), pp. 1509-1516.

92. G. Neumann and G. M. Neumann, "Surface Self-Diffusion of Metals," Diffusion Information Center, Ohio, 1972.

93. D. W. James and G. M. Leak, "Grain Boundary Diffusion of Iron, Cobalt and Nickel in Alpha-iron and of Iron in Gamma-Iron," *Phil. Mag.*, 12 (1965), pp. 491-503.

94. ASME Section III, Nuclear Power Plant Components, 1971 Edition.

95. ANSI B31.7, "Nuclear Power Piping," 1969.

96. ASME Section III, Nuclear Vessels, 1968 Edition.

97. C. F. Lucks and H. W. Deem, "Thermal Properties of Thirteen Metals," *ASTM STP-227* (1958), p. 29.

98. D. E. Furman, "Thermal Expansion Characteristics of Stainless Steels Between -300 and 1000°F," *Trans. Metall. Soc. AIME*, 88 (1950), pp. 688-691.

99. G. Arthur and J. A. Coulson, "Physical Properties of Uranium Dioxide-Stainless Steel Cermets," *J. Nucl Mater.*, 13 (1964), pp. 242-253.

100. W. F. Simmons and H. C. Cross, "The Elevated Temperature Properties of Stainless Steel," *ASTM STP-124*, 1952.

101. W. F. Simmons and J. A. VanEcho, "The Elevated Temperature Properties of Stainless Steel," *ASTM DS5-S1*, 1965.

102. R. L. Rickett, W. F. White, C. S. Walton and J. C. Butler, "Isothermal Transformation, Hardening, and Tempering of 12% Cr Steel," *Trans. ASM*, 44 (1952), pp. 138-168.

103. K. Masubuchi, "Analysis of Welded Structures," Pergamon Press, New York, 1980, pp. 189-234.

104. W. R. Martin and J. R. Weir, "Solution to the Problems of High-Temperature Irradiation Embrittlement," *ASTM STP-426*, 1967, pp. 440-457.

105. E. E. Bloom and J. R. Weir, " Development of Austenitic Stainless Steel with Improved Resistance to Elevated-Temperature Irradiation Embrittlement," *ASTM STP-457*, 1969 pp. 261-289.

106. E. E. Bloom and J. O. Steigler, "Effect of Irradiation on Titanium-Modified Type 316 Stainless Steel," *Trans. ANS*, 15 (1972), pp. 253-254.

107. E. E. Bloom, J. M. Le[illegible]aker and J. O. Steigler, "Effect of Neutron Irradiation [illegible] Microstructure and Properties of Titanium-Stabilize[illegible]16 Stainless Steels," *Nucl. Technol.*, 31 (1976), pp. 23[illegible]

108. P. J. Maziasz and E. E. Bloom, "Comparison of 316 + Ti with 316 Stainless Steel Irradiated in a Simulated Fusion Environment," *Trans. ANS*, 27 (1977), pp. 268-269.

109. A. F. Rowcliffe, G. J. C. Carpenter, H. F. Merrick and R. B. Nicholson. "An Electron Microscope Investigation of High-Temperature Embrittlement of Irradiated Stainless Steels," *ASTM STP-426*, 1967, pp. 161-199.

110. D. R. Harries and A. C. Roberts, "Effects of Heat-Treatment and Irradiation of the High Temperature Tensile Properties of Austenitic Stainless Steels," *ASTM STP-426*, 1967, pp. 21-47.

111. P. J. Maziasz, "Microstructural Stability and Control for Improved Irradiation Resistance and for High-temperature Strength of Austenitic Stainless Steels," *ASTM STP-979*, 1988, pp. 116-161.

112. P. J. Maziasz and D. N. Braski, "Grain Boundary Microstructural Development and Stability for Various Pretreatments of Path A Prime Candidate Alloy Irradiated in HFIR," pp. 39-48 in *ADIP Semiannu. Prog. Rep. March 31, 1983*, DOE/ER-0045/10, U. S. DOE, Office of Fusion Energy.

113. P. J. Maziasz and D. N. Braski, "Microstructural Design of PCA Austenitic Stainless Steel for Improved Resistance to Helium Embrittlement under HFIR Irradiation," *J. Nucl. Mater.*, 122&123 (1984), pp. 305-310.

114. W. Kesternich and J. Rothaut, "Reduction of Helium Embrittlement in Stainless Steel by Finely Dispersed TiC Precipitates," *J. Nucl. Mater.*, 103&104 (1981), pp. 845-852.

115. W. Kesternich, "A Possible Solution of the Problem of Helium Embrittlement," *J. Nucl. Mater.*, 127 (1985), 153-160.

116. G. M. Goodwin, "Development of a New Hot-Cracking Test - The Sigmajig," *Welding Journal*, 66 (1987), pp. 33-s-38-s.

APPENDIXES

APPENDIX A

MACROSCOPIC FEATURES OF WELDED TYPE 316 STAINLESS STEEL

(HYDROGEN-CHARGED AND HELIUM-DOPED)

YE-13858

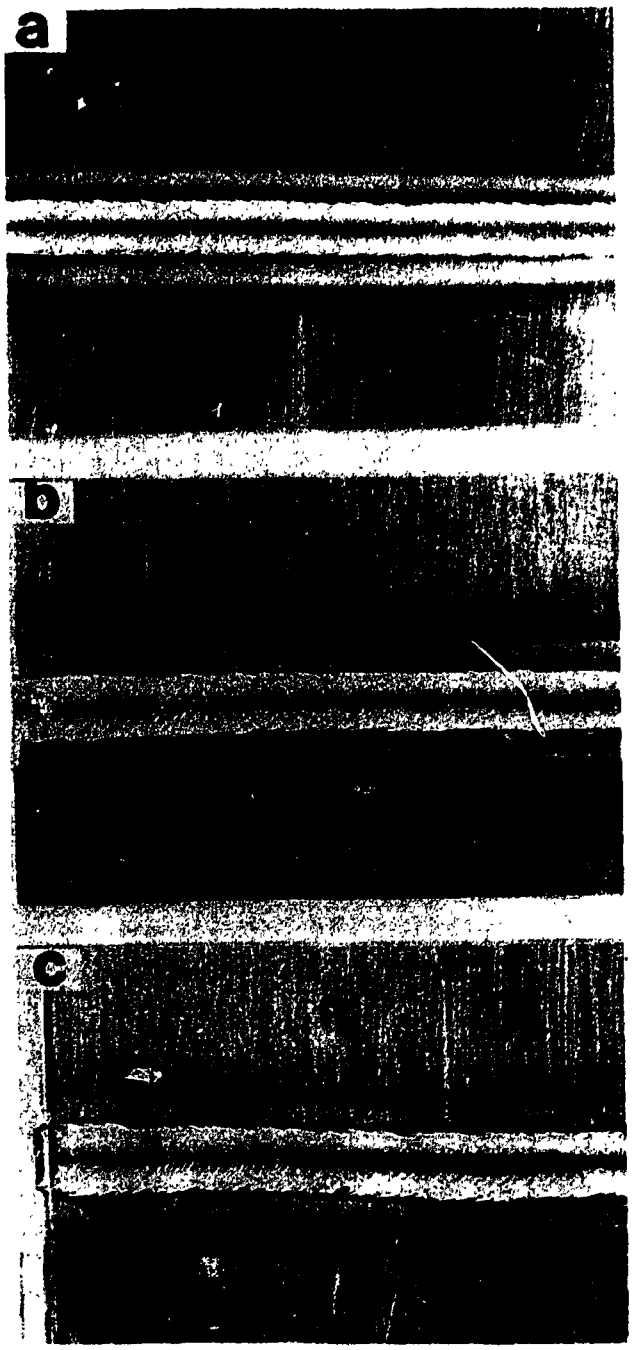

Fig. 56. Macroscopic features of as-welded type 316 stainless steel. (a) Hydrogen-charged materials, (b) 27 appm, and (c) 256 appm.

APPENDIX B

MICROSCOPIC FEATURES OF WELDED TYPE 316 STAINLESS STEEL (HELIUM-DOPED)

YE-13859

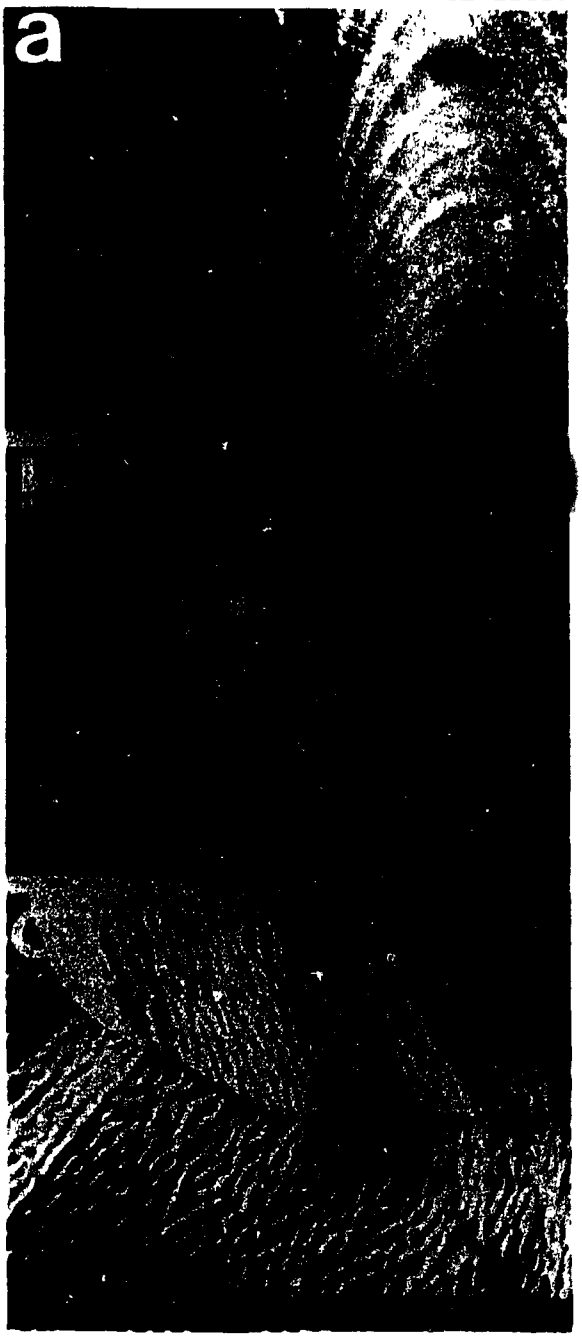

Fig. 57. Structure of as-welded type 316 stainless steel with 27 appm helium.

YE-13860

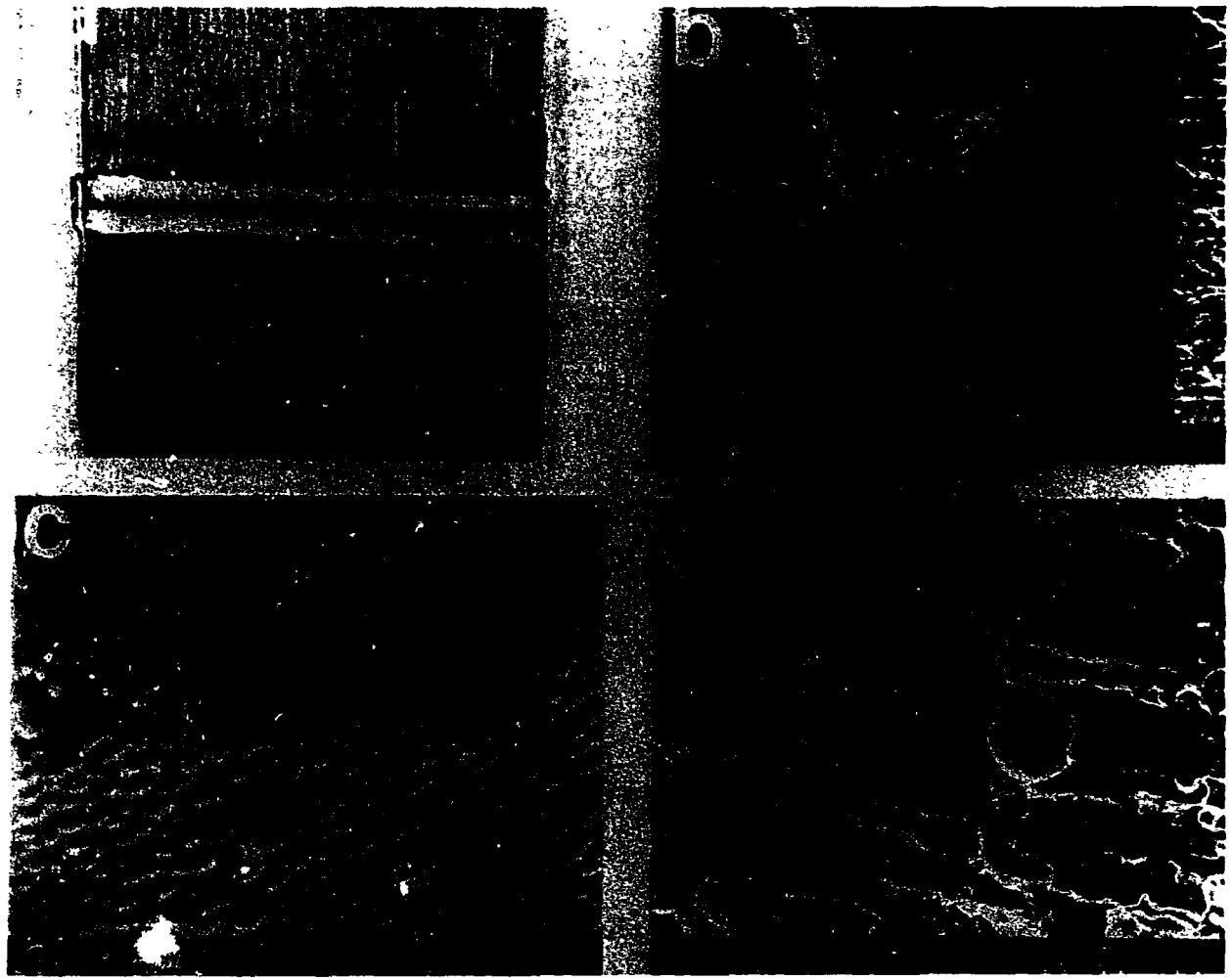

Fig. 58. Structure of as-welded type 316 stainless steel with 256 appm helium.

APPENDIX C

METALLOGRAPHY OF WELDED TYPE 316 STAINLESS STEEL AND HT-9 (HYDROGEN-CHARGED AND HELIUM-DOPED)

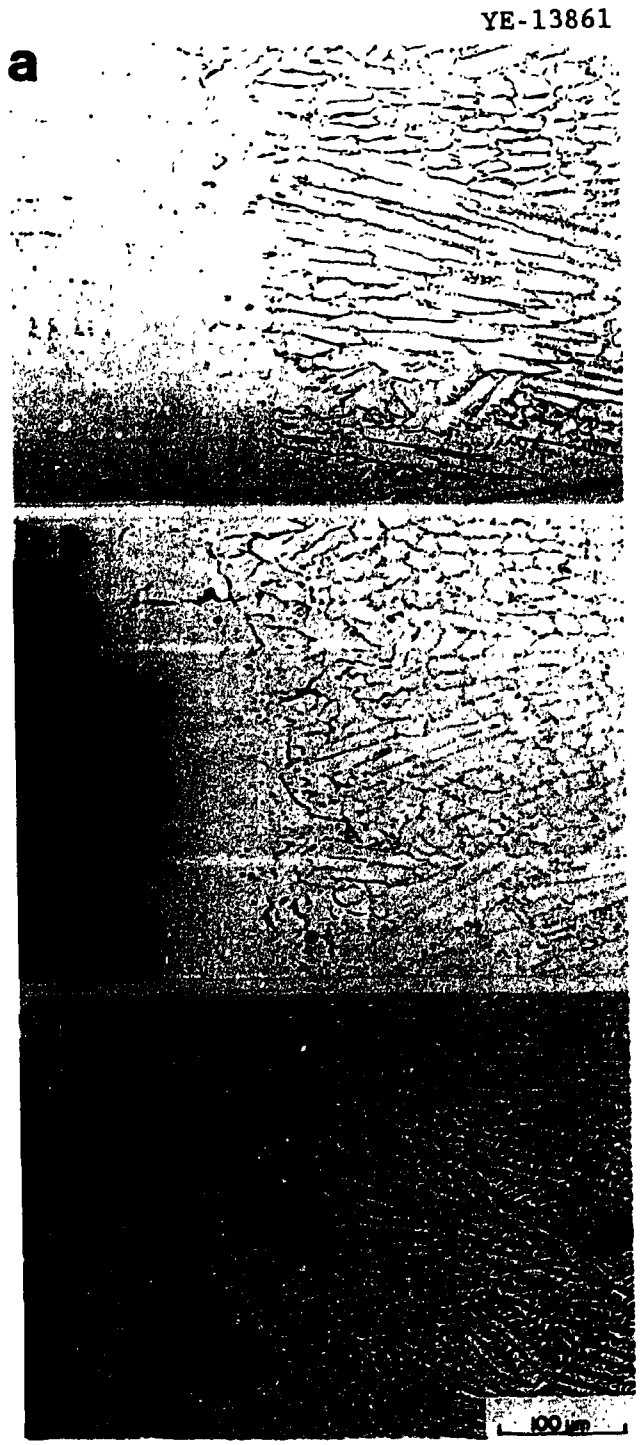

Fig. 59. Optical metallography of normal heat input welds of type 316 stainless steel taken transverse to the welding direction. (a) Hydrogen-charged material, (b) 2.5 appm, and (c) 256 appm.

YE-13862

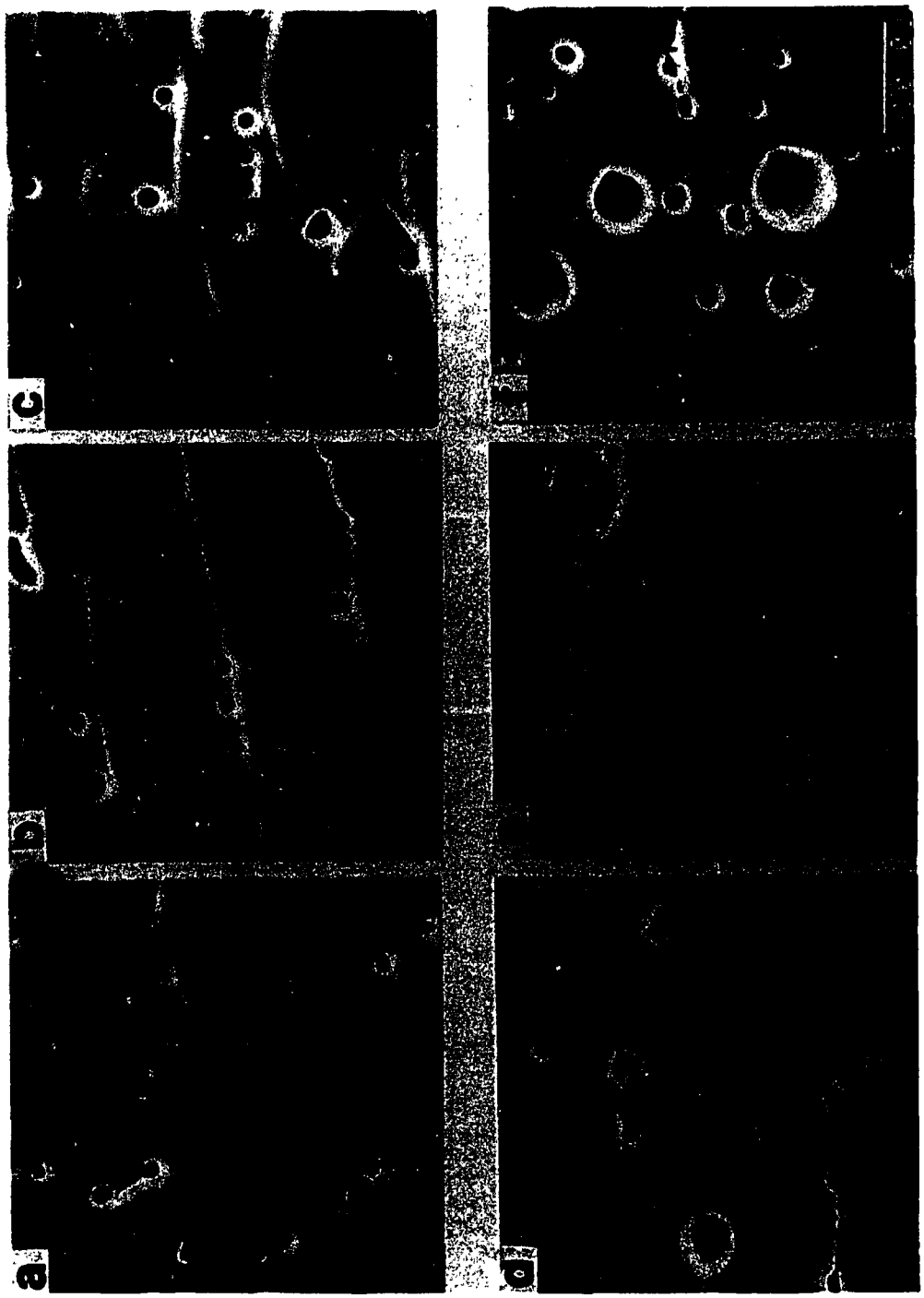

Fig. 60. SEM micrographs of the fusion zone. (a) Control material, (b) 0.18 appm, (c) 2.5 appm, (d) 27 appm, (e) 105 appm, and (f) 256 appm.

YE-13863

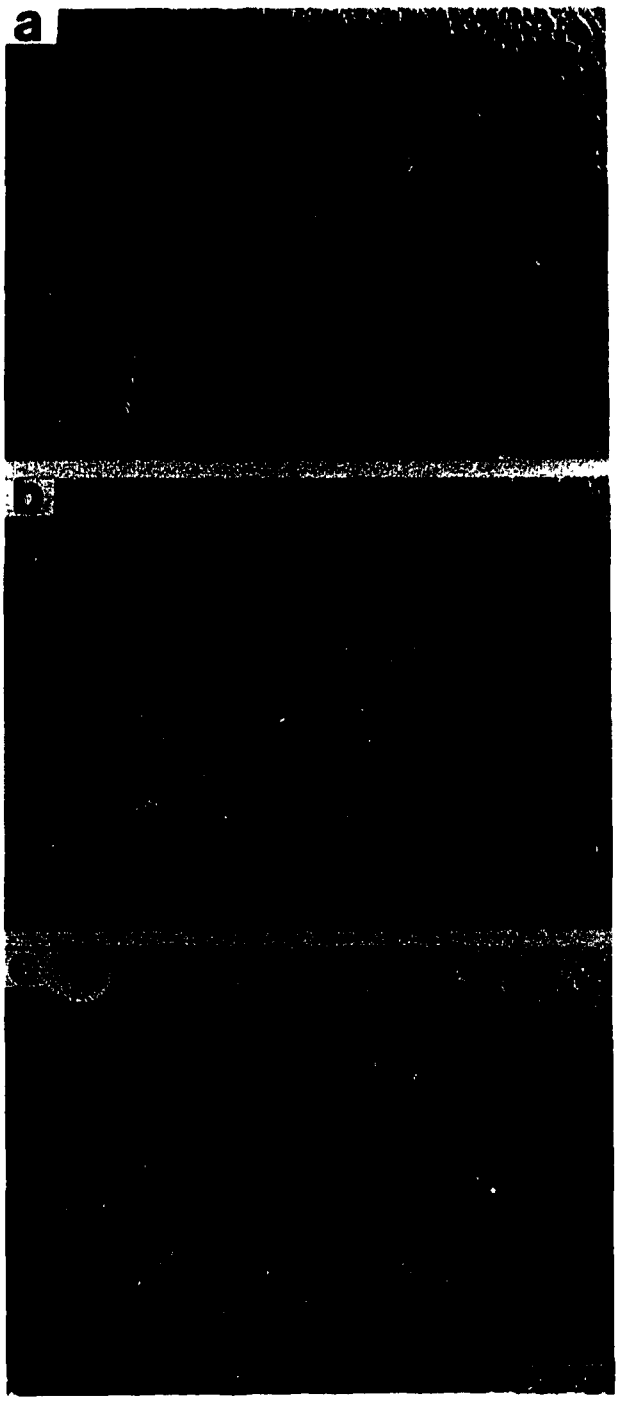

Fig. 61. SEM micrographs of partial penetration welds of type 316 stainless steel. (a) 2.5 appm, (b) 27 appm, and (c) 256 appm.

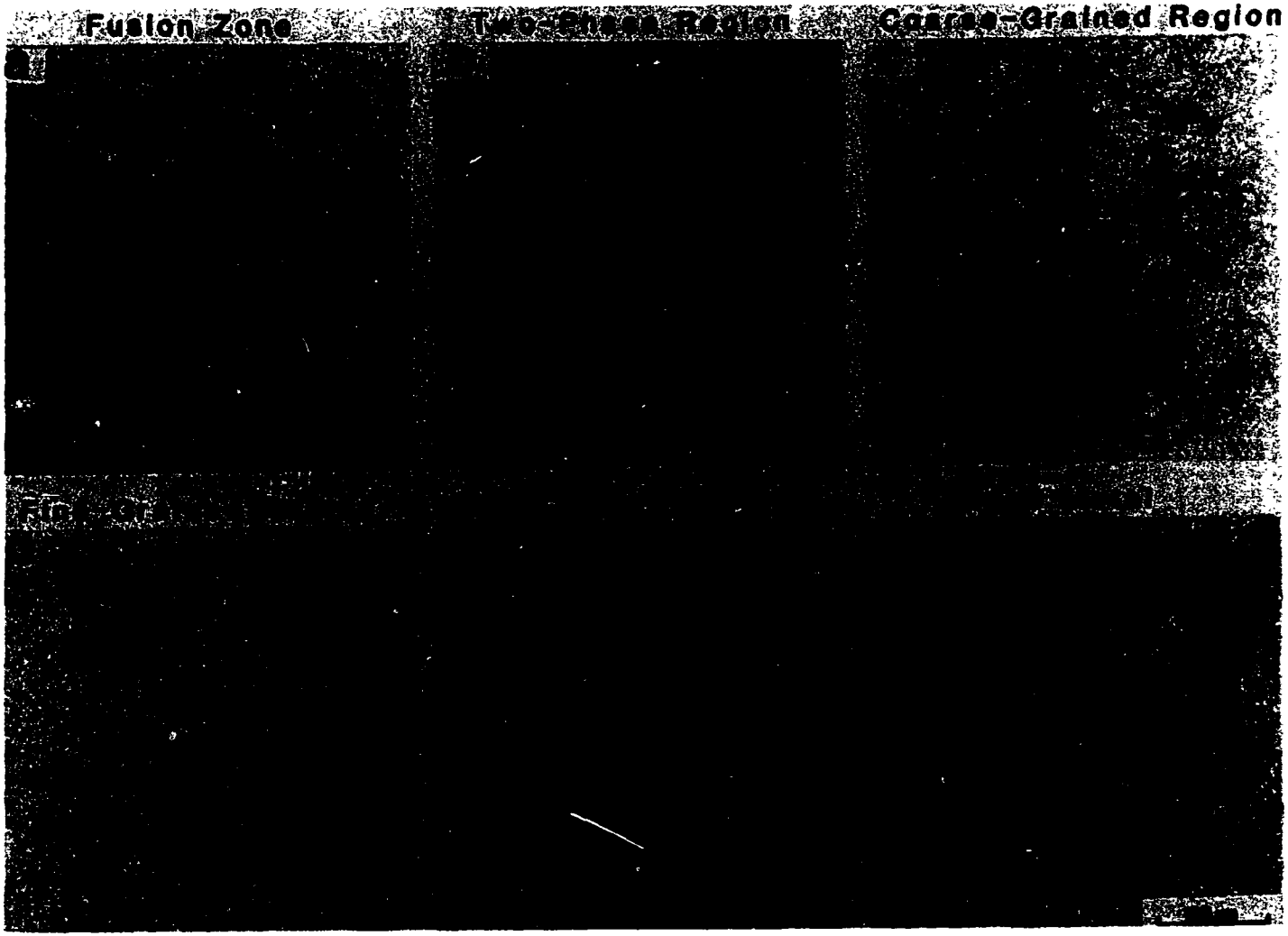

Fig. 62. Typical optical microstructure of HT-9 (control and 0.3 appm).

APPENDIX D

MEASUREMENTS OF FUSION-ZONE PORE SIZE AND DENSITY

Helium Concentration: 256 appm
Specimen Number: 1
Heat Input: Normal
Cavities Counted: 263
Cavity Density (cm^3): 1.36E+8
Average Cavity Diameter (nm): 1552.34

Zeiss Class	No. of Cavities	Cavity Size (nm)	Cavity %
1	82	250.00	31.18
2	39	341.96	14.83
3	10	433.91	3.80
4	8	525.87	3.04
5	5	617.82	1.90
6	22	709.78	8.37
7	23	801.73	8.75
8	20	893.69	7.60
9	11	985.64	4.18
10	8	1077.59	3.04
11	3	1169.55	1.14
12	5	1261.50	1.90
13	2	1353.46	0.76
14	4	1445.42	1.52
15	1	1537.37	0.38
16	1	1629.33	0.38
17	1	1721.28	0.38
18	1	1813.24	0.38
19	3	1905.19	1.14
20	1	1997.14	0.38
30	1	2916.70	0.38
31	1	3008.65	0.38
33	1	3192.56	0.38
35	4	3376.47	1.52
45	1	4296.02	0.38
48	1	4571.89	0.38
50	4	4755.80	1.52

Helium Concentration: 256
Specimen Number: 2
Heat Input: Normal
Cavities Counted: 223
Cavity Density (cm^3): 1.15E+8
Average Cavity Diameter (nm): 1434.28

Zeiss Class	No. of Cavity	Cavity Size (nm)	Cavity %
1	59	250.00	26.46
2	17	341.96	7.62
3	7	433.91	3.14
4	3	525.87	1.35
5	13	617.82	5.83
6	20	709.78	8.97
7	26	801.73	11.66
8	15	893.69	6.73
9	18	985.64	8.07
10	5	1077.59	2.24
11	8	1169.55	3.59
12	2	1261.50	0.90
13	6	1353.46	2.69
14	5	1445.42	2.24
15	5	1537.37	2.24
19	2	1905.19	0.90
20	1	1997.14	0.45
21	1	2089.10	0.45
24	1	2364.97	0.45
28	1	2732.78	0.45
30	1	2916.70	0.45
31	1	3008.65	0.45
33	1	3192.56	0.45
43	3	4112.11	1.35
45	1	4296.02	0.45
48	1	4571.89	0.45

Helium Concentration: 256
Specimen Number: 3
Heat Input: Normal
Cavities Counted: 278
Cavity Density (cm^3): 1.43E+8
Average Cavity Diameter (nm): 1223.46

Zeiss Class	No. of Cavities	Cavity Size (nm)	Cavity %
1	98	250.00	35.25
2	28	341.96	10.07
3	13	433.91	4.68
4	12	525.87	4.32
5	26	617.82	9.35
6	26	709.78	9.35
7	16	801.73	5.76
8	11	893.69	3.96
9	16	985.64	5.76
10	9	1077.59	3.24
11	5	1169.55	1.80
12	3	1261.50	1.08
13	3	1353.46	1.08
14	1	1445.42	0.36
19	2	1905.19	0.72
21	1	2089.10	0.36
24	1	2364.97	0.36
29	1	2824.74	0.36
30	1	2916.70	0.36
33	1	3192.56	0.36
41	1	3928.20	0.36
43	1	4112.11	0.36
45	1	4296.02	0.36
48	1	4571.89	0.36

Helium Concentration: 105
Specimen Number: 1
Heat Input: Normal
Cavities Counted: 174
Cavity Density (cm^3): 8.98E+7
Average Cavity Diameter (nm): 1366.78

Zeiss Class	No. of Cavities	Cavity Size (nm)	Cavity %
1	50	250.00	28.74
2	29	341.96	16.67
3	1	433.91	0.57
4	4	525.87	2.30
5	2	617.82	1.15
6	12	709.78	6.90
7	12	801.73	6.90
8	11	893.69	6.32
9	9	985.64	5.17
10	14	1077.59	8.05
11	8	1169.55	4.60
12	6	1261.50	3.45
13	3	1353.46	1.72
15	1	1537.37	0.57
17	1	1721.28	0.57
18	1	1813.24	0.57
19	1	1905.19	0.57
22	1	2181.06	0.57
24	1	2364.97	0.57
26	1	2548.88	0.57
29	2	2824.74	1.15
31	2	3008.65	1.15
48	1	4571.89	1.15
50	1	4755.80	0.57

Helium Concentration: 105
Specimen Number: 2
Heat Input: Normal
Cavities Counted: 192
Cavity Density (cm^3): 9.91E+7
Average Cavity Diameter (nm): 1396.88

Zeiss Class	No. of Cavities	Cavity Size (nm)	Cavity %
1	65	250.00	33.85
2	13	341.96	6.77
3	8	433.91	4.17
4	7	525.87	3.65
5	13	617.82	6.77
6	12	709.78	6.25
7	22	801.73	11.46
8	19	893.69	9.90
9	8	985.64	4.17
10	6	1077.59	3.13
11	2	1169.55	1.04
12	2	1261.50	1.04
14	1	1445.42	0.52
15	1	1537.37	0.52
16	1	1629.33	0.52
17	1	1721.28	0.52
19	1	1905.19	0.52
21	1	2089.10	0.52
22	1	2181.06	0.52
24	1	2364.97	0.52
29	1	2824.74	0.52
31	1	3008.65	0.52
32	1	3100.60	0.52
43	2	4112.11	1.04
48	2	4571.89	1.04

Helium Concentration: 105
Specimen Number: 3
Heat Input: Normal
Cavities Counted: 233
Cavity Density (cm^3): 1.20E+8
Average Cavity Diameter (nm): 1192.77

Zeiss Class	No. of Cavities	Cavity Size (nm)	Cavity %
1	71	250.00	30.47
2	16	341.96	6.87
3	11	433.91	4.72
4	9	525.87	3.86
5	10	617.82	4.29
6	22	709.78	9.44
7	21	801.73	9.01
8	30	893.69	12.88
9	13	985.64	5.58
10	5	1077.59	2.15
11	4	1169.55	1.72
12	4	1261.50	1.72
13	2	1353.46	0.86
14	1	1445.42	0.43
15	2	1537.37	0.86
16	3	1629.33	1.29
17	1	1721.28	0.43
18	1	1813.42	0.43
21	1	2089.10	0.43
22	1	2181.06	0.43
29	1	2824.74	0.43
34	1	3284.51	0.43
48	2	4571.89	0.86

Helium Concentration: 27
Specimen Number: 1
Heat Input: Normal
Cavities Counted: 87
Cavity Density (cm^3): 4.49E+7
Average Cavity Diameter (nm): 1287.59

Zeiss Class	No of Cavities	Cavity Size (nm)	Cavity %
1	13	250.00	14.94
2	3	341.96	3.45
3	1	433.91	1.15
4	3	525.87	3.45
5	5	617.82	5.75
6	16	709.78	18.39
7	8	801.73	9.20
8	5	893.69	5.75
9	6	985.64	6.90
10	3	1077.59	3.45
11	6	1169.55	6.90
12	2	1261.50	2.30
13	3	1353.46	3.45
14	2	1445.42	2.30
15	1	1537.37	1.15
16	2	1629.33	2.30
17	2	1721.28	2.30
19	2	1905.19	2.30
21	1	2089.10	1.15
24	1	2364.97	1.15
29	1	2824.74	1.15
39	1	3744.29	1.15

Helium Concentration: 27
Specimen Number: 2
Heat Input: Normal
Cavities Counted: 118
Cavity Density (cm^3): 6.09E+7
Average Cavity Diameter (nm): 815.54

Zeiss Class	No. of Cavities	Cavity Size (nm)	Cavity %
1	22	250.00	18.64
2	9	341.96	7.63
3	12	433.91	10.17
4	8	525.87	6.78
5	9	617.82	7.63
6	13	709.78	11.02
7	17	801.73	14.41
8	7	893.69	5.93
9	6	985.64	5.08
10	5	1077.59	4.24
11	4	1169.55	3.39
12	1	1261.50	0.85
14	2	1445.42	1.69
15	2	1537.37	1.69
19	1	1905.19	0.85

Helium Concentration: 27
Specimen Number: 3
Heat Input: Normal
Cavities Counted: 120
Cavity Density (cm^3): 6.19E+7
Average Cavity Diameter (nm): 831.28

Zeiss Class	No. of Cavities	Cavity Size (nm)	Cavity %
1	19	250.00	15.83
2	6	341.96	5.00
3	6	433.91	5.00
4	7	525.87	5.83
5	13	617.82	10.83
6	16	709.78	13.33
7	18	801.73	15.00
8	12	893.69	10.00
9	8	985.64	6.67
10	6	1077.59	5.00
11	2	1169.55	1.67
12	1	1261.50	0.83
13	3	1353.46	2.50
14	1	1445.42	0.83
16	1	1629.33	0.83
17	1	1721.28	0.83

Helium Concentration: 2.5
Specimen Number: 1
Heat Input: Normal
Cavities Counted: 59
Cavity Density (cm^3): 3.04E+7
Average Cavity Diameter (nm): 809.64

Zeiss Class	No. of Cavities	Cavity Size (nm)	Cavity %
1	16	250.00	27.12
2	7	341.96	11.86
3	3	433.91	5.08
4	5	525.87	8.47
5	2	617.82	3.39
6	4	709.78	6.78
7	5	801.73	8.47
8	2	893.69	3.39
9	4	985.64	6.78
10	3	1077.59	5.08
11	3	1169.55	5.08
12	3	1261.50	5.08
13	1	1353.46	1.69
14	1	1445.42	1.69

Helium Concentration: 2.5
Specimen Number: 2
Heat Input: Normal
Cavities Counted: 82
Cavity Density (cm^3): 4.23E+7
Average Cavity Diameter (nm): 767.34

Zeiss Class	No. of Cavities	Cavity Size (nm)	Cavity %
1	6	250.00	7.32
2	10	341.96	12.20
3	13	433.91	15.85
4	6	525.87	7.32
5	15	617.82	18.29
6	8	709.78	9.76
7	5	801.73	6.10
8	8	893.69	9.76
9	2	985.64	2.44
10	3	1077.59	3.66
11	2	1169.55	2.44
12	1	1261.50	1.22
14	3	1445.42	3.66

Helium Concentration: 2.5
Specimen Number: 3
Heat Input: Normal
Cavities Counted: 68
Cavity Density (cm^3): 3.51E+7
Average Cavity Diameter (nm): 825.07

Zeiss Class	No. of Cavities	Cavity Size (nm)	Cavity %
1	12	250.00	17.65
2	4	341.96	5.88
3	7	433.91	10.29
4	2	525.87	2.94
5	7	617.82	10.29
6	10	709.78	14.71
7	9	801.73	13.24
8	6	893.69	8.82
9	1	985.64	1.47
10	3	1077.59	4.41
11	2	1169.55	2.94
12	1	1261.50	1.47
13	2	1353.46	2.94
15	1	1537.37	1.47
16	1	1629.33	1.47

Helium Concentration: 105 appm
Specimen Number: 1
Heat Input: High
Cavities Counted: 85
Cavity Density (cm^3): 2.19E+7
Average Cavity Diameter (nm): 1479.64

Zeiss Class	No. of Cavities	Cavity Size (nm)	Cavity %
1	7	250.00	8.42
2	14	341.96	16.47
3	16	433.91	18.82
4	13	525.87	15.29
5	4	617.82	4.71
6	5	709.78	5.88
7	4	801.73	4.71
8	4	893.69	4.71
9	3	985.64	3.53
10	3	1077.59	3.53
11	1	1169.55	1.18
13	1	1353.46	1.18
14	1	1445.42	1.18
15	2	1537.37	2.35
20	1	1997.14	1.18
23	1	2273.01	1.18
33	2	2916.70	2.35
38	2	3376.47	2.35
41	1	4296.02	1.18

Helium Concentration: 105 appm
Specimen Number: 2
Heat Input: High
Cavities Counted: 79
Cavity Density (cm^3): 2.04E+7
Average Cavity Diameter (nm): 1187.68

Zeiss Class	No. of Cavities	Cavity Size (nm)	Cavity %
1	11	250.00	13.92
2	21	341.96	26.58
3	11	433.91	13.92
4	12	525.87	15.19
5	6	617.82	7.59
7	5	801.73	6.33
8	5	893.69	6.33
9	2	985.64	2.53
10	1	1077.59	1.27
11	1	1169.55	1.27
13	1	1353.46	1.27
17	1	1721.28	1.27
24	1	2364.97	1.27
48	1	4571.89	1.27

Helium Concentration: 105 appm
Specimen Number: 3
Heat Input: High
Cavities Counted: 95
Cavity Density (cm^3): 2.45E+7
Average Cavity Diameter (nm): 1109.59

Zeiss Class	No. of Cavities	Cavity Size (nm)	Cavity %
1	11	250.00	11.58
2	20	341.96	21.05
3	16	433.91	16.84
4	15	525.87	15.79
5	8	617.82	8.42
6	4	709.78	4.21
7	3	801.73	3.16
8	5	893.69	5.26
9	2	985.64	2.11
10	2	1077.59	2.11
11	3	1169.55	3.16
12	2	1261.50	2.11
13	1	1353.46	1.05
24	1	2364.97	1.05
27	1	2640.83	1.05
43	1	4112.11	1.05

Helium Concentration: 27 appm
Specimen Number: 1
Heat Input: High
Cavities Counted: 61
Cavity Density (cm^3): 1.57E+7
Average Cavity Diameter (nm): 1258.78

Zeiss Class	No. of Cavities	Cavity Size (nm)	Cavity %
1	21	250.00	34.43
2	14	341.96	22.95
3	2	433.91	3.28
4	4	525.87	6.56
5	2	617.82	3.28
6	3	709.78	4.92
7	3	801.73	4.92
8	1	893.69	1.64
9	4	985.64	6.56
10	1	1077.59	1.64
11	1	1169.55	1.64
12	3	1261.50	4.92
20	1	2364.97	1.64
48	1	4571.89	1.64

Helium Concentration: 27 appm
Specimen Number: 2
Heat Input: High
Cavities Counted: 38
Cavity Density (cm^3): 9.80E+6
Average Cavity Diameter (nm): 1526.05

Zeiss Class	No. of Cavities	Cavity Size (nm)	Cavity %
1	4	250.00	10.53
2	11	341.96	28.95
3	6	433.91	15.79
4	4	525.87	10.53
5	2	617.82	5.26
6	4	709.78	10.53
7	1	801.73	2.63
8	1	893.69	2.63
9	1	985.64	2.63
12	2	1261.50	5.26
32	1	3100.60	2.63
48	1	4571.89	2.63

Helium Concentration: 27 appm
Specimen Number: 3
Heat Input: High
Cavities Counted: 52
Cavity Density (cm^3): 1.34E+7
Average Cavity Diameter (nm): 1010.87

Zeiss Class	No. of Cavities	Cavity Size (nm)	Cavity %
1	11	250.00	21.15
2	9	341.96	17.31
3	11	433.91	21.15
4	4	525.87	7.69
5	4	617.82	7.69
6	5	709.78	9.62
7	1	801.73	1.92
8	1	893.69	1.92
9	2	985.64	3.85
11	1	1169.55	1.92
36	1	3468.42	1.92

APPENDIX E

TEM MICROSTRUCTURES OF TYPE 316 STAINLESS STEEL

(CONTROL AND HELIUM-DOPED)

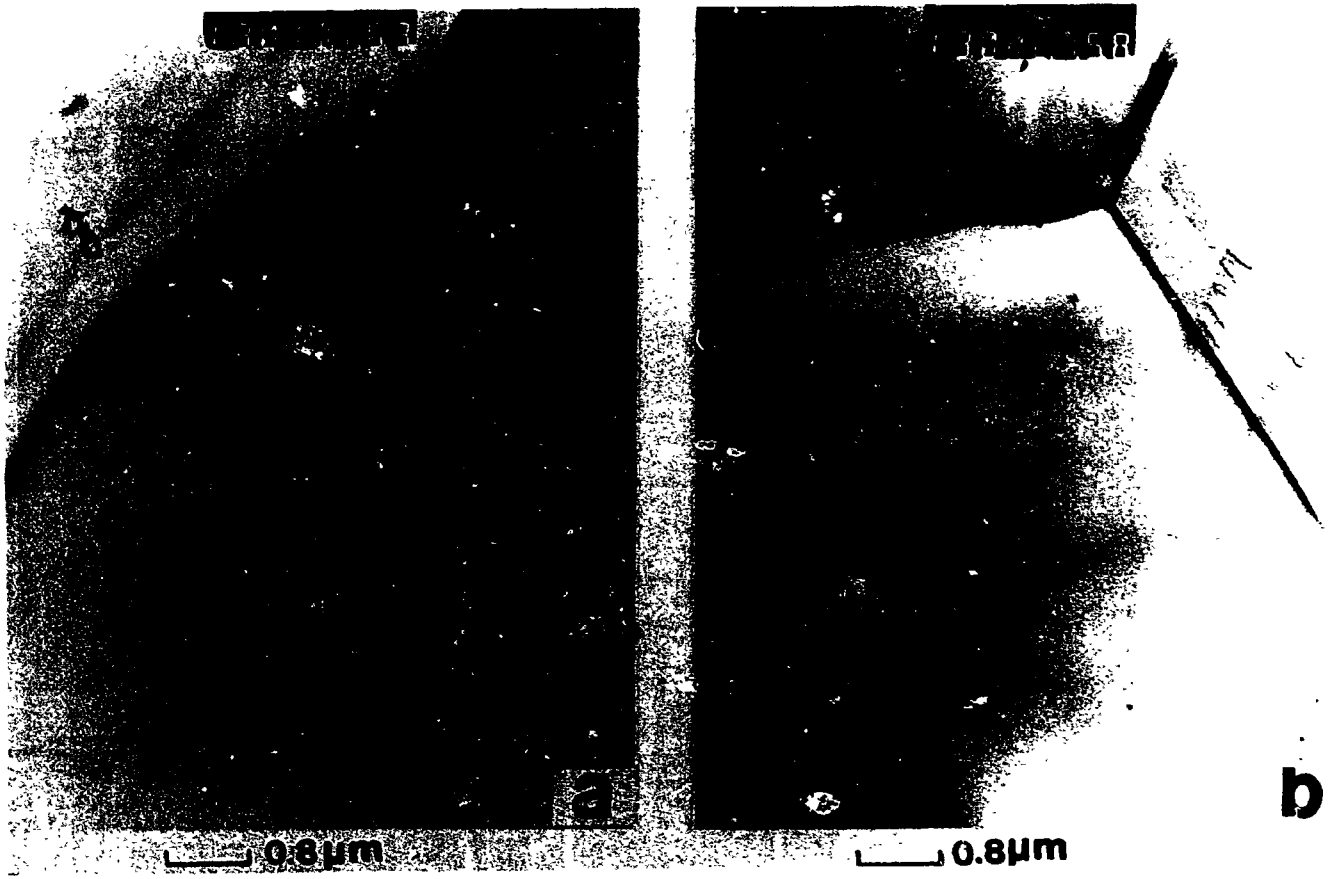

Fig. 63. TEM micrographs of type 316 stainless steel. (a) Control material, and (b) hydrogen-charged material.

YE-13866

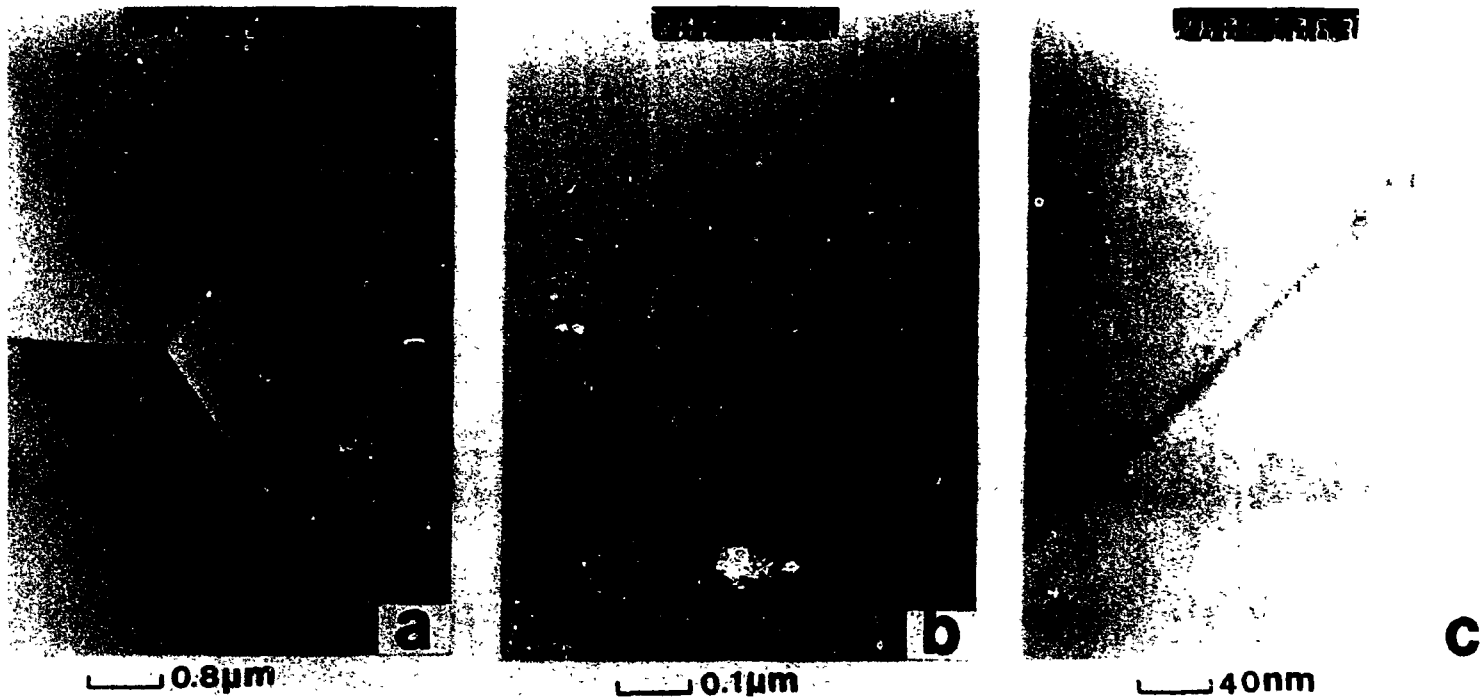

Fig. 64. TEM micrographs of type 316 stainless steel with 0.18 appm helium.

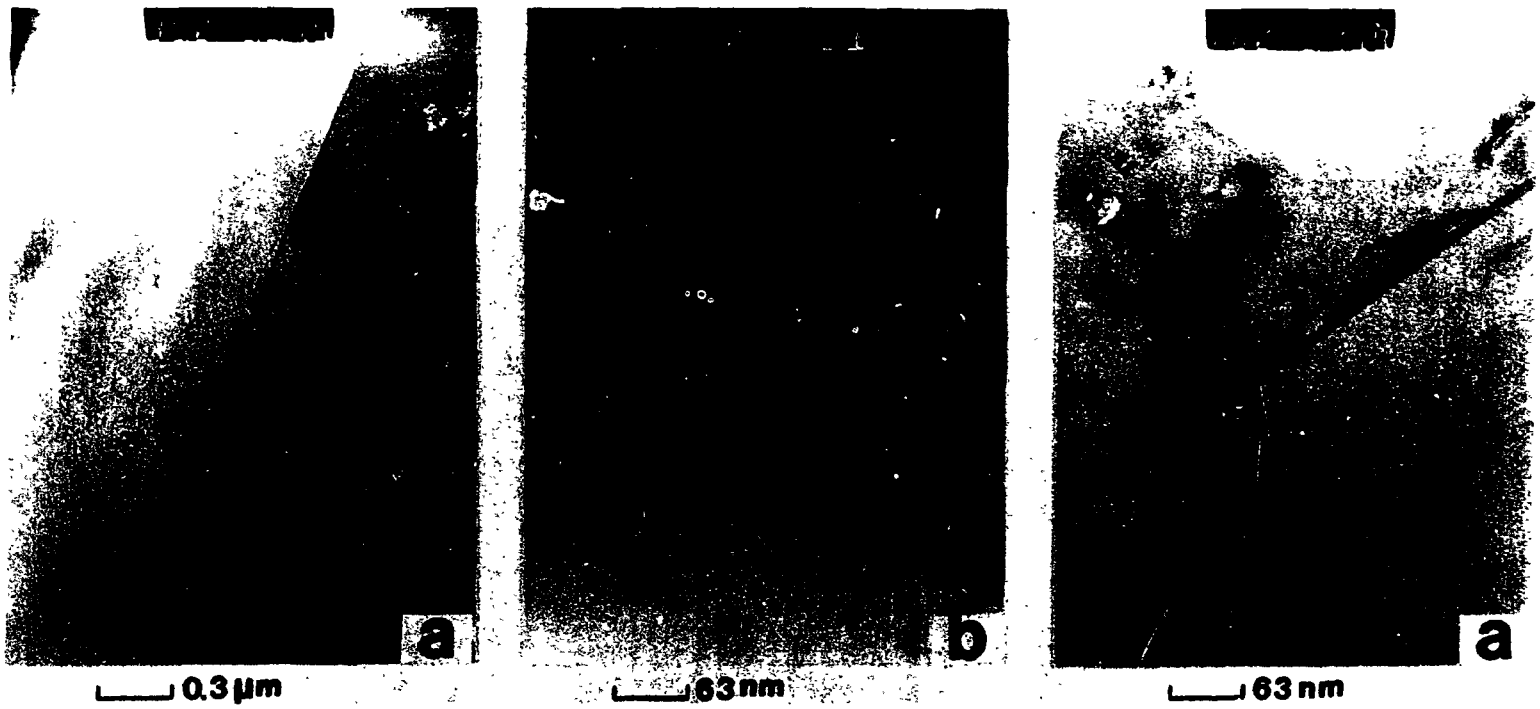

Fig. 65. TEM micrographs of type 316 stainless steel with 2.5 appm helium.

Fig. 66. TEM micrographs of type 316 stainless steel with 27 appm helium.

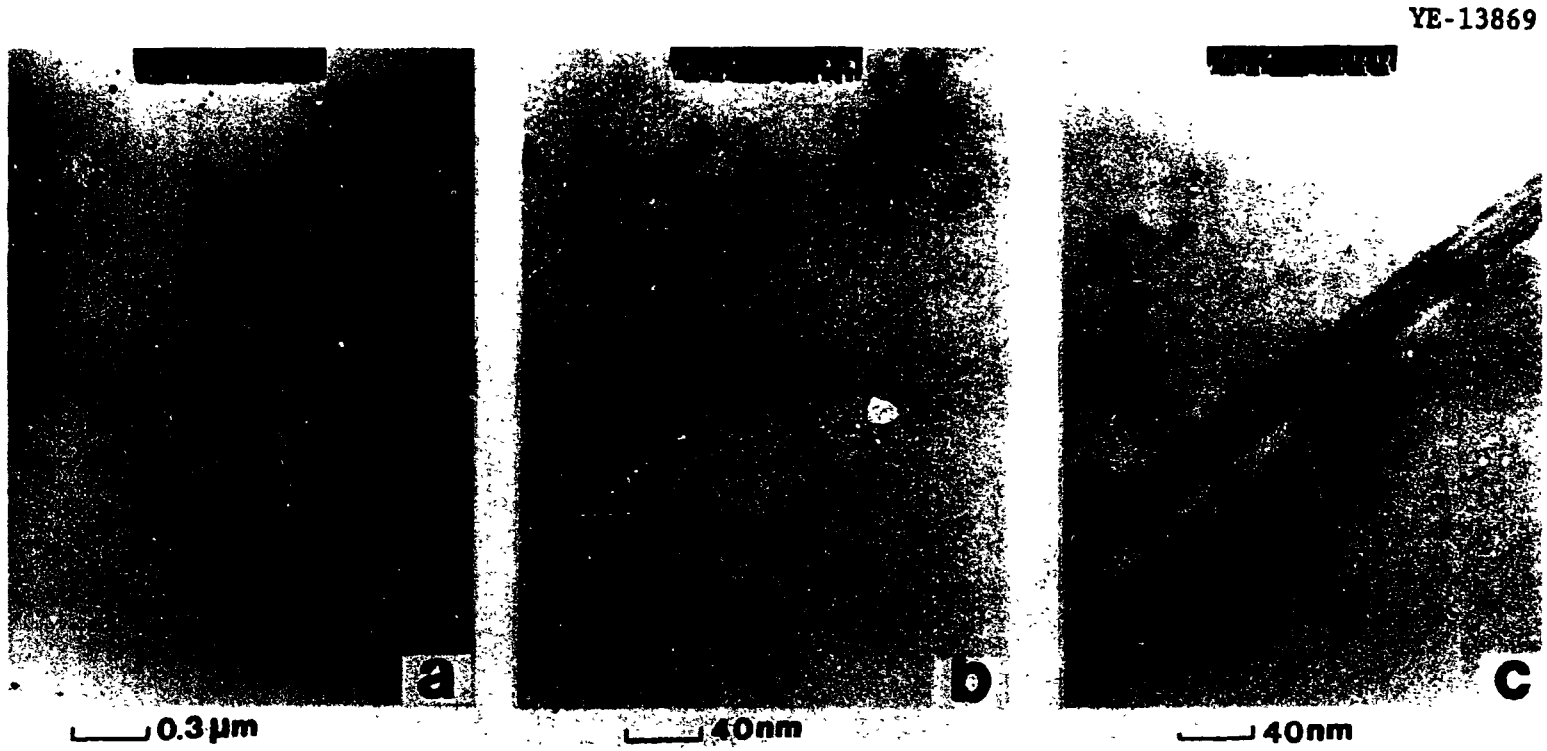

Fig. 67. TEM micrographs of type 316 stainless steel with 105 appm helium.

APPENDIX F

TEM MICROSTRUCTURES OF WELDED TYPE 316 STAINLESS STEEL

(HELIUM-DOPED)

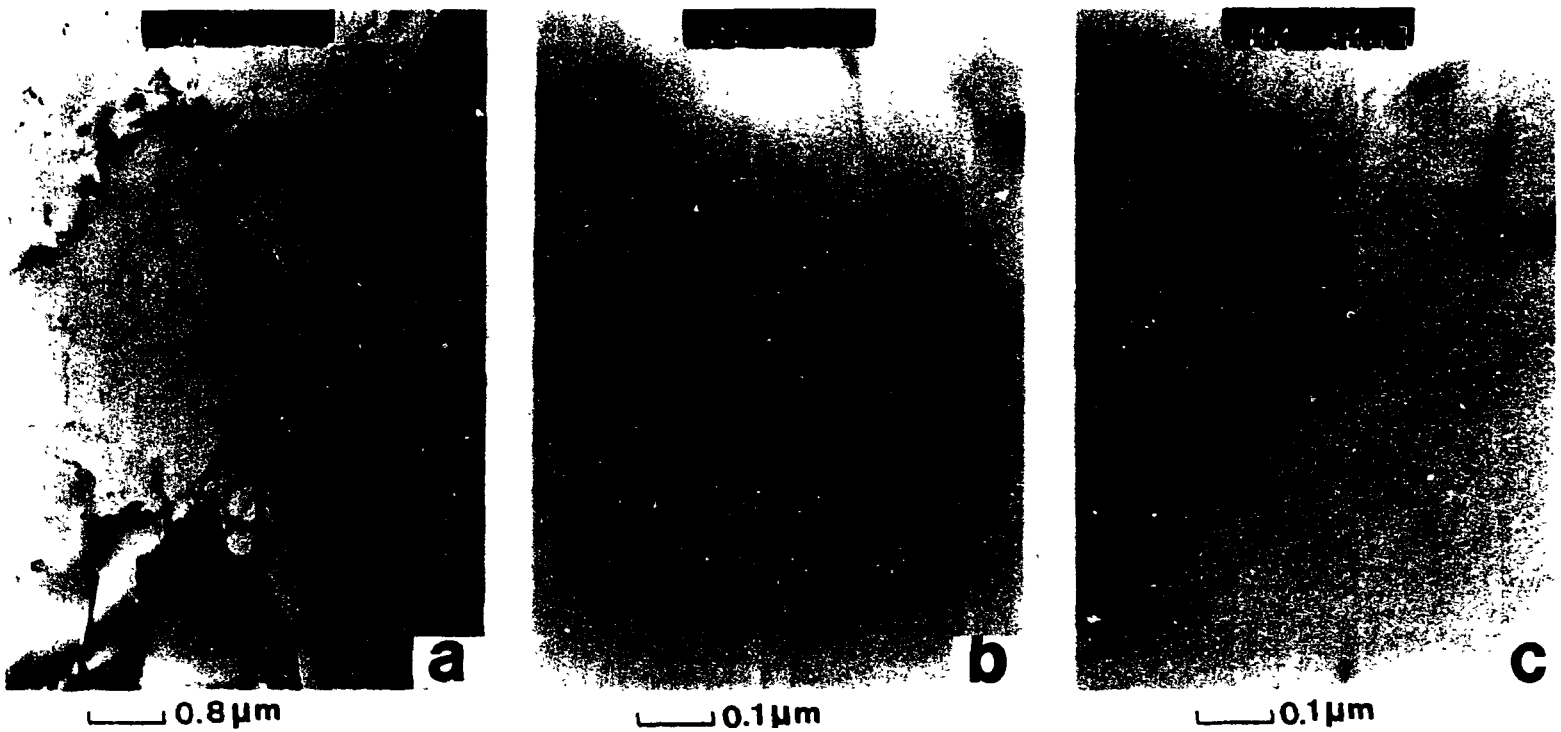

Fig. 68. TEM micrographs of the heat-affected zone of 0.18 appm weld with normal heat input.

YE-13871

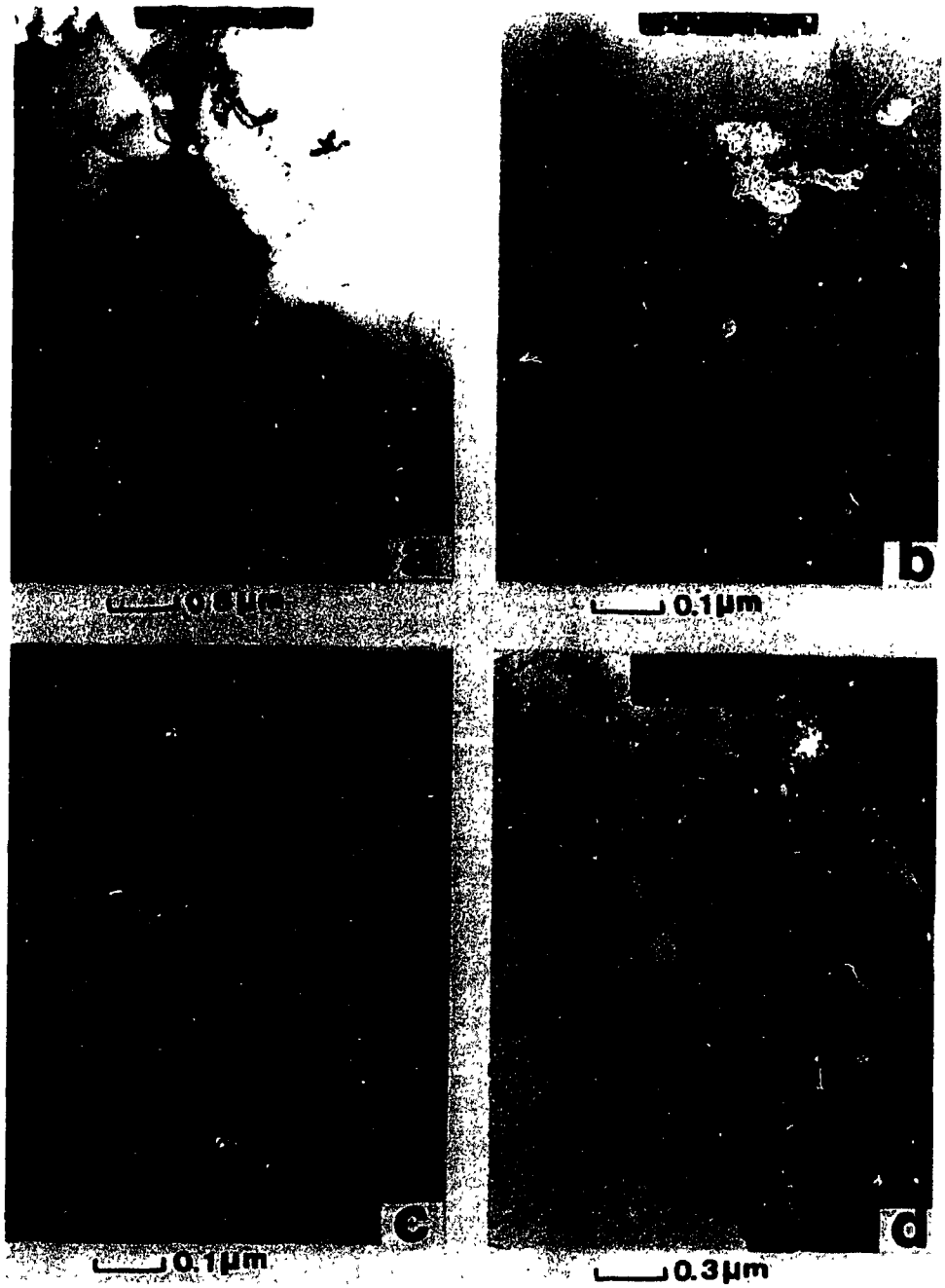

Fig. 69. TEM micrographs of the heat-affected zone of 2.5 appm weld with normal heat input.

YE-13872

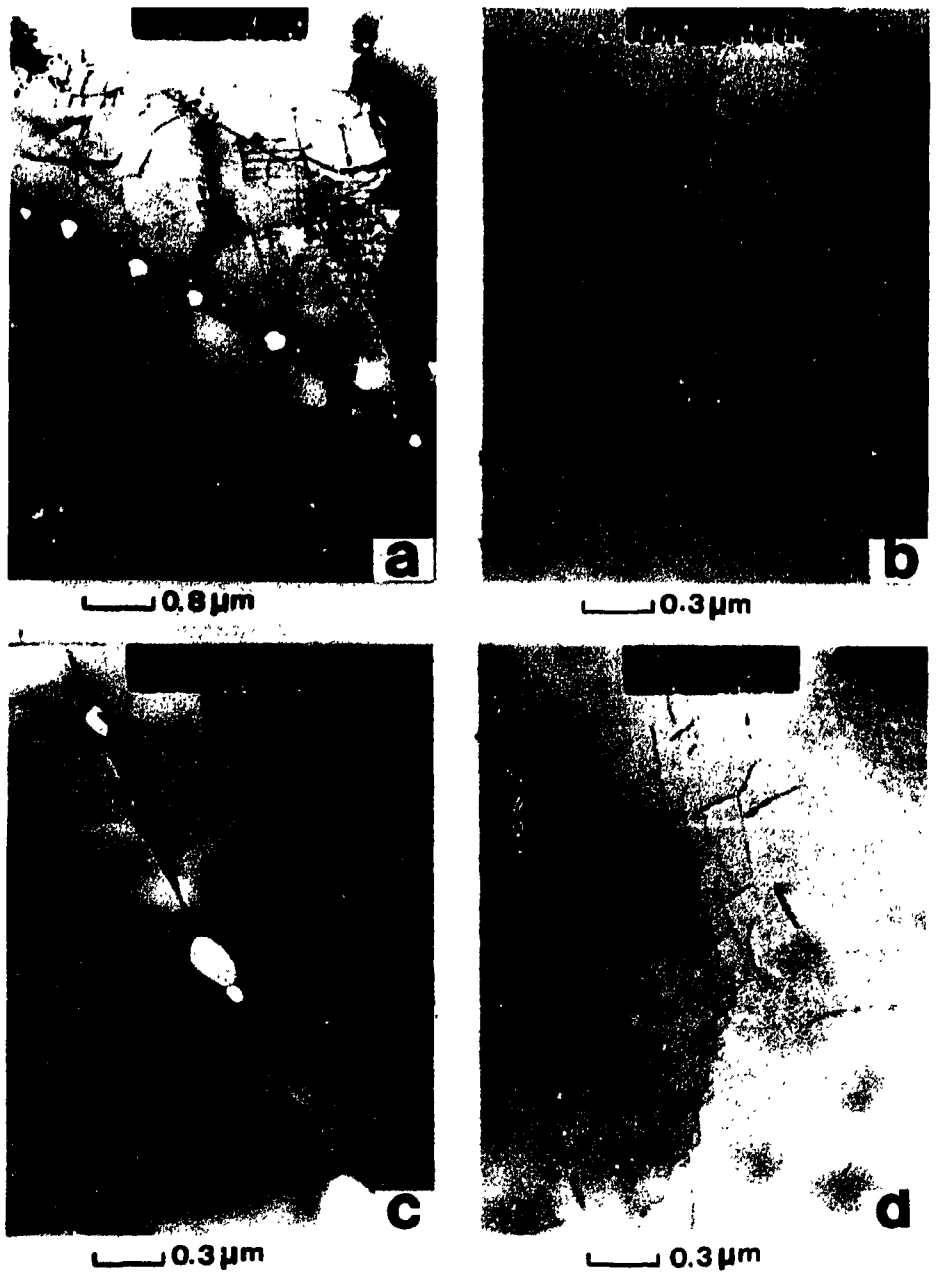

Fig. 70. TEM micrographs of the heat-affected zone of 27 appm weld with normal heat input.

YE-13873

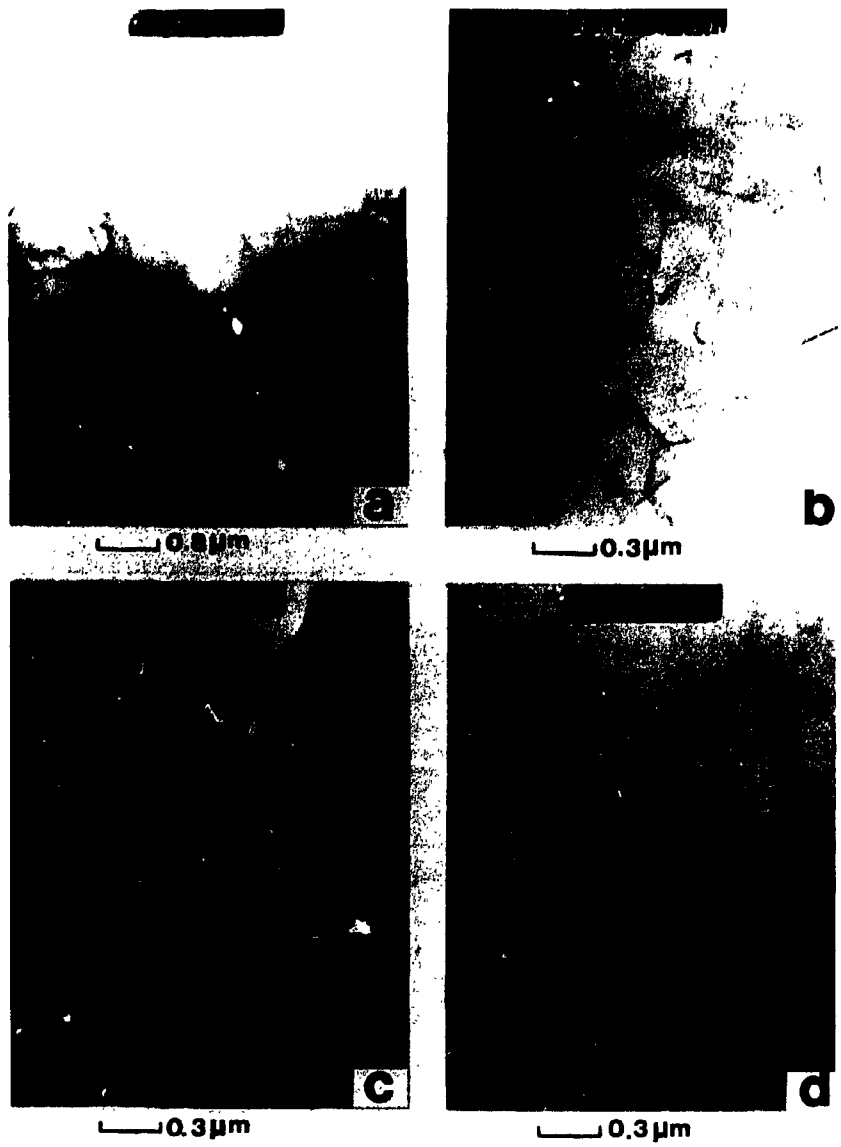

Fig. 71. TEM micrographs of the heat-affected zone of 105 appm weld with normal heat input.

YE-13874

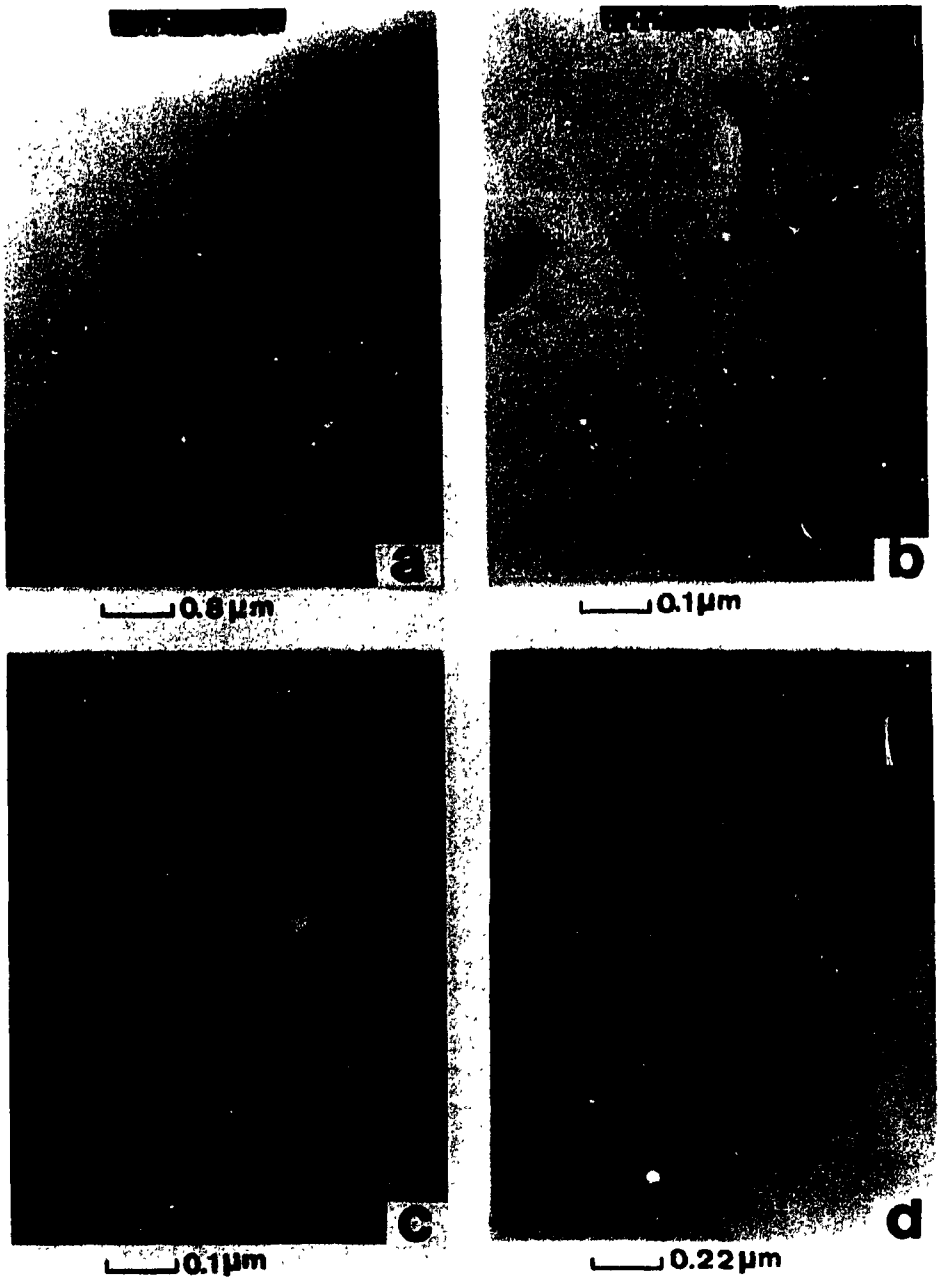

Fig. 72. TEM micrographs of the heat-affected zone of 27 appm weld with high heat input.

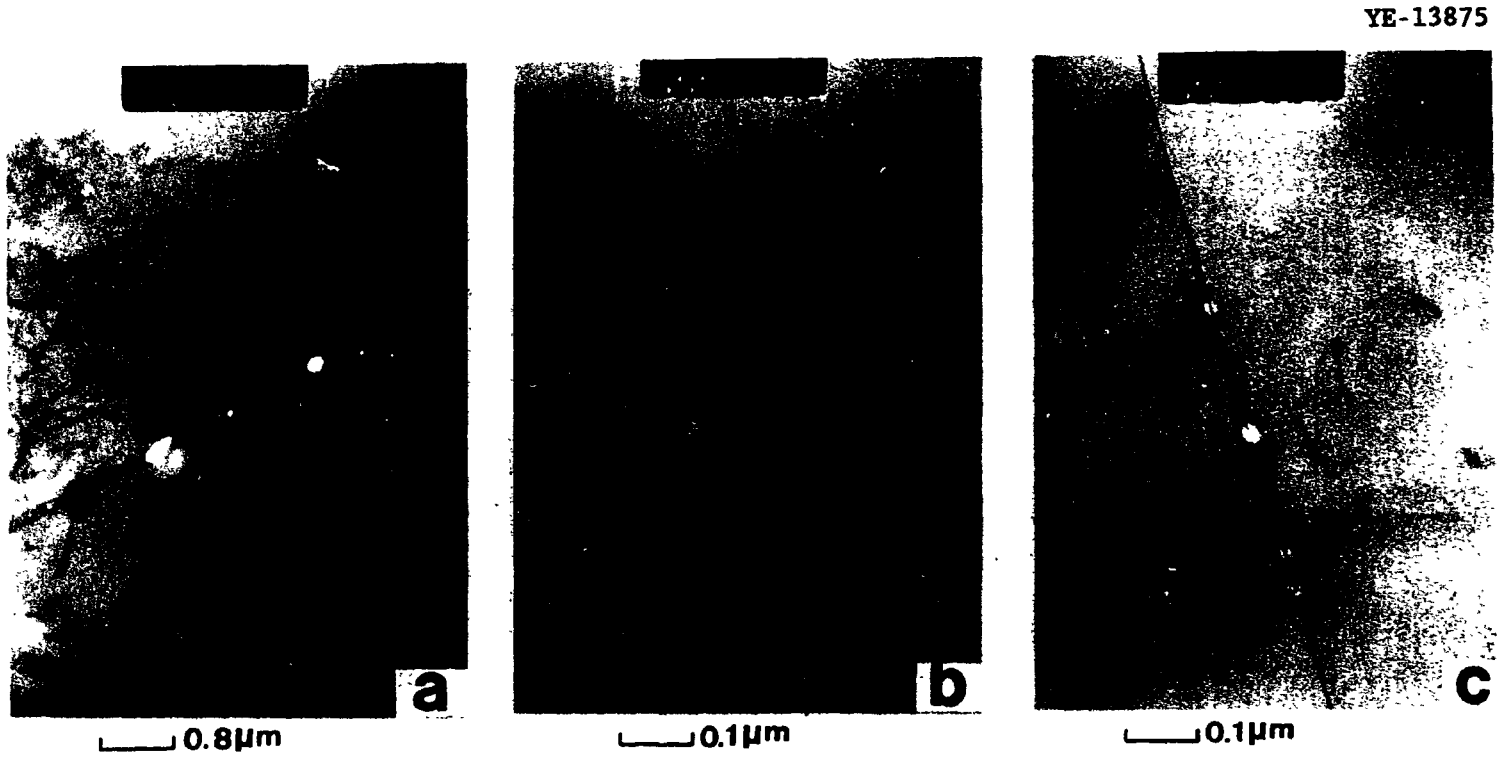

Fig. 73. TEM micrographs of the heat-affected zone of 105 appm butt-joint weld.

YE-13876

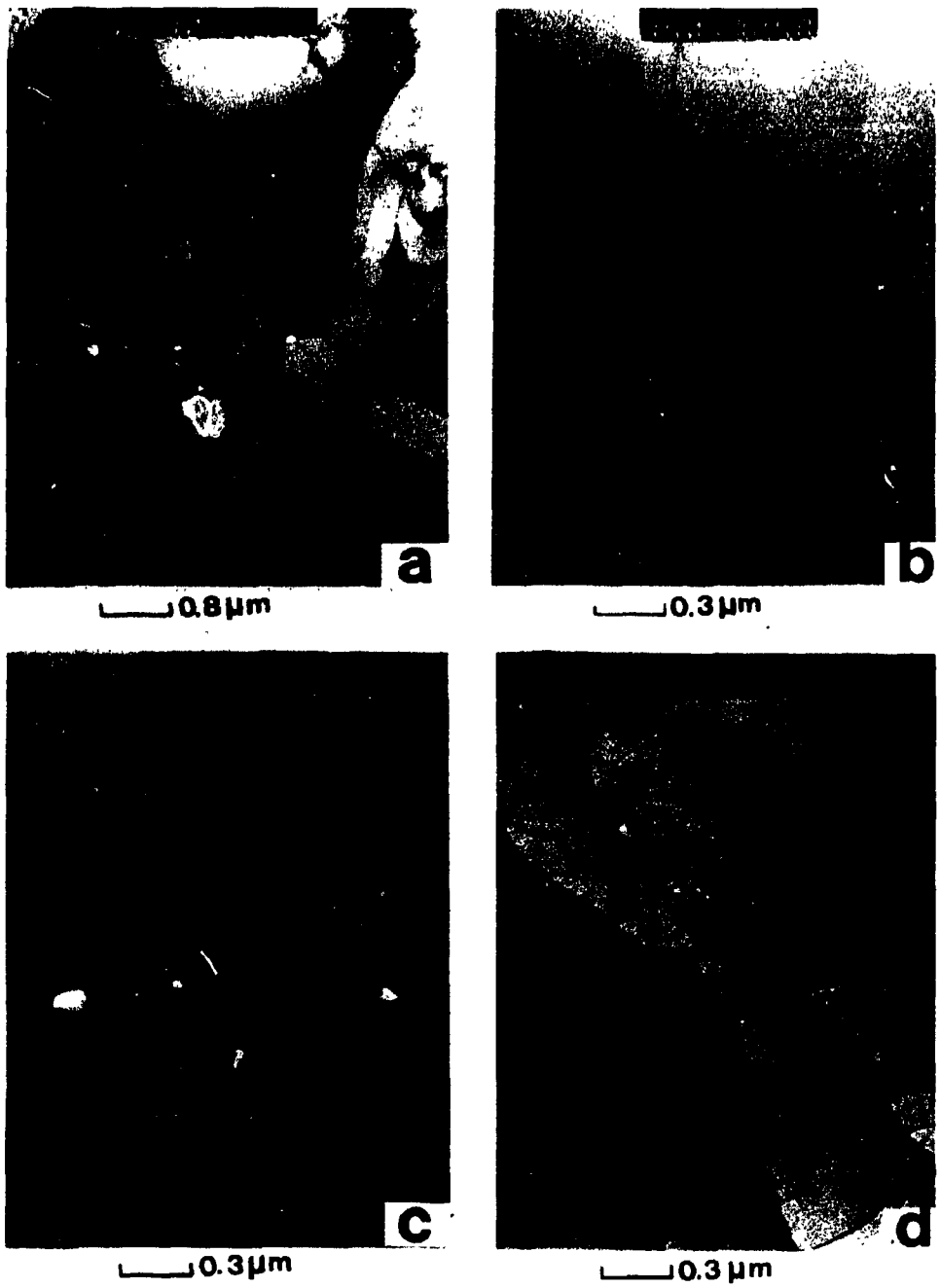

Fig. 74. TEM micrographs of the heat-affected zone of 2.5 appm partial penetration weld.

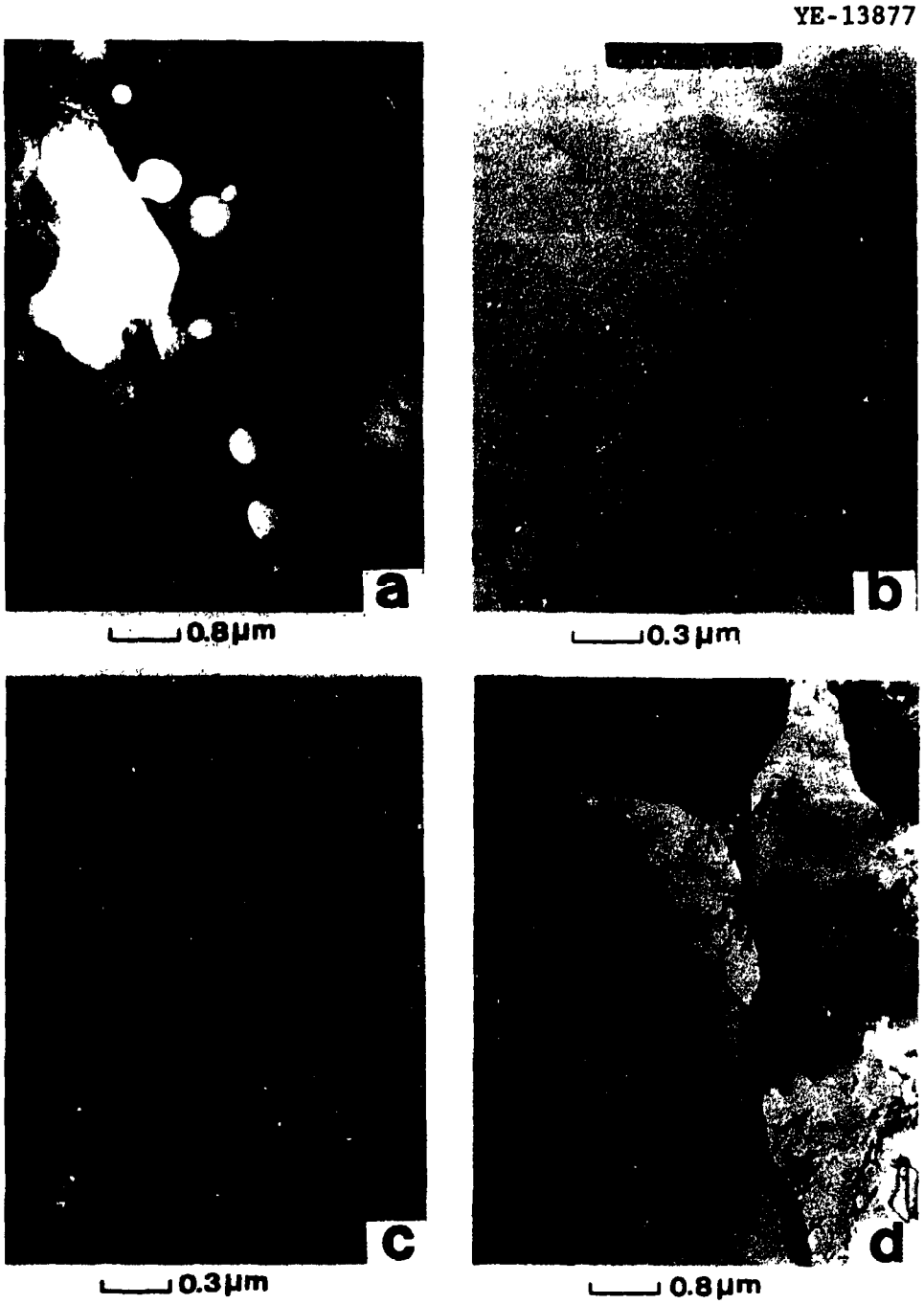

Fig. 75. TEM micrographs of the heat-affected zone of 27 appm partial penetration weld.

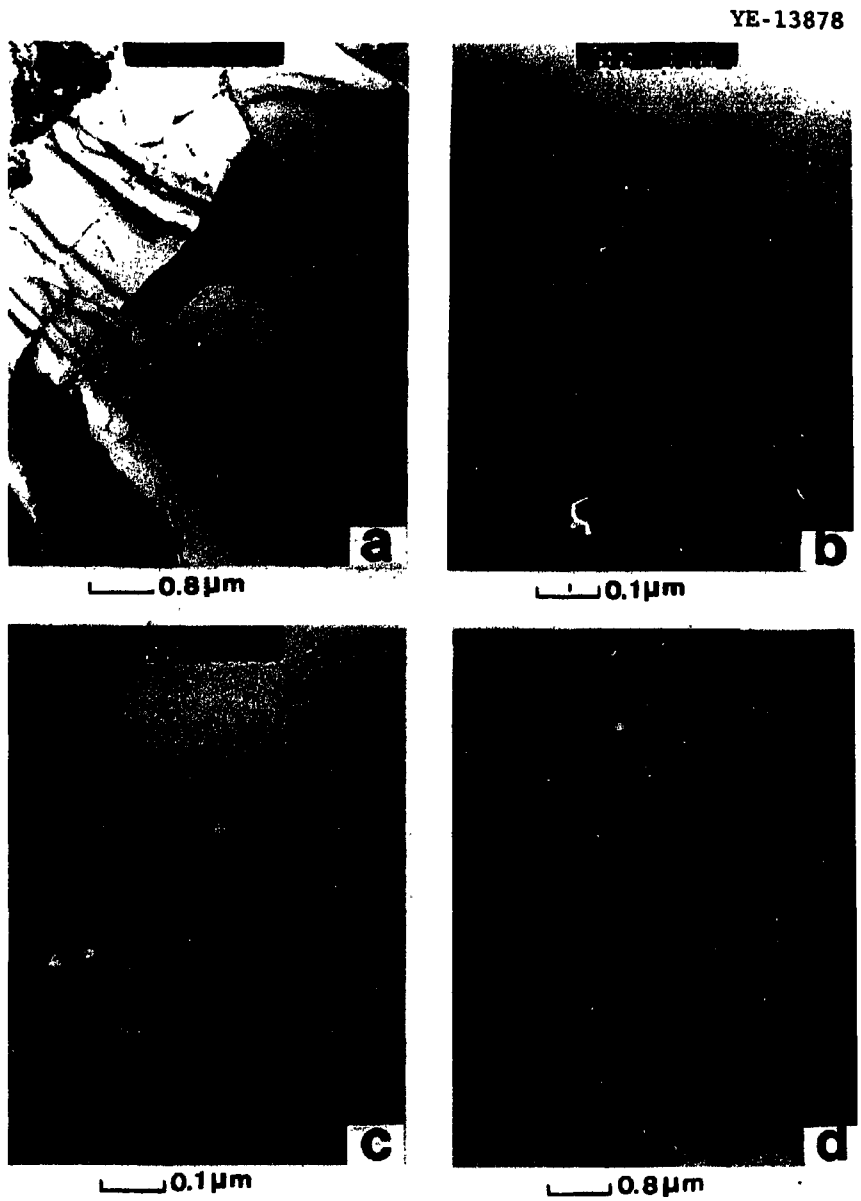

Fig. 76. TEM micrograph of the heat-affected zone of 105 appm partial penetration weld.

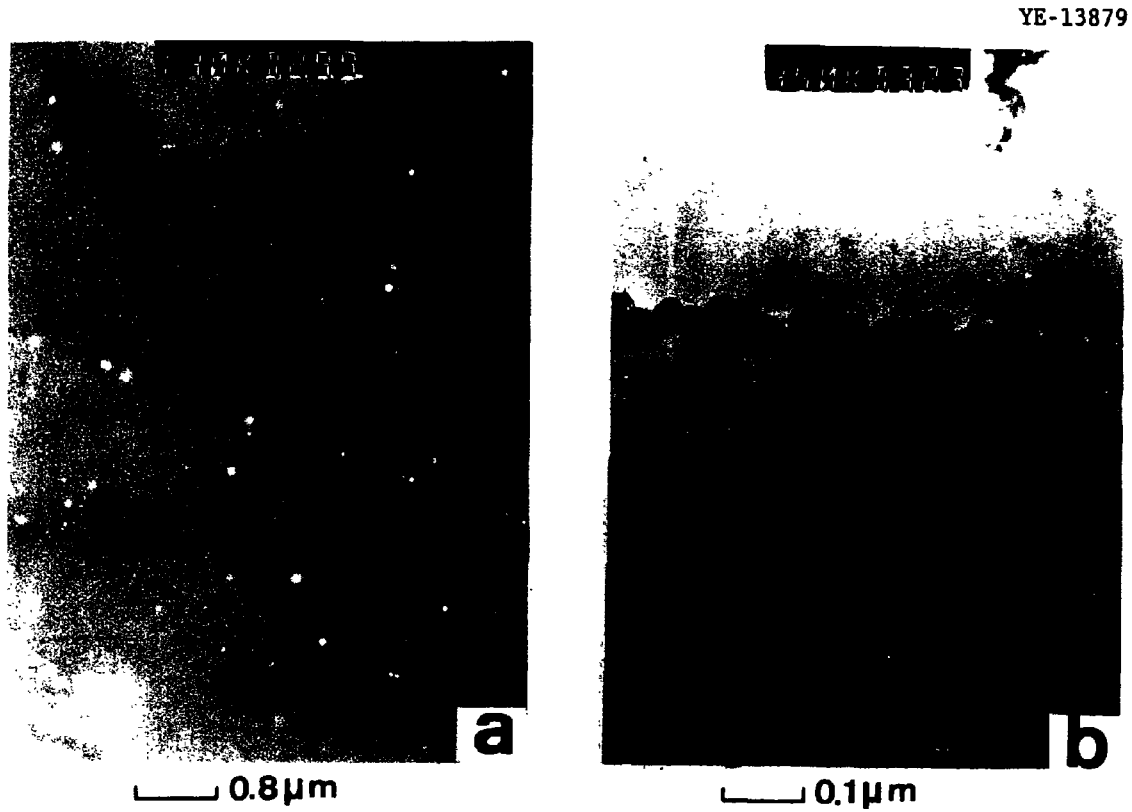

Fig. 77. TEM micrographs of the aged specimens with 256 appm helium. (a) 1050°C, and (b) 800°C.

APPENDIX G

DIMENSION MEASUREMENTS OF TENSILE SPECIMENS

Table 8. Measurements of tensile specimen dimensions of unwelded type 316 stainless steel

Material	Temp (°C)	Thickness (mm)	Width (mm)	Gage Length (mm)
Control	20	0.723	3.185	12.70
	20	0.749	3.188	12.70
	500	0.737	3.185	12.70
	500	0.742	3.180	12.70
	600	0.742	3.170	12.70
	600	0.737	3.175	12.70
	700	0.744	3.175	12.70
	700	0.737	3.175	12.70
0.18 appm	20	0.726	3.176	12.70
	500	0.714	3.179	12.70
	600	0.719	3.177	12.70
	700	0.726	3.181	12.70
2.5 appm	20	0.744	3.180	12.70
	500	0.729	3.178	12.70
	600	0.747	3.175	12.70
	700	0.744	3.176	12.70
27 appm	20	0.752	3.175	12.70
	500	0.744	3.180	12.70
	600	0.744	3.176	12.70
	700	0.747	3.180	12.70
105 appm	20	0.744	3.162	12.70
	500	0.724	3.160	12.70
	600	0.747	3.167	12.70
	700	0.754	3.162	12.70
256 appm	20	0.742	3.162	12.70
	500	0.742	3.175	12.70
	600	0.726	3.175	12.70
	700	0.729	3.178	12.70

Table 9. Measurements of tensile specimen dimensions of welded type 316 stainless steel

Material	Temp (°C)	Thickness (mm)	Width (mm)	Gage Length (mm)
Control	20	0.645	3.200	12.70
	20	0.572	3.200	12.70
	500	0.615	3.202	12.70
	500	0.668	3.208	12.70
	600	0.622	3.211	12.70
	600	0.668	3.208	12.70
	700	0.673	3.213	12.70
	700	0.635	3.203	12.70
0.18 appm	20	0.668	3.211	12.70
	500	0.658	3.216	12.70
	600	0.638	3.208	12.70
	700	0.686	3.211	12.70
2.5 appm	20	0.584	3.200	12.70
27 appm	20	0.671	3.213	12.70
	500	0.653	3.218	12.70
	600	0.625	3.226	12.70
	700	0.625	3.167	12.70
105 appm	20	0.620	3.233	12.70
	500	0.693	3.233	12.70
	600	0.650	3.236	12.70
	700	0.660	3.228	12.70
256 appm	20	0.676	3.190	12.70
	500	0.653	3.190	12.70
	600	0.635	3.193	12.70
	700	0.663	3.191	12.70

Table 10. Measurements of tensile specimen dimensions of HT-9

Material	Temp (°C)	Thickness (mm)	Width (mm)	Gage Length (mm)
		Unwelded		
Control	20	0.742	3.175	12.70
	20	0.744	3.213	12.70
	500	0.744	3.231	12.70
	500	0.734	3.226	12.70
	600	0.739	3.175	12.70
	600	0.732	3.175	12.70
	700	0.744	3.170	12.70
	700	0.729	3.210	12.70
0.3 appm	20	0.734	3.233	12.70
	500	0.734	3.226	12.70
	600	0.724	3.226	12.70
	700	0.742	3.226	12.70
1 appm	20	0.721	3.208	12.70
	500	0.744	3.213	12.70
	600	0.721	3.213	12.70
	700	0.731	3.211	12.70
		Welded		
Control	20	0.711	3.213	12.70
	20	0.630	3.213	12.70
	500	0.696	3.213	12.70
	500	0.676	3.205	12.70
	600	0.632	3.208	12.70
	600	0.711	3.211	12.70
	700	0.688	3.226	12.70
	700	0.625	3.188	12.70
0.3 appm	20	0.681	3.200	12.70
	500	0.701	3.205	12.70
	600	0.714	3.213	12.70
	700	0.699	3.213	12.70
1 appm	20	0.754	3.208	12.70
	500	0.724	3.216	12.70
	600	0.729	3.208	12.70
	700	0.726	3.208	12.70

APPENDIX H

TENSILE PROPERTIES OF TYPE 316 STAINLESS STEEL AND HT-9

Table 11. Tensile test data of unwelded 316 stainless steel

Material	Temp (°C)	UTS (MPa)	YS (MPa)	Elong (%)
Control	20	584.5	231.5	44.1
	20	580.1	223.5	45.2
	500	466.4	123.2	26.0
	500	487.5	124.8	25.2
	600	458.3	103.7	26.8
	600	447.0	104.6	27.2
	700	357.0	98.5	23.7
	700	340.3	99.1	21.0
0.18 appm	20	588.2	231.4	41.9
	500	480.9	127.6	29.0
	600	454.1	111.1	27.9
	700	322.1	96.4	17.6
2.5 appm	20	595.0	232.3	41.8
	500	480.0	121.1	27.2
	600	450.3	140.7	25.7
	700	335.1	103.5	16.9
27 appm	20	549.7	190.1	37.8
	500	481.2	141.0	25.0
	600	458.3	117.4	25.1
	700	372.7	123.0	15.9
105 appm	20	583.0	244.5	39.8
	500	494.0	149.0	27.1
	600	456.1	121.0	26.1
	700	328.4	126.4	11.3
256 appm	20	601.2	250.4	44.1
	500	476.0	155.0	27.6
	600	462.9	144.7	25.6
	700	340.2	144.1	10.1

Table 12. Tensile test data of welded 316 stainless steel

Material	Temp (°C)	UTS (MPa)	YS (MPa)	Elong (%)
Control[a]	20	560.2	351.2	17.8
	20	569.1	347.8	18.5
	500	387.5	244.2	7.2
	500	408.9	232.5	10.3
	600	369.7	222.3	6.0
	600	357.3	211.0	8.1
	700	325.0	197.5	7.7
	700	291.0	175.0	9.1
0.18 appm[a]	20	518.5	358.1	10.4
	500	370.1	241.8	8.1
	600	361.0	224.0	8.6
	700	262.0	198.0	3.2
2.5 appm[b]	20	428.3	356.9	2.9
27 appm[b]	20	386.0	386.0	0.2
	500	296.4	266.8	0.6
	600	262.8	227.6	1.2
	700	200.0	191.0	0.3
105 appm[b]	20[a]	404.0	373.0	1.5
	500	261.9	253.9	1.4
	600	253.1	244.1	0.6
	700	199.6	191.5	1.2
256 appm[b]	20	247.6	247.6	1.1
	500	153.8	153.8	0.7
	600[a]	186.5	186.5	1.7
	700[a]	137.9	137.9	1.5

[a]Specimens Failed in the Fusion Zone.
[b]Specimens Failed at the Fusion Boundary.

Table 13. Tensile test data of HT-9 steel

Material	Temp (°C)	UTS (MF	YS (MPa)	Elong (%)
		Unw		
Control	20	1001.4	835.0	4.7
	20	1013.8	866.9	5.4
	500	869.5	777.0	3.0
	500	845.3	760.8	3.2
	600	654.0	616.0	7.4
	600	670.3	622.4	7.0
	700	425.5	414.2	10.5
	700	447.8	422.8	12.2
0.3 appm	20	1034.5	903.3	6.1
	500	760.8	695.1	4.5
	600	653.4	604.0	5.5
	700	409.0	399.7	9.1
1 appm	20	1038.0	893.8	5.1
	500	855.6	744.1	5.0
	600	702.4	681.3	6.6
	700	426.2	416.7	10.6
		Welded		
Control[a]	20	983.0	895.4	5.5
	20[b]	965.3	890.1	0.7
	500	815.6	765.8	4.2
	500	739.4	708.6	1.8
	600	756.4	701.6	3.4
	600	713.0	676.0	3.8
	700	418.2	408.2	7.2
	700	475.7	464.5	6.2
0.3 appm[a]	20[b]	961.0	827.0	0.3
	500	795.7	736.4	1.6
	600	688.6	633.4	3.9
	700	372.6	356.8	8.7
1 appm[a]	20	992.6	882.3	3.1
	500	812.1	764.4	2.6
	600	696.2	675.2	5.3
	700	410.4	400.8	8.0

[a]Specimens Failed in the Base Metal.
[b]Specimens Failed in the HAZ.

APPENDIX I

FRACTURE SURFACE CHARACTERIZATION OF TENSILE SPECIMENS

This appendix provides information on the deformation and fracture characteristics, as a function of test temperature, for helium containing welded and unwelded specimens of type 316 stainless steel and HT-9. This work was performed using scanning electron microscopy. Figure 78 shows the macroscopic fracture features of control and helium-doped type 316 stainless steel (256 appm) tested at 25 and 700°C respectively. The macroscopic fracture features of specimens containing 0.18, 2.5, 27 and 105 appm helium tested at 700°C are also given in Figure 79. Observations in the gage section indicated that all of the control specimens tested at temperatures between 25 and 700°C revealed necking in the gage section. For the unwelded helium-doped specimens, the gage section also showed necking for temperatures of 600°C and below. No necking occurred at 700°C, implying a transition in fracture mode. The features of control specimens tested at 700°C showed microcracks at grain junctions (Figure 78b). These microcracks near the fracture region were attributed to separation of grains by shear stresses along the shear plane. The macroscopic fracture features of unwelded helium-doped specimens tested at 700°C revealed surface intergranular microcracks (Figures 78d and 79). The orientation of these microcracks is perpendicular to the tensile axis. In addition, the number of intergranular microcracks tended to increase with increasing helium concentration. It was interesting to note that specimens containing helium as low as 0.18 appm exhibited a tendency for high-temperature helium embrittlement. Consequently, Figure 80 shows the fracture

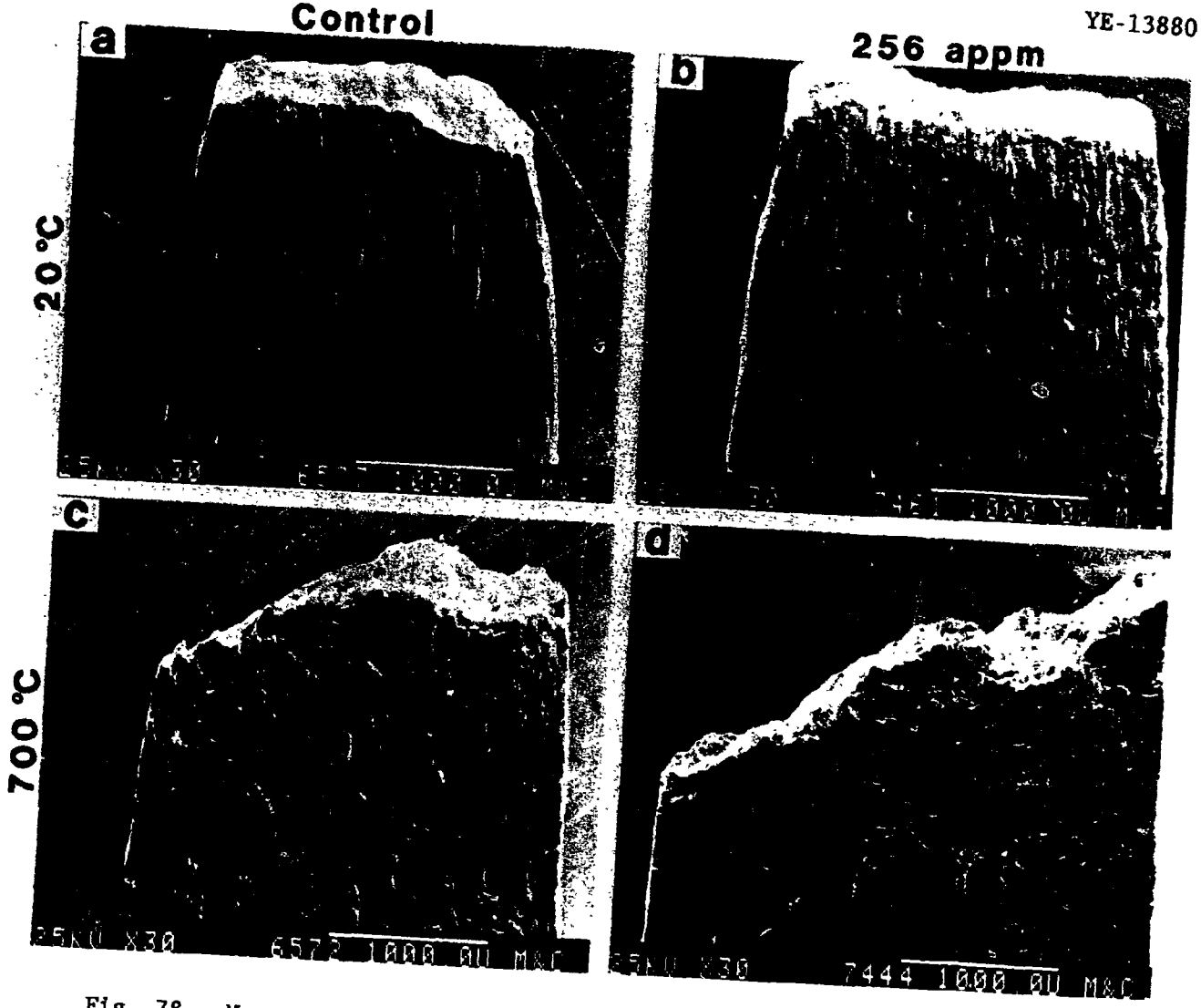

Fig. 78. Macroscopic fracture features of type 316 stainless steel.

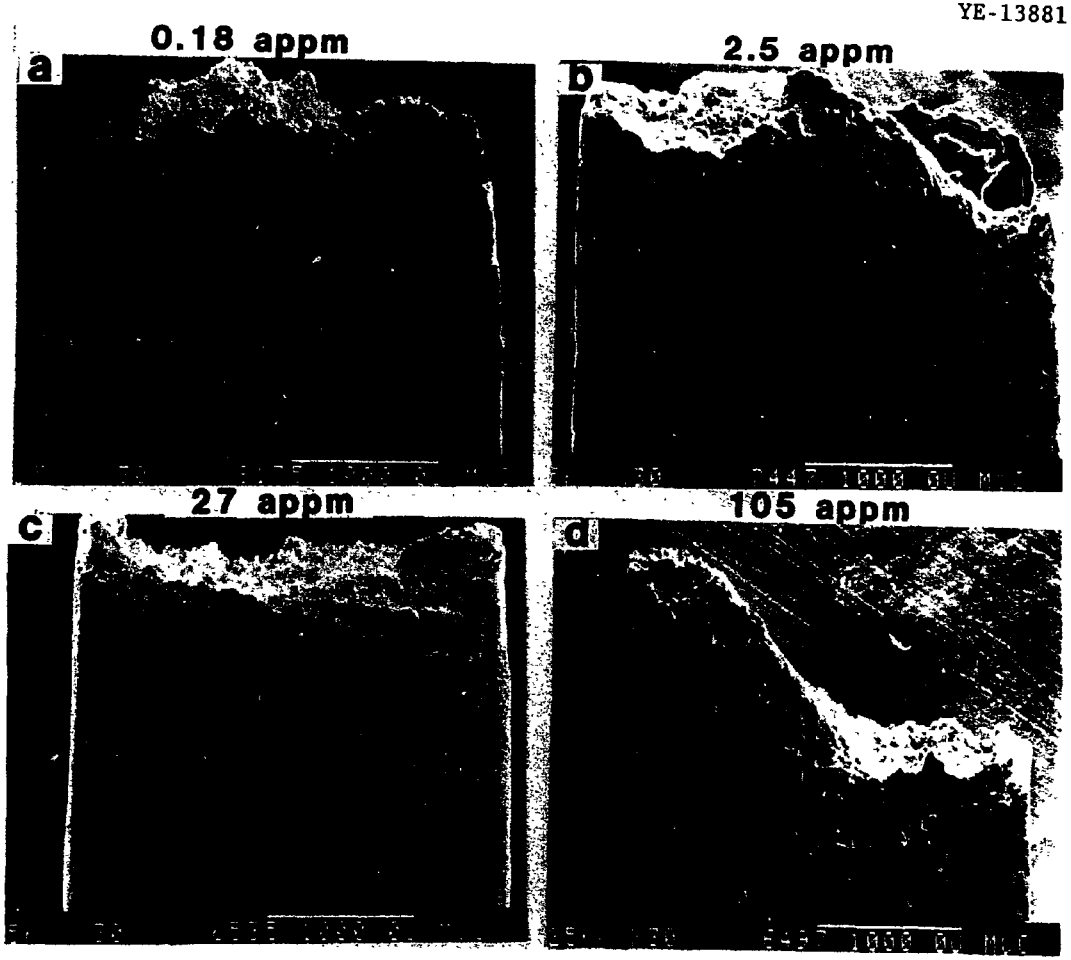

Fig. 79. Macroscopic fracture features of helium-doped type 316 stainless steel tested at 700°C.

surfaces of the material shown in Figure 78. The control specimens showed transgranular dimple rupture at all test temperatures. Unwelded helium-doped specimens showed transgranular dimple rupture at 600°C and below. Mixed mode features, intergranular and transgranular fracture, were seen at 700°C. Observations of fractography of helium-doped specimens tested at 700°C indicated that the degree of intergranular fracture increased with increasing helium content (Figure 81). In addition, the grain facets were feature less as opposed to those observed on the welded material HAZ fracture surfaces which were decorated with a uniform distribution of dimples. Surface diffusion of helium bubbles along the grain boundaries occurs rapidly at these high temperatures resulting in feature less grain facets. The fracture surface features of welded helium containing type 316 stainless steel have been discussed in Chapter IV.

Figure 82 shows the fractography of the unwelded, control and helium-doped, HT-9 tested at temperatures of 20 and 700°C. Generally, all materials tested revealed transgranular dimple rupture along lath boundaries at these test temperatures. The size of the dimples tended to increase with increasing test temperatures. This was consistent with total elongation measurements (Figure 44). The fracture surface features of welded control and helium-doped materials which were tested at 20 and 700°C are shown in Figure 83. All welded materials failed in a fashion of transgranular dimple rupture at these test temperatures, except for the welded specimen with 0.3 appm helium. This specimen when tested at room temperature failed predominantly by

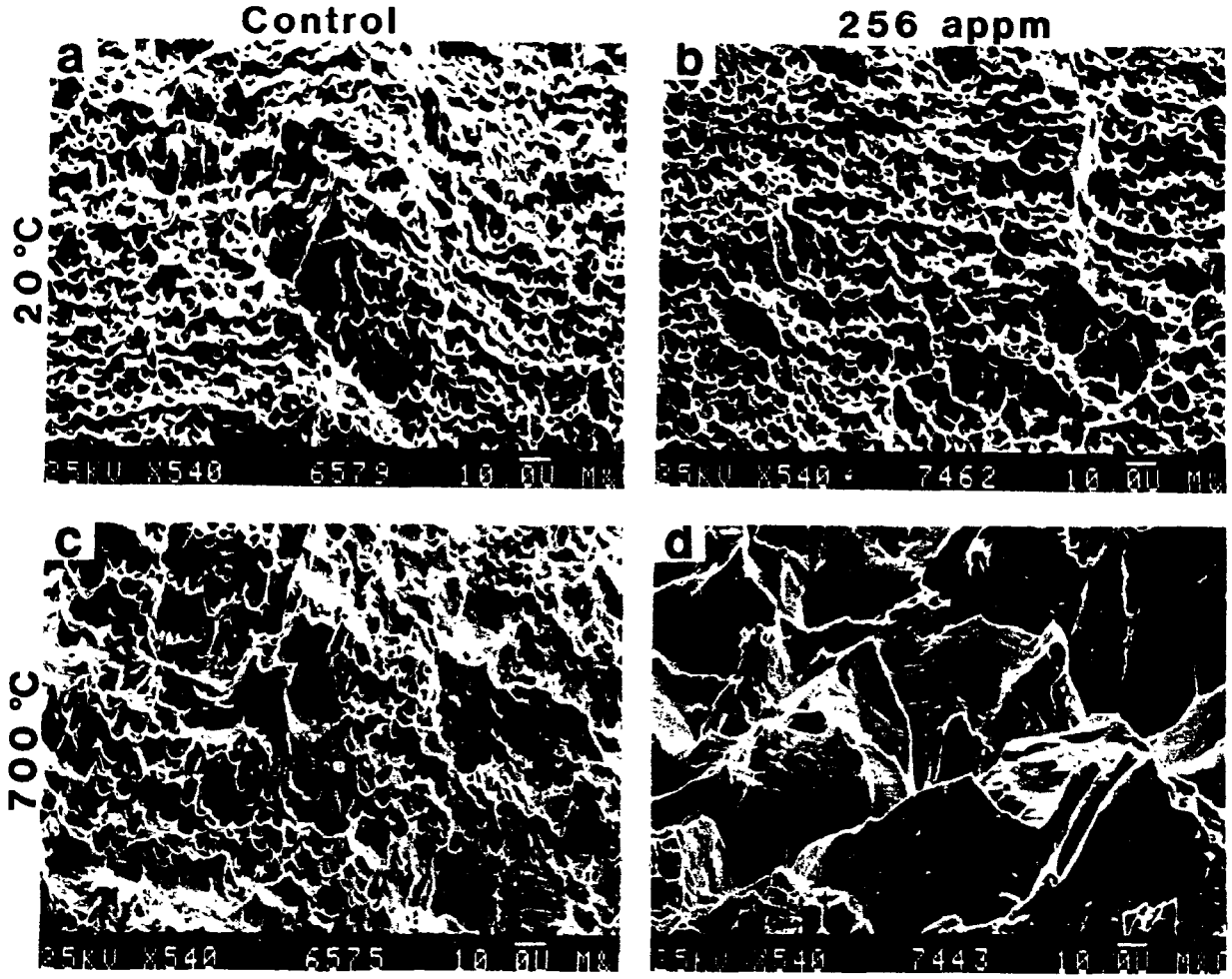

Fig. 80. Microscopic fracture surface features of type 316 stainless steel.

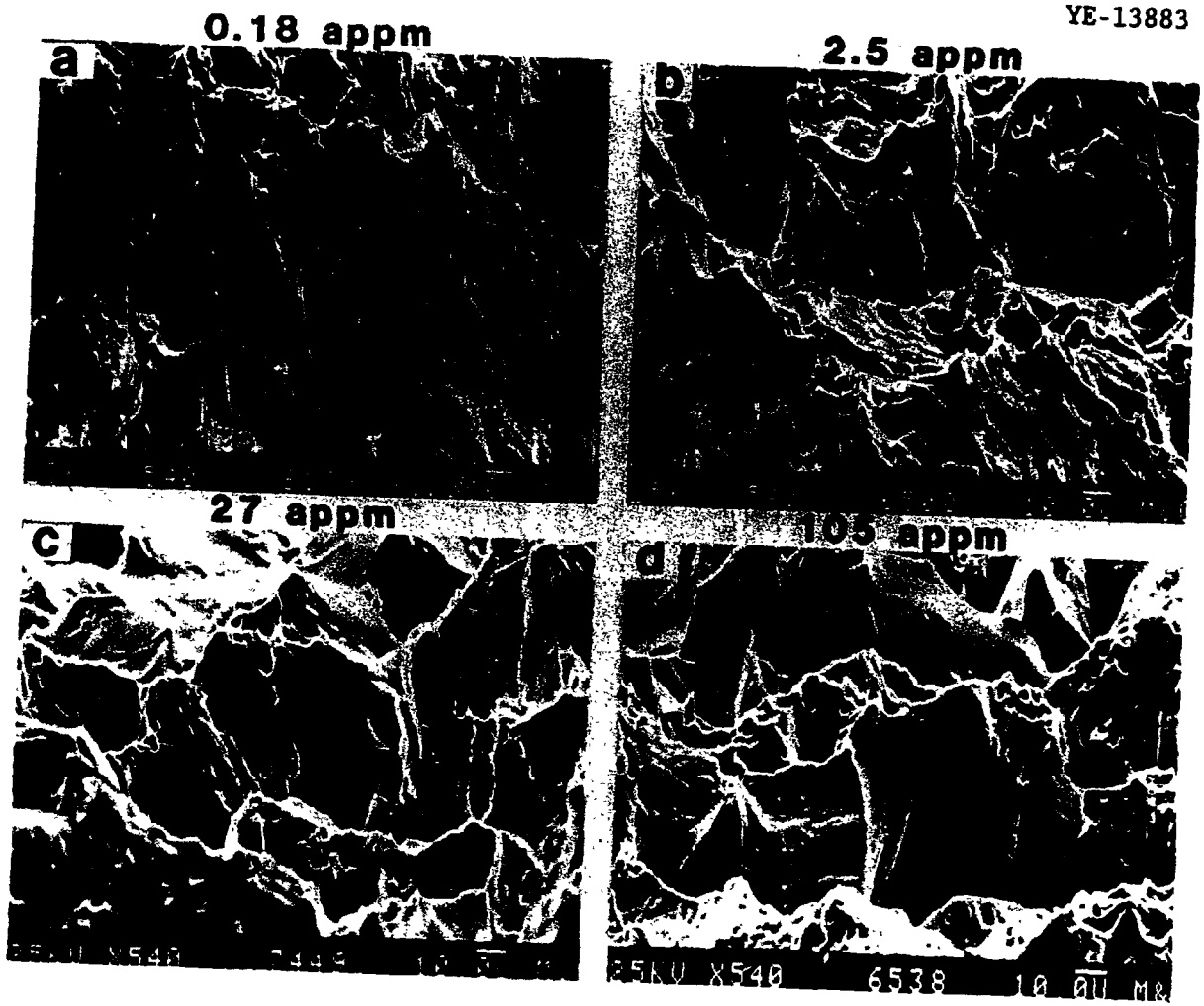

Fig. 81. Microscopic fracture surface features of helium-doped type 316 stainless steel tested at 700°C.

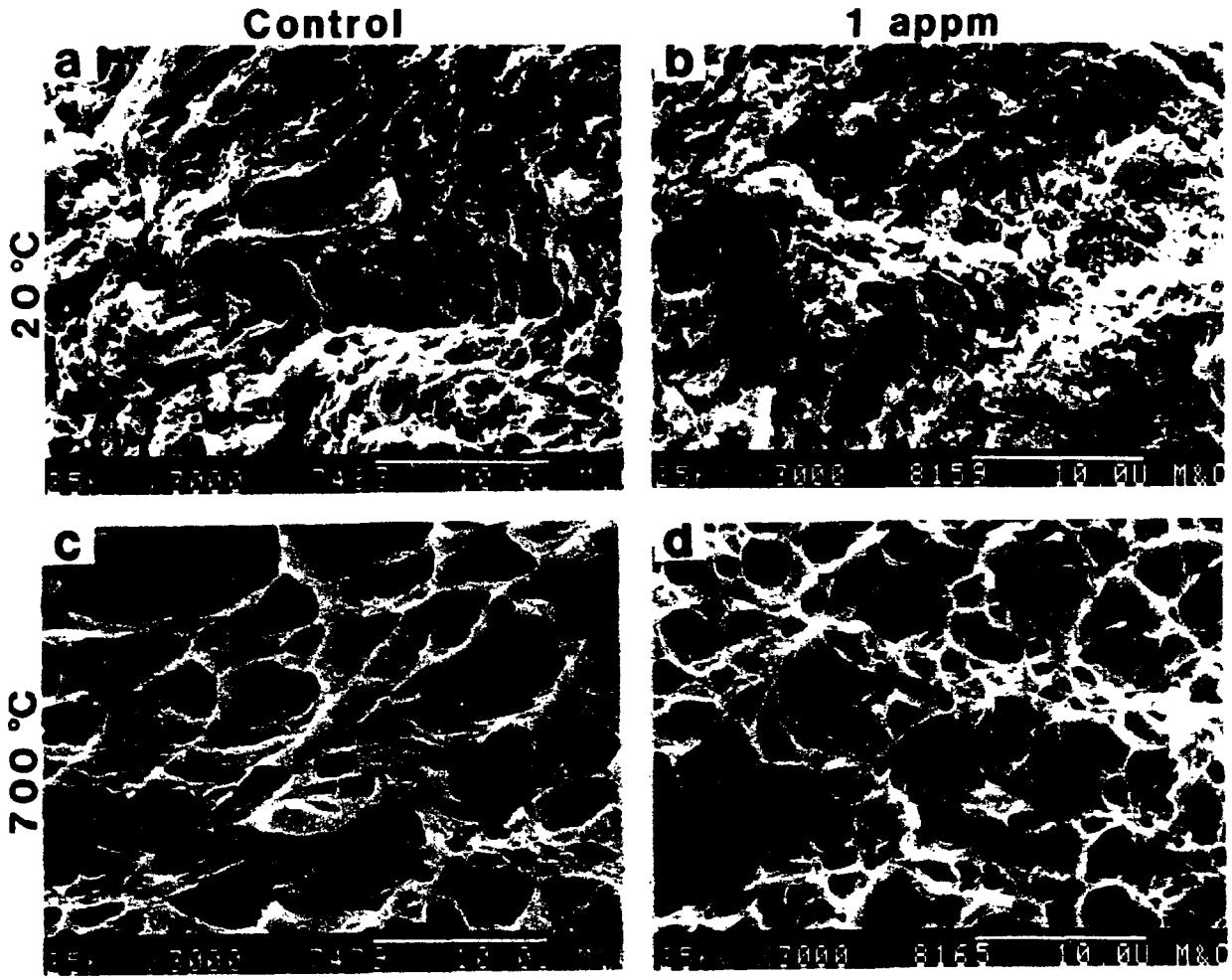

Fig. 82. Microscopic fracture surface features of unwelded HT-9.

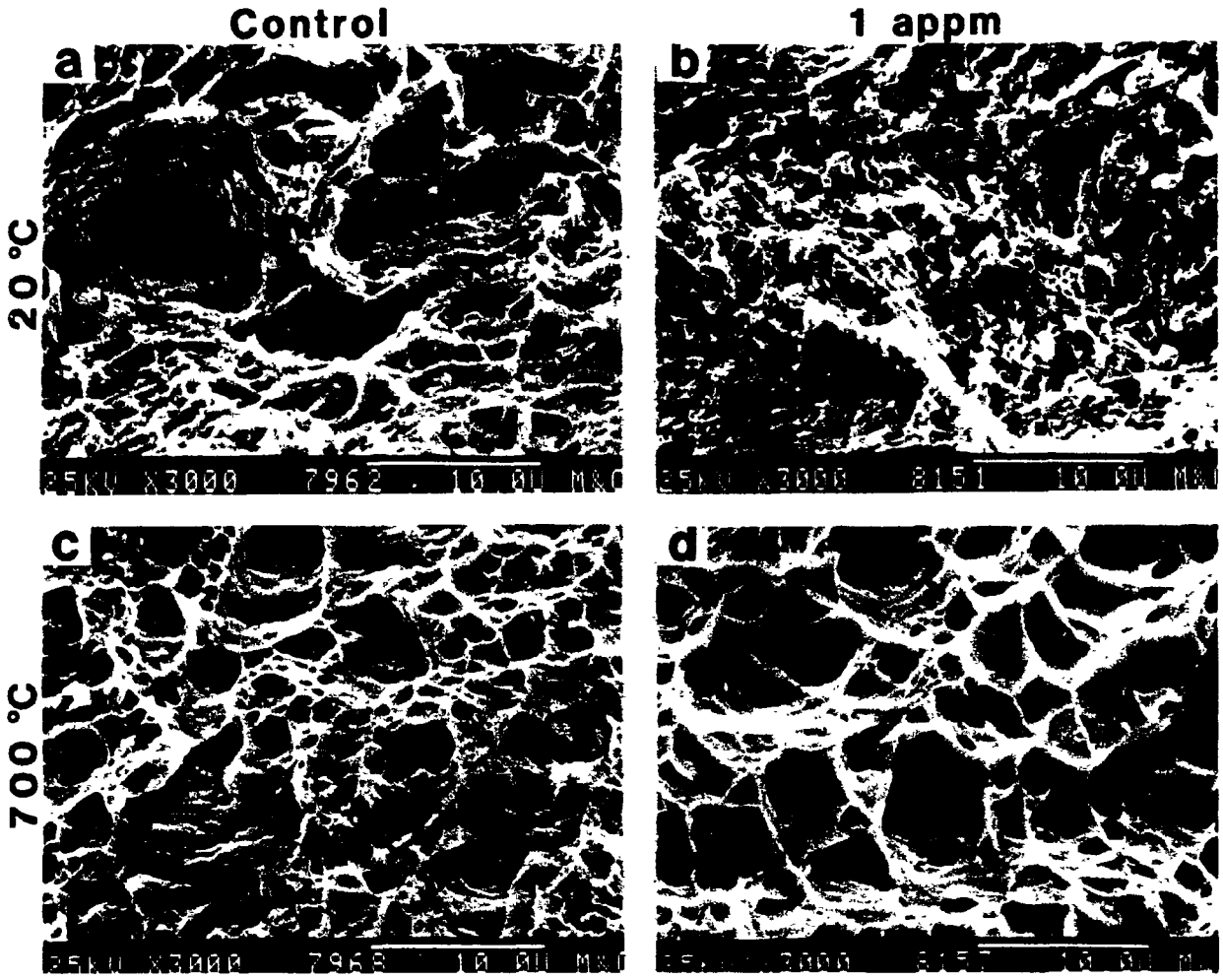

Fig. 83. Microscopic fracture surface features of welded HT-9.

brittle (cleavage) fracture. The 0.3 appm welds failed at the HAZ in which untempered martensite was present leading to brittle fracture. In spite of the brittle fracture in the HAZ, tensile results and fracture characteristics of 0.3 appm welds from uncracked regions still showed the same behavior as that of control welds.

APPENDIX J

COMPUTER PROGRAM FOR CALCULATION OF HELIUM BUBBLE GROWTH IN THE HEAT-AFFECTED ZONE

This appendix details a computer program for calculation of GB bubble size as a function of time in the HAZ during regime III. This program consists of four subprograms: Title-Input, Function-1, Print-Data and Plot-Data. In the Title-Input subprogram, titles for x and y axes and the legend for the plot, as shown in Figures 48 and 49, are designated. The Function-1 subprogram is the routine which calculates the bubble size as a function of time for a specific peak temperature. In this routine, the initial bubble size of regime III (final bubble size after regime II) needs to be specified. Also, the peak temperature (Tmax) in the Rosenthal equation (equation (17)) needs to be changed for each desired peak temperature. The Print-Data subprogram prints out bubble size, shrinkage stress, and temperature as a function of time. The Plot-Data subprogram plots the bubble size as a function of cooling time, as shown in Figures 48 and 49. An HP 9122 computer, HP 7470A plotter and HP thinjet printer (manufactured by Hewlett-Packard Company, Fort Collins, CO) were used to operate this computer program.

```
10 !  CALCULATION OF GRAIN BOUNDARY HELIUM BUBBLE SIZE AS A FUNCTION OF TIME
      IN THE HAZ DURING REGIME III.
20    COM /Aa/ X(1:1000),Y(1:1000),D(1:1000),T(1:1000),INTEGER N
30    COM /Aa/ Dr(1:1000),E(1:1000),C(1:1000),A(1:1000),B(1:1000)
40    COM /Aa/ S(1:1000)
50    COM /Bb/ X$[40],Y$[40],Title$[40],Text$[40]
60    DIM R$[70],D$[40],A$[40]
70    GRAPHICS OFF
80 Function_data:          ! *** Input data from FUNCTION ***
90    OFF KEY
100   Title_input
110   Func_1
120   GOTO Print_data
130 Print_data:    R1$="N"
140   Prompt_alpha("OUTPUT data to PRINTER ?? <y> or <n>",R1$)
150   IF R1$<>"N" THEN
160   PRINTER IS 701
170   Print_out
180   PRINTER IS 1
190   END IF
200   GOTO Plot_data
210 Plot_data:                          ! *** plot ***
220   R$="Y"
230   Prompt_alpha("Do you want to plot these data?? <Y> or <N>",R$)
240   IF R$="Y" OR R$="y" THEN
250   Plot
260   END IF
270   END
280 Plot:SUB Plot
290   COM /Aa/ X(1:1000),Y(1:1000),T(1:1000),D(1:1000),INTEGER N
300   COM /Aa/ Dr(1:1000),E(1:1000),C(1:1000),A(1:1000),B(1:1000)
310   COM /Aa/ S(1:1000)
320   COM /Bb/ X$[40],Y$[40],Title$[40],Text$[40]
330     INTEGER I,Xlog,Ylog,Axis,Xtic_num,Ytic_num,P1x,P1y,P2x,P2y,Crt,Pc,Xn,Yn
340     INTEGER Connect,Lineno
350     DIM Ques$[70],Ans$[70],Temp$[70]
360     GINIT
370     PRINT CHR$(12);TABXY(28,11);"Now in subprogram XYPlot.";TABXY(1,18);
380     Stopped=0                       ! Did user stop plot early?
390     Axis=0                          ! Axis type must be chosen.
400 New_plot:   ALPHA ON                !
410     GRAPHICS OFF
420     PLOTTER IS 3,"INTERNAL"
430     GOSUB Connect_pts               ! Symbol type? & connect points?
440     GOSUB Axes_types                ! LINEAR or LOG axes types.
450     GOSUB Plot_limits               ! min, max, & tick values.
460     GOSUB Plot_the_data
470     IF Stopped THEN Plot_prompt
480     GOSUB Plot_the_axes
490     IF Stopped THEN Plot_prompt
500     GOSUB Plot_the_text
510     BEEP
520     IF Crt THEN PAUSE               ! pause to view CRT graphics.
530     GRAPHICS OFF
540 Plot_prompt: GOTO Re_plot           ! Plot this data again?
550     SUBEXIT                         ! return to calling routine.
560 Connect_pts:Connect=1
570     Ans$="Y"
580     Ques$="Do you want to connect the points with a straight line?"
590     Prompt_alpha(Ques$,Ans$)
```

```
600     IF Ans$<>"Y" THEN
610       Connect=0
620       Sym$=" "
630       Ques$="What symbol should be used to plot the points?"
640       Prompt_alpha(Ques$,Sym$)
650     END IF
660     RETURN
670 Axes_types:ON KEY 0 LABEL "X LIN:Y LIN" GOTO Lin_lin
680     ON KEY 1 LABEL "X LOG:Y LIN" GOTO Log_lin
690     ON KEY 2 LABEL "X LIN:Y LOG" GOTO Lin_log
700     ON KEY 3 LABEL "X LOG:Y LOG" GOTO Log_log
710     GCLEAR
720     DISP "CHOOSE AN AXIS TYPE."
730     GOTO 730
740 Lin_lin:OFF KEY
750     IF Axis=1 THEN
760       New_axis_type=0
770     ELSE
780       New_axis_type=1
790       Axis=1
800       Xlog=0
810       Ylog=0
820     END IF
830     RETURN
840 Log_lin: OFF KEY
850     IF Axis=2 THEN
860       New_axis_type=0
870     ELSE
880       New_axis_type=1
890       Axis=2
900       Xlog=1
910       Ylog=0
920     END IF
930     RETURN
940 Lin_log:OFF KEY
950     IF Axis=3 THEN
960       New_axis_type=0
970     ELSE
980       New_axis_type=1
990       Axis=3
1000      Xlog=0
1010      Ylog=1
1020    END IF
1030    RETURN
1040 Log_log:OFF KEY
1050    IF Axis=4 THEN
1060      New_axis_type=0
1070    ELSE
1080      New_axis_type=1
1090      Axis=4
1100      Xlog=1
1110      Ylog=1
1120    END IF
1130    RETURN
1140 Plot_limits:IF NOT (New_axis_type) THEN Limits
1150    Xmin=X(1)
1160    Xmax=Xmin
1170    Ymin=Y(1)
1180    Ymax=Ymin
1190    FOR I=1 TO N
```

```
1200          !       Find Min & Max values.
1210      IF X(I)<Xmin THEN Xmin=X(I)
1220      IF X(I)>Xmax THEN Xmax=X(I)
1230      IF Y(I)<Ymin THEN Ymin=Y(I)
1240      IF Y(I)>Ymax THEN Ymax=Y(I)
1250    NEXT I
1260                                        ! Trap out LOG(-#) values.
1270    IF (Xlog AND (Xmin<=0)) THEN
1280      DISP "Negative value(s) of X.  LOG undefined."
1290      BEEP 250,.3
1300      WAIT 3
1310      GOTO Plot_prompt
1320    END IF
1330    IF (Ylog AND (Ymin<=0)) THEN
1340      DISP "Negative value(s) of Y.  LOG undefined."
1350      BEEP 300,.3
1360      WAIT 3
1370      GOTO Plot_prompt
1380    END IF
1390                                        ! Default tick values.
1400    IF NOT Xlog THEN                    ! LINEAR scale.
1410      Xtic_num=4                        ! # of major ticks.
1420      Xn=4                              ! Minor Ticks/major.
1430      Xm=.08*(Xmax-Xmin)
1440      Xmin=Xmin-Xm
1450      Xmax=Xmax+Xm
1460      Xtic=DROUND((Xmax-Xmin)/20,1)  ! divide into 20 units
1470      PRINT " XMIN=";Xmin," XMAX=";Xmax," XTIC=";Xtic
1480      Xaxmin=Xtic*INT(Xmin/Xtic)
1490      Xaxmax=Xtic*INT((Xmax/Xtic)+1)
1500    ELSE                                ! LOG scale.
1510      Xaxmin=.7*Xmin
1520      Xaxmax=1.4*Xmax
1530      Xtic_num=1
1540    END IF
1550    IF NOT Ylog THEN                    ! LINEAR scale
1560      Ytic_num=4                        ! # of major ticks.
1570      Yn=4                              ! Minor/Major ticks.
1580      Ym=.08*(Ymax-Ymin)
1590      Ymin=Ymin-Ym
1600      Ymax=Ymax+Ym
1610      Ytic=DROUND((Ymax-Ymin)/20,1)!divide into 20 units
1620      PRINT " YMIN=";Ymin," YMAX=";Ymax," YTIC=";Ytic
1630      Yaxmin=Ytic*INT(Ymin/Ytic)
1640      Yaxmax=Ytic*INT((Ymax/Ytic)+1)
1650    ELSE                                ! LOG scale
1660      Yaxmin=.7*Ymin
1670      Yaxmax=1.4*Ymax
1680      Ytic_num=1
1690    END IF
1700 Limits:PRINTER IS 1
1710    PRINT "Plot Limits are:"
1720    IMAGE A," Min : ",9D.7D,4X,A," Max : ",9D.7D
1730    PRINT USING 1720;"X",Xaxmin,"X",Xaxmax
1740    PRINT USING 1720;"Y",Yaxmin,"Y",Yaxmax
1750    IF NOT Xlog THEN PRINT "X Tic : ",Xtic
1760    IF NOT Ylog THEN PRINT "Y Tic : ",Ytic
1770    Ans$="N"
1780    Prompt_alpha("Change the plotting limits? (Y or N)",Ans$)
1790    IF Ans$="N" THEN GOTO Borders
```

```
1800 Lim_changes:Prompt_num("X axis min?",Xaxmin)
1810    Prompt_num("X axis max?",Xaxmax)
1820    Prompt_num("Y axis min?",Yaxmin)
1830    Prompt_num("Y axis max?",Yaxmax)
1840    IF NOT Xlog THEN
1850      Prompt_num("X axis tic?",Xtic)
1860      Xtic_num=INT((Xaxmax-Xaxmin)/Xtic)
1870      Xn=1
1880    END IF
1890    IF NOT Ylog THEN
1900      Prompt_num("Y axis tic?",Ytic)
1910      Ytic_num=INT((Yaxmax-Yaxmin)/Ytic)
1920      Yn=1
1930    END IF
1940    GOTO Limits
1950 Borders:      ! Q1& Q2 are Page Borders,  R1 & R2 are Plot Borders.
1960    IF Xlog THEN
1970      R1x=LGT(Xaxmin)
1980      R2x=LGT(Xaxmax)
1990    ELSE
2000      R1x=Xaxmin
2010      R2x=Xaxmax
2020    END IF
2030    IF Ylog THEN
2040      R1y=LGT(Yaxmin)
2050      R2y=LGT(Yaxmax)
2060    ELSE
2070      R1y=Yaxmin
2080      R2y=Yaxmax
2090    END IF
2100    Q1x=R1x-.2*(R2x-R1x)
2110    Q1y=R1y-.2*(R2y-R1y)
2120    Q2x=R2x+.1*(R2x-R1x)
2130    Q2y=R2y+.2*(R2y-R1y)
2140    RETURN
2150 Plot_dest:DISP "Where do you want the plot to go?"
2160    ON KEY 0 LABEL "     CRT" GOTO Crt_plot
2170    ON KEY 1 LABEL " X-Y Plotter" GOTO Xy_plot
2180    GOTO 2180
2190 Crt_plot:OFF KEY                    ! CRT graphics.
2200    Crt=1
2210    RETURN
2220 Xy_plot:OFF KEY                     !  HP 9872C X-Y Plotter.
2230    Crt=0
2240    PRINT "  SET P1 & P2 OF PLOTTER THEN <CONT>"
2250    PAUSE
2260    PLOTTER IS 705,"HPGL"            ! 40 plotter units/mm
2270    OUTPUT 705;"DF;OP"               ! find P1 & P2 of plotter.
2280    ENTER 705;P1x,P1y,P2x,P2y
2290    IF P1x=520 AND P1y=380 AND P2x=15720 AND P2y=10380 THEN
2300      OUTPUT 705;"IP";1000,500,10000,7500   ! Set P1 & P2 for 8.5" x 11"
2310      DISP "Paper size has been set for 8.5 x 11 HORIZONTAL Plot."
2320      BEEP 1500,.5
2330      WAIT 2
2340      GOTO 2260
2350    END IF
2360    RETURN
2370 Plot_the_axes:OFF KEY
2380    ON KEY 9 LABEL "Stop Plot" GOTO Stop_axes
2390    PEN 4
```

```
2400    LINE TYPE 1
2410    SELECT Axis
2420    CASE 1
2430      AXES Xtic,Ytic,R1x,R1y,Xtic_num,Ytic_num
2440    CASE 2
2450      AXES (R2x-R1x),Ytic,R1x,R1y,1,Ytic_num
2460      GOSUB Tick_xlog
2470    CASE 3
2480      AXES Xtic,(R2y-R1y),R1x,R1y,Xtic_num,1
2490      GOSUB Tick_ylog
2500    CASE 4
2510      GOSUB Tick_xlog
2520      GOSUB Tick_ylog
2530    END SELECT
2540    PEN 1
2550    FRAME
2560    LDIR 0
2570    PEN 4
2580    CSIZE 2
2590    LORG 6
2600    CSIZE 3
2610    IF NOT Xlog THEN
2620      CLIP OFF
2630      FOR I=0 TO 20
2640        L=R1x+DROUND(I*Xtic*Xn,2)
2650        IF L>R2x THEN 2690
2660        MOVE L,R1y-.005*(R2y-R1y)
2670        LABEL L
2680      NEXT I
2690      CLIP ON
2700    END IF
2710    IF NOT Ylog THEN
2720      CLIP OFF
2730      LORG 8
2740      FOR I=0 TO 20
2750        L=R1y+DROUND(I*Ytic*Yn,2)
2760        IF L>R2y THEN 2800
2770        MOVE R1x-.005*(R2x-R1x),L
2780        LABEL L
2790      NEXT I
2800      CLIP ON
2810    END IF
2820    RETURN
2830 Stop_axes:Stopped=1
2840    PEN 0
2850    RETURN
2860 Tick_xlog:       ! Makes LOG tick maks on the X axis
2870    T1=.012*(R2y-R1y)                 ! Ticks are 1.2% of plot range.
2880    MOVE R1x,R1y
2890    New_x=DROUND(Xaxmin,1)
2900    Lastx=New_x
2910    REPEAT
2920      Xm=LGT(New_x)
2930      DRAW Xm,R1y
2940      RPLOT 0,T1                      ! Make a tick here.
2950      CLIP OFF
2960      IF INT(LGT(New_x))>INT(LGT(Lastx)) THEN
2970        RPLOT 0,1.8*T1
2980        PENUP
2990        RPLOT 0,-6*T1
```

```
3000        PENUP
3010        CSIZE 3
3020        LORG 5
3030        LABEL "10"
3040        MOVE Xm,R1y
3050        RPLOT 0,-5*T1
3060        PENUP
3070        CSIZE 2
3080        LORG 1
3090        LABEL INT(LGT(New_x))
3100      ELSE
3110        IF LGT(Xaxmax)-LGT(Xaxmin)>3 THEN 3190
3120        CSIZE 2
3130        PENUP
3140        RPLOT 0,-2*T1
3150        PENUP
3160        LORG 5
3170        LABEL DROUND(New_x,1)/10^(INT(LGT(New_x)))
3180      END IF
3190      CLIP ON
3200      MOVE Xm,R1y
3210      Lastx=New_x
3220      New_x=DROUND(New_x+10^(INT(LGT(New_x))),1)
3230    UNTIL New_x>Xaxmax
3240    IF Lastx<Xaxmax AND New_x>Xaxmax THEN DRAW R2x,R1y
3250    RETURN
3260  Tick_ylog:                          ! Makes LOG tic marks on the Y axis
3270    LORG 5
3280    T1=.007*(R2x-R1x)                 ! Ticks are .7% of plot range.
3290    MOVE R1x,R1y
3300    New_y=DROUND(Yaxmin,1)
3310    Lasty=New_y
3320    IF New_y<Yaxmin THEN New_y=New_y+10^(INT(LGT(Yaxmin)))
3330    REPEAT
3340      Ym=LGT(New_y)
3350      DRAW R1x,Ym
3360      RPLOT T1,0                      ! Make a tick here.
3370      CLIP OFF
3380      IF INT(LGT(New_y))>INT(LGT(Lasty)) THEN      ! label the axis
3390        RPLOT 1.5*T1,0
3400        PENUP
3410        RPLOT -7*T1,0
3420        PENUP
3430        CSIZE 3
3440        LORG 5
3450        LABEL "10"
3460        MOVE R1x,LGT(1.15*New_y)
3470        RPLOT -6*T1,0
3480        PENUP
3490        CSIZE 2
3500        LORG 2
3510        LABEL INT(LGT(New_y))
3520      ELSE
3530        IF LGT(Yaxmax)-LGT(Yaxmin)>3 THEN 3610
3540        CSIZE 2
3550        PENUP
3560        RPLOT -2*T1,0
3570        PENUP
3580        LORG 5
3590        LABEL DROUND(New_y,1)/10^(INT(LGT(New_y)))
```

```
3600      END IF
3610      CLIP ON
3620      MOVE R1x,Ym
3630      Lasty=New_y
3640      New_y=DROUND(New_y+10^(INT(LGT(New_y))),1)
3650    UNTIL New_y>Yaxmax
3660    IF Lasty<Yaxmax AND New_y>Yaxmax THEN DRAW R1x,R2y
3670    RETURN
3680 Plot_the_data:   OFF KEY
3690    GINIT
3700    GRAPHICS ON
3710    GCLEAR
3720    LORG 5
3730    WINDOW Q1x,Q2x,Q1y,Q2y
3740    CLIP R1x,R2x,R1y,R2y
3750    IF Connect THEN
3760      INPUT "LINE TYPE <max=10> : ",Lineno
3770      LINE TYPE Lineno
3780    END IF
3790    GOSUB Plot_dest
3800    IF Crt THEN
3810      DISP "Push <continue> after plot is through."
3820      WAIT 2
3830      ALPHA OFF
3840    ELSE
3850      DISP "Now plotting on HP 9872C X-Y Plotter."
3860    END IF
3870    ON KEY 9 LABEL "Stop Plot" GOTO Stop_data
3880    CSIZE 2.5
3890    PEN 4
3900    IF Xlog THEN
3910      New_x=LGT(X(1))
3920    ELSE
3930      New_x=X(1)
3940    END IF
3950    IF Ylog THEN
3960      New_y=LGT(Y(1))
3970    ELSE
3980      New_y=Y(1)
3990    END IF
4000    MOVE New_x,New_y
4010    FOR I=2 TO N
4020      IF Xlog THEN
4030        New_x=LGT(X(I))
4040      ELSE
4050        New_x=X(I)
4060      END IF
4070      IF Ylog THEN
4080        New_y=LGT(Y(I))
4090      ELSE
4100        New_y=Y(I)
4110      END IF
4120      IF Connect THEN
4130        DRAW New_x,New_y
4140      ELSE
4150        MOVE New_x,New_y
4160        LABEL Sym$
4170      END IF
4180    NEXT I
4190    PEN Up
```

```
4200     WAIT 2
4210     RETURN
4220 Stop_data:Stopped=1
4230     PEN 0
4240     RETURN
4250 Plot_the_text:                          ! Plot all the labels in this routine.
4260     OFF KEY
4270     ON KEY 9 LABEL "Stop Plot" GOTO Stop_text
4280     CLIP OFF
4290     PEN 1
4300     LORG 6
4310     CSIZE 5
4320     LINE TYPE 1
4330     MOVE R1x+.5*(R2x-R1x),R2y+.1*(R2y-R1y)
4340     LABEL Title$
4350     CSIZE 4
4360     PENUP
4370     MOVE R1x+.5*(R2x-R1x),R1y-.09*(R2y-R1y)
4380     LABEL X$
4390     MOVE R1x-.16*(R2x-R1x),R1y+.5*(R2y-R1y)
4400     LDIR PI/2
4410     LABEL Y$
4420     LDIR 0
4430     CSIZE 3
4440     MOVE R1x+.5*(R2x-R1x),R1y-.15*(R2y-R1y)
4450     PEN 4
4460     LABEL Text$
4470     PEN 0
4480     MOVE Q2x,Q2y
4490     RETURN
4500 Stop_text:Stopped=1
4510     PEN 0
4520     RETURN
4530 Re_plot:OFF KEY
4540     ON KEY 0 LABEL "Re-Plot data" GOTO New_plot
4550     ON KEY 1 LABEL "Exit XYPlot" GOTO Ex_plt
4560     ON KEY 2 LABEL "Swap X with Y" GOTO Swap_xy
4570     ON KEY 3 LABEL "Swap titles" GOTO Sw_titl
4580     ON KEY 4 LABEL "Change titles" GOTO Ch_title
4590     Stopped=0
4600     BEEP
4610     DISP "Make a choice"
4620     GOTO 4620
4630 Swap_xy:OFF KEY
4640     DISP "Now swapping X axis data with Y axis data."
4650     Axis=0                              !  set new axis limits
4660     Temp$=X$
4670     X$=Y$
4680     Y$=Temp$
4690     FOR I=1 TO N
4700       Temp=X(I)
4710       X(I)=Y(I)
4720       Y(I)=Temp
4730     NEXT I
4740     WAIT 2.5
4750     DISP " "
4760     GOTO Re_plot
4770 Sw_titl:OFF KEY
4780     DISP "Now swapping plot title with plot subtitle."
4790     Temp$=Title$
```

```
4800    Title$=Text$
4810    Text$=Temp$
4820    WAIT 2.5
4830    DISP " "
4840    GOTO Re_plot
4850 Ch_title:OFF KEY
4860    PRINT " Correct the plot & axis titles"
4870    Print_titles
4880    Title_input
4890    GOTO Re_plot
4900 Ex_plt:GRAPHICS OFF
4910    PLOTTER IS 3,"INTERNAL"
4920    ALPHA ON
4930    PRINT CHR$(12);TABXY(25,12);"XYPlot is over."
4940    DISP
4950  SUBEND
4960  SUB Prompt_num(Q$,A)
4970    DISP Q$;
4980    OUTPUT 2;A;"#H";
4990    INPUT "",A
5000  SUBEND
5010  SUB Prompt_alpha(Q$,A$)
5020    DISP Q$;
5030    OUTPUT 2;A$;"#H";
5040    LINPUT "",A$
5050  SUBEND
5060  SUB Print_out
5070  COM /Aa/ X(1:1000),Y(1:1000),T(1:1000),D(1:1000),INTEGER N
5080  COM /Aa/ Dr(1:1000),E(1:1000),C(1:1000),A(1:1000),B(1:1000)
5090  COM /Aa/ S(1:1000)
5100    IMAGE 5X,3D,3X,6D.DD,3X,6D.DDDD,15X,3D,3X,6D.DD,3X,6D.DDDD
5110    IMAGE 6X,"No.",7X,"X=",10X,"Y=",18X,"No.",7X,"X=",10X,"Y="
5120    PRINT USING 5110
5130    FOR I=1 TO N STEP 2
5140      PRINT USING 5100;I,X(I),Y(I),I+1,X(I+1),Y(I+1)
5150    NEXT I
5160  SUBEND
5170  SUB Title_input
5180  COM /Bb/ X$[40],Y$[40],Title$[40],Text$[40]
5190    REPEAT
5200      Prompt_alpha("X axis title?",X$)
5210      Prompt_alpha("Y axis title?",Y$)
5220      Prompt_alpha("Plot title?",Title$)
5230      Prompt_alpha("Plot subtitle?",Text$)
5240      Print_titles
5250      R$="Y"
5260      Prompt_alpha("Are all data correct? <Y> or <N>",R$)
5270    UNTIL R$="Y"
5280   SUBEND
5290   SUB Func_1
5300    COM /Aa/ X(1:1000),Y(1:1000),D(1:1000),T(1:1000),INTEGER N
5310    COM /Aa/ Dr(1:1000),E(1:1000),C(1:1000),S(1:1000),A(1:1000)
5320    COM /Aa/ B(1:1000)
5330    N=401
5340    Y(79)=5.E-2      ! Initial Bubble Size after Regime II
5350    T(1)=0
5360    C(1)=0
5370    FOR I=2 TO N
5380    X(I)=(I-1)/100
5390    T(I)=293+1906/SQR(X(I))*EXP(-.39127/X(I))    ! Temperature
```

```
5400    A(I)=T(I-1)-T(I)      ! Delta T (C)
5410    IF A(I)>0 THEN
5420    B(I)=1.8*T(I)-460     ! Transform to F
5430   E(I)=6.894757E+9*(28.33669-(2.882211E-3*B(I))-(3.69785E-6*B(I)^2)+(7.7091
88E-10*B(I)^3))              ! Young's Modulus
5440    C(I)=(1.8E-6*(8.09139+(5.496948E-3*B(I))-(2.679852E-6*B(I)^2)+(4.95473E-
10*B(I)^3)))*A(I)+C(I-1)     ! Strain
5450    S(I)=E(I)*C(I)        ! Thermal Stress
5460    D(I)=2.E-4*EXP(-38000/1.98/T(I))   ! GB Diffusivity
5470    Y(I)=Y(I-1)/2.E+6
5480    Dr(I)=1.821E-11*D(I)*S(I)/T(I)/Y(I)
5490    Y(I)=(Y(I)+Dr(I))*2.E+6
5500    X(I)=X(I)-.79
5510    PRINT X(I),Y(I),S(I),T(I)
5520    END IF
5530    NEXT I
5540   SUBEND
5550   SUB Print_titles
5560   COM /Bb/ X$[40],Y$[40],Title$[40],Text$[40]
5570      PRINTER IS 1
5580      PRINT "   TITLE         :";Title$
5590      PRINT "   SUBTITLE      :";Text$
5600      PRINT "   X AXIS TITLE :";X$
5610      PRINT "   Y AXIS TITLE :";Y$
5620    SUBEND
```

ORNL/TM-11158
Distribution
Category UC-423

INTERNAL DISTRIBUTION

1-2. Central Research Library
3. Document Reference Section
4-5. Laboratory Records Department
6. Laboratory Records, ORNL RC
7. ORNL Patent Section
8-10. M&C Records Office
11. D. J. Alexander
12. C. C. Baker
13. P. F. Becher
14. L. Berry
15. T. M. Besmann
16. D. N. Braski
17. D. F. Craig
18. C. K. DuBose
19. K. Farrell
20. G. M. Goodwin
21. M. L. Grossbeck
22. C. M. Hammonds
23. J. A. Horak
24. T. Inazumi
25. O. F. Kimball
26. E. H. Lee
27-36. H. T. Lin
37. D. C. Lousteau
38. L. K. Mansur
39. J. A. Mayhall
40. P. J. Maziasz
41. H. E. McCoy, Jr.
42. D. J. McGuire
43. A. J. Moorhead
44. R. K. Nanstad
45. B. E. Nelson
46. P. L. Rittenhouse
47. A. F. Rowcliffe
48. M. J. Saltmarsh
49. T. Sawai
50. T. E. Shannon
51. J. Sheffield
52. V. K. Sikka
53. G. M. Slaughter
54. R. E. Stoller
55. M. Takeyama
56. J. M. Vitek
57. C. Wassilew
58. F. W. Wiffen
59. M. H. Yoo
60. S. J. Zinkle

EXTERNAL DISTRIBUTION

61-62. AERE HARWELL, Oxfordshire, OX11, ORA, United Kingdom

S. M. Murphy
T. Williams

63-64. ARGONNE NATIONAL LABORATORY, 9700 S. Cass Avenue, Argonne, IL 60439

R. Mattas
D. L. Smith

65-66. AUBURN UNIVERSITY, Department of Mechanical Engineering, Auburn, AL 36849

B. A. Chin
R. Zee

67-72. BATTELLE PACIFIC NORTHWEST LABORATORY, P.O. Box 999, Richland, WA 99352

A. Ermi
F. A. Garner
D. S. Gelles
E. R. Gilbert
M. L. Hamilton
R. F. Klein

73-74. ECN PETTEN, Materials Department, P.O. Box 1, 1755 ZG Petten, The Netherlands

M. I. DeVries
B. Vander Schaaf

75. GA TECHNOLOGIES, INC., P.O. Box 81608, San Diego, CA 92138

T. A. Lechtenberg

76-80. IFF, Kernforschungsanlage, Postfach 1913, D-5170 Jülich 1, F. R. Germany

P. Jung
W. Kesternich
H. Schroeder
H. Trinkaus
H. Ullmaier

81. INSTITUT FÜR MATERIAL - UND FESTKÖRPERFORSCHUNG, Kernforschungszentrum Karlsruhe, D-7500 Karlsruhe, F. R. Germany

K. Ehrlich

82-87. JAERI, Nuclear Fuel Research Division, Tokai-mura, Naka-gun 319-11, Ibaraki-ken, Japan

S. Hamada
A. Hishinuma
S. Jitsukawa
T. Kondo
H. Nakajima
M. Suzuki

88-90. JOINT RESEARCH CENTRE, Ispra Establishment, Materials Science Division 21020 - ISPRA (Varese) Italy

P. Fehici
P. Schiller
P. Von der Hardt

91. JOINT RESEARCH CENTRE, Petten Establishment, Postbus 2, 1755ZG Petten, The Netherlands

H. Scheurer

92. McDONNELL DOUGLAS ASTRONAUTICS COMPANY, EAST, P.O. Box 516, St. Louis, MO 63166

J. W. Davis

93-94. NATIONAL RESEARCH INSTITUTE FOR METALS, Tsukuba, Japan

J. Nagakawa
M. Okada

95-96. NET TEAM, Max-Planck - Institut Für Plasmaphysik, Boltzmannstrasse 2, D-8046 Garching bei München

J. L. Boutard
J. Nihoul

97. RISO NATIONAL LABORATORY, Metallurgy Department, DK 4000, Roskilde, Denmark

B. N. Singh

98-99. SCK, Boeretang 200, B-2400 MOL (Belgium)

M. Snykers
W. Vander Mevlen

100. SANDIA NATIONAL LABORATORIES, Livermore Division 8316, Livermore, CA 94550

S. Goods

101-102. SAVANNAH RIVER LABORATORY, Aiken, SC 29801

A. K. Birchenall
G. R. Caskey, Jr.

103. SCIENCE UNIVERSITY OF TOKYO, Faculty of Engineering, Kagurazaka, Shinjuku-ku, Tokyo, 162, Japan

R. R. Hasiguti

104-107. UNIVERSITY OF CALIFORNIA, 5532 Boelter Hall, Los Angeles, CA 90024

M. A. Abdou
R. W. Conn
N. Ghoniem
R. E. Nygren

108-109. UNIVERSITY OF CALIFORNIA, Department of Chemical and Nuclear Engineering, Santa Barbara, CA 93106

G. E. Lucas
G. R. Odette

110. UNIVERSITY OF MISSOURI, Nuclear Engineering, Rolla, MO 65401

A. Kumar

111. UNIVERSITY OF TOKYO, Engineering Research Institute, Bunko-ku, Tokyo, 113, Japan

S. Ishino

112-113. UNIVERSITY OF TOKYO, Materials Science Department, Bunko-ku Tokyo, 113, Japan

N. Igata
S. Iwata

114-115. UNIVERSITY OF WISCONSIN, Nuclear Engineering Department, Madison, WI 53706

G. L. Kulcinski
M. E. Sawah

116-119. DOE, OFFICE OF FUSION ENERGY, Reactor Technologies Branch, MS G-234 (GTN), Washington, DC 20545

M. M. Cohen
R. Dowling
Robert Price
T. C. Reuther

120. DOE, OAK RIDGE OPERATIONS OFFICE, P.O. Box 2001, Oak Ridge, TN 37831-8600

Office of Assistant Manager for Energy Research and Development

121-168. DOE, OFFICE OF TECHNICAL AND SCIENTIFIC INFORMATION, Office of Information Services, P.O. Box 62, Oak Ridge, TN 37831

For distribution as shown in DOE/TIC-4500, Distribution Category UC-423 (Magnetic Fusion Reactor Materials)

☆U.S. GOVERNMENT PRINTING OFFICE 1989-648-119/00040